Dynamical evolution of intense mesoscale Ierapetra eddies in connection with orographic wind forcing

Artemis Ioannou

Sorbonne Université

Ecole doctorale des sciences de l'environnement d'île-de-France (Paris)

Laboratoire Météorologie Dynamique

Dynamical evolution of intense mesoscale Ierapetra eddies in connection with orographic wind forcing

Par Artemis Ioannou

Thèse de doctorat de l'oceanographie physique

Dirigée par Alexandre Stegner et Sabrina Speich

Présentée et soutenue publiquement le 02 octobre 2019

Devant un jury composé de :

M.	Doglioli Andrea	Professeur	Rapporteur
M.	Roullet Guillaume	Professeur	Rapporteur
Mme	Taupier-Letage Isabelle	Chargée Researcher	Examinateur
M.	D'Ovidio Franscesco	CNRS Researcher	Examinateur
M.	Kalfas Anestis	Professeur	Examinateur
M.	Alexandre Stegner	Professeur	Directeur de thèse
Mme.	Sabrina Speich	Professeur	Directrice de thèse

Résumé

Le tourbillon Ierapetra (IE) est l'un des plus grands et des plus longs tourbillons de mésoéchelle de la Méditerranée orientale (MED). Situé au sud-est de la Crète, la formation récurrente de IE a été attribuée au forçage éolien régional. Pourtant, il n'y a pas que très peu d'informations sur les caractéristiques de leur dynamique, ni aucune preuve que l'IE soit forcé par le vent. Dans cette étude, une caractérisation complète de la dynamique des tourbillons Ierapetra est réalisée. Premièrement, en utilisant des observations satellites de la hauteur de surface de la mer ainsi que l'algorithme de détection de tourbillons AMEDA, les tourbillons Ierapetra sont suivis sur 22 ans (1993-2014). Des informations sur les caractéristiques (telles que le rayon, les vitesses etc.) et les trajectoires des tourbillons sont extraites. On observe une forte variabilité dans leur intensité ($Ro = 0.07 - 0.27$) et une potentielle réintensification un an après leur formation. Ce processus d'intensification est d'abord observé ici et peut conduire à un doublement de l'intensité en moins de 3 mois. Pour les tourbillons Ierapetra, nous avons observé que les termes d'accélération centrifuge ne peuvent pas être négligés. Une méthode itérative est optimisée sur des tourbillons idéalisés pour retrouver avec la meilleure précision possible, l'équilibre cyclogéostrophique. L'importance des corrections cyclogéostrophiques est évaluée pour la MED. Lorsqu'elles sont prises en compte, les estimations de vorticité du tourbillon de base IE peuvent atteindre des valeurs fortement négatives $\zeta(0)/f = -1$. Trois campagnes océanographiques spécifiques (EGYPTE/EGITTO, BOUM et PROTEVS-PERLE) fournissant des mesures de vitesses de tourbillons sont également présentées. La comparaison enre les observations et les mesures in situ démontre l'importance des termes cyclogéostrophiques pour l'estimation correcte des vitesses de tourbillon. Enfin, le forçage du vent est étudié en tant que mécanisme principal de la dynamique des IE. Une forme idéalisée de forçage du vent climatologique pouvant représenter le régime de forçage étésien est construite à partir des jeux de données de vent de la réanalyse ALADIN. L'effet transitoire du forçage étésien idéalisé est ensuite évalué avec un modèle de gravité réduite. Différentes simulations numériques sont effectuées afin d'étudier l'effet isolé d'un tel forçage sur la surface de l'océan. Globalement, les résultats démontrent la formation d'un anticyclone persistant. La magnitude de forçage du vent mais aussi sa durée sont des paramètres clés permettant de contrôler l'intensité des tourbillons. Le rayon du tourbillon est principalement contrôlé par les caractéristiques spatiales du forçage du vent. De plus, nous retrouvons le processus d'intensification des anticyclones préexistants en présence de cisaillement. Les résutats de cette thèse suggèrent que les tourbillons Ierapetra sont parmi les plus forts tourbillons de moyenne échelle de la mer Méditerranée. De plus le forçage régional par le vent est suffisant pour expliquer les caractéristiques des tourbillons observés. Un jet de vent orographique asymétrique ou des valeurs γ élevées de forçage orographique symétrique sont les conditions préalables nécessaires pour favoriser la formation d'anticyclones puissants dans l'océan.

Abstract

The Ierapetra eddy (IE) is one of the largest and longest-lived mesoscale eddies of the eastern Mediterranean Sea (MED). Located in the South East corner of Crete, the IE recurrent formation has been attributed to the regional Etesian wind forcing. Yet there are no many information on the eddy dynamical characteristics nor evidences that the IE is wind-forced. In this study, a full characterization of the Ierapetra eddy dynamics is attempted. Firstly, by using satellite observations of sea surface height and AMEDA eddy detection algorithm, the Ierapetra eddies are followed over 22 years (1993-2014). Information on the eddy characteristics (such as radius, velocities, vorticity) and the eddy trajectories are retrieved. The Ierapetra eddies are found to experience strong variability in their intensity (Ro=0.07-0.27) while one year after formation they may re-intensify. This intensification process is firstly observed here and can lead to an doubling of the eddy intensity in less than 3 months. For the Ierapetra eddies, we found that the centrifugal acceleration terms cannot be omitted. An iterative method is optimized on idealized eddies to recover with best accuracy the cyclogeostrophic balance. The importance of cyclogeostrophic corrections are evaluated for the total MED. When taken into account, estimations on the IE core vorticity may reach values of highly negative vorticity $\zeta(0)/f = -1$. Three specific oceanographic campaigns (EGYPT/EGITTO, BOUM and PROTEVS-PERLE) that provide information on measured eddy velocities are also presented. Comparison between the observations and in-situ measurements demonstrate the importance of the cyclogeostrophic terms for the correct estimation of the eddy velocities. Lastly, the Etesian wind forcing is investigated as the driving mechanism for the IEs dynamics. An idealized climatological wind forcing shape that can represent the Etesian forcing regime is build based on ALADIN reanalysis wind datasets. The transient effect of the idealized Etesian forcing is then evaluated with a reduced gravity model. Various numerical simulations are performed in order to investigate the isolated effect of such forcing to the ocean surface. Overall the results demonstrate the formation of a persistent anticyclone. Both the wind forcing magnitude but also the wind forcing duration are key parameters that control the formed eddy intensity. The eddy radius is mainly controlled by the spatial characteristics of the applied wind forcing. Moreover, we recover the intensification process for pre-existing anticyclones in the presence of the shear wind. The findings of this thesis suggest that the Ierapetra eddies are among the strongest mesoscale eddies of the Mediterranean Sea while the regional wind forcing is sufficient to explain the observed eddy characteristics. An asymmetric orographic wind jet or high γ values of a symmetric orographic forcing are the necessary preconditions to favor the formation of strong anticyclones in the ocean.

Contents

CHAPTER 1

Introduction

1.1 Oceanic Eddies

The synoptic view ($\sim 100\,km$) of the global ocean as captured from satellite observations reveals the predominance of oceanic eddies. Eddies of various sizes and shapes as well as cold or warm fronts interact with each other and move constantly, modifying perpetually the ocean. Meandering of intense currents (ex. Gulf-Stream and Kuroshio), flow past obstacles (such as islands), interactions with complex topography and coastlines, temperature fronts as well as external forces such as the wind, are some of the various processes that could trigger instabilities and lead to eddy genesis. One of the main characteristics of oceanic eddies is that they have closed streamlines and as a consequence they can trap in their core, water masses from the region of their formation. Depending on their size, the volume of the water mass that they may entrap could be significant. These trapped water masses physically can remain isolated from lateral exchanges with the surrounding environment. As the eddies propagate, water can be advected over long distances and for a long time period. Eddies participate in the larger scale circulation transferring heat and momentum, promoting mixing and diffusion across the ocean. Oceanic eddies are main sources for exchanges between chemical tracers and biological species while they enhance the surface oceanic biological productivity. For various domains such as geophysical and marine sector, the marine renewable technology, shipping routes as far as oil platforms etc., knowledge of how and where these phenomena occur is of major importance. With the global ocean to already experience major heat and carbon absorption, there is an necessity to understand better eddy dynamics, how they may affect the climate as well as how they might be changing in the future.

Among the chaotic turbulent oceanic fields several coherent and long-lived eddies stand out (ex. Agulhas Rings, eddies of the Gulf Stream, eddies in the Kuroshio extend, the Alboran eddies etc.). Their lifetimes sometimes are remarkable long (Agulhas Rings >3 years) given the continuous turbulent interactions they undergo. The mechanisms that lead to eddy formation and that guarantee their robustness are not yet fully understood. So far numerous observational, theoretical and experimental studies (Dewar and Killworth (1995); Stegner and Dritschel (2000); Baey and Carton (2002); Perret et al. (2006a); Benilov and Flanagan (2008); Lazar et al. (2013b,a); Lahaye and Zeitlin (2015); Yim et al. (2018).etc) have been carried out in order to identify the key dynamical parameters that control the eddy dynamics, their stability, their dispersion and dissipation due to internal processes as well as external forcing.

The dynamics of oceanic eddies are mainly controlled by both the effects of the Earth's rotation and the ocean stratification. In order to determine the relative magnitudes of the various forces contributing to their dynamics, their horizontal scale (L) is usually compared with the radius of deformation R_d. The radius of deformation R_d is an intrinsic scale of the ocean that accounts for the ocean stratification. Contrary with homogeneous density fluids, the ocean could be considered as a finite superposition of layers of fluid with different densities $\rho = \rho(T, S, p)$ (linear stratified) that is function of temperature T but also salinity S and pressure p. Estimations of the first baroclinic

deformation radius in the global ocean spans from $20 - 200\,km$ (Chelton et al., 1998). Eddies with horizontal scales R that are equal ($L \geqslant R_d$) or larger ($L > 2 - 3R_d$) than the local deformation radius are considered mesoscale. For mesoscale eddies the Earth's rotation is a dominant force. For eddies of smaller scale than the radius of deformation ($L < R_d$) the effect of Earth's rotation is negligible and they are characterized as submesoscale. In this thesis we focus on the Mediterranean Sea where the radius of deformation ranges between $10 - 15\,km$. Therefore, a typical mesoscale eddy will have a length scale that ranges between $10 - 50\,km$.

The vertical extent of mesoscale eddies is usually much smaller than their horizontal length scale ($H \ll L$). Thus, their dynamics in many cases could be considered as two-dimensional. Of special importance is how the eddy turn–over time compares with the Earth's rotation. This is quantified with the Rossby number Ro which is defined as the ratio between rotation and advection terms in the momentum balance of the Navier-Stokes equations:

$$Ro = \frac{(\underline{u} \cdot \nabla)\underline{u}}{2\Omega \times \underline{u}} = \frac{U}{fL}$$

where U is the typical velocity scale and L the typical length scale, f the Coriolis parameter $f = 2\Omega sin(\phi)$ where Ω and ϕ is the latitude. This particular Ro definition is only one of the several ways that are frequently used to characterize the advective flow of an eddy. A different measure of eddy strength, is the eddy vorticity (same scale U/L) compared with the Coriolis term as $Ro = \zeta/f$ (Douglass and Richman, 2015). Regardless, the choice of metric, when Ro is relatively small ($Ro \ll 1$), the main balance in the momentum equation reduces to the balance of the Coriolis force and the acceleration is due to pressure gradients ($-\frac{1}{\varrho}\nabla p$) associated with the eddy density anomaly. In that case the flow is characterized as geostrophic ($f\hat{\mathbf{k}}\times\underline{u} + \frac{1}{\varrho}\nabla p = 0$). The geostrophic motion, requires that the flow remains along the pressure isobars. For the Northern Hemisphere, this means that the flow is directed perpendicular and to the right of the pressure gradient term. In the oceans, usually the eddy maximum density anomaly is surface intensified and this results in a positive or negative anomaly in the sea surface height (SSH). In the Northern Hemisphere, positive SSH anomaly will lead to a counterclockwise rotation and the eddy is characterized as anticyclonic (see Figure 1.1). Opposite a cyclonic eddy is associated with a clockwise rotation as a result of a negative SSH anomaly.

Observations show that mesoscale vortices are close to the geostrophic equilibrium. Nevertheless, it is not the only equilibrium that could dominate them. For slightly stronger Ro numbers Ro∼O(0.1) the balance becomes cyclogeostrophic. In those scales, the flow curvature becomes important and the centrifugal force can not be omitted ($-\frac{V_\theta^2}{r} + fV_\theta + \frac{1}{\varrho}\frac{\partial p}{\partial r} = 0$). The leading orders in the momentum balance are between the Coriolis force and the pressure force and the centrifugal force. The balance between the 3 forces is shown in Figure 1.1. The centrifugal force is directed always outward of the motion. This means that in the case of an anticyclone, it will act complementary to the pressure gradient, while in the case of a cyclone the same pressure gradient should balance both the Coriolis and the centrifugal force. It results in an increase(decrease) of the tangential velocity in an anticyclonic(cyclonic) system. For intense meandering currents or eddies this may lead to high underestimations on the flow velocities. Penven et al. (2014) illustrated for the case of the Mozambique channel that omitting the cyclogeostrophic term can lead to significant underestimations in the current velocities but also in the eddy velocities. Errors were estimated to account for 40% in the case of anticyclones.

Usually anticyclonic (cyclonic) eddies have a warm (cold) sea surface temperature due their sense of rotation. Depression of the isopycnals for the anticyclones will lead

to depression of warmer surface water in their core. Contrary, the uplifting of the isopycnals in the cyclonic eddies usually results in colder patched of water in their center. Energy is contained within the isopycnal deviations of a mesoscale eddy in the form of available potential energy (PE). The ratio of the kinetic (KE) over the potential energy (PE) stored within an eddy is defined with the dimensionless Burger number defined as:

$$Bu = \left(\frac{Rd}{L}\right)^2$$

The larger the eddy scale L from the R_d the larger the available PE energy that is stored in the sloped isopycnals. Contrary towards smaller eddy scales the energy is mainly kinetic (KE). The way the dimensionless quantities Ro and Bu differ for the mesoscale eddies set different dynamical regimes (Perret et al., 2006a,b, 2011; Stegner, 2014).

Apart from the dynamical point of view, the depression or uplifting of the deviations caused by eddies are crucial to ocean biology. Cyclonic eddies due to their contribution in the upward-tilting of the isopycnals, bring waters rich in nutrient from the interior of the ocean to the surface eyphotic zone (first $100\,m$ of the ocean). This is an important process in order to sustain chlorophyll concentration in the upper layers and achieve photosynthesis which results in an enhancement of the surface oceanic biological productivity (McGillicuddy et al., 2007). Even if, cyclones are major contributors to formation of plumes, anticyclones could also contribute to the deeper ocean ventilation. The Ekman pumping mechanism in the eddy interiors that results from their interaction with the wind forcing generates upwelling in the interiors of anticyclones and downwelling in the interiors of cyclones (McGillicuddy et al., 2007; Gaube et al., 2015). Brannigan (2016) illustrated that wind forcing above an eddy promotes the vertical mixing and upwelling of nutrients in their core through submesoscale processes that enhance vertical transport and mixing of properties to smaller scales (direct energy cascade).

The oceanic circulation responds strongly to the wind forcing variations that can change daily, seasonally and inter annually. Even if the role of wind forcing above pre-existing eddies has been highlighted there are less studies that investigate its role to eddy generation. Usually the lee of islands are areas of strong seasonal wind forcing that has been associated with high eddy kinetic energy. Such areas provide motivation to examine the wind forcing role as a driving mechanism for eddies.

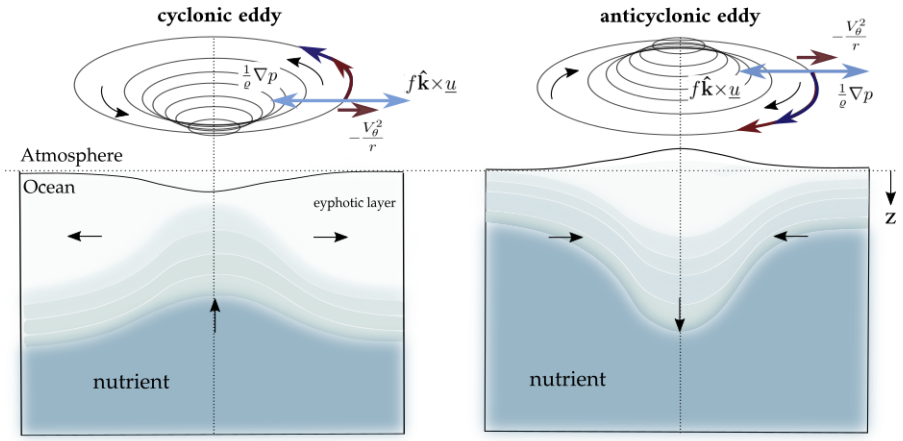

Figure 1.1: *Schematic representation of the isopycnal structure and surface signature of a mesoscale surface-intensified a) cyclonic and b) anticyclonic eddy. Geostrophic and cyclogeostrophic balances are depicted.*

1.2 Oceanic eddies and orographic wind forcing

Generation of eddies by orographic wind forcing has been previously detected in several regions around the world (Figure 1.2). The physical process involved is the formation of a wake behind an obstacle which in this case is caused by the island topography. The upstream wind is blocked by the island terrain, creating a high upwind pressure system. Contrary downstream, in the island wake, low velocities are observed and due to mass conservation, flow is accelerated in the island edges. Strong shears are created sidewards forming positive and negative wind stress curl regions. The resulting wind stress curl areas in the island edges could spin-up the ocean surface and lead to oceanic eddy formation through the Ekman pumping mechanism. The upper layer of the ocean will experience a convergence or divergence of the velocity fields depending on the sign of the wind stress curl (negative or positive respectively). Based on continuity equation it should be compensated by a downward or upward movement of the isopycnals. The upwelling and downwelling is proportional to the wind stress curl as follows:

$$W_E = -\frac{1}{\rho_{sea}}\hat{\mathbf{k}}\nabla \times \left(\frac{\tau}{f}\right) \tag{1}$$

where τ is the wind stress, ρ_{sea} the water density and f is the Coriolis parameter defined as $f = 2\Omega \sin\theta$, where θ is the latitude and $\Omega = 7.27 \times 10^{-5}\, s^{-1}$ the angular Earth's velocity.

However, the intensity of the upstream flow can also modulate the response of the downstream wake. At specific conditions vortex shedding could be triggered (Figure 1.2). Based on laboratory experiments, in the case of deep islands the ratio of the island size D in comparison with the radius of deformation was found to play a significant role in the downstream wake response. When the island size is similar with the radius of deformation a Von-Kármán vortex street is created similar to the non-rotating case. For mesoscale wakes ($R \gg R_d$), only a street of anticyclonic eddies will occur further downstream (Perret et al., 2006a; Stegner, 2014). Numerical investigations by Perret et al. (2006b) support this asymmetry, as the more unstable modes of the oceanic response are found to associate with the anticyclonic growth rates.

The contribution of the wind forcing shear in comparison with the oceanic shedding is difficult to distinguish in the real ocean. In the Hawaiian islands, high mountainous islands act as a barrier to the upstream wind speeds, which range between $5 - 10\, {}^{m}/_{s}$ during summer, and create an array of positive and negative wind stress curl in the islands lee areas. The curl is ranging from $(-2.6, 2.9)10^{-6} Nm^{-3}$ curl and the estimated Ekman pumping velocities of the order of $w_E = 3 - 4\, {}^{m}/_{day}$. Downstream on the oceanic side both cyclonic and anticyclonic eddies are generated. Their typical radii are ranging $R_{max} = 40 - 60\, km$ and their drifting speeds are estimated around $5 - 9\, {}^{km}/_{day}$. Cyclones seem to be trapped in the lee of the islands while anticyclones propagate westward. The relative eddy vorticity reach finite values of $\zeta/f > 1$. The involvement of an upstream current was investigated by Jia et al. (2011). Based on a fully stratified numerical model, Jia et al. (2011) illustrated that a westward upstream flow alone could explain the formation of the eddies in the region and capture their westward propagation. However, the wind forcing mechanism was found to be more consistent with the observed eddy characteristics in terms of time of occurrence, strength and eddy kinetic energy (EKE). Yoshida et al. (2010) tried to explain which mechanism prevails, by associating the timescale variability of the kinetic energy and sea surface height of the eddies with the wind stress curl variability downstream of the islands. A lag of 2 weeks between the oceanic and atmospheric response was found, emphasizing that the ocean acts like an integrator of the wind forcing for small frequencies rather than the fast ones. Jiménez

et al. (2008), from numerical outputs, highlighted that an upstream current could induce downstream eddies in the absence of wind forcing, while wind forcing alone could only lead to the generation of stationary dipole. In the Hawaiian islands complex (Calil et al., 2008; Jia et al., 2011; Chavanne et al., 2002), as well as in the lee of Madeira island (Caldeira et al., 2014; Couvelard et al., 2012; Piedeleu et al., 2009) both oceanic shedding and wind stress shear seems to be equally important.

Formation of oceanic dipoles, in the absence of background current has been mentioned only in few studies. In the Philippines islands (Wang et al., 2007; Pullen et al., 2008), the formation of an oceanic a dipole has been detected and associated with specific wind events during the monsoon period. Strong wind jets that reached $10 - 16\,^{m}/_{s}$ wind speed prevail in the region as a result of the monsoon surges and their interactions with the complex topography of the volcanic island. Numerical investigation by Pullen et al. (2008) showed that steady monsoon winds could result in the formation and detachment of an oceanic dipole. Wind temporal variations drove a westward propagation of the dipole with the anticyclone to survive the longest. The absence of any background current emphasizes the role of the shear wind forcing as a robust mechanism for eddy formation. Connection of offshore directed orographic wind jets through mountain gaps of ($\sim 2000\,m$ height) with the formation of oceanic eddies was already mentioned in the Gulf of Tehuantepec and Gulf of Papagayo (Stumpf and Legeckis, 1977) in Mexico. Based on meteorological station measurements at the mountain gaps exits and sea surface temperature analysis, the formation of three anticyclonic gyres offshore of the Gulfs has been associated with upstream wind forcing events. Moreover, based on thermal images coastal induced upwelling was detected to be entrained and directed by the strong wind jets further offshore. The sea level response followed with no time-lag the wind forcing variations. A ship survey was conducted few days after a strong wind event and cross one of the formed anticyclonic eddies. VMADCP measurements revealed eddy velocities that reached $80\,^{cm}/_{s}$. McCreary et al. (1989) investigated numerically the response of the ocean to such orographic wind jets based on an idealized representation of their spatial distribution and temporal variation of the forcing. In order to reproduce the observed redirection of cold coastal upwelled waters further offshore, he used a non-linear shallow water model that allowed entrainment of water from the deeper layer to the upper one. The orographic wind jets were found to spin-up the ocean and result in the formation of an oceanic dipole. When entrainment of cool water was considered, the cyclonic gyre was eliminated providing a first explanation of the observed prevalence of the anticyclonic eddies in the region. Chang et al. (2012) investigated the orographic wind jet gaps in the same area. They emphasized that the Tehuantepec wind forcing jet was asymmetric in comparison with the mean jet direction axis, a fact that could also explain the stronger anticyclonic eddies in comparison with the cyclonic ones.

More recently in the Red Sea (Zhai and Bower, 2013), orographic wind jets exiting the Tokar mountain gaps were associated with spin-up of a vortex dipole. Similarly, the atmospheric variability was linked with the oceanic dipole formation (Sofianos and Johns, 2007). The pair of cyclonic and anticyclone eddy was reproduced with a 1.5 shallow-water model moving eastwards due to self-advection. Nicholls et al. (2015) investigated the ocean response for the same orographic wind forcing with a fully stratified model (ROMS). An asymmetry between the formed eddy dipole was observed. The model reproduced consistently anticyclonic eddies that were stronger than the cyclonic ones. Although that was not captured in the idealized simulations performed by Zhai and Bower (2013). The difference between the two studies were attributed to the different temporal variations of the wind forcing used. The applied unsteady forcing (Nicholls et al., 2015) in comparison with steady one used in Zhai and Bower (2013) is assumed the main reason for explaining this asymmetry.

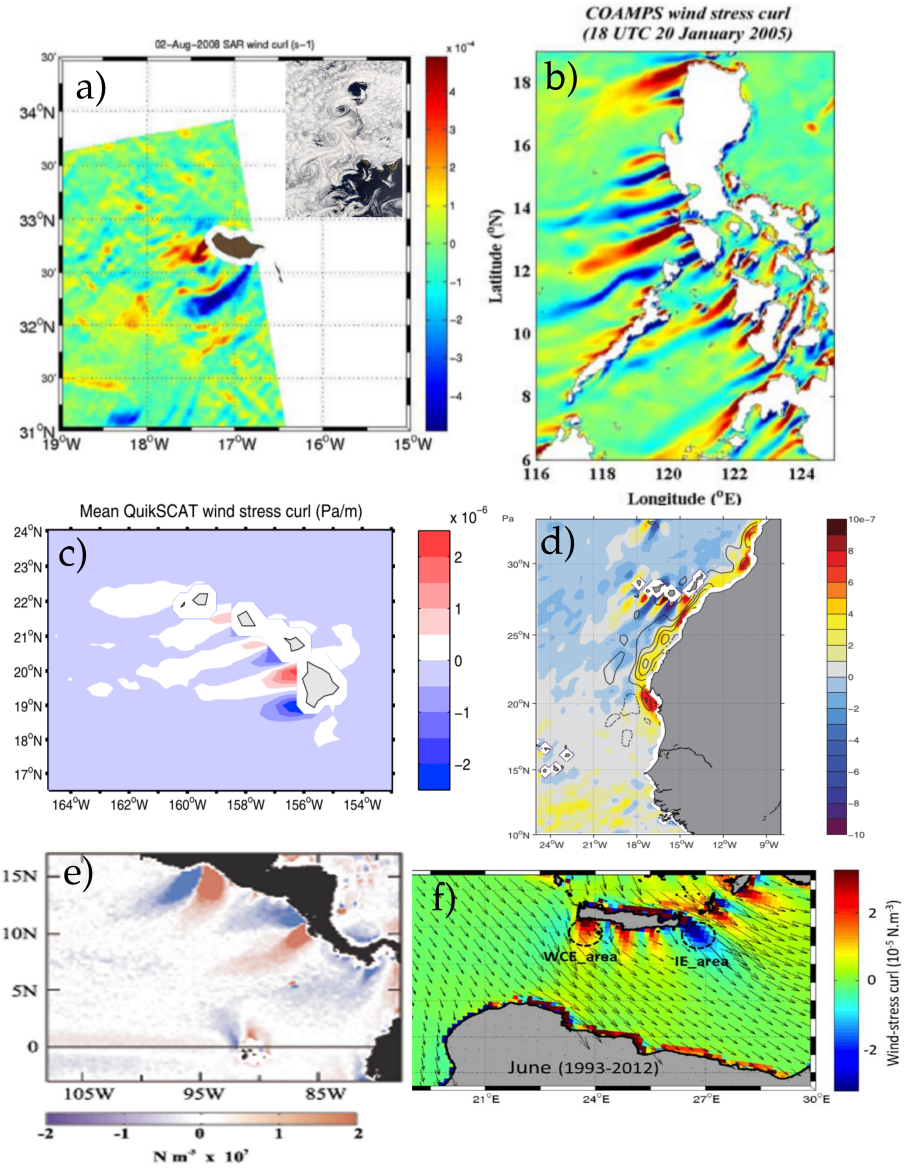

Figure 1.2: *Typical examples of atmospheric wake formed in the lee of islands resulting in positive(red) and negative(blue) wind stress curl $\nabla \times \tau$ regions: a) the Madeira islands b) Philippines Islands c) Hawaiian islands d) Gran-Canaria Islands e) Gaps of Tuahantepec & Papagayo in Mexico and f) in the Crete Island in Greece.*

1.3 Monitoring mesoscale eddies

Nowadays remote sensing has enabled the full *2-D characterization of the oceanic fields*. Satellites can provide daily snapshots of the sea surface temperature of the ocean (Figure 1.3(a)). For specific bands of the electromagnetic signals (from visible part to near-infrared (IR)), the atmosphere becomes almost transparent and the surface temperature of the ocean can be obtained in high resolutions ($1-4\,km$). Moreover, information on the surface oceanic topography can be obtained by radar altimeters. This is achieved by transmitting signals to the Earth along the satellite tracks and receiving their echoes. Radar altimeters can measure the sea surface height with at least $3\,cm$ accuracy depending on the spatial homogeneity of the measured surface (ocean, ice, rivers or land surface). Even if the information they provide is narrowed along the satellites tracks, one of their main advantages in contrast with thermal images, is that they are not affected by the cloud coverage. Daily observations from satellite altimeters are not enough to capture the simultaneous evolution of the ocean surface. Nevertheless, as the ocean is evolving in larger timescales than the atmosphere, the signal of altimeters from several days could be combined and create merged sea surface height maps (Figure 1.3(b)). Such techniques have been developed the last decades while objective interpolation methods (LeTraon et al. (1998)) are used to create a gridded product that describes the ocean surface height. Oceanic eddies can be then recognized from their sea surface signature. An eddy has a sea surface height (SSH) and sea surface temperature (SST) signature that is visible from space and corresponds to its density structure (Figure 1.3(a-b)).

To describe the oceanic topography at least 3 altimeters are required in order to capture reliable information and observe eddies and mesoscale phenomena (Ducet, 2000). For the Mediterranean Sea, the gridded maps of the SSH and geostrophic velocities are provided ($1/8^o$) horizontal resolution ($dX \simeq 12km$). The spatial resolution is higher than the global products ($1/4^o$) (https://www.aviso.altimetry.fr/en/techniques/altimetry.html). Although, due to the small Rossby radius of the Mediterranean which is around $10-15\,km$ (Escudier et al., 2016), the altimetric products cannot fully resolve the internal deformation radius R_d, a fact that has prevented a systematic monitoring of mesoscale activity. However, the surface signature of large mesoscale eddies with a typical radius that exceed the deformation radius are generally detected (Isern-Fontanet et al., 2006; Pascual et al., 2007; Rio et al., 2007; Amitai et al., 2010; Mkhinini et al., 2014).

The characterization of the sea surface height fields in spatial and temporal basis was followed by the development of eddy detection algorithms. Based on physical and geometrical characteristics of the gridded maps, eddies can be tracked and followed in real time (Nencioli et al., 2010; Le Vu et al., 2018). Most recent algorithms provide new methods to identify also splitting and merging events (Li et al., 2014; Du et al., 2014; Le Vu et al., 2018; Laxenaire et al., 2018) as well as interactions between eddies during their evolution in time. Information on eddies dynamical properties can be easily and automatically retrieved. In this study we will use the AMEDA eddy detection algorithm which identifies eddies based on a minimized angular momentum criterion (Le Vu et al., 2018). The eddy main characteristics such as the radius, velocities, intensity, kinetic energy, ellipticity, shapes, centers etc. ca be identified as well as their evolution time Figure 1.3(c). Dimensionless numbers such as the Rossby number of the eddy ($Ro = \frac{V_{max}}{fR_{max}}$) or the Burger number ($Bu = (\frac{R_d}{R_{max}})^2$) can be easily estimated based on the detection of the maximum eddy velocity V_{max} and corresponding eddy radius R_{max}.

Automatic detection algorithms have eased the eddy identification. Although, the sparsity of measurements from the satellite tracks to monitor the total ocean surface remains a challenge and could sometimes also lead to erroneous detections (see section 2.7). Moreover, usually the velocity fields are associated with the sea surface height

based on the geostrophic approximation that may result in underestimations for eddies of high intensity Ro. Still, satellite altimetry remains a powerful and essential tool to recover information on eddy dynamical characteristics and monitor their mesoscale variability.

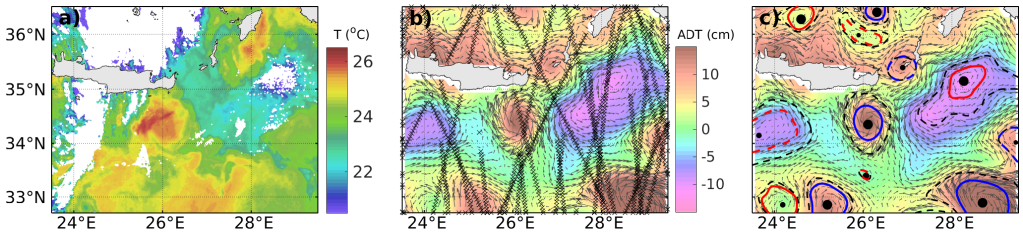

Figure 1.3: *Monitoring the ocean surface topography from satellites. a) Snapshot of Sea surface temperature (^oC) fields for the Eastern Mediterranean Sea. b) Sea surface height (cm) as derived by combined satellite tracks ($\pm 5 days$). AVISO product illustrated for the 3 November 2018. Satellite tracks are shown with the x crosses. c) AMEDA eddy detection algorithm (Le Vu et al., 2018) applied in the sea surface height fields.*

Even if, the eddy surface signature can be observed from remote sensing, there are still open questions on how the eddies structure may vary *below the ocean's surface*. Many oceanographic campaigns are devoted to that purpose, as unlike the atmosphere the ocean is not transparent and information on their vertical structure can be only obtained with in-situ measurements. We mention few among the numerous techniques (CTD, LADCP,VMADCP, SEASOR, GLIDER, XBT,etc.) that have been developed and used over the years. One of the common ways of vertical profiling can be achieved with conductivity-temperature-depth profilers (CTD). Sampling of their water properties such as temperature $T\,(^oC)$, and salinity $S\,(psu)$ along the vertical $p\,(dbar)$ can be used in order to distinguish water masses. Density profiles along the eddy center can provide information in their velocities due to the thermal wind balance. One of the few ways that directly measure oceanic velocities are the Vessel Mounted Acoustic Doppler Current Profilers (VMADCP). The VMADCP is installed in the bottom of the ship and measures oceanic velocities along the boat route (see Figure 1.5(a)). Based on the Doppler effect, beams are transmitted in specific frequencies of $150\,kHz$ and $38\,kHz$. Each measurement provides an backscattered signal that is usually averaged in a period of 3 or 10 minutes. The absolute oceanic velocity can be obtained by tracking the ocean bottom. When the ocean bottom is out of range (deep bathymetry), velocities can be acquired only relative to the vessel motion. VMADCP are among the few measurements techniques that can provide directly velocity measurements when crossing an eddy providing high resolution of the eddy velocity vertical distribution along the few first hundred meters $(300-350)\,m$.

Moreover, towards achieving continuous monitoring in the ocean, the Argo program started in 2000. Argo floats are subsurface Lagrangian drifters that operate in a repeated cycle and measure temperature $T\,(^oC)$ and salinity $S\,(psu)$ every cycle period t_i. More than 3000 Argo profilers (http://argo.ucsd.edu) are drifting freely and sample in real time water properties. If a float is trapped within an eddy it can provide useful information on the eddy vertical structure. The profiler contains a hydraulic pump that allows the float to change (increase/decrease) its internal volume by pumping oil to an internal bladder. This permit them to move vertically (upward/downward) in the water column. Floats descend to a prescribed parking depth where they evolve freely with the background oceanic motion for a given time. Each float carries a thermistor and a conductivity sensor. Before resurfacing, the floats descend in a lower depth typically $1000-2000\,m$ and start the data acquisition until they rise up to the surface. Once in the surface, data can be transmitted in real time via the Argos satellite system. The floats

return on their parking depth for the next cycle. Each float is preprogrammed to operate usually for more than 200 cycles for a 10 days cycle. Although this can be modified depending on the mission. Argo floats can maintain continuous independent operation that could reach up to 6 years. An example of Argo float measurements that where trapped in an Ierapetra eddy is shown in Figure 1.5(b). The different hydrodynamic characteristics of the eddy interior compared with the surrounding environment is visible. Inside the eddy, a strong vertical homogeneous layer in temperature and salinity is observed that suggests strong vertical mixing in the upper layers. The eddy anomaly can be defined in comparison with the surrounding environment characteristics. In this case the eddy anomaly is estimated of the order of 5^oC.

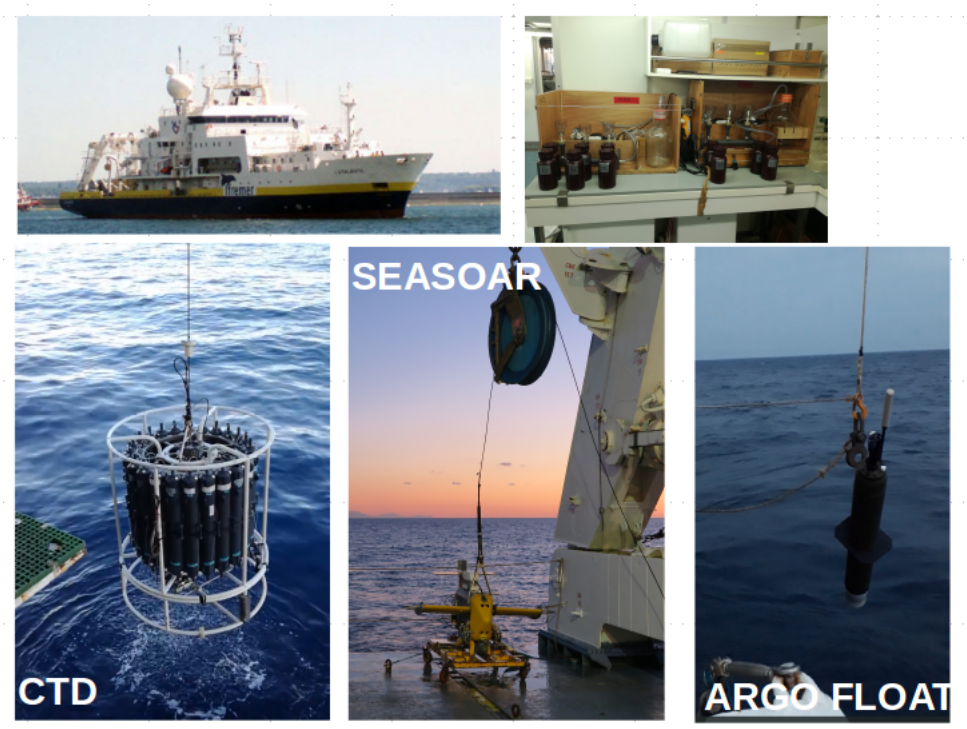

Figure 1.4: *Monitoring the ocean vertical extend during field campaigns. Few of the different measurement equipments used are illustrated.*

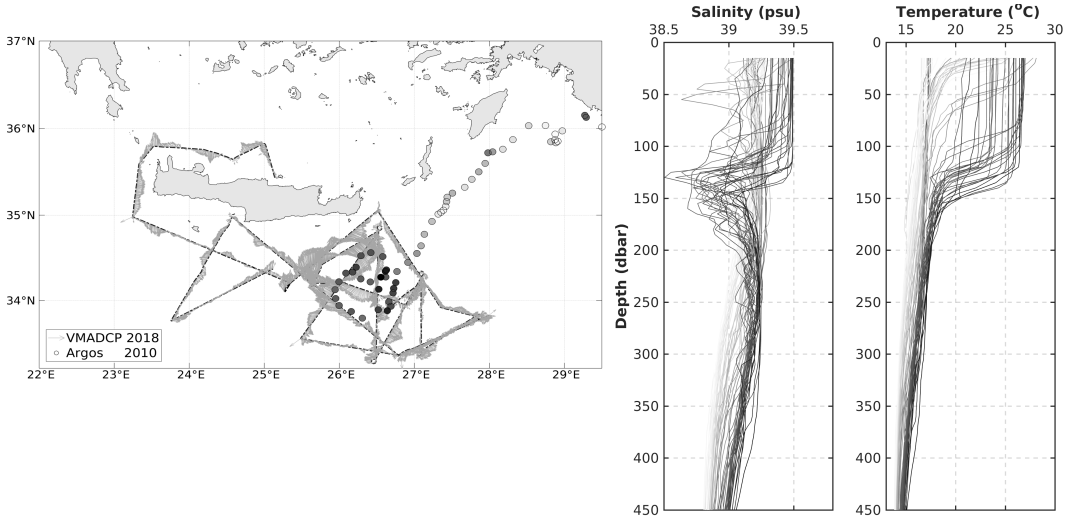

Figure 1.5: *(a) VMADCP measurements during PROTEVS-PERLE campaign leg 2 held in 2018 in the Levantine basin. (b) The trajectory of an Argo float drifted in the Northern Levantine from February to December 2010 where it was captured in the Ierapetra eddy in 2010 c) Temperature and Salinity measurements from Argo profile along its trajectory in winter 2010.*

1.4 Mediterranean Circulation

We focus in this thesis on the Mediterranean Sea (MED) which constitutes compared with the global ocean, a small basin. Even if the Mediterranean Sea is relatively small, its circulation system is complex and dominated by many coastal currents and long-lived mesoscale eddies (Figure 1.6). Up to now numerous studies have been conducted, with purpose to describe the general MED circulation and identify the main dynamics that control it. Its seasonal and interannual variations has been investigated with observations of sea surface temperature SST, satellite altimetry, in-situ measurements and numerical models. The *thermohaline processes*, the *prevailing wind forcing regimes* but also the *mesoscale eddy fields* are found to be important components that drive the total MED circulation system.

In-situ observations in the Strait of Gibraltar confirm that the MED undergoes a *thermohaline cycle*. Fresh Atlantic waters (AW) enter the MED in the upper layers and follow a counterclockwise circulation due to their deflection by the Coriolis force (Millot and Taupier-Letage, 2005; Hamad et al., 2005, 2006). Density differences between surface MED waters and surface Atlantic waters result to strong anticyclonic eddies called *Alboran eddies* that spread AW waters further east (Viudez et al., 996a,b). Contrary, in deeper layers, in the Gibraltar strait, saline colder waters are observed to exit MED (Millot and Taupier-Letage, 2005)! The spreading of colder and denser waters (T,S,σ)$\sim$($15-16^oC$, $38-38.5\,psu$, $28-29\,kgm^{-3}$) is detected at $\sim 1000\,m$ depth and it can lead to the formation of subsea vortices called Meddies (Bashmachnikov et al., 2015). Back in the MED further East, along the Algerian continental slope, the AW are regrouped in the *Algerian current* that follows the continental slope eastward Taupier-Letage et al. (2003). The Algerian current is usually detached from the African coast near the Sardinia region forming many mesoscale anticyclonic eddies and spreading the AW further offshore. Numerical studies, provide evidence that these eddies can be indeed be a result of current instabilities that may occur along the sloping topography. The instability is mainly controlled by the current intensity and the steep bathymetric slope (Sutyrin et al., 2009; Pennel et al., 2012). Some of these Algerian eddies are

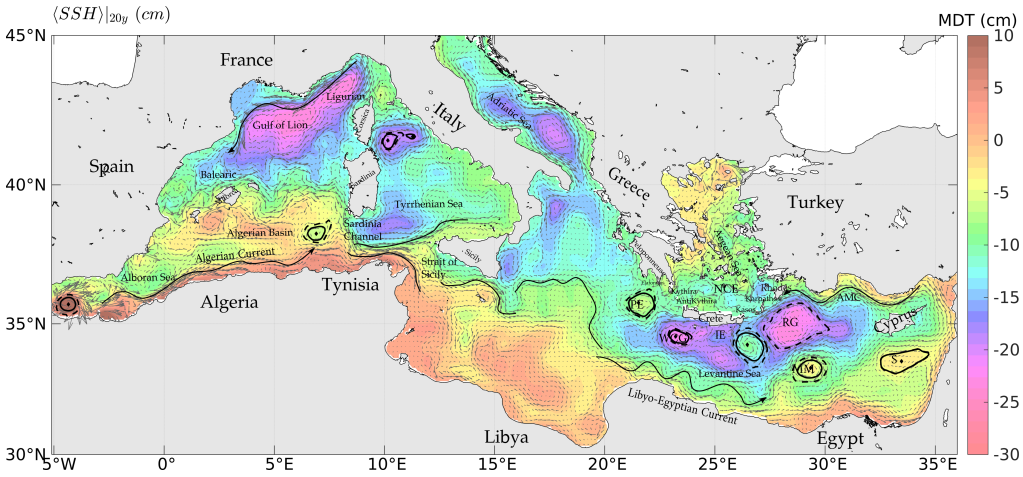

Figure 1.6: *Mean Dynamic topography of the Mediterranean Sea as derived by AVISO data 20 year reference. The averaged signature of mesoscale eddies are illustrated with the black contours. We mention few of the mesoscale features that are recurrently observed in the MED sea. The Ierapetra eddy (IE), the Pelops Eddy (PE), the Mersa-Matruh (MM), the Western Cretan Gyre (WCC), the Rhodes Gyre (RG), the Norther Cretan Eddy (NCE), the Shikmona (S), the Cyprus eddy (CE), the Asia Minor Current (AMC), the Alboran eddies (Al), the Algerian current (AC), the Libyo-Egyptian Current.*

tracked for more than 3 years (Millot and Taupier-Letage, 2005). In the North WMED, the Northern coastal current flows along the Gulf of Lion, a well established site where winter deep convection occurs. Deep waters are formed by the combination of cold winds and high salinity waters that cause a sink towards the vertical. The Gulf of Lion is regularly under the influence of Tramontane and Mistral wind forcing regimes during winter. Episodes of deep convection have been monitored (Schott et al., 1996; Margirier et al., 2016; Testor et al., 2017) with measured vertical downward motions that could reach $5 - 10\,cm/s$.

Even though the Western and the Eastern basins are geographically separated they interact with each other. Atlantic waters (AW) can be tracked as far as the EM while the two sub-basins are found to exchange water masses in the Sicily Strait. Similarly with the Gibraltar strait, in deeper layers in the Sicily Strait, a saline water mass of Eastern Med (EM) origin enters the Western Med (WM). This water mass is called *Levantine Intermediate Waters* (LIW) and are recognized by a subsurface vertical maximum of salinity between $200 - 600\,m$ and hydro-graphic characteristics of salinity $S = 38.95 - 39.15\,psu$, temperature $T = 14.7 - 16.95\,^oC$ (Theocharis et al., 1993). Considering that the mixing scale is much smaller than the advection one, water masses can be tracked for a long period of time. Evidence of LIW water masses were tracked to propagate north-westward for more than a year south of Sardinia and form eddies, called "*Leddies*" (Testor and Gaspard, 2003). The LIW flow along the Sardinia and Corsica coast while is argued that they take part in the winter deep convection occurring in the Gulf of Lion. The LIW and the Western Mediterranean Intermediate Waters (WMIW) are progressively entering deeper layers and finally exit the Gibraltar Strait completing the thermohaline circuit. However, due to fewer observations in the EM, its general circulation is still debated and the origins of the LIW remain uncertain.

Based on observations from thermal images (Hamad et al., 2005, 2006), the EM is proposed to exhibit, similar with WM, a counterclockwise circulation. The Libyo-Egyptian current flows and meanders along the steep Libyo-Egyptian shelf and is associated with the formation of the recurrent Mersa-Matruh anticyclone as a result of current

instabilities similarly with the Alboran current in the WM (Millot and Taupier-Letage, 2005; Sutyrin et al., 2009). Both Western and Eastern Med sub-basins are characterized by high turbulent fields and many recurrent mesoscale eddies. However, the EM several long-lived and recurrent mesoscale eddies could be distinguished thought the years. Such eddies are: the Ierapetra eddy (IE), the Pelops eddy (PE) in the northeastern Ionian, the cyclone southwest of Crete (WCE), the cyclonic Rhodes gyre (which is considered an area of deep water formation), the anticyclone Mersa-Matruh in the southern part of the basin, the Shikmona near the northern coast of Israel and the West Cyprus eddies in the Levantine Basin.

Mesoscale eddies are considered among the main mechanisms that promote turbulent mixing and play a role in the distribution of heat and salt across the basins. However, the way the presence of mesoscale eddies may modify the general EM circulation is uncertain. Lascaratos and Nittis (1998) trying to reproduce the LIW in the Rhodes Gyre argued that the presence of neighboring mesoscale features near the Rhodes Gyre such as the Ierapetra eddy or the Asia Minor Current could speed up the convection process. He concluded that without the presence of the eddies the same deepening was reached after doubled time, highlighting the importance of eddy resolving model. Kontoyiannis et al. (1999, 2005) emphasized on the complex interactions between the Rhodes Gyre and the neighboring Ierapetra eddy as well as the Northern Cretan Eddy (NCE) in the Cretan Sea. Outflows from the Kasos, Karpathos and Rhodes straits were reported (Theocharis et al., 1993; Velaoras et al., 2014). Two flow regimes were distinguished depending on the seasons. During winter, the Ierapetra eddy is absent while the Rhodes gyre extend is larger and warmer waters from the Asia Minor current intrude the South Aegean. During summer, the Rhodes gyre is bounded by the Ierapetra eddy generation and there is an outflow of waters from Kasos and Karpathos Strait. Similar flow reversal was mentioned during POEM group experiment. LIW was reported to be entrapped in both Pelops and Ierapetra eddy cores during POEM campaign (Theocharis et al., 1993). Velaoras et al. (2013) proposed that the LIW formation could be a result of the winter convection in the Cretan Sea and that later is exported in the Levantine. Analyzing the seasonal and interannual variability of water masses from fixed stations at the North, central and Southern Aegean, the winter convection did not exceed $100\,m$ depth in the North Aegean while in the Central Cretan Sea the intermediate water production was frequent at least $250\,m$ (Velaoras et al., 2013). Previous observations from the PELAGOS cruise held from Athens to Alexandria on 2000 Zervakis et al. (2003), showed that the Cretan Sea during winter 2000, exhibited strong convection that exceeded $450\,m$ depth in the vertical homogenization! During the same period on the Levantine basin the convection did not exceed $200\,m$.

The dominance of many mesoscale eddies in the EM is evident although the mechanisms behind formation and their role in spreading water masses are difficult to distinguish. The *atmospheric variability* has been considered the main driving mechanism for mesoscale eddies (Demirov and Pinardi, 2002). In the Northern Levantine basin, the recurrent formation of the Ierapetra anticyclone (IE), the Pelops eddy (PE) (in the northeastern Ionian), the cyclone southwest of Crete (WCE) and the cyclonic Rhodes gyre (RG) has been associated with the prevailing Etesian wind forcing regime during the summer months (Horton et al., 1994). However, the role of wind forcing on generating individual eddy structures is still not well known. Regional models account for the total MED complexity in terms of hydrography, bathymetry and atmospheric forcing. The resulting circulation patterns when regional atmospheric wind forcing is simulated are in good agreement with the mean variations of the MED circulation (Pinardi and Masetti, 2000; Béranger et al., 2010). The seasonal wind forcing drives a cyclonic circulation, produces the Rhodes gyre as well as captures the LIW formation. Nevertheless, mesoscale eddies are not well reproduced, not in the right position or time. If the presence of mesoscale eddies modifies the spreading of water masses in the MED sea

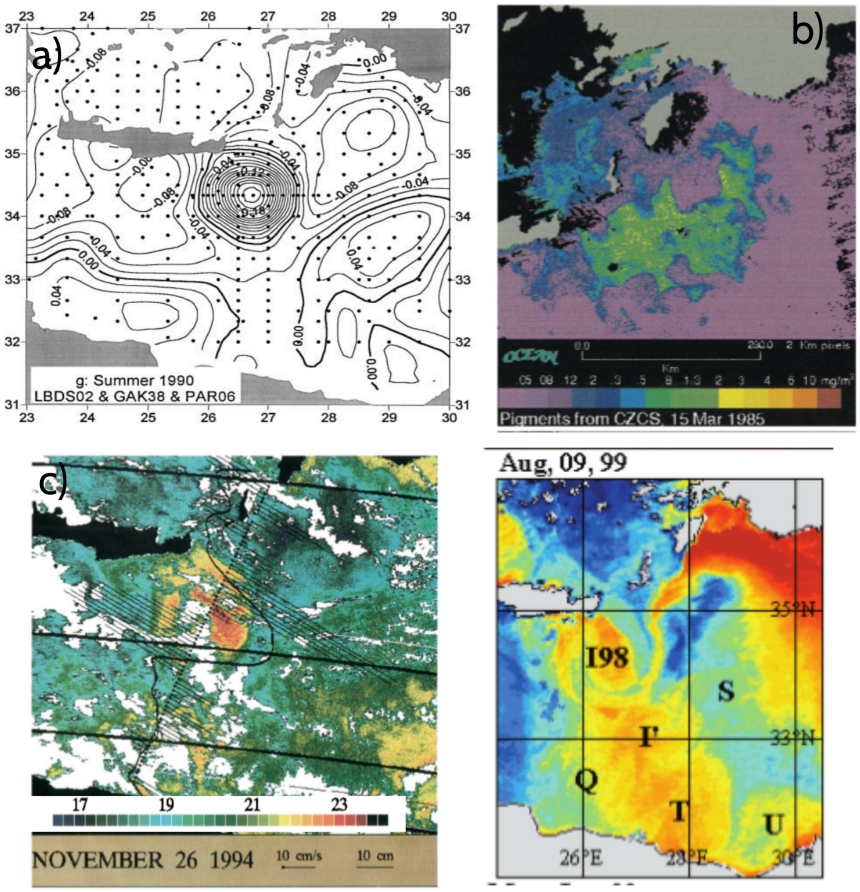

Figure 1.7: *a) The Ierapetra eddy as derived during first surveys (POEM&GOIN) in the Levantine in summer 1990 (Hecht and Gertman, 2001). b) High biological productivity bloom in the Rhodes Gyre as shown from the sea surface chlorophyll concentrations in spring 1985 (Napolitano et al., 2000). c) Ierapetra sea surface temperature signal during autumn 1994 (Iudicone et al., 1998)and summer 1999 (Hamad et al., 2006; Taupier-Letage, 2008).*

there is a need for increasing our understanding on how does each forcing mechanism individually triggers or affects the formation of eddies.

1.5 State of the Art

Ierapetra eddy as part of the MED

The Ierapetra eddy constitutes one of the largest and longest-lived anticyclones of the Mediterranean Sea. Located in the south-east corner of Crete and it recurrently forms during the summer months. The IE was first identified during the POEM group experiment that was held from 1987 to 1989 in the Eastern Mediterranean Sea. Up to now, the IE has been stabled upon in numerous studies recognized from its strong surface temperature and from mean sea surface height signal. The occurrence of the IE was reported systematically among the years: in September 1987 & August 1990 and 1991 (Theocharis et al., 1993; Horton et al., 1994; Violette et al., 1998; Hecht and Gertman, 2001; Hamad et al., 2005), 1992 (Isern-Fontanet et al., 2006), May 1993-1994 (Matteoda and Glenn, 1996; Ayoub et al., 1998; Iudicone et al., 1998; Kontoyiannis et al.,

2005), 1996-1997 (Larnicol et al., 1995, 2002; Hamad et al., 2006, 2005), 1994-1995 (Marullo et al., 2003), 1999 (Zervakis et al., 2003), 2005-2006 (Millot and Gerin, 2010; Millot and Taupier-Letage, 2005; Taupier-Letage, 2008; Mkhinini et al., 2014).

Combined satellite observations showed that the IE goes trough a seasonal and inter-annual cycle. During summer it generates, intensifies at late summer till early autumn while during winter weakens and disappears during spring (Ayoub et al., 1998; Larnicol et al., 2002; Lascaratos and Tsantilas, 1997). The IE was considered a stationary structure while the area of its generation is characterized by the highest variability of the Levantine Basin (Pujol and Larnicol, 2005). Hamad et al. (2006), showed from satellite thermal images that the IE can stay stationary but also travel long distances. The evolution of the Ierapetra eddy formed in 1996 (IE96) was captured and tracked to drift towards the South. One year after formation the IE96 was detected to merge with a newly formed Ierapetra (IE97).

Unfortunately, there is no direct way to associate the sea surface temperature with any dynamical property of the eddy such as velocities. Therefore, even though is a well known feature of the EM, there are few information on the IE dynamical characteristics. Matteoda and Glenn (1996) were the first to provide quantitative information on the Ierapetra eddy. Based on few drifters trapped in the eddy core for more than one month during February 1990, they found based on the eddy revolution period, that its intensity can reach relative vorticity of the order of $\zeta/f = -0.8$! Moreover, by digitizing AVHRR images they estimated the typical eddy size around $48\,km$. Additional information on the eddy intensity was provided by Mkhinini et al. (2014) for another Ierapetra. During spring 2006, few drifters were trapped within an Ierapetra eddy that initially was formed in 2005 for more than 2 months. At that time, the Ierapetra eddy was detected to merge with the newly formed Ierapetra during summer 2006. Velocities of the order of $70\,cm/s$ where recorded after the merging event with estimated eddy radius of $50\,km$. The few information on the eddy velocities, suggest high intensity for the anticyclone. The geostrophic Rossby number associated with the azimuthal velocities during the merging in 2006 was estimated at $Ro = 0.14$. Moreover, the strong relative vorticity of the order of $\zeta/f = -0.8$ was substantial for a mesoscale eddy.

Important questions remain to be fully addressed for the Ierapetra. Regarding the eddy occurrence and intensities we still don't know if the Ierapetra eddies actually form every year. How long they could survive ? how far they could travel in the eastern basin ? how does the eddy size and intensity vary during their lifetime? or among the IEs? how frequently can the anticyclone reach high velocities ? Does after all geostrophic balance holds for the IEs ?

Moreover, the regional summer wind forcing has been proposed as the generation mechanism of the IEs. Horton et al. (1994) has hypothesized that both the Ierapetra eddy and the Rhodes Gyre could be a result of the Etesian wind forcing occurring in the Aegean blocked by the Cretan Orography. This hypothesis, even though widely agreed upon, is has not yet been confirmed. Indeed the South east corner of Crete is a region of strong wind forcing potential. Every summer, the Aegean sea and Northern Levantine Basin is subject to the Northern Etesian winds (Bakun and Agostini, 2001; Tyrlis and Lelieveld, 2013). Crete's orography, 3 mountains in the row, acts as an obstacle in the wave and wind propagation inducing channeling and deflection effects towards the south Aegean and the Levantine basin. Kotroni et al. (2001) demonstrated the intensification and deflection of the Etesians by performing simulations with and without Crete island. Moreover, based on observational data from meteorological stations (Koletsis et al., 2009, 2010) confirmed that the Etesians decelerate upstream of Crete and deflect leftward while intensifying between the mountain gaps. Velocities of the maximum wind gusts were recorded to reach $25\,m\,s^{-1}$ in 2007 persisting for 3 days. The Etesians are observed every summer while their duration is intermittent. They are characterized by recurrent periods of gale-force northerlies interrupted by quieter spells (Tyrlis

and Lelieveld (2013)). Based on Etesian trends and climatology from to 1979 to 2009 (Poupkou et al. (2011)), the total number of Etesian days from June to September is on average 45 days with wind forcing values that range between $5 - 15\, m\, s^{-1}$.

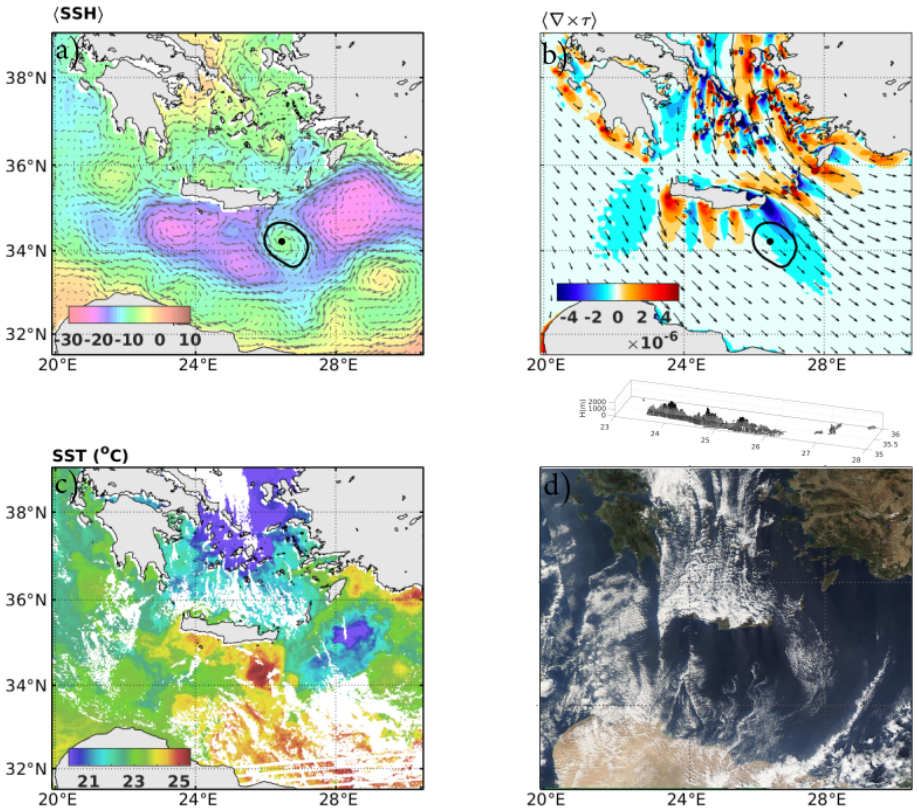

Figure 1.8: *a) Mean Dynamic Topography (MDT) as derived from 20 years average of Sea Surface Height (AVISO/DUACS) from 1993-2015 b) Mean climatological wind stress curl during the summer months $\langle \nabla \times \tau \rangle$ as derived from ALADIN datasets from 1993-2012 (c) Sea Surface temperature for the 14 November 2018. The Ierapetra eddy warm core is visible in the South east corner of Crete. (d) Etesian wind forcing blocked by the Cretan orography for the 14 November 2018 as obtained from https://podaac-tools.jpl.nasa.gov. (c) Crete's orography is shown 3 mountains in the row create blocking effect.*

This coincidence is striking and is difficult to be overlooked. So far regional models highlight the importance of atmospheric forcing the EM circulation. Nevertheless, the Ierapetra eddy cannot always be reproduced (Alhammoudand et al., 2005). Nittis et al. (2003) and Marullo et al. (2003) highlighted the importance of high resolution wind forcing in order to reproduce the IE in the models. Towards investigating further the connection of the IE with the Etesian forcing, Mkhinini et al. (2014) analyzed 20 years of high resolution wind forcing data (ALADIN datasets (Tramblay et al., 2013)). They concluded that the mean dynamical position of the IE coincides with a region of strong negative wind stress curl. The highly negative wind stress curl is found in the South-East corner of Crete and associates with strong shear caused by the Etesian blocking from Crete's orography. This sets the IE area as a favorable site for generating negative oceanic vorticity. However, this remains a correlation and the isolated regional wind forcing has not been evaluated on its capacity to generate eddies. Is the Etesian orographic wind enough to explain the occurrence of an Ierapetra eddy?

The Ierapetra eddy may constitutes another example of an eddy generated by oro-

graphic wind forcing. All studies for wind forced eddies (section 1.2) provide observational and numerical evidences that the wind forcing shear caused by mountainous islands could drive oceanic eddies. In most cases an oceanic dipole is formed. Nevertheless there are specific cases that the orographic wind forcing jet could lead to the formation of a stronger anticyclone (Chang et al., 2012; Nicholls et al., 2015). However, the source of this asymmetry in the oceanic response is not yet clear. If we assume that the Etesian wind forcing blocked by the Crete's orography could be the generation mechanism for the Ierapetra eddy; why only an anticyclonic eddy is observed south-east of Crete and not a dipole? Are there necessary preconditions to form only an anticyclonic eddy?

1.6 Research Objectives

This dissertation has been highly motivated by the recurrent formation of the Ierapetra eddy in the south east corner of Crete. The complexity of the formation area of the Ierapetra eddy is undeniable, including a steep bathymetric slope, strong regional wind forcing, that is modulated by Crete's orography and an important site for the general thermohaline circulation of the MED (Rhodes Gyre). So far there is a correlation between the area where the IE eddy forms and the area where a strong negative wind stress curl is observed (Mkhinini et al., 2014). However, the hypothesis that the IE is wind-induced has not been investigated further. Moreover, even though the eddy is well-known, there are only few studies (Matteoda and Glenn, 1996) that provide information of the eddy dynamical characteristics.

The objectives of this dissertation are twofold. Firstly, the Ierapetra eddies are followed over 22 years in order to gain information on their dynamical characteristics. Satellite observations, the AMEDA eddy detection algorithm (Le Vu et al., 2018) and available in-situ observations are used in order to quantify the IEs. Secondly, the regional wind forcing is evaluated as the possible mechanism for the IEs formation. The isolated effect of the wind forcing orographic jet will be evaluated in an idealized framework. The main goal is to provide a better characterization of the eddy dynamics and improve our understanding on the possible involvement of the regional wind forcing in the regional oceanic response. The overall research questions that will be addressed in this work, are summarized as follows:

do Ierapetra eddies form every year ? how long they could survive ?
how far they could travel in the eastern basin ?
what is their maximal intensity ? how does their intensity vary among the years?
does the regional wind forcing create eddies?
Is the Etesian orographic wind enough to explain the occurrence of an Ierapetra eddy?
why only an anticyclonic eddy is observed south-east of Crete and not a dipole? Are there necessary preconditions to form only an anticyclonic eddy?

1.7 Thesis outline

The thesis outline is presented as follows.

Chapter 1	The introduction begins with a general overview of the study framework. The state of the art & motivations are presented for the Ierapetra eddy. The research objectives and the scope of this thesis are outlined.
Chapter 2	The second chapter includes the results from monitoring the surface signature of the Ierapetra eddy from satellite observations in 22 years time period. Details on the eddy dynamical evolution are provided. Comparison's with sea surface temperature fields as well as few oceanographic campaigns are discussed.
Chapter 3	In this chapter the importance of the cyclogeostrophic corrections is quantified. Both for idealized eddies but also for realistic fields we present an method the recover cyclogeostrophy starting from the geostrophic fields. Area's prone to cyclogeostrophic dynamics are identified for the MED sea.
Chapter 4	In this chapter a 3-D reconstruction of the Ierapetra eddy vertical structure is attempted. Argo floats that were trapped in the eddy core for more than 3 months are used. A methodology to handle the heterogeneity of measurements in both spatial and temporal scale is developed. All available information on the eddy characteristics during this period are compared.
Chapter 5	This chapter presents the response of the ocean surface to the Etesian orographic wind forcing jet. The results of the performed simulations are analyzed and compared with the IE observed dynamical characteristics.
Chapter 6	This contains a brief summary of the thesis, some conclusive remarks and points for future work.
Appendix A	The one-and-a-half shallow water model subject to transient wind forcing is introduced in this chapter. The computational environment is presented as well as sensitivity tests that were performed to establish the model convergence before used in chapter 5.
Appendix B	This chapter investigates the differences that arise from using the SLA or ADT fields provided by AVISO products. Comparisons for an Ierapetra eddy are discussed.

CHAPTER 2

Dynamical evolution of intense Ierapetra Eddies over a 22 year long period

In this chapter we follow the Ierapetra eddies over a 22 years period with satellite altimetric observations and the AMEDA eddy detection algorithm. Information on the dynamical characteristics o the eddies are retrieved. This chapter was published in the Journal of Geophysical Research and is reproduced below.

Dynamical evolution of intense Ierapetra Eddies on a 22 year long period

Artemis Ioannou, Alexandre Stegner, Briac Le Vu, Isabelle Taupier-Letage and Sabrina Speich

(Published in *Journal of Geophysical Research: Oceans* (2017), **122**, 1-23, https://doi.org/10.1002/2017JC013158)

Abstract Considered as wind forced, the recurrent formation of Ierapetra eddy affects the Eastern Mediterranean Sea circulation. Even though this large, coherent and long-lived anticyclone has been extensively studied, there are only few quantitative information on its dynamical characteristics. The main goal of this study is to quantify the Ierapetra Eddies (IEs) intensity and examine their seasonal and interannual variability over a 22 year period (1993-2014). We choose the automatic eddy detection algorithm AMEDA to estimate the main IEs dynamical parameters such as their size, their intensities and their lifetimes. Applied to daily AVISO altimetric products, the AMEDA algorithm allows a full characterization providing additional information on vortex velocity profiles as well as on merging and splitting events. Among the years of observations, the IEs Rossby number experience a strong variability and could vary by a factor 4 ($Ro = 0.07 - 0.27$). This is mainly due to the eddy velocity variations rather than size variations. Moreover, we found that after their formation IEs could re-intensify. This intensification process may lead to a doubling of the vortex intensity in less than four months. That extra input of energy coincides with the Etesian winds period. Such high intensities are not expected from large-scale anticyclones and require cyclogeostrophic corrections. Considering this ageostrophic part, the maximum values of the core vorticity were derived and we found that the IEs might sometimes exhibit a negative potential vorticity core. Evidences on the eddy intensity from two oceanographic campaigns suggest that the IEs are probably more intense than we even estimate.

2.1 Introduction

The regional circulation in the Eastern Mediterranean Sea (EMS) is a complex system dominated by large gyres and long-lived eddies. The investigation of the EMS started with the pioneering work of Nielsen (1912) a hundred years ago. Nielsen (1912), Ovchinnikov (1966) and Lacombe and Tchernia (1972) depicted an overall counter-clockwise circulation in the whole basin. Since then, several oceanographic campaigns and in-situ measurements were conducted with higher spatial sampling that revealed the existence of mesoscale features especially large scale anticyclones. The POEM (Physical Oceanography of the Eastern Mediterranean) project used a large hydro-graphic data base collected during 1985-1987 (Malanotte-Rizzoli et al., 1997; Robinson et al., 1987, 1991; Robinson and Golnaraghi, 1993) to derive the geostrophic surface circulation and identify several gyres and mesoscale eddies considered as quasi-permanent or recurrent. Indeed, the temporal sampling of these hydro graphic surveys could not capture the dynamical evolution of the meso-scale eddies. However, the technological development of remote sensing measurements had opened a new window for the detection of surface eddies from 1980's. The satellite sea surface temperature (SST) images first Millot (1985); Matteoda and Glenn (1996); Puillat et al. (2002); Taupier-Letage et al. (2003); Zervakis et al. (2003) and later the sea surface height (SSH) maps (Isern-Fontanet et al., 2006; Pascual et al., 2007; Rio et al., 2007; Amitai et al., 2010; Mkhinini et al., 2014) provide an efficient way to identify the long lived eddies and follow their trajectories. The analysis of Lagrangian drifters were also used to quantify the intensity of the surface eddies, for instance the typical angular velocities within the eddy core (Matteoda and Glenn, 1996; Sutyrin et al., 2009; Gerin et al., 2009; Menna et al., 2012; Mkhinini et al., 2014). However, the drifters data or the various in-situ measurements available, CTD transects or vessel mounted ADCP sections, are still sparse especially in the eastern basin. It is only recently that the combination of the high resolution altimetric maps (gridded at $1/8^{\circ}$ in the Mediterranean Sea) with automatic eddy detection and tracking algorithms allow to quantify more adequately the dynamical evolution and the temporal variability of meso-scale eddies over long time periods.

Among the various eddies detected in the EMS, the Ierapetra anticyclone is probably one of the most fascinating structures. It has one of the strongest signal on the SSH (Isern-Fontanet et al., 2006; Rio et al., 2007; Amitai et al., 2010; Mkhinini et al., 2014) and quite often an amazing signature on the SST. The following Figure 2.1 is a typical example of the strong SST pattern induced by this anticyclone. This intense and large scale anticyclone is generally formed during the summer months at the south-east corner of Crete. The Ierapetra Eddy (IE) was first identified from the POEM hydro graphic data by Theocharis et al. (1993), then, by Horton et al. (1994) based on two extensive airborne expendable bathythermograph (AXBT) surveys conducted during December 1991 and July 1992. Horton et al. (1994) suggested that this intense anticyclone is a consequence of the strong Etesian winds being blocked by the Cretan orography. The seasonal correlation, averaged over twenty years, between the formation area of the IE and the localized area of negative wind-stress curl seems to confirm this hypothesis Mkhinini et al. (2014).

Matteoda and Glenn (1996) were the first to perform a quantitative analysis of several years of satellite imagery and a detailed examination of four drifting buoys to monitor five recurrent mesoscale eddies in the EMS. They found that the IE, which was observed in 85% of the AVHRR images during the four years period (1990-1994), was the most persistent of them. The frontal boundaries on the SST fields were digitized to perform a statistical analysis of the typical eddy size, i.e. the mean radius of the quasi-circular patch of warm water. The statistical distribution of this radius for the Ierapetra anticyclone range between $25km$ to $65km$ with a mean value of $48km$ which is much larger than the local deformation radius ($Rd = 10 - 12km$) while its center

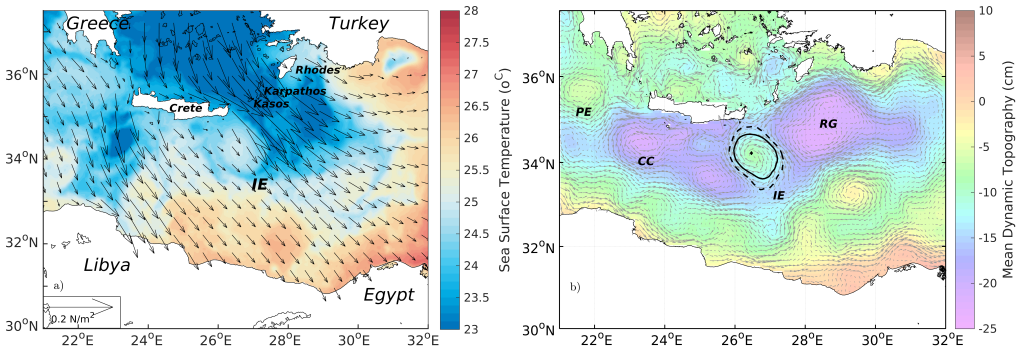

Figure 2.1: *(a) Sea Surface Temperature in the Eastern Mediterranean Sea the 4th of October 2006 (Project, 2010). The warm core of the Ierapetra eddy (IE) is centered at $(26.5^oE, 34.2^oN)$ while the predominant direction of the Etesian winds between Crete and Kasos island is indicated with the black arrows. The vectors represent climatological (1993-2012) wind stress components of the summer months (Tramblay et al., 2013). (b) Location of the climatological mean Ierapetra Eddy (IE), the Pelops eddy (PE), the Cretan Cyclone (CC) and the Rhodes Gyre (RG) on the 20 years (1993-2015) mean dynamic topography (MDT) of the Eastern Mediterranean Sea. The characteristic contour of the IE is plotted with a black solid line while the black dashed line indicates the last closed contour.*

location clusters around $(34.3°N, 26.7°E)$. The looping buoy trajectories of one surface drifter trapped inside the IE for two months was analyzed. The mean orbital period of the clockwise elliptical loops was about 3 days and associated with a mean negative surface vorticity around $z = -5\,10^{-5}s^{-1}$. This first estimation of the core vorticity of IE is quite large in comparison with the local Coriolis parameter f and corresponds to a relative vorticity of $z/f' - 0.8$! Matteoda and Glenn (1996) also observed the signature of inertial waves inside two meso-scale anticyclones. Surprisingly, no other data analysis or in-situ campaign tried to confirm such strong (negative) vorticity value which indicates a cyclogeostrophic balance for the large Ierapetra anticyclone. A more recent study Mkhinini et al. (2014) approximates the IE with a gaussian profile and shows that its intensity may vary significantly during the year. The typical speed radius of the eddy range from $35km$ to $50km$ while weaker values were found for the relative core vorticity $(-0.45 \leq \zeta/f \leq -0.25)$ and the Rossby number $(Ro = 0.08 - 0.15)$. Hence, the real intensity of the IE and how it varies during the eddy lifetime are still open questions.

The use of altimetric data, which are not affected by cloud coverage as the SST images, provides one of the most powerful time series to analyse the seasonal variability of mesoscale structures. The pioneering study of Larnicol et al. (1995) uses the TOPEX/ POSEIDON (T/P) altimetric data to study the mean sea level variations. Using suboptimal space-time objective analysis, the seasonal variability of the sea level anomaly (SLA) of the Mediterranean Sea was quantified. Moreover, strong anticyclonic mesoscale signals, such as the Alboran gyres or the Ierapetra eddy, were shown to have a clear seasonal variability, with a maximum in summer. However, the SLA is an indirect measure of the eddy intensity and high resolution maps were needed to estimate correctly the geostrophic surface velocities which are proportional to the gradients of the sea surface height (SSH). Few years later, the combined altimetric tracks of T/P and ERS-1/2 provide higher resolution maps of the SLA (Larnicol et al., 2002). This study confirms that the IE constitutes the most intense signal of the EMS variability with a maximum intensity in August. Besides, this study mentions a possible merging of the IE with another anticyclone in 1995.

The thorough analysis of weekly composite SST images during the period 1985-2001 performed by Hamad et al. (2005),(2006) shows that IE can be tracked for years,

sometimes several hundreds of km away from the main formation area and interact with the general circulation (Puillat et al., 2002; Hamad et al., 2006). Besides, they observed that IEs can merge with the IE of the forthcoming year co-exist or merge with another eddy, with life durations above 3 years. These studies emphasize the complex flow circulation in the Levantine basin driven by the turbulent eddy field. The large meso-scale patterns and especially the IE cannot be seen as a quasi-permanent and steady features that stay at their formation area. However, such analysis based on the temperature signature of the meso scale eddies at the sea surface cannot provide quantitative information for their intensity.

The improvements on eddy detection and tracking algorithms (Chaigneau et al., 2009a; Nencioli et al., 2010; Chelton et al., 2011; Mkhinini et al., 2014; Le Vu et al., 2018; Laxenaire et al., 2018) allow to characterize the main dynamical parameters of the detected eddies such as their size, their maximal azimuthal velocities and therefore their typical Rossby numbers. Moreover, the most recent algorithms provide new methods to identify the specific splitting and merging events (Li et al., 2014; Du et al., 2014; Le Vu et al., 2018; Laxenaire et al., 2018). The recent study of Mkhinini et al. (2014) used a hybrid eddy tracking algorithm applied on the surface geostrophic velocity gridded at $1/8^{\circ}$ for the Mediterranean Sea (AVISO products) to follow the dynamical variations and the trajectories of long lived meso scale eddies in the eastern basin. The generation area of the IE anticyclones for the 1994-2014 period was clearly identified in the south-east of Crete during summer months when the mean wind stress-curl, averaged over 20 years, reaches the strongest negative values. Besides, it was shown that the intensity of the IE could vary by at least a factor two between July to October 2006. This example shows that the Rossby number of this specific anticyclone may experience a strong seasonal variability.

According to the previous studies there are a few evidences that the IE experience significant variations of its intensity. Besides, such large mesoscale anticyclones ($R \simeq 2-3R_d$) are generally assumed to satisfy the geostrophic balance while for the IE it seems that the relative core vorticity could reach strong negative values. Surprisingly, very few studies quantify accurately the intensity and the dynamical evolution of this very robust and coherent anticyclone which can strongly impact the surface circulation of the EMS. There are still many open questions and we don't know precisely if an IE is formed every year ? how long it could survive ? how far it could travel in the eastern basin ? or what could be its maximal intensity ? Therefore, the main goal of this study is to estimate by the combination of the most recent altimetric products and in-situ measurements the surface velocity structure and the dynamical variability of the Ierapetra eddies. The paper is organized as follows. In section 2, we describe the various data sets and the specifications of the eddy detection and tracking algorithm AMEDA that we used. The section 3 presents a throughout analysis of the vortex intensity deduced from AVISO products and its seasonal and/or interannual variability over the 1993-2014 period. The lifetimes, typical trajectories and specific events are detailed in section 4. Next, several comparisons with available in-situ measurements are carried out in section 5. Finally, we sum up, in section 6, the main dynamical characteristics of the IE and conclude on their potential impacts on the local transport and mixing.

2.2 Data and Methods

Eddy Detection

Remote Sensing with Sea Surface Height

To quantify the temporal evolution of the Ierapetra eddies we used the geostrophic velocity fields, produced by Salto/Duacs and distributed by AVISO and derived from the Absolute Dynamical Topography (ADT). Unlike the Seal Level Anomaly (SLA) which

represents the variable part of sea surface height, the ADT is the sum of this variable part and of the constant part averaged over a 20-year reference period. The "all-sat-merged" series distributed for the Mediterranean sea combines, for the years 1993-2015, up-to-date data sets with up to four satellites at a given time, using all missions available (Topex/Poseidon, ERS-1 and -2, Jason-1 and -2, Saral, Cryosat- 2 and Envisat missions). This merged satellite product, for the Mediterranean sea, is projected on a $1/8°$ Mercator grid, with a time interval of 24 hours.

We should note that the horizontal resolution of the $1/8°$ gridded velocity fields ($dX \simeq 12km$) cannot fully resolve the internal deformation radius R_d which is around $10 - 15\,km$ in the Eastern Mediterranean Sea (Escudier et al., 2016). However, the surface signature of large mesoscale eddies with a typical radius that exceed the deformation radius are generally detected (Isern-Fontanet et al., 2006; Pascual et al., 2007; Rio et al., 2007; Amitai et al., 2010; Mkhinini et al., 2014). But, we should keep in mind that the spatio-temporal heterogeneity of the altimetric tracks of satellites, could also induce spurious eddy detection or systematic bias to the eddies intensity.

AMEDA Eddy Detection Algorithm

We use in this study the Angular Momentum Eddy Detection and tracking Algorithm (AMEDA) which is based on physical parameters and the geometrical properties of the velocity field Le Vu et al. (2017). We apply this algorithm to the surface geostrophic velocities provided by AVISO (Figure 2.2 (a)) to identify the eddy centers and quantify their intensity. The eddy centers correspond to an extremum of the local normalized angular momentum. The streamlines surrounding this center are then computed (Figure 2.2 (b)). The mean radius $\langle R \rangle$ and the mean velocity $\langle V \rangle$ are evaluated for each closed contour. As described by Eqn.(1), the mean radius $\langle R \rangle$ is defined as the equivalent radius of a circular disc with the same area A as the one delimited by the closed streamline, while the mean velocity amplitude $\langle V \rangle$ is derived from the circulation along the closed streamline, where L_p is the streamline perimeter - Eqn.(2).

$$\langle R \rangle = \sqrt{A/\pi} \tag{1}$$

$$\langle V \rangle = \frac{1}{Lp} \oint V dl \tag{2}$$

We plot in Figure 2.2(c) the pair of mean eddy velocity $\langle V \rangle$ and mean radius $\langle R \rangle$ for each closed contour. We can see on this example that the mean velocity increases when the radius increases until a maximum velocity V_{max} is reached. The corresponding radius is named R_{max}, also called the *speed radius* in previous studies (Chelton et al., 2011). The *characteristic contour* of the detected eddy (blue contours in Figure 2.2) is associated with the closed streamline of maximal speed. After this maxima, the azimuthal speed of the eddy decreases until the last closed contour (black dashed contour in Figure 2.2) is reached. When V_{max} and V_{end} are too close from each other ($V_{end} > 0.97 V_{max}$) the *characteristic contour* is then plotted with a dashed line to indicate that the maximal velocity is reached at the edge of the eddy.

We mainly use in this study R_{max} , V_{max} and the velocity profile $\langle V \rangle = F(\langle R \rangle)$ to quantify respectively the size, the intensity and the horizontal shape of the eddy. The eddy intensity is estimated with the use of the vortex Rossby number as follows

$$Ro = \left| \frac{V_{max}}{R_{max} f} \right| \tag{3}$$

Moreover, the velocity profiles are fitted with a generic function

$$V_\theta(r) = \frac{V_{max}}{R_{max}} r\, e^{(1-(r/R_{max})^\alpha)/\alpha} \tag{4}$$

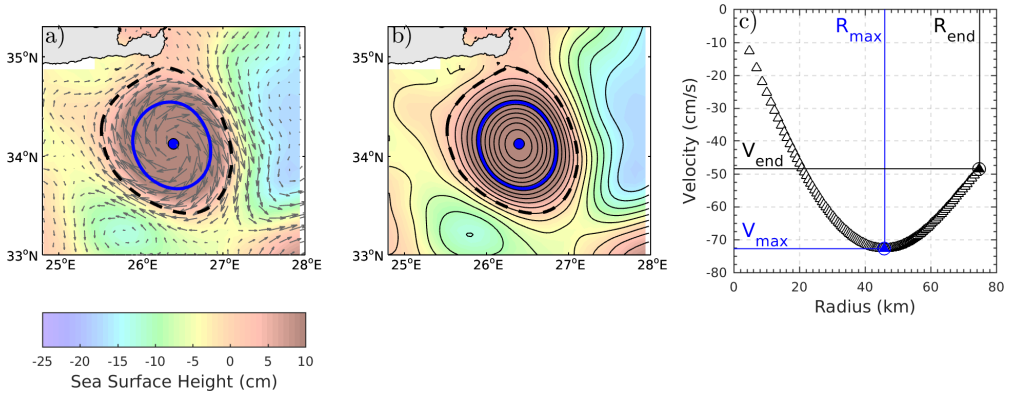

Figure 2.2: *The first panel (a) shows the characteristic contour (solid blue line) and the last contour (black dashed line) calculated by the AMEDA algorithm for an Ierapetra eddy. The background colors correspond to the ADT map while the black vectors to the surface geostrophic velocities. The central panel (b) shows the streamlines associated with the velocity field and the correspondence with the characteristic (solid blue line) and the last closed contour (black dashed line). The velocity profile $\langle V \rangle = F(\langle R \rangle)$ deduced from the streamlines analysis is plotted in the right panel (c). We use here negative values for the mean velocities $\langle V \rangle$ of anticyclones.*

where $r = \langle R \rangle$ and α is the steepness parameter. Such generic profiles were used by Carton et al. (1989) and Stegner and Dritschel (2000) to study the stability of isolated eddies. Note that when $\alpha = 2$ the velocity profile corresponds to a Gaussian vortex. Once we quantify the Rossby number and the steepness parameter, we can estimate for circular eddies based on Eqn.(4) the relative core vorticity according to the relation

$$\frac{\zeta_0}{f} = \frac{1}{f}\left(\partial_r V_\theta + \frac{V_\theta}{r}\right)_{r=0} = 2e^{1/\alpha}\, Ro \tag{5}$$

We also interpolate the characteristic contour by an ellipse and estimate an equivalent ellipticity $\epsilon = 1 - b/a$ (also called the flattening parameter) where b is the semi minor axis and a is the semi major axis. Moreover, the tracking procedure of the AMEDA algorithm identifies merging and splitting events (for more details see Le Vu et al. (2017)). Hence, we are able to track the long term evolution of meso scale eddies even if they merge or split during their lifetime.

Thermal Satellite Images

Although impaired by the cloud cover, satellite images from NOAA/AVHRR have been used for the 1980s to spot and track eddies, and contributed to general circulation studies. The use of thermal images (hereafter SST: Sea Surface Temperature) for circulation studies and their limitations are detailed in (Taupier-Letage, 2008). For this study only a few cases of IEs have been tracked with SST images, sometimes on limited periods, in order to check both methods results.

In Situ Observations/Oceanographic Campaigns

EGYPT Campaign

The EGYPT-1 campaign was held in April 2006 within the frame of the EGYPT (Eddies and GYres Paths Tracking) and EGITTO observational programs to study the role of the mesoscale eddies on the general circulation in the Eastern Basin (Taupier-Letage

et al., 2007). Among the 125 CTD casts performed, one section crossed the Ierapetra eddy generated in 2005 (Taupier-Letage, 2008), with 18 CTD profiles every 8-10km along a total distance of 180km. This hydrologic transect provides useful information on the vertical structure of IE05 and allows to compute the geostrophic velocities across the anticyclone. Furthermore over the 90 surface drifters (with $15m$ sockets) launched in the EGYPT/EGITTO program (Gerin et al., 2009), 5 were deployed in IE05, 2 of which remained trapped inside the anticyclone for almost 3 months.

BOUM Campaign

The BOUM (Biogeo- chemistry from the Oligotrophic to the Ultraoligotrophic Mediterranean) campaign (http://mio.pytheas.univ-amu.fr/BOUM/) was held in summer 2008, from the 16th of June to the 20th of July, with the French Research Vessel l'Atalante. The cruise consisted of a $3000\,km$ transect from the Rhone river mouth (western Mediterranean) to the Eratosthenes Seamount (eastern Mediterranean). This eastward-westward BOUM transect, covering essentially the southern part of the basins, enabled the physical and biogeochemical states of the EMS to be observed during the summer 2008 (Moutin and Prieur, 2012). Among the 30 stations that were performed along this transect, we focus on the few ones around the IE05 that was crossed in June 2008. One CTD and LADCP cast was performed inside the eddy core the 23rd of June. Moreover, Vessel-Mounted Acoustic Doopler Current Profilers (VMADCP) were used to obtain vertical profiles of current speed and direction in the upper layer. We focus on the VMADCP data when the ship crossed IE05's core the 30th of June on its way back to the Western Mediterranean. The maximum depth of VMADCP measurements was about $200\,m$.

2.3 Dynamical Evolution of Ierapetra anticyclones

Climatological Signature of IEs

The 20 year averaged mean dynamic topography (MDT) of the Eastern Mediterranean Sea is plotted in Figure 1.1(b). It exhibits the recurrent and energetic patterns of the North Levantine region: the IE centered at $(27^oE, 34.3^oN)$, the Rhodes Gyre (RG) centered at $(28^oE, 34.5^oN)$, the Cretan Cyclone (CC) centered at $(25^oE, 34^oN)$ and the Pelops Eddy (PE) centered at $(21.5^oE, 35.8^oN)$. The IE is marked with two black contours: the characteristic (solid line) and the latest contour (dashed line) respectively. It has, according to the MDT, a mean diameter of $\overline{R} = 55\,\mathrm{km}$ and relatively weak intensity of $\overline{Ro} = 0.02$. However, many studies have shown that the IE is not stationary (Larnicol et al., 1995, 2002; Hamad et al., 2005, 2006). It experiences seasonal variations and could move over long distance away from its generation point. Hence, since we know that the IE moves around its formation area or escapes far away, this twenty years average of the surface circulation will strongly underestimate its intensity.

The density of the center positions of the IEs, during the 20 year period (1993-2012), is shown in Figure 2.8(d). More than 56% of the IE centers are located inside the last contour (black dashed line). Therefore, we named this area: the *IE area*. This statistical distribution shows that the IEs could stay a long time in the same area and strongly impact the regional circulation south of Crete. The analysis of the first Empirical Orthogonal Function (EOF) of the SLA fields performed by Amitai et al. (2010) confirms that the principal feature of the EMS is the strong Ierapetra anticyclone. However, to estimate precisely the intensity and the dynamical evolution of this large scale anticyclone, we need to process the daily products provided by AVISO.

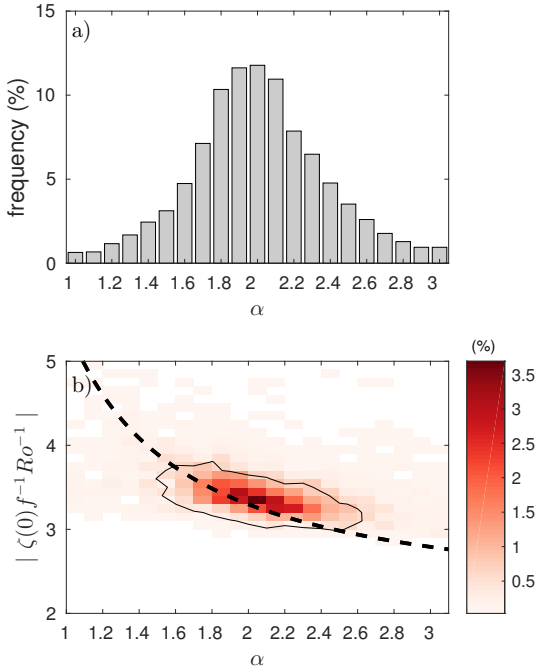

Figure 2.3: *(a) Distribution of steepness parameter α for Ierapetra eddies when the ellipticity is lower than $\varepsilon < 0.3$. The impact of the steepness parameter α on the dimensionless ratio $\zeta(0)f^{-1}Ro^{-1}$ is plotted in panel (b). The black dashed line corresponds to the Eqn.(8) while the colors illustrate the density distribution of the dynamical values obtained with the AMEDA algorithm for the Ierapetra eddies. The black contour delimits $\sim 70\%$ of the data.*

Seasonal Variability

In order to investigate the seasonal variability of mesoscale eddies, we compute the monthly means of the main dynamical parameters such as the dimensionless radius R_{max}/R_d ($R_d = 10km$), the Rossby number Ro or the ellipticity ϵ. We chose the Ierapetra Eddy formed in 1998 (IE98) to illustrate the seasonal evolution of these dynamical parameters in Figure 2.4. This anticyclone was initially detected in the AVISO products the 14th of July 1998 and its surface signature was tracked by the AMEDA algorithm during more than two years till October 2000. The eddy center stays in the *IE area* for 23 months and move inside it with a drifting velocity that does not exceed $1.2\,km/day$. Then, during the last 5 months of detection the IE98 drifted south towards the Egyptian slope with a mean speed of $\sim 2.5\,km/day$.
Figure 2.4 reveals various stages in the dynamical evolution of the IE98. The first stage corresponds to the eddy formation which occurs in summer 1998. We cannot guarantee that a small structure, which has no signature on the altimetric products, exists before that period. However, with no evidence of such pre-existing structure, we will consider that the first detection obtained with the eddy detection algorithm corresponds to the formation point of the IE. This is coherent with the SST analysis which shows that IE98 is created after the 5th of July and before the 17th of August 1998 (Fig. 12-13 of Hamad et al. (2006)). During this initial period, from July to October 1998, both the radius and the intensity of the anticyclone increase while the ellipticity of the structure, which is initially high, decays (Figure 2.4(c)). As we can see in the Figure 2.5 (a) the characteristic contour of the IE98 is indeed strongly elliptical during this formation stage. In October-November, the IE98 reaches a “mature stage”, where both the size and the Rossby number reach a plateau. The IE98 is then fully developed with an

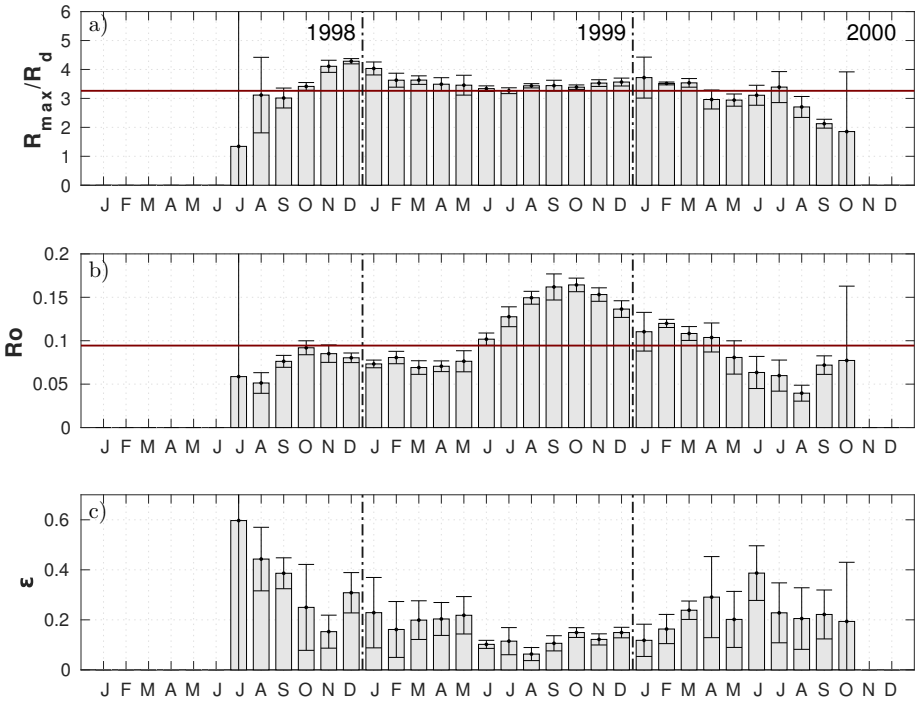

Figure 2.4: *Temporal evolution of the relative size ($Rmax/Rd$) (a), the Rossby number (Ro) (b) and the ellipticity ($\epsilon = 1 - a/b$) (c) of the Ierapetra anticyclone formed in 1998 (IE98). The error bars correspond to the monthly RMS of the parameters while the horizontal lines indicate the mean values for the eddy lifetime.*

intensity of $Ro = 0.1$ and a radius $R_{max} = 37\,km$ which is 3.5 times larger than the local deformation radius ($R_d = 10km$). For simplicity this stage will be refereed as *maturity* stage. A snapshot of the eddy structure which reaches its maturity in October is shown in Figure 2.5 (b). At this stage the characteristic contour is quasi-circular and both the location and the size are in correct agreement with the SST signature (Hamad et al., 2006). Then the IE98 survives the following year (1999), keeping roughly the same size and intensity. This period corresponds to a quasi-steady stage and according to Figure 2.4 and Figure 2.5 we do not see strong changes from October 1998 to May 1999. During the following summer, IE98 is thus still located SE of Crete, and prevents the creation of a new Ierapetra anticyclone in 1999.

Then quite surprisingly, in less than four months, from June to September 1999, the intensity of the IE98 doubles while its characteristic radius R_{max} stays constant. Such intensification of a pre-existing Ierapetra anticyclone, with a monthly mean Rossby number that rises from $Ro = 0.08$ in May up to $Ro = 0.16$ in September 1999 was never studied or emphasized before. The fact that the geometrical characteristics of the eddy, especially its radius and its ellipticity, remain unchanged may explain why such event, that has no signature on the SST or the chlorophyll patterns, can hardly be detected by satellite imagery. The analysis of altimetric products is therefore the only way to detect such variations in the intensity. Amitai et al. (2010) exhibits a strong EKE associated to the Ierapetra anticyclone in fall 1999 but didn't make the link with the IE98 formed the preceding year. More recently, Mkhinini et al. (2014) mentioned the intensification of a pre-existing IE in summer 2006 but did not study the phenomena in details. These specific events will be refereed to what follows as *intensification* stages. Our analysis shows that such *intensification* occurs at least four times during the 22 years period: in 1995 (for IE94), 1999 (for IE98), 2001 (for IE00) and 2006 (for IE05). This specific

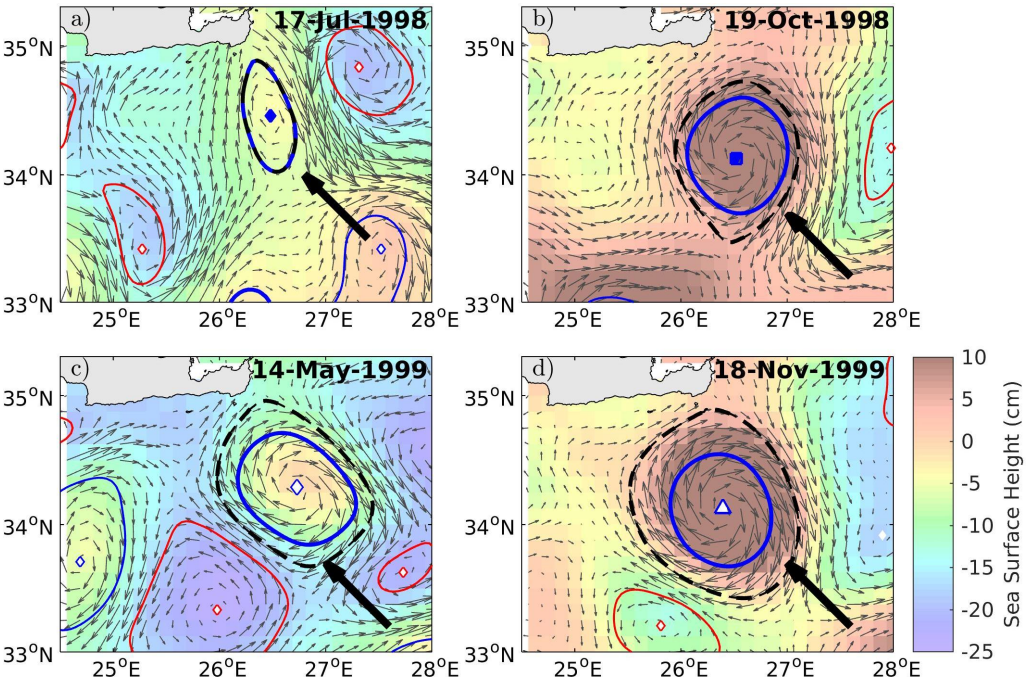

Figure 2.5: *Snapshots of the temporal evolution of the IE98. The formation of the eddy occurs in July 1998 (a) it reaches maturity in October 1998 (b) and after a quasi-steady stage (c) the intensity of the anticyclone increases strongly from June 1999 and reaches its maximum intensification in September 1999 (d). The background colors correspond to the ADT while the gray arrows correspond to the surface geostrophic velocities. The characteristics contours computed by the AMEDA algorithm are plotted in red and blue for cyclonic and anticyclonic eddies, respectively.*

event always occurs the next year after the IE reached its *maturity* stage. We should note that the increase of the vortex intensity coincide with the period of strong Etesian winds, while the maximum of *intensification* occurs in September-October. This coincidence is striking, but it cannot guarantee that this additional input of energy, inside a pre-existing IE, is only due to the wind forcing. After this *intensification* a decay in the Rossby number is usually observed. As it is shown in Figure 2.4(b) it takes 8 months for the IE98 to reduce its intensity by a factor two. The decay could be even shorter, as in 1995 and 2000 when it took less than four months for an equivalent reduction of the Rossby number.

Cyclogeostrophic Balance of IE

Our first analysis reveals that the Ierapetra anticyclones often reach Rossby numbers that exceed $Ro = 0.15$ during the *maturity* or the *intensification* stages. Such Rossby numbers seem small but they are not negligible and we could wonder if the geostrophic balance, which is a major assumption for the derivation of surface velocity from altimetric data sets, still holds. The study of Penven et al. (2014) has shown that the effects of centrifugal acceleration, are significant when deriving velocities from AVISO gridded altimetry in the Mozambique Channel. Moreover, the analysis of Tuel et al. (2016) has shown that for moderate values of the Rossby number the centrifugal correction might be significant especially for circular anticyclones. For instance, a Rossby number around $Ro \simeq 0.15$ could lead to a systematic underestimation of the azimuthal velocities

(-35%) for a gaussian anticyclone (i.e. $\alpha = 2$).

We've noticed, for the IE, that the highest value of the Rossby numbers generally coincides with smallest ellipticity values (as shown in Figure 2.4). Hence, it makes sense to consider quasi-circular Ierapetra anticyclones with small ellipticity $\epsilon < 0.1$. At the first order of approximation we will then assume a steady circular structure that satisfies the cyclogeostrophic balance:

$$\frac{V_\theta^2}{r} + fV_\theta = g\partial_r\eta = fV_g \tag{6}$$

where $V_\theta(r)$ is the azimuthal velocity, $\eta(r)$ is the sea surface deviation and $V_g(r)$ the geostrophic velocity corresponding to the standard AVISO products. Note that for an anticyclone (cyclone) the azimuthal velocities are negative (positive). It is then quite simple to calculate the cyclogeostrophic velocity V_θ from a circular geostrophic velocity profile $V_g = \langle V \rangle = F(\langle R \rangle)$, where $\langle V \rangle$ is the mean velocity averaged along each closed streamline of mean radius $\langle R \rangle$ (see Figure 2.2(c)). Solving the second order Eqn.(6) we get:

$$\langle V_\theta \rangle = -\frac{f\langle R \rangle}{2}\left(1 - \sqrt{1 + \frac{4V_g}{f\langle R \rangle}}\right) \tag{7}$$

Figure 2.6(a) shows the impact of the centrifugal correction on the velocity profile for the IE98 in early September 1999 when the vortex is quasi-circular ($\epsilon = 0.06$) and the Rossby number reaches $Ro = 0.15$. The black filled circles correspond to the mean values ($\langle R \rangle, \langle V \rangle$) computed from the geostrophic streamlines while the red ones are obtained from the cyclogeostrophic equation Eqn.(7). The maximal velocity V_{max} increases by 25% when the centrifugal correction is added while the speed radius R_{max} is reduced by 10% and therefore the vortex Rossby number rises up to $Ro = 0.21$. Both velocity profiles are then fitted with the generic function Eqn.(4). The shape of the geostrophic profile is close to a Gaussian vortex with a steepness parameter $\alpha = 2.2$. We then use the equation:

$$\zeta(r) = \partial_r V_\theta + \frac{V_\theta}{r} \tag{8}$$

to estimate the vorticity profiles of the circular eddies Figure 2.6(b). The amplitude of the centrifugal correction is even more pronounced for the vorticity than the velocity. Indeed, the relative core value of the geostrophic profile is around $\zeta(0)/f = -0.45$ while the cyclogeostrophic solution goes down to $\zeta(0)/f = -0.8$! Even if the pioneering analysis of Matteoda and Glenn (1996) indicates such large vorticity values it is still quite unexpected that a large meso-scale anticyclone ($R_{max} \simeq 4R_d$) could reach such negative vorticity values in his core. Our analysis confirms that during the *maturity* or $intensification$ stages the IE are not geostrophic and therefore the cyclogeostrophic balance should be taken into account to estimate correctly their intensity.

Interannual Variability

Variability in the IE's intensity

In order to study the interannual variability of the IEs we consider the maximum intensity reached by the anticyclones during their lifetime. For the 22 years of analysis, 16 IE's were identified and the maximum values of the Rossby number measured at the *maturity* or the *intensification* stages are plotted in Figure 2.7. The cyclogeostrophic balance was used to calculate the maximum value of the monthly averaged Rossby numbers

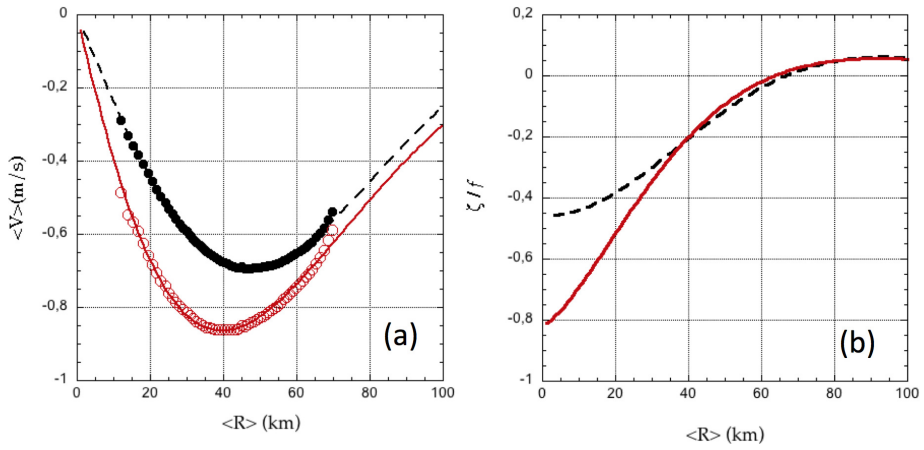

Figure 2.6: *Velocity (a) and vorticity (b) profiles of the IE98 the first of September 1999 when the ellipticity is weak* $\epsilon = 0.06$*. The geostrophic profile is depicted with the black dotted line while cyclogeostrophic profile, calculated with* Eqn.(6)*, is shown in red. The Rossby number associated to the cyclogeostrophic profile* $Ro = 0.21$ *is higher than the geostrophic one* $Ro = 0.15$*.*

Ro_{max}. On one hand, we notice a high interannual variability of the eddies intensity especially for the *mature* stage (filled square in Figure 2.7) with $0.07 \leq Ro_{max} \leq 0.27$. The maximum vortex intensity could vary by a factor two from one year to another. On the other hand, the intensity reached by the intensification of a pre-existing IE is always high. Four IE's (IE94, IE98, IE00, IE05) experience such *intensification* stage during the second year of their detection and they get similar values around $Ro_{max} = 0.23 - 0.27$.

We also estimate the maximum vorticity values within the eddy core. To do so we combine the maximum Rossby number and the steepness parameter α obtained for the cyclogeostrophic velocity profile Figure 2.6(a). Then we used Eqn.(5) to compute the relative core vorticity ζ_0/f reached at the *maturity* or the *intensification* stages every year Figure 2.6(b). We confirm here that the intense vorticity value estimated by Matteoda and Glenn (1996) from the loops of a surface drifter in 1990 was not an isolated case. Quite often the core vorticity goes below $-0.5/f$ in the late fall or early winter. Moreover, we found for at least three years (1995, 1999 and 2004), very intense values with a surface vorticity below $-f$ in the core of the IE. Hence, such intense circular vortices are prone to inertial or symmetric instabilities (Kloosterzielt and Heijst, 1991; Holton, 1992; Mutabazi and Normand, 1992) if we neglect the effective turbulent dissipation. If it occurs, such instability could induce small-scale and three-dimensionnal perturbations at the edge of the anticyclonic structure (Kloosterzielt and Heijst, 1991; Teinturier et al., 2010; Lazar et al., 2013a).

Hence, our analysis of a long time series of altimetric measurements reveals that, during specific period of the year, the IE's are much more intense than what is generally expected for such large meso-scale eddies.

Spatial Variability of the IEs

According to previous studies and to Figure 2.3 the climatological mean position of the IEs is centered in a specific area southeast of Crete $(27^oE, 34.3^oN)$. However, such long-term temporal averaging could mask a more complex situation. We illustrate in Figure 2.8 the monthly mean location of the centers of all the Ierapetra anticyclones at different stages of their dynamical evolution. The first detection points, which are considered here as the formation points, are plotted in the upper left panel of Figure 2.8(a).

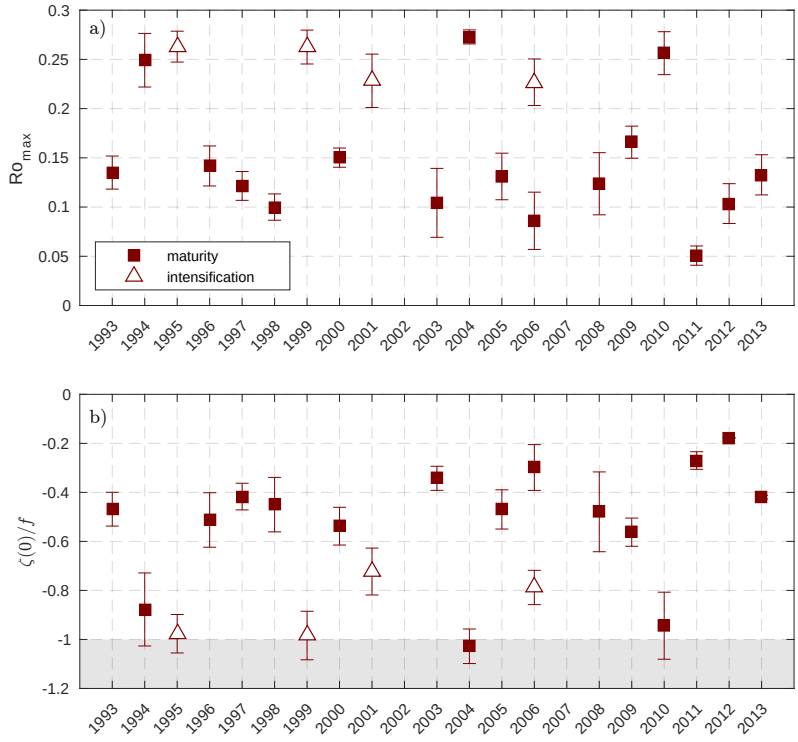

Figure 2.7: *Extremal values of the monthly mean Rossby number Ro_{max} (a) and the relative core vorticity $\zeta_0/f = \zeta(r=0)/f$ (b) for all the IE's detected during the 1993-2014 period. The values reached at the maturity or the intensification stages are respectively plotted with filled squares or open triangles. The errors bars correspond to the root mean square of the monthly fluctuations around the mean value. The gray area in the bottom panel indicates negative values of the absolute core vorticity $\zeta_0 + f < 0$.*

These formation points are not centered around the climatological mean position of IEs deduced from the 22 years averaged of the surface velocities which are computed from the Mean Dynamic Topography (MDT). If we assume that the location of the very first formation points is driven by the strong negative wind stress curl in the summer months (Mkhinini et al., 2014) it is not surprising to find a cluster of points aligned with the mean direction of the wind shear downstream (i.e. southeast) of the Kasos strait. But, if we consider the eddy location during the maturity or the intensification stages (Figure 2.8(b) and (c)) the centers are distributed around the climatological mean position. It makes sense, because the long-term temporal averaging gives more weight to the intense eddies and therefore the climatological mean will mainly capture the spatial signature of the IEs when they reach maturity or the intensification stages. The positions of the various IEs at the end stage (i.e. the last detection point) are plotted in the bottom panel of Figure 2.8. We do see here a large dispersion of the final location of the IEs with few eddies which escape from the formation area and propagate far away and reach the Libyo-Egyptian slope. Let us mention here that the automatic eddy detection and tracking algorithm as well as the SST analysis sometimes yield different IE trajectories. This rapid analysis shows that the region where the IEs gain a significant amount of kinetic energy (during the maturity or the intensification stages) is localized. It corresponds to a relatively small area centered southeast of Crete around the climatological mean

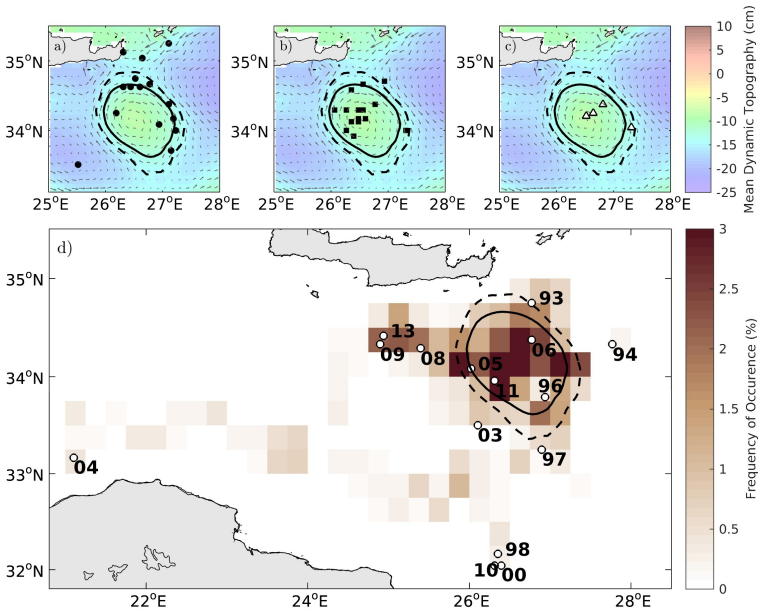

Figure 2.8: *Monthly mean position of the centers of IEs at various stage of their dynamical evolution. The first points of detection are plotted in panel a), the eddy location where they reach maturity or intensification are plotted in panels (b) and (c) while the point of last detection are depicted in the bottom panel (d). The background map and geostrophic velocity vectors correspond to the MDT. The characteristic contour and the latest contour deduced from this climatological mean are plotted in black solid and dashed lines respectively.*

position $(27^oE, 34.3^oN)$.

2.4 Lifetime of the Ierapetra Anticyclone

The use of automatic eddy detection and tracking algorithm based on sea surface altimetry, which is not limited by clouds coverage or wind induced air-sea fluxes such as SST images, allows to track meso-scale eddies with no interruptions and to improve considerably the estimation of their lifetimes. Besides, we used in this study the AMEDA algorithm (Le Vu et al., 2018) which is also able to detect the merging and the splitting events (see Figure 2.10). Such events may indeed impact the reconstruction of the eddy trajectory and its estimated lifetime if the tracking procedure do not account for them. During the 22 years of analysis 16 Ierapetra's were detected and their dynamical evolution is summarized in Figure 2.9. Each IE is labeled according to its year of formation (i.e. first detection) and the main dynamical events encountered during the eddies lifetime are indicated with specific symbols. The maturity and the intensification stages are marked respectively with black filled squares and white open triangles. The major merging events are indicated with green triangles while the few splitting events are marked with green crosses. A gray background is used when the centers of IEs remain inside the IE area (the closed contour in Figure 2.3(a)) while a white background indicates that the anticyclones escape from it and drift away.

A quick look to the Figure 2.9 shows a large variability in the dynamical evolution of the eddies. There is no standard evolution and many distinct events could impact the eddy life time and its intensity. It is well known that IEs are long-lived eddies but we should note that most of them (9 over 15) survive at least one year while the longest one was tracked by the AMEDA algorithm for almost four years. Besides, Ierapetra anticyclones are not formed every year. When a preexisting IE is present in the formation

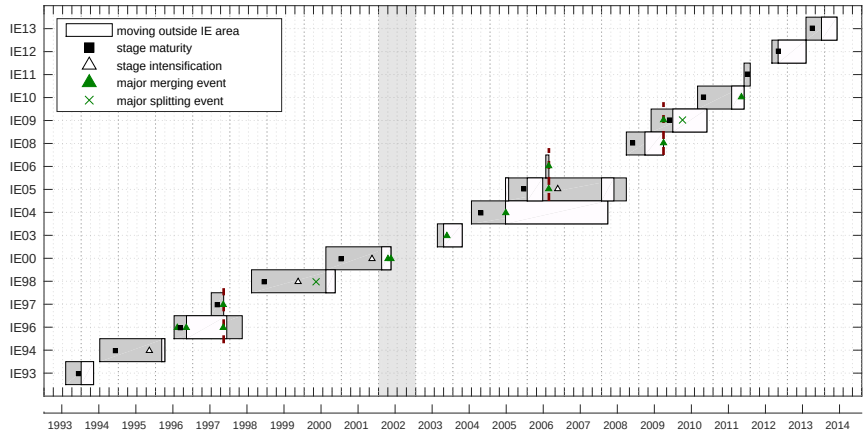

Figure 2.9: *Chronology of the various dynamical events (formation, maturity (black square), intensification (open triangle), mergings (green triangle) or splittings (green crosses)) for all the IEs detected between 1993 and 2015. The gray (white) areas indicate the position of each IE centers inside (outside) the mean IE area depicted in Figure 2.3 and Figure 2.8. The vertical dashed red lines indicate mergings between IE's.*

area it will be intensified, usually in autumn, and prevent the formation of a new one. This phenomena explain why only 16 eddies were identified during the 22 years period. However, if we sum the four eddies which are intensified (IE94, IE99, IE00 and IE05) with the sixteen eddies newly formed one is missing over the 22 years period. Indeed, we didn't detect any long-lasting IE formation in 2002 (the gray area in Figure 2.9).

During those years several merging events between the IEs were identified and indicated with a red and dashed vertical line in Figure 2.9. We first recover some mergings that were mentioned in previous studies: in October 1997 the newly IE97 merges with the pre-existing IE96 (Hamad et al., 2006) and at the end of June 2006 the IE05 merged with the newly formed IE06 (Taupier-Letage, 2008; Mkhinini et al., 2014)). Moreover, in late August 2009 the newly IE09 merges with the IE08 after 4 months of detection. However, we found at least one important merging that was not captured by the automatic tracking procedure of the AMEDA algorithm. According to SST images (see section 2.7 - Figure 2.16) it seems that the IE05 merges in September 2008 with the newly formed IE08 while IE05 has been lost from detection by AMEDA after the 4th September 2008. This missed event is mostly due to a lack of altimetric tracks, between 29th August and 25th September, which then leads to misleading maps of gridded absolute dynamic topography for few days in this specific area. If we merge the trajectories of IE08 with IE05, the latter will then be one of the longest lived Ierapetra anticyclone that survive more than four years, while it could be tracked on SST images till December 2009.

On the other hand, the coexistence of IEs does not always guarantee the merging between them. Sometimes, the IEs may coexist in distinct regions. We can see, for instance, on Figure 2.9 that the IE04 coexists for approximately 2.5 years with IE05. They remain far away from each other and their trajectories never crossed. Indeed, the oldest IE04 propagates in the south of the EMS, along the Libyo-Egyptian slope, while the IE05 remains around its formation area south of Crete island. Another example is the newly formed IE00 which coexists with the IE98. Four months earlier the latter splits in two and the IE00 coexists with both parts for more than 3 months. This was one of the few splitting events that were detected but we should note that during the 22 years period of analysis the mergings prevail.

No IE in 2002

The fact that among the 22 years period we didn't detect any formation or preexisting IEs in 2002 is puzzling. If we assume that the Etesian winds are mainly responsible for the initial formation or the intensification of Ierapetra anticyclones we should notice some specific anomaly in the seasonal wind forcing for this specific year. Following the work of Mkhinini et al. (2014) we use the same ALADIN data set (Tramblay et al., 2013) and compute the seasonal wind stress curl in summer and fall inside the *IE area* and analyse its interannual variability. We found, in comparison with the other years, a significant reduction of the summer wind stress-curl by $\sim$40% in 2002. However, this correlation does not imply causation and we do believe that a full analysis on the wind-vortex interaction related to the specific formation and/or the intensification process of the IEs is the only way to understand what happens in 2002. Such dynamical analysis requires a deeper investigation which is postpone to a future paper.

IE04 Lasts 43 Months and Drifts more than 1200km Away

The history of the IE04, one of the longest lived Ierapetra anticyclone that last for at least 43 months, is rare but very instructive. The location of its first detection is quite unusual. The altimetric signature of the eddy was first detected the 23rd of June 2004 far away from the Kasos strait in an area where the wind stress-curl is generally weak. It seems that this initial eddy, detected in June, detached from a large Libyo-Egyptian anticyclone. Unfortunately, this detachment was not identified as a splitting event by the AMEDA algorithm. Then this pre-existing anticyclone enters the IE area and reaches its highest intensity at mid-October 2014 just after the strong Etesian wind forcing. The monthly mean Rossby number ($Ro \simeq 0.27$), attained at this stage, is the strongest value among all the IE's. Due to the fact, that the generation of the pre-existing anticyclone doesn't seems to be correlated to any wind forcing and then the IE04 intensifies downward the Kasos strait, when strong wind-stress curl occurs, we associate this maximum of kinetic energy to an intensification stage (rather than a maturity stage). During the seven months that follow its intensification the IE04 slowly drifts to the southwest. Then, the AMEDA algorithm detects in May and July 2005 two successive mergings with other anticyclones. The green contour plotted in Figure 2.10 indicates the eddy-eddy interaction which occurs at mid-July. Hence, this large Ierapetra gain the energy of two other anticyclones who comes from the west Levantine where meso-scale anticyclones are often formed (Mkhinini et al., 2014) and where (Millot and Taupier-Letage, 2005; Hamad et al., 2006) observed that eddies accumulate and interact. These successive mergings didn't affect significantly the size or the intensity of IE04 but it has probably impacted its lifetime. Indeed, this coherent structure was then tracked for more than two years along the Libyo-Egyptian slope until January 2008. This long and unusual trajectory of the IE04 was confirmed by a careful analysis of its SST signature. This large anticyclone that drift westward was identified as a Libyo-Egyptian eddy by previous studies (Taupier-Letage, 2008; Sutyrin et al., 2009; Gerin et al., 2009; Mkhinini et al., 2014). Several surface drifters, trapped inside the eddy from May to September 2006, and a full CTD transect, performed in May 2006 (Taupier-Letage et al., 2007, 2010), quantify the horizontal velocity and the vertical structure of this surface-intensified anticyclone (Sutyrin et al., 2009) but no connection was made with the Ierapetra eddy formed in 2004. To make such link a complete reconstruction of the eddy trajectory that takes into account the merging with other structures should be done. It is only due to the recent improvements of the tracking procedure of the AMEDA algorithm (Le Vu et al., 2017) that such analysis becomes now possible.

We cannot ensure that the IE04 keeps the same water masses from the beginning to the end of its life. Indeed the two merging encountered for this specific Ierapetra anticyclone could lead to significant mixing of the water trapped in its core and therefore

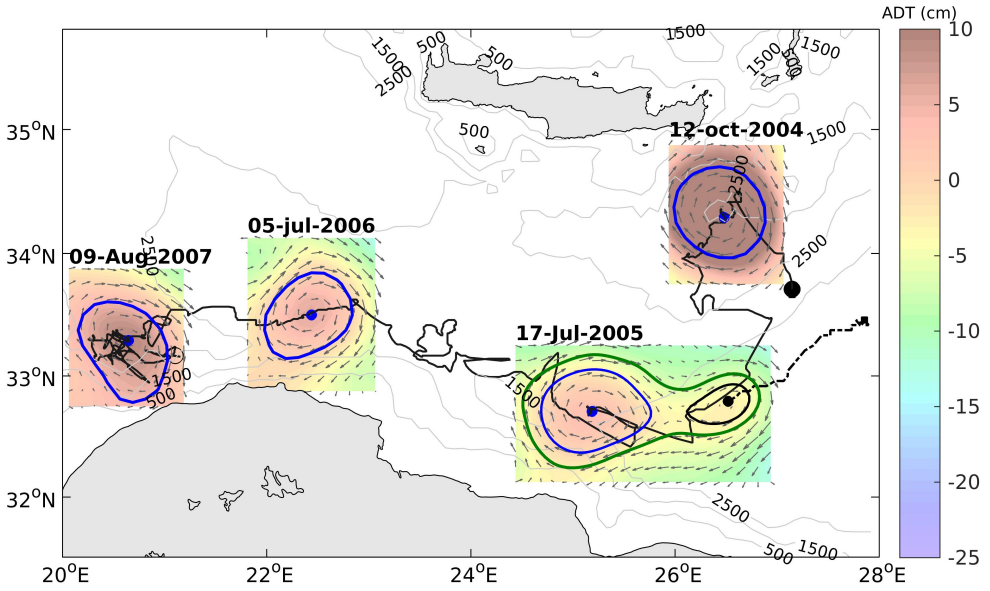

Figure 2.10: *Full trajectory (black solid line) of the Ierapetra anticyclone IE04 from the first (23/06/2004) to the last (10/01/2008) detection point. The characteristic contour (blue line) of the anticyclone in addition to the background ADT and the velocity field are plotted at different stages of its evolution. A major merging event that occurs in July 2005 is indicated with a green contour. The trajectory (black dashed line) and the origin of the other anticyclone who merged with IE04 are also plotted.*

affect its hydrological structure. Nevertheless, according to this peculiar trajectory of the IE04 we could expect that a fraction of the initial water trapped in the southeast of Crete may travel to the south of the Levantine along the Libyo-Egyptian coast.

Relation between the maximum Intensity and the Lifetime

According to Figure 2.9 there is a high variability in the IE lifetimes ranging from 2 months to 4 years. Besides, the history of IE04 shows that many non-linear processes, such as wind intensification or merging events could contribute to reinforce this large anticyclone and most probably extend its lifetime. In order to check if there is a correlation between the maximum amount of kinetic energy gained by an eddy and its lifetime we plot in Figure 2.11 the latter as a function of the maximum Rossby number (Ro_{max}) reached by each eddy. The cyclogeostrophic balanced is taken into account to compute the Ro_{max}. We use different symbols to make the distinction between eddies who attained their maximum intensity at a maturity stage (red squares) or later on during an intensification stage (open red triangles). When the IE encounter one or several merging with other meso-scale anticyclones green triangles are used.

We first found that there is almost a linear relation between the lifetime and Ro_{max} when the eddy reached its maxima at a *maturity stage* few months after its formation. For these eddies (black squares) we can reasonably assume that they accumulate all their energy during the formation process. Then they will slowly lose their energy with time probably due to small-scale turbulent dissipation. However, few eddies deviate from this linear trend. Higher lifetimes are indeed observed when an additional amount of energy is provided by another process such as intensification (open red triangles) or merging (filled green triangles). The IE04 combines both an *intensification stage* and merging events. On the other hand, we should note that even if there is extra gain of energy

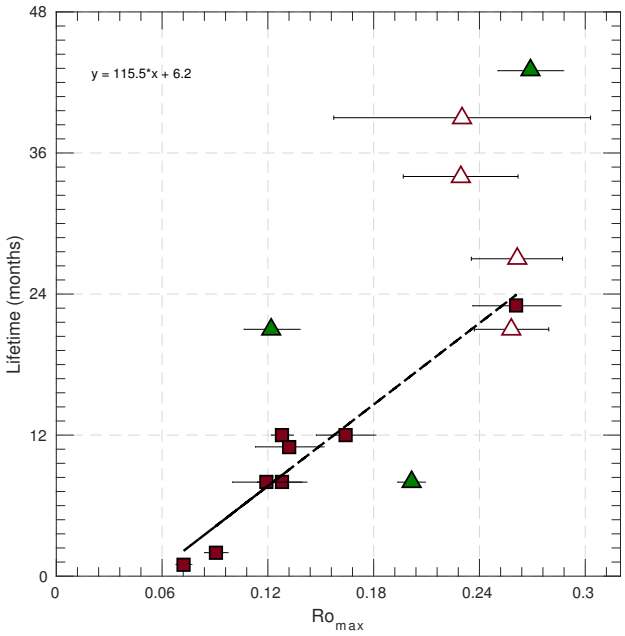

Figure 2.11: *Lifetimes of the various IEs (tracked during the 1993-2015 period) as a function of the maximum Rossby number reached during their lifetime.*

the maximum eddy intensity do not exceed $Ro_{max} < 0.28 - 0.3$. We suspect here that this upper bound may be due to the centrifugal-inertial instability of cyclogeostrophic anticyclones (Kloosterzielt and Heijst, 1991; Teinturier et al., 2010; Lazar et al., 2013a).

2.5 Comparison with In Situ Measurements

The dynamical analysis presented so far rely only on the AVISO data sets. In order to check if the altimetric products and the use of AMEDA algorithm estimate correctly the IEs intensity we compare the previous analysis with available in-situ measurements. On the contrary with the Western basin, there are very few direct measurements of the surface velocity in the Eastern Mediterranean Sea and we will mainly focus on what follows in two specific campaigns that survey the Ierapetra anticyclone: EGYPT-1 in spring 2006 and BOUM in summer 2008. Surprisingly, those two distinct oceanographic campaigns that have crossed and performed several measurements into the same eddy, the IE05 with a two year interval. According to AMEDA and the Figure 2.9, the IE05 was the second most long lived Ierapetra anticyclone, initially formed in May 2005 it survived until August 2008 for almost four years (up to ∼57 with sst).

EGYPT-1 Campaign

Drifters Measurements

Among the hundredth of SVP drifters launched during the period of the EGYPT/EGITTO program, from 2005 to 2007, few of them were launched and got trapped inside eddies (Gerin et al., 2009). Five drifters were launched in the IE05 and only two remained trapped inside the anticyclone from April to July 2006. These drifters looped inside the eddy with a typical period of 3–5 days. Hence, when filtering out these rapid oscillations on both latitude and longitude we can estimate the slow evolution of the eddy center. We calculate for each successive position $(X(t),\, Y(t))$ the radial distance $R(t)$ from the

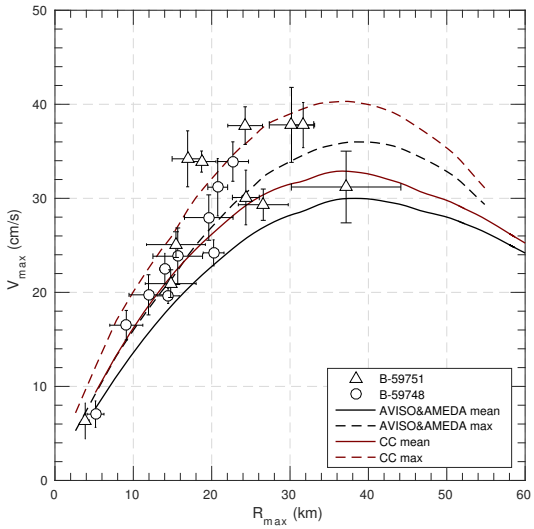

Figure 2.12: *Points of mean tangential velocity V_i and mean eddy radius R_i with their rms error (errorbars) corresponding to the quasi-circular loops performed by the two drifters B-59751 (triangles) and B-59748 (circles) inside the IE05 from* April to July 2006. *The black solid line represent the three months mean velocity profile computed by the AMEDA algorithm applied to the AVISO data set. The red solid line depict the most intense velocity profile reached the 16th of April 2006. The dashed lines indicates the cyclogeostrophic velocity profiles computed both from the mean (black) and the maximum (red) geostrophic velocity profiles.*

drifter to the eddy center. We then select specific loops corresponding to quasi-circular trajectories in the relative frame of the eddy center and we calculate, for all of them the time averaged radius R_i and the mean tangential velocity V_i. Figure 2.12, similar to the figure 6(a) of (Mkhinini et al., 2014), shows the data pair (R_i, V_i) for 21 loops having a low ellipticity values: $\varepsilon < 0.3$. The intermittency of the local wind stresses or the small-scale wave activity induces dispersion in the drifter dynamics and a wide range of R_i values are then explored while the drifters loop inside the eddy. In order to compare these in-situ velocity measurements with the typical velocity profile estimated from the AVISO geostrophic surface velocity we plot on Figure 2.12 the mean profile $(\langle R \rangle, \langle V \rangle)$ computed by the AMEDA algorithm and averaged during the three months period (black solid line). We can see that all the (R_i, V_i) points are above the black curve, in other words the monthly mean velocity average of the AVISO data set underestimate the intensity of the real eddy. If we apply the cyclogeostrophic correction to this mean circular velocity profile, following the method described in Figure 2.3, we get closer to the in-situ measurements (black dashed lines). But, it is only if we consider the most intense altimetric signal (red solid line), reached the 16th of April 2006, and apply on it the cyclogeostrophic correction (dashed red line) that we were able to reach the highest azimuthal velocity values ($V_{max} \simeq 35 - 40\, cm.s^{-1}$) estimated from the drifter loops. Hence, if we consider only the monthly mean Rossby number obtained from the AVISO surface geostrophic velocities ($Ro \simeq 0.1$) we tend to underestimate the real eddy intensity ($Ro_{drifters} \simeq 0.132$) by 30%.

CTD transect

In April 2006 a 21–CTD transect crossed the Ierapetra eddy with 18 CTD profiles, one out of two down to $1000(resp.2000)m$ depth. The typical distance between two CTD was about $8km$ which is significantly less than the typical eddy radius of $R_{max} \simeq 35 - 40km$.

This transect was planned to cross the center of an IE according to EGYPT-1 previous CTD transects and to SST images analysed in real-time during the campaign. The superimposition of the CTD positions on the ADT map and the characteristic eddy contours computed from the surface geostrophic velocities confirms that this transect crosses the center of the IE05 at the constant latitude $\theta = 33^o 37.5N$ (Figure 2.13(a)). Then, assuming a reference level of zero velocity at $z = -1000\,m$ we can reconstruct, according to the thermal wind relation, a vertical section of the geostrophic velocity across the eddy (Figure 2.13(b)). The strong baroclinic structure of the anticyclone is clearly shown here with an intensification of the velocity within the first $100\,m$. However, the dynamical signature of the eddy is still significant at $400\,m$ depth with typical velocity amplitudes that could reach $10 - 15\,cm\,s^{-1}$ in the eddy core. The comparison between the surface velocity profile provided by the AVISO data set and the velocity derived from the CTD transect (averaged over the first 150m) is shown Figure 2.13(c). All these profiles correspond to the meridional component of the geostrophic velocity and there is no need to add any cyclogeostrophic corrections here.

We can notice that the meridional geostrophic velocities, derived from altimetric products, in the western side of the eddy, are underestimated in comparison with the in-situ measurements. The geostrophic velocities derived from the CTD transect could reach $45\,cm\,s^{-1}$ while the meridional velocities provided by AVISO do not exceed $32\,cm\,s^{-1}$. Hence, in the western side between $(25^\circ E - 26^\circ E)$ the maximal velocities derived from the $L4$ altimetric products (i.e. gridded velocity fields) could be $35 - 40\%$ below the measured velocities. We test the sensitivity to the vertical averaging and we didn't find significant changes in the meridional velocity profile if we integrate the meridional velocities (Figure 2.13(b)) over the first $60\,m$, $100\,m$ or $150\,m$.

BOUM Campaign

CTD measurements

Two years after the EGYPT-1 cruise the IE05 was crossed for a second time during the BOUM campaign held in 2008. After the CTD transect of April 2006 this Ierapetra anticyclone experience one major merging event: the IE05 merged with the IE06 in summer 2006, as mentioned above. Then, the IE05 passed through a strong intensification stage in autumn 2006 with a monthly mean Rossby number that reaches extremal values up to $Ro \simeq 0.22$ if the cyclogeostrophic balance is taken into account. Then the anticyclone intensity decays till spring 2007 down to $Ro = 0.06 - 0.08$ with a mean speed radius and maximal velocity that stayed respectively around $R_{max} = 35 - 45\,km$ and $V_{max} = 25 - 30\,cm\,s^{-1}$. The IE05 was tracked by the AMEDA algorithm until early August 2008. In the last year of its detection no major events or significant changes in size or intensity were identified. However, as it was mentioned before (Figure 2.4), according to the analysis of high resolution SST images the IE05 seems to merge with the new IE08 formed in the late August 2008. Hence, the lifetime of Ierapetra anticyclone initially formed in 2005 probably extend to 2009 thanks to successive merging events.

The 22 and the 23 of June 2008, 5 "short duration" (SD) stations were performed in the south of Crete. The positions of the stations are plotted in comparison with the altimetric signature of the IE05 (Figure 2.14(a)). It shows that the station labeled SD6 was located inside the eddy core while the four other ones (SD4, SD5, SD7 and SD8) are outside the last closed contour (the blue dashed line in Figure 2.14(a)) of the eddy. The LADCP measurements at SD6 show surface intensified velocities inside the IE05 in comparison with the four other stations performed outside the IE05. The estimated velocity reach quite large values, up to $V_{LADCP} = 45 - 50\,cm/s$ in the first $200\,m$, in comparison with the mean values ($V_{max} = 25 - 30\,cm\,s^{-1}$) derived from the altimetric products. Both the velocity and the density anomaly show a strong signature of this anticyclone down to $300\,m$. Below, the dynamical signature is much less pronounced

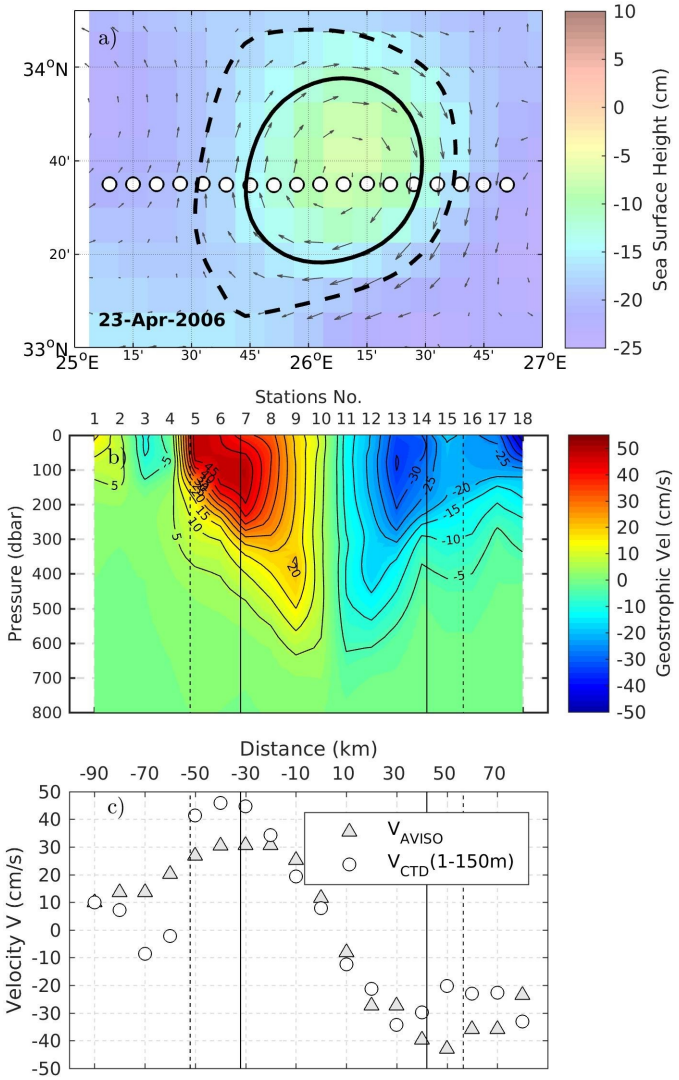

Figure 2.13: *Locations of the CTD casts performed the 23th of April 2006 during the EGYPT-1/EGITTO cruise across the IE05 (a). The meridional component of the geostrophic velocities derived from the vertical density field is plotted in (b). To apply the thermal wind relation, we used here a zero velocity level at* $z = -1000\,m$*. The comparison between the meridional geostrophic velocity profiles provided by AVISO or derived from the CTD transect (averaged over 150m) is plotted in (c).*

even if positive salinity or temperature anomalies (not shown here) could be detected down to $700\,m$ depth.

VMADCP Measurements

The IE05 was crossed a second time the 30th of June 2008. The VMADCP was active and thus provided direct velocity measurements through the eddy down to $200-250\,m$ depth. The superposition of the geostrophic surface velocities with the VMADCP velocity transect Figure 2.15(a) confirms that this specific track crossed the eddy central zone (only 1 CTD). Besides, the location of two velocity maxima measured with the VMADCP are in a very good agreement with the location of the characteristic contour, the solid blue line in Figure 2.15(a), computed by the AMEDA algorithm. More surprisingly, the vertical cross-section of the meridional velocities (Figure 2.15(b)) shows that the core of the IE05 is intensified below the surface. The highest velocity amplitudes, around $V_{VMADCP} = 45-55\,cm/s$, are reached at $z \simeq -125\,m$! This subsurface intensification was not detected in the LADCP profile SD6 one month before, even if the maximum of the velocity amplitude reach the same value. Due to the fact that the VMADCP measured the subsurface intensification on both sides of the anticyclone and at the same depth, we tend to give more confidence to the vertical structure of the velocity transect in Figure 2.15(b) rather than the LADCP profile in Figure 2.14(b). As far as we know this is the first time that such subsurface intensification was observed for meso scale eddies in the Eastern basin. If the mixed layer is usually well developed in winter and often extend down to $100-150\,m$ depth, the spring restratification may reduce the horizontal density gradient from the vortex center to its edge. Hence, due to the geostrophic balance, the upper layer could exhibit reduced velocities in comparison with the deeper layers that were not affected by the spring restratification.

In order to perform relevant comparisons between the VMADCP measurements and the velocities, derived from altimetric measurements, it is needed to apply the cyclogeostrophic correction to the surface velocity provided by AVISO. However, due to the elliptical shape of the eddy (Figure 2.15(a)) the 30th of June we cannot apply directly the equation (Eqn.(6)) which is valid only for circular eddies. Hence, we compute with an iterative method, proposed by Penven et al. (2014) and Tuel et al. (2016), the cyclogeostrophic velocity field in a large domain around the IE center which contains the last closed streamline (i.e. the dashed blue line in Figure 2.15(a)). As we can see on Figure 2.15(c), the cyclogeostrophic correction (red dots) is relatively weak and the meridional velocity profile is close to the geostrophic one (black dots). Both of them strongly underestimate, by at least 45%, the measured velocities (close to the surface $z = -29\,m$) in the Western side of the anticyclone. The underestimation could be even stronger (60%) if we compare with the velocities measured $125\,m$ below the surface. Hence, both in-situ measurements, performed during the EGYPT-1 cruise in 2006 and the BOUM campaign in 2008, showed that if the eddy size is accurately captured by the AVISO products, the geostrophic velocities underestimate the surface velocities especially in the Western side of the IE. The dynamical asymmetry between the Western and the Eastern side of the IE, in this specific area $(25°E-27°E, 34°N)$, remain nevertheless unclear.

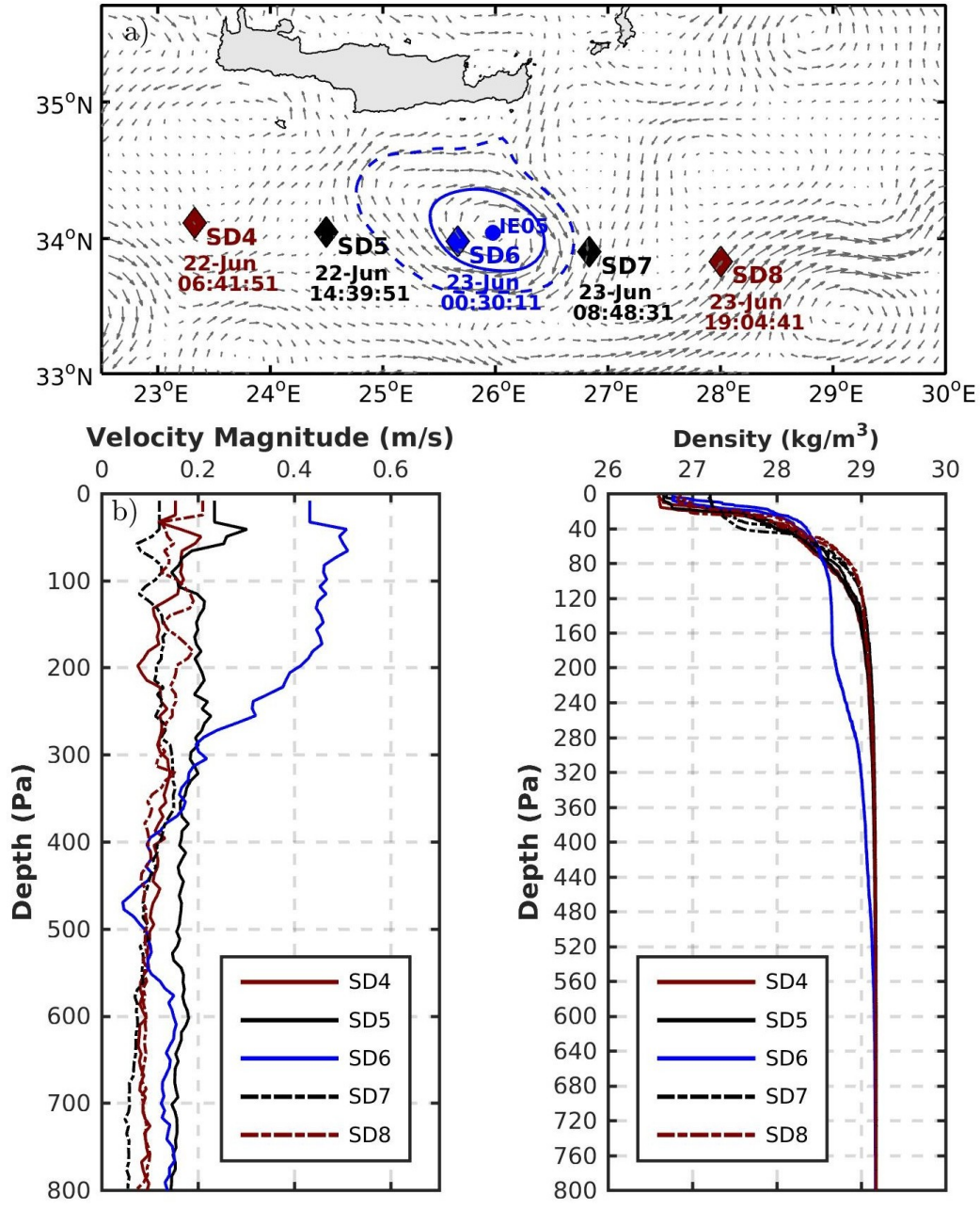

Figure 2.14: *(a) Location of 5 CTD stations during BOUM campaign superimposed on the velocity field derived from AVISO for the 23 June 2008 (a). The characteristic contour (solid) last contour (dashed) of the IE05 are plotted in blue. The vertical velocity profile (LADCP) and the density profile are plotted in panel (b) and (c) respectively. The blue lines correspond to the profiles performed inside the characteristic contour of the IE05.*

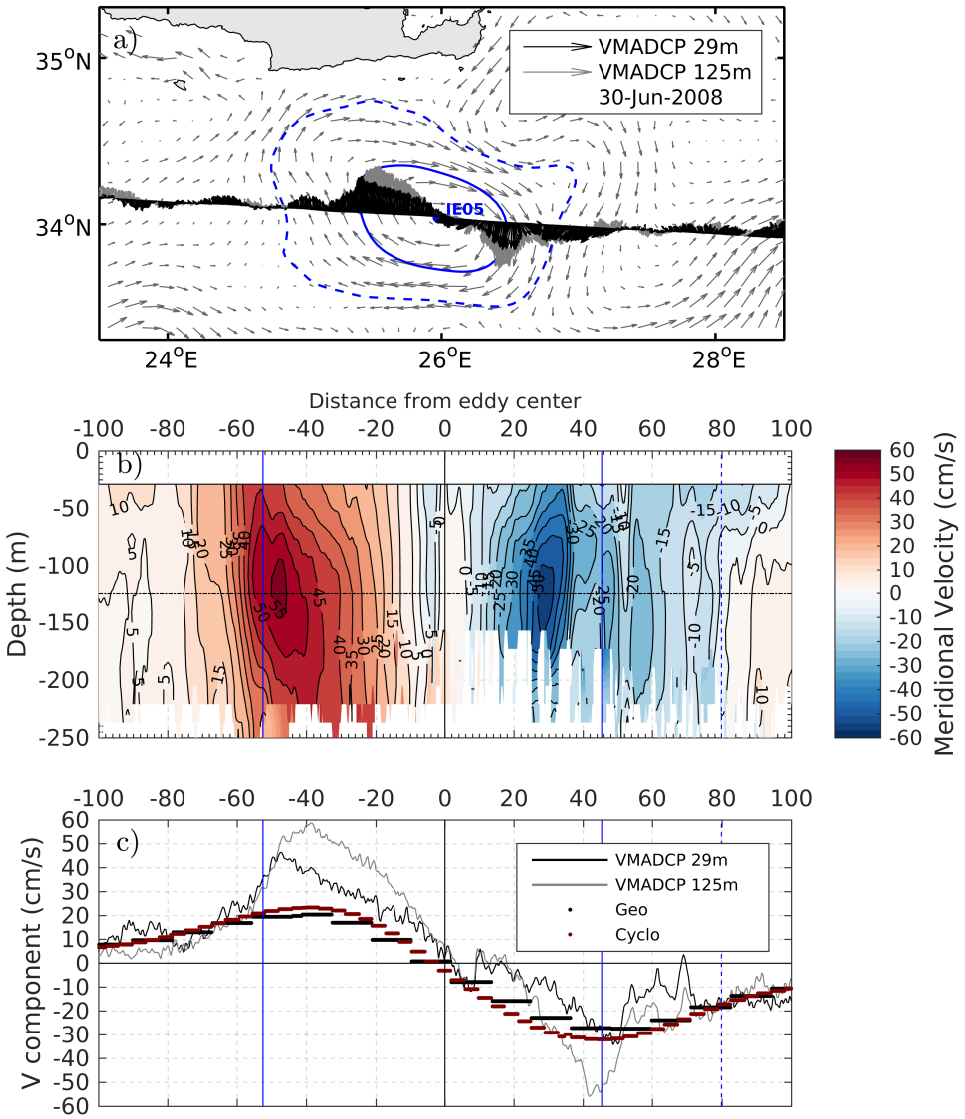

Figure 2.15: *Vessel mounted ADCP measurements performed the 30 of June 2008, when the Atalante oceanographic vessel crossed the core of IE05. The AVISO surface geostrophic velocity map is superimposed to the VMADCP transect in the upper panel (a). The characteristic eddy contours are plotted with blue solid or dashed lines as in Figure 2.14(a). The vertical cross section of the meridional velocity, in the first* $250\,m$*, is plotted in (b). The geostrophic (black dots) and cyclogeostrophic (red dots) velocity profiles derived from the AVISO data set are compared to the VMADCP measurements at* $29\,m$ *(black line) or* $125\,m$ *(gray line) in the bottom panel (c).*

2.6 Conclusions

In this study, we use the $L4$ gridded products, the surface geostrophic velocities, provided by AVISO for the Mediterranean Sea and we apply the AMEDA algorithm in order to evaluate the Ierapetra Eddy variability over a 22 years period from 1993 to 2014. The dynamical properties of each Ierapetra Eddy (IE) were quantified and we analyzed their seasonal and interannual variabilities. Once it is formed, the eddy size remains almost constant with a mean speed radius $R_{max} = 30 - 40km = 3 - 4R_d$. On the other hand, the IE intensity could experience significant variations with a maximal azimuthal speed V_{max} that varies from to $30\,cm\,s^{-1}$ to almost $1\,m\,s^{-1}$. For such strong values, the Rossby number could exceed $Ro = 0.15 - 0.2$ and the cyclogeostrophic balance should then be taken into account. The maximum eddy intensity is usually reached in fall when the IEs is located around its climatological mean position southeast of Crete $(27^oE, 34.3^oN)$. The maximum monthly mean Rossby number Ro_{max}, reached every year, experiences a strong interannual variability with $Ro_{max} = 0.07 - 0.27$ and we did not detect any climatological trend over the 22 years period.

The first surprising result was to find that the IE could be re-amplified, in other words that it could gain a large amount of energy, one year after its formation. If previous studies were able to follow the trajectories of the long-lived Ierapetra anticyclones for several years (Matteoda and Glenn, 1996; Taupier-Letage, 2008; Hamad et al., 2006) none of them quantifies, for such a long period, the evolution of their intensity (V_{max} or Ro for instance). Following the work of Mkhinini et al. (2014) on long-lived eddies in the EMS we used a recent eddy detection and tracking algorithm able to estimate the average velocity profile (Le Vu et al., 2018) of each structure and we were therefore able to quantify the seasonal variations of the monthly mean Rossby number for each IEs. We found that the rapid increase of the vortex intensity could double the mean Rossby number in less than four months while keeping the mean speed radius R_{max} almost unchanged. We called such dynamical event an *intensification stage* and we make a distinction with the *maturity stage* that corresponds to the highest intensity reached just after the formation (2-4 months) of the eddy. When a preexisting IE is already present in the formation area it is likely to be intensified and therefore prevent the formation of a new one. These two distinct stages always coincide with the period of strong Etesian winds when the IEs are located in the southeast of Crete in the lee of the Kasos strait. Hence, both the formation and the intensifications of the IEs are most probably driven by the prevailing atmospheric wind stress. Nevertheless, correlation does not imply causation and the full non-linear Ekman pumping ((Dewar and Flierl, 1987; Gaube et al., 2015)) should be taken into account for a correct explanation of such amplification rates. The impact of Ekman pumping and wind-eddy interactions on the *maturity* or the *intensification stages* of IEs deserve a thorough analysis and will be studied in a future work.

The second unexpected result was to find that the estimated core vorticity of the IEs could sometimes, especially during the *intensification stages*, become very strong. These large meso-scale anticyclones may even reach negative PV in their center ! The previous analysis of Matteoda and Glenn (1996) and Mkhinini et al. (2014) provides some evidence of strong core vorticity but the intensity did not exceed the standard threshold $\zeta < -f$ of inertial instability (Kloosterzielt and Heijst (1991); Holton (1992); Mutabazi and Normand (1992)). Our analysis shows that this theoretical threshold was crossed at least three times in fall 1995, 1999 and 2004. Besides, the comparisons with in-situ measurements indicate that the AVISO products tend to underestimate the maximal velocity amplitude of the IEs. Moreover, the monthly mean Rossby numbers, that we derived from the AVISO data set, also tend to smooth out extreme events. Hence, the real core vorticity is probably more intense than our estimations and the inertial instability threshold crossed more often. This type of ageostrophic instability leads to

intense vertical motions at small-scale and may induce a significant mixing at the vortex edge especially in the upper mixed layer where the stratification is weak (Kloosterzielt et al. (2007); Lazar et al. (2013a,b)). If such unstable ageostrophic perturbations do occur, the vertical mixing could be locally amplified and it will impact the heat transfer from the ocean surface to deep layers below the thermocline. The signature of the inertial instability should be found in the eddy density field with transient overturnings and layers or patches of uniform density in the periphery of the maximum velocity contour. To confirm such hypothesis, a deeper analysis of the Argo profilers or a dedicated in-situ survey in the late summer or fall is needed.

Our analysis confirms that IEs are robust and coherent structures, which are predominantly located southeast of Crete in a well defined area. However, these large meso-scale eddies are not steady. We have shown that their intensity varies significantly, besides they could often merge with another anticyclone or split in two. The consecutive mergings are likely to lead to very long lifetimes that could exceed three years (case of IE05). The dynamical evolution and the trajectory of each individual IE is complex and does not seem to follow a general path as the Algerian Eddies in the Western Basin for instance (Puillat et al. (2002); Escudier et al. (2016)). The recent development of eddy tracking algorithms (such as AMEDA) which take into account the merging and the splitting events, are needed to build these long term trajectories and estimate the water mass transport over long distance. However, due to the spatio-temporal heterogeneity of the altimetric tracks, we are aware that the AVISO products may induce some uncertainty or errors in the eddy tracking. Therefore the complementary analysis of high resolution satellite images (ocean color and temperature), when they are available, cannot be avoided. A reliable analysis of the trajectories of meso scale IEs requires this double analysis. If we consider the merging of IE05 with IE08 (section 2.7) we can get a structure that can be tracked for more than 5 years ! However, it is difficult to know the amount of mixing in the eddy core, due to the multiple merging events, for such a complex structure. If the IEs are able to trap water masses in their core for several years, they will have a crucial impact on the distribution of heat and salt at intermediate levels, within and below the thermocline, in the EMS.

2.7 Eddy detection vs. SST

The figure below shows the discrepancies that may occur between the automatic eddy detection and the visual inspection of SST images. We present here the evolution of the IE05 from July to September 2008, three years after its first detection. The contours of the eddies detected by the AMEDA algorithm applied to the AVISO data set are superimposed on the SST images. In early July 2008, Figure 2.16 (a), the location of the IE05 is in correct agreement with its signature on the SST. However, one month later, Figure 2.16 (b,c), the analysis of the AMEDA algorithm identify a merging event between IE05 and a neighboring meso scale eddy (labeled E1) while it is clearly visible on the SST that these two anticyclones remain coherent and do not merge. At this stage the tracking procedure consider that E1 absorbed IE05 because the new eddy that results from this merging is closer in distance, size and intensity to E1. Hence, the tracking of IE05 is stopped and if seven days later the splitting of E1 leads to a new anticyclone E2 the later is not connected to IE05. According to the analysis of the SST images these consecutive merging and splitting events are erroneous and the eddy labeled E2 by the AMEDA algorithm does correspond to the IE05. Then, according to the SST images (Figure 2.16 (e,f)) the newly formed IE08 growth in early September and takes the position of E2 (i.e. the « lost » IE05). Hence this final merging between the IE08 and the IE05 was not detected by the automatic analysis of the altimetric data sets. This missed event is probably due to a lack of altimetric tracks in the South of Crete between $25^\circ E$ and $26^\circ E$ in August 2008.

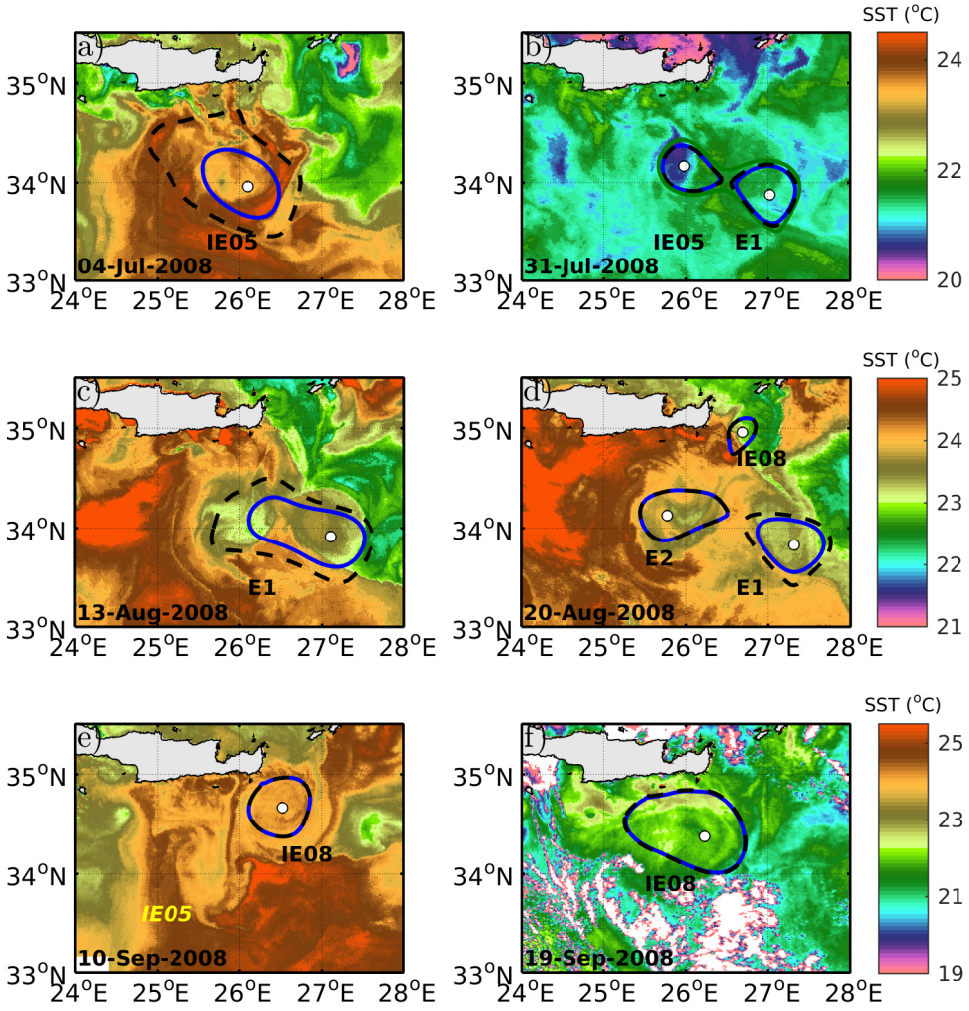

Figure 2.16: *Images of Sea Surface Temperature for a) 04 July 2008, b) 31 July 2008, c) 13 August 2008, d) 20 August 2008, e)10 September 2008 and f) 19 September 2008. The characteristic and last eddy contours detected by AMEDA algorithm are shown with blue solid and black dashed lines. The green contour represents a merging event. The eddy names are shown with black color as tracked by AMEDA and in yellow as tracked with the SST.*

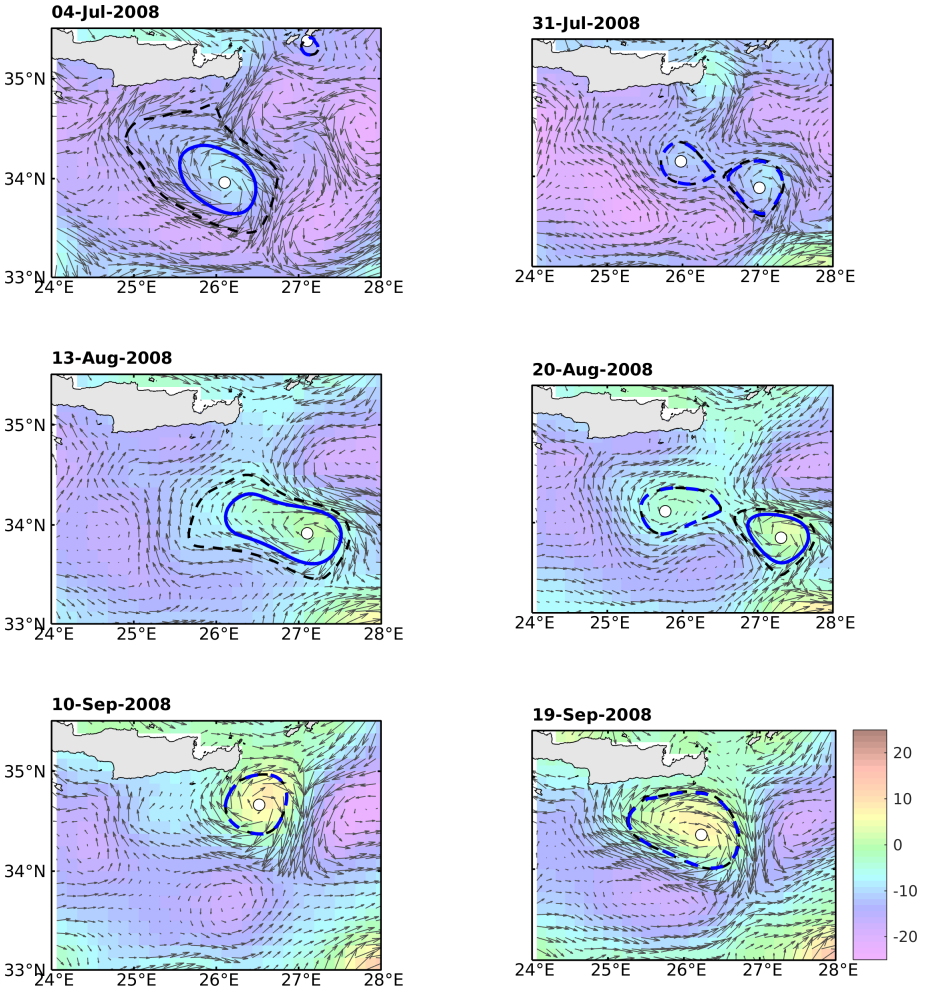

Figure 2.17: *Images of geostrophic velocities superimposed on the sea Surface Height from AVISO for a) 04 July 2008, b) 31 July 2008, c) 13 August 2008, d) 20 August 2008, e)10 September 2008 and f) 19 September 2008. The characteristic and last eddy contours detected by AMEDA algorithm are shown with blue solid and black dashed lines.*

CHAPTER 3

Cyclostrophic corrections of AVISO/DUACS surface velocities and its application to mesoscale eddies in the Mediterranean Sea

As discussed in chapter 2, satellite altimetry provides the geostrophic velocity fields of the ocean's surface, assuming that the reconstructed oceanic sea surface height is in geostrophic balance. The geostrophic approximation holds when the Rossby number Ro is small and is a standard approximation when investigating mesoscale phenomena O(1). Even if an adequate approximation, it cannot satisfy flows with relatively high Ro numbers or flows with curvature (ex. eddies, currents). The importance of accounting for the centrifugal force has been previously emphasized by several authors (Penven et al. (2014); Arnason et al. (1962)). The seasonal variability of the IE intensity also showed that during the maturity and intensification stages the geostrophic assumption could systematically underestimate the structure intensity. The cyclogeostrophic balance was retrieved for a specific examples where the Ierapetra remained circular and the analytical solution could be used to obtain the cyclogeostrophic components. In this chapter we extend the analysis to include cyclogeostrophic corrections given any geostrophic field. An optimized iterative method is directly applied in the AVISO geostrophic velocities and is evaluated on its accuracy to recover the cyclogeostrophic balance. In order to quantify the accuracy of the method, the iterative method is tested both in circular and elliptical idealized eddies of various intensities. The following analysis is published in the Journal of Geophysical Research and is reproduced below.

Cyclostrophic corrections of AVISO/DUACS surface velocities and its application to mesoscale eddies in the Mediterranean Sea

Artemis Ioannou, Alexandre Stegner, Alexandre Tuel, Briac LeVu, Sabrina Speich and Franck Dumas

(Published in *Journal of Geophysical Research: Oceans* (2019), **124**, 1-20, https://doi.org/10.1029/2019JC015031)

Abstract Mesoscale eddies, having a characteristic radius equal or larger than the local deformation radius, are generally considered to be geostrophic. Even if this is true for most of them, there are few cases where the ageostrophic velocity components induced

by the local curvature of the streamlines are not negligible. In order to account for this ageostrophic part, we investigate the performance of an optimized iterative method which computes the cyclostrophic corrections starting from the geostrophic surface velocity of the AVISO/DUACS. We optimized the convergence of the iterative method using an intermediate cubic interpolation. The performance and the accuracy of the optimized iterative method is first evaluated on idealized eddies for which we can obtain their exact cyclogeostrophic solution. Mesoscale eddies of various shapes, intensities and different ellipticity are investigated. The iterative method is then applied to fifteen years (2000-2015) of AVISO/DUACS geostrophic velocity fields, gridded at $1/8^o$ for the Mediterranean Sea. We found that these ageostrophic corrections are needed for most of the mesoscale anticyclones that have a geostrophic vortex Rossby number larger than $Ro > 0.1$. Both the Alboran and the Ierapetra eddies are frequently affected by the cyclostrophic corrections that may exceed $50\,cm\,s^{-1}$. Lastly, the corrected velocity fields are compared with available in-situ observations of velocity measurements (VMADCP) performed within the Ierapetra eddy confirming the benefit of the proposed method.

3.1 Introduction

The increase of the spatial resolution of remote sensing observations has revealed the prevalence of mesoscale eddies throughout the oceans. These coherent structures can survive several months and sometimes several years (Puillat et al., 2002; Ioannou et al., 2017; Laxenaire et al., 2018). They are able to trap and transport heat, mass, and momentum from their regions of formation to remote areas. However, a correct assessment of eddy properties and how they vary temporally is still a challenge. The existing estimations are derived by analyzing satellite altimetry gridded fields which provide daily global 2D maps of sea surface height and surface geostrophic velocity that are not affected by cloud coverage.

In the last 10 years, eddy detection algorithms have been developed and used to identify automatically ocean mesoscale eddies (Doglioli et al., 2007; Chelton et al., 2007; Chaigneau et al., 2009b; Nencioli et al., 2010; Chelton et al., 2011; Mason et al., 2014; Le Vu et al., 2018). These methods locate the eddy center and estimate the eddy size. The eddy intensity is then usually defined as the difference of sea surface height (i.e. hydrostatic pressure gradient) between the eddy center and its periphery (Chaigneau et al., 2009b; Chelton et al., 2011; Souza et al., 2011; Mason et al., 2014) or from some dimensionless parameters derived from the eddy surface velocity field: the relative eddy-core vorticity (Doglioli et al. (2007)), the Okubo-Weiss parameter (Isern-Fontanet et al., 2006) or the vortex Rossby number (Mkhinini et al., 2014; Le Vu et al., 2018; Laxenaire et al., 2018). The main advantage in using the latter is that it is easily comparable with direct in-situ measurements such as VMADCP, LADCP (Ioannou et al., 2017), high frequency radar (HFR) current measurements (Chavanne et al., 2010) or trajectories inferred from surface drifters (Sutyrin et al., 2009; Mkhinini et al., 2014; Ioannou et al., 2017). However, the derivation of ocean surface velocity from remote sensing altimetry is based on the strong assumption that oceanic currents and, in particular, mesoscale eddies satisfy the geostrophic balance. This approximation is inaccurate for submesoscale structures whose ageostrophy is large (Chang et al., 2013), but it could also induce significant bias for mesoscale eddies.

The dynamical characteristics of small-scale surface eddies ($5-20\,km$) that were not accessible before with traditional oceanographic campaigns, can now be obtained from high frequency radar (HFR) current measurements (Paduan and Washburn, 2013; Schaeffer et al., 2017) or from an intensive scanning of a small oceanic area with shipboard ADCP (Hasegawa et al., 2004; Chang et al., 2013). These recent observations of submesoscale eddies, having a radius smaller than the first baroclinic deformation radius, have shown that their relative vorticity ζ_0/f, where ζ_0 is the surface vorticity measured in the

eddy core and f the Coriolis parameter, could exceed unity and could reach values up to $|\zeta_0/f| = 5 - 10$ (Chang et al., 2013). Such strongly ageostrophic structures which evolve rapidly cannot be detected by the current spatio-temporal resolution of altimetry products and are therefore, out of the scope of this paper.

On the other hand, mesoscale eddies, having a characteristic radius equal or larger than the local deformation radius, are generally considered to be geostrophic. Even if this is true for most of them, there are nevertheless few cases where the ageostrophic velocity components induced by the local curvature of the streamlines are not negligible (Penven et al., 2014; Douglass and Richman, 2015; Ioannou et al., 2017). To make the distinction with the ageostrophic velocities induced by the surface wind-stress, we use here and in what follows, the term cyclostrophic velocity correction for these ageostrophic velocity components which take into account the centrifugal acceleration. The pioneering work of Uchida et al. (1998), has shown that adding small ageostrophic velocity components, induced by the curvature of the Kuroshio, improves the comparison of surface velocities calculated from satellite altimetry (TOPEX/POSEIDON at that time) with the drifting buoys velocities. More recent studies have shown that cyclostrophic corrections should be applied to the geostrophic velocity, derived from altimetry maps, to assess correctly the azimuthal velocity of some intense mesoscale eddies in the Mozambique channel (Penven et al., 2014) or for the intense Gulf stream rings (Douglass and Richman, 2015). Similarly, in the Mediterranean Sea strong ageostrophic components have been reported for anticyclonic eddies in two specific areas. The Western Alboran Gyre, located between the Strait of Gibraltar and Cape Tres Forcas, constitutes one of the strongest anticyclonic features of the western Mediterranean Sea, with surface currents which exceed $1\,m/s$ (Viudez et al., 996a,b; Gomis et al., 2001; Flexas et al., 2006). Moreover, in the eastern Mediterranean Sea, the Ierapetra anticyclones, located at the south-east corner of Crete, could also reach finite vorticity values (Matteoda and Glenn, 1996). For these two specific anticyclones, in-situ measurements revealed the inadequacy of the geostrophic approximation to describe the eddy dynamics. The standard AVISO/DUACS products, may often underestimate the eddy intensity. However, in the Mediterranean Sea, ageostrophic corrections may not be limited to these two eddies.

Two approaches were used to compute the cyclostrophic velocity corrections on AVISO/DUACS products so far. The first one is to solve the quadratic cyclogeostrophic equation (i.e. Eqn.(7) in section 3.4) for circular eddies which were detected in the geostrophic velocity field. It was applied by Ioannou et al. (2017) for a few quasi-circular configurations of the Ierapetra anticyclone and by Douglass and Richman (2015) who assumed a Gaussian shape for all the quasi-circular eddies of the Atlantic ocean. This method is quite simple but it requires to know precisely the velocity profile of the geostrophic eddy and it is valid only for circular eddies. The second one, is based on an iterative method which adds at each step small corrections to the surface velocity field in order to account for the centrifugal acceleration induced by the local curvature (Arnason et al., 1962; Penven et al., 2014). The main advantage of this global approach is that it provides a cyclostrophic correction for all eddies regardless their initial shapes. The main drawback is that the iteration may not converge to the exact cyclogeostrophic balance and so careful accuracy tests should be done.

In the present study, we optimized the convergence of the iterative method using an intermediate cubic interpolation. Besides, we tested thoroughly the accuracy of the method on idealized eddies for which we can obtain a direct solution of the cyclogeostrophic balance. We explore a wide distribution of sizes and intensities but also various shapes that correspond to the statistical distribution of mesoscale eddies in the Mediterranean Sea. Then, we applied this cyclostrophic correction to fifteen years (2000-2015) of daily geostrophic velocity fields provided by AVISO/DUACS for the Mediterranean Sea at the high grid resolution of $1/8°$. We found that it may signifi-

cantly impact the estimated intensities of mesoscale anticyclones, especially the Alboran and the Ierapetra eddies but not only. Finally, the corrected surface velocity fields were compared with direct in-situ measurements performed within the Ierapetra anticyclone during the PROTEVS-PERLE campaign of October-November 2018.

3.2 Data

AVISO Data set

We used in the present study the geostrophic velocity fields, for the years 2000–2015, produced by SSALTO/ Data Unification and Altimeter Combination System (DUACS) and distributed by AVISO and derived from the absolute dynamical topography (ADT). Unlike the seal level anomaly (SLA), which represents the variable part of sea surface height, the ADT is the sum of this variable part and the constant part averaged over a 20-year reference period. The "all sat merged" series distributed regional product for the Mediterranean Sea combines, up-to-date datasets with up to four satellites at a given time, using all the missions available at a given time [TOPEX/Poseidon, ERS-1 and ERS-2, Jason-1 and Jason-2, the Ka-band Altimeter (AltiKa) on the Satellite with the Argos Data Collection System (Argos) and AltiKa (SARAL), Cryosat-2 and Envisat missions]. This merged satellite product, for the Mediterranean Sea, is projected on a $1/8^{\circ}$ Mercator grid, with a time interval of 24 h.

The spatial resolution of this regional dataset is 2 times higher than the global altimetric products at $1/4^{\circ}$. Nevertheless, it remains a coarse-resolution product, because the horizontal resolution of the $1/8^{\circ}$ gridded velocity fields ($dX \simeq 12\,km$) cannot fully resolve the internal deformation radius that is around $Rd \simeq 8$–$12\,km$ in the Mediterranean Sea (Robinson et al., 2001; Escudier et al., 2016). Moreover, the recent analysis of (Amores et al., 2018), which compares the eddies detected on a high-resolution numerical simulation ($1/60^{\circ}$) with those detected on a synthetic AVISO field ($1/8^{\circ}$), showed that only eddies, with a characteristic eddy radius smaller than $R_{max} \leq 25\,km$ (i.e. $R_{end} \leq 35\,km$) couldn't be correctly detected with the regional AVISO/DUACS dataset. It will be therefore useless to apply any cyclostrophic correction on inaccurate submesoscale structures that may appear on the AVISO field.

Shipboard Acoustic Doppler Current Profilers Measurements During the PROTEVS-PERLE Campaign

The PROTEVS-PERLE campaign was held in October-November 2018 in the eastern Mediterranean Sea. Among the various measurements (CTD, LADCP, SEASOR etc.) performed during the PERLE experiment we focus here on the vertical current profiles that were acquired with Ocean Surveyors $150\,kHz$ and $38\,kHz$ (Teledyne RDI) when the Ierapetra eddy was crossed between the 28th of October until the 2nd of November. These systems are two Vessel-Mounted Acoustic Doppler Current Profilers (ADCP) on the R/V L'Atalante. In order to obtain vertical profiles of current speed and direction in the upper layer, we use the $150\,kHz$ Ocean Surveyors that provide velocity measurements every $8\,m$ with maximum depth of about $220\,m$. The first bin sampled is located $26\,m$ beneath the surface in order to avoid any reflections and interactions with the vessel. The range covered by the OS150 instrument varied between $150\,m$ and $220\,m$ over the diurnal cycle. Despite it's short range it provides permanently an assessment of the horizontal components of the current between $26\,m$ and $100\,m$. The velocities obtained are averaged over $2\,min$. The ensemble and the bin size provide a precision of the horizontal velocity that was assessed to be below $8\,cm\,s^{-1}$. Compared to the velocities observed in the vicinity of the Ierapetra periphery, this corresponds to an error of a bit less than 10%.

3.3 Methods

AMEDA Eddy Detection Algorithm

In order to quantify the eddy size and their intensity, we apply the Angular Momentum Eddy Detection and tracking Algorithm (AMEDA) which is based on physical parameters and the geometrical properties of the velocity field (Le Vu et al., 2018). The eddy centers are first identified and correspond to an extremum of the local normalized angular momentum. The streamlines surrounding this center are then computed (Figure 3.1(b)). The mean radius $\langle R \rangle$ and the mean velocity $\langle V \rangle$ are evaluated for each closed streamline. This mean radius $\langle R \rangle$ is defined as the equivalent radius of a circular disc with the same area A as the one delimited by the closed streamline (Eqn.(1)), while the mean velocity amplitude $\langle V \rangle$ is derived from the circulation along the closed streamline C, where L_p is the streamline perimeter (Eqn.(2)).

$$\langle R \rangle = \sqrt{A/\pi} \tag{1}$$

$$\langle V \rangle = \frac{1}{L_p} \oint_C V dl \tag{2}$$

We plot in Figure 3.1(c) the pair of the mean eddy velocity $\langle V \rangle$ and the mean radius $\langle R \rangle$ for each closed streamline of the mesoscale anticyclone located at the east of Sardinia the 2nd of November 2004. We can see on this example that the mean velocity increases when the radius increases until a maximum velocity V_{max} is reached. The corresponding radius is named R_{max}, also called the speed radius (Chelton et al., 2011; Le Vu et al., 2018; Laxenaire et al., 2018). The *characteristic contour* of the detected eddy (blue contours in Figure 3.1) is associated with the closed streamline of maximal speed. After this maxima, the azimuthal speed of the eddy decreases until the last closed streamline is reached. The latter is plotted with a black dashed line in Figure 3.1.

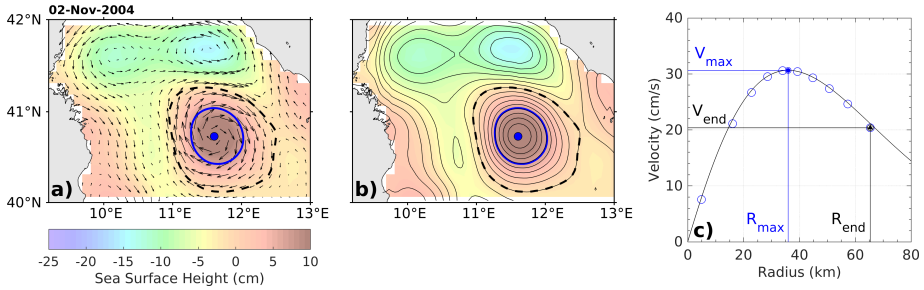

Figure 3.1: *Principle of the automatic eddy detection algorithm AMEDA. The characteristic contour (solid blue line) and the last contour (black dashed line) are calculated from the surface velocity field (a) for an large anticyclone located at the east of Sardinia. The background colors correspond to the ADT map while the black vectors to the surface geostrophic velocities. The streamlines associated with the velocity field are plotted in (b) and also the correspondence with the characteristic contour (solid blue line) and the last closed contour (black dashed line). The mean velocity profile $\langle V \rangle = F(\langle R \rangle)$ deduced from the streamlines analysis and the characteristic eddy radii R_{max} and R_{end} are plotted in (c).*

From the characteristic eddy velocity V_{max} and the corresponding radius R_{max}, we compute the vortex Rossby number to quantify the eddy intensity:

$$Ro = \left| \frac{V_{max}}{f \, R_{max}} \right| \tag{3}$$

where f is the Coriolis parameter. The eddy shape is characterized by two geometrical parameters. The first one is the ellipticity ε of the closest ellipse that fits the characteristic contour. The second one is the steepness parameter α which is used to fit the mean velocity profile $\langle V \rangle = F(\langle R \rangle)$ of quasi-circular eddies ($\varepsilon < 0.2$). These mean velocity profiles are fitted with the generic function:

$$V_\theta(r) = \frac{V_{max}}{R_{max}} r e^{(1-(r/R_{max})^\alpha)/\alpha} \tag{4}$$

Such generic profiles were used by Carton et al. (1989); Stegner and Dritschel (2000); Lazar et al. (2013b); Yim et al. (2018) to study the stability of various isolated eddies. Moreover, Ioannou et al. (2017) found that such generic velocity profile (Eqn.(4)) provides a high correlation fit for the 22 year analysis of the Ierapetra anticyclones. Note that when $\alpha = 2$ the eddy has a Gaussian velocity profile.

We apply the AMEDA algorithm to fifteen years (2000-2015) of surface velocity fields provided by AVISO/DUACS for the Mediterranean Sea. These velocity fields are derived from the absolute dynamical topography (ADT) according to the geostrophic balance. Hence, all the following results are valid for geostrophic structures. The global statistics of the dynamical and geometrical properties of these geostrophic mesoscale eddies, detected by the AMEDA algorithm and having a characteristic radius larger than $18\,km$, are plotted separately for cyclones and anticyclones in Figure 3.2. The total number of detected cyclones (~ 295000) is slightly larger than the detected anticyclones (~ 220000). However, if we consider intense eddies, the proportion is strongly reversed and we get 16600 anticyclones and 5000 cyclones having a geostrophic Rossby number larger than 0.1. For larger values, for instance $Ro \geq 0.15$, there is a large predominance of anticyclones as shown in Figure 3.2(a). A significant cyclone anticyclone asymmetry is also visible on the eddy shape. The mesoscale cyclones tend to be more elliptical than the mesoscale anticyclones. There is a clear predominance of cyclonic structures when the ellipticity ε exceeds 0.3 (Figure 3.2(b)). However, as far as quasi-circular eddies are concerned, there is no clear asymmetry for the azimuthal velocity profiles. Both cyclones and anticyclones exhibit a similar distribution of the steepness parameter α which varies between $\alpha = 1.2$ and $\alpha = 2.7$ while the highest probability is close to the Gaussian shape ($\alpha = 2$). Hence, this statistical analysis of the AVISO/DUACS data set, suggests that there is no universal velocity profile for mesoscale eddies in the Mediterranean Sea. The geostrophic Rossby number could be quite large exceeding 0.2 while a quite large number of eddies deviate from the circular symmetry with a mean ellipticity which exceeds $\varepsilon > 0.3$.

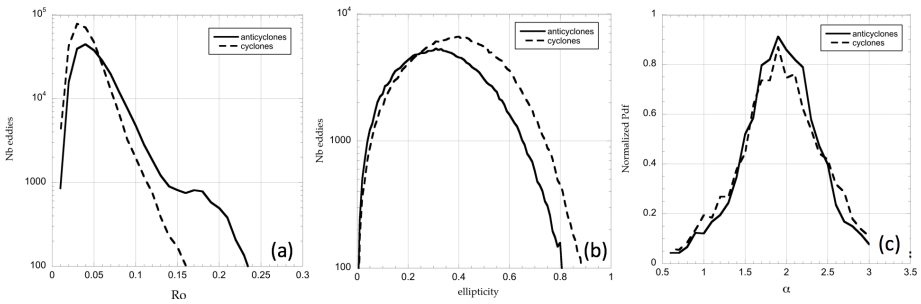

Figure 3.2: *Probability distributions of the vortex Rossby number (a), the ellipticity ε (b) and the steepness parameter α (c) for cyclones (solid line) and anticyclones (dashed line) in the Mediterranean sea for the 2000-2015 period. We consider here only geostrophic mesoscale eddies having a characteristic radius larger than $R_{max} \geq 18\,km$. The steepness parameter α was computed here only for quasi circular eddies ($\varepsilon < 0.2$).*

Iterative method to compute the cyclogeostrophic velocities

We consider in what follows large oceanic eddies that evolve and propagate slowly over time. For such mesoscale oceanic eddies, the flow acceleration is negligible in comparison with the centrifugal acceleration induced by the streamlines curvature and therefore the surface velocity field $\mathbf{U}$ should satisfy the cyclogeostrophic balance:

$$\mathbf{U}.\nabla\mathbf{U} + f\,\mathbf{k}\times\mathbf{U} = -g\nabla\eta = f\,\mathbf{k}\times\mathbf{U_g} \tag{5}$$

where $\mathbf{U}_\mathrm{g}$ is the geostrophic velocity which is directly proportional to the gradient of the sea surface deviation $\nabla\eta$. For the case of a steady circular eddy, this balance relation is strictly identical to the Bolin-Charney balance on a f-plane (Charney, 1955). Higher order balanced equations were proposed for synoptic-scale weather systems which evolve rapidly over a few days in order to account for the divergent components of the flows (Iversen and Nordeng, 1982, 1984; McIntyre, 2015). However, most of the mesoscale oceanic eddies are, at the first order of approximation, non-divergent and they evolve slowly if we neglect rapid merging and splitting events.

For non-circular eddies there is no analytical solution for $\mathbf{U}$ when $\mathbf{U}_\mathrm{g}$ is known. Besides, this non-linear balance may have no solution at all, for instance when the geostrophic Rossby number of a circular anticyclone exceeds the critical value $Ro = V_g/(fR) > Ro_c = 0.25$ (Knox and Ohmann, 2006; Penven et al., 2014). However, according to the Figure 3.2(a) such intense anticyclones are extremely rare (less than 0.01%) in the Mediterranean Sea and we therefore expect that the wide majority of mesoscale eddies detected on the AVISO/DUACS database satisfy the cyclogeostrophic balance (Eqn.(5)).

In order to calculate the ageostrophic velocity components of intense eddies having various shapes and velocity profiles we use an iterative method that was first proposed in atmospheric science (Arnason et al., 1962) and used for intense oceanic eddies in Penven et al. (2014) to approximate the cyclogeostrophic balance Eqn.(5). This iterative scheme is given by:

$$\mathbf{U^{n+1}} = \mathbf{U_g} + \frac{1}{f}\mathbf{k}\times(\mathbf{U^n}.\nabla\mathbf{U^n}) \tag{6}$$

where $\mathbf{U^0} = \mathbf{U}_\mathrm{g}$. We first project, with a cubic interpolation, the initial geostrophic velocity field gridded at $1/8°$ on a finer grid at $1/24°$ in order to improve the computation of the velocity derivatives in the equation Eqn.(6).

There is no proof of convergence for this iterative scheme and for intense eddies it may even diverge after few iterations (Arnason et al., 1962; Penven et al., 2014). An example of the divergence of the velocity profile, for an initial geostrophic anticyclone with $Ro = 0.23$, is given in Figure 3.4(a). Hence, to prevent such local divergence, we performed, as Penven et al. (2014), a constraint iteration which stops the iteration at a grid point when the local residual $\left\|\mathbf{U}^{n+1} - \mathbf{U}^n\right\|$ starts to increase. The local norm $\|\|$ is computed here on nine grid points: the central one and the eight closest neighbors. For the example shown in Figure 3.4, the iteration will stop in the core of the anticyclone after two steps. The Rossby number of the final cyclogeostrophic anticyclone (red curve) will reach $Ro = 0.48$ which is twice its initial value (Figure 3.3).

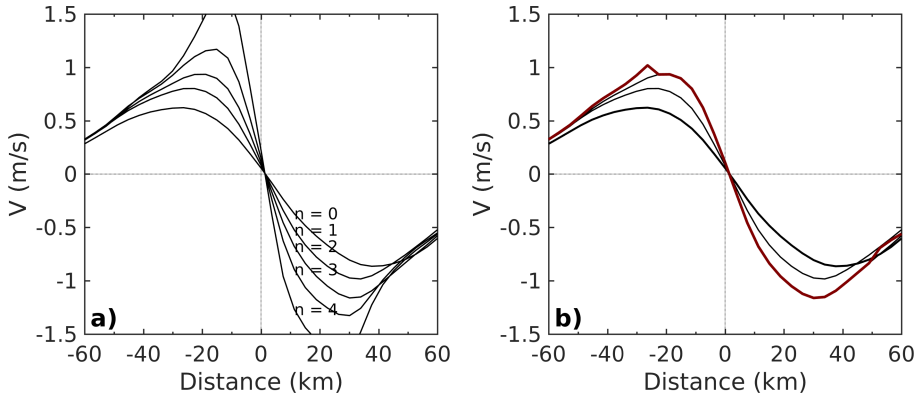

Figure 3.3: *Modifications of the meridional velocity profile of the Alboran eddy (depicted Figure 3.4) along the longitude axis at each step of the iterative process Eqn.(6) for the free iteration (a) and for the constrained iteration (b). The vortex Rossby number, of the initial geostrophic eddy (bold profile in (b)) , is* 0.24 *while at the end of the constrain iteration (red profile in (b)) it reaches* $Ro = 0.48$ *.*

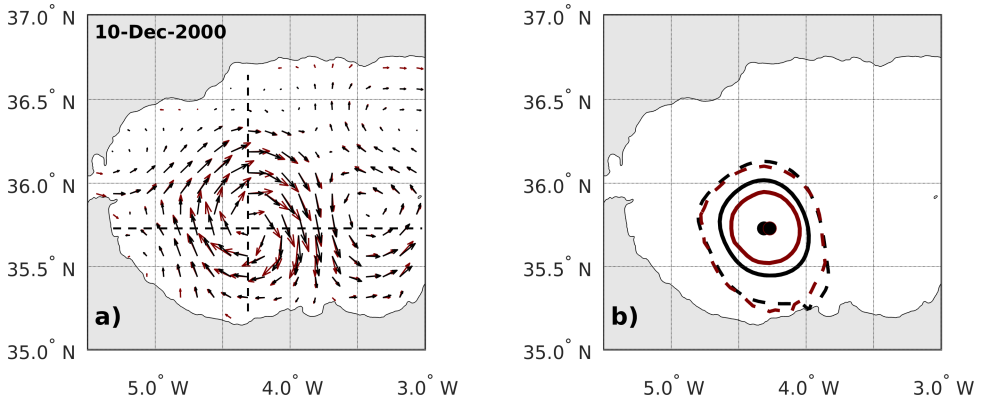

Figure 3.4: *Example of the cyclogeostrophic corrections (red) applied to the AVISO/DUACS surface geostrophic velocity field (black) on the Alboran anticyclone in December 2000 (a). The characteristic eddy contour computed by the AMEDA algorithm (b) is also modified by the cyclogeostrophic correction (red) in comparison with the initial contour computed from the geostrophic field (black) as shown in Figure 3.3.*

3.4 Cyclogeostrophic balance of steady and isolated eddies

In order to test the accuracy of the iterative method Eqn.(6) and to develop some algorithmic optimizations, it was needed to compare the results with several test cases. We first consider circular eddies for which we can get simple analytical solutions for both the geostrophic and the cyclogeostrophic balance Eqn.(5). Then, assuming a slow evolution of the velocity field, we also consider steady elliptical eddies for the test cases.

Impact of the cyclogeostrophic corrections on circular eddies

Circular eddies are steady solutions of the cyclogeostrophic equation Eqn.(5) which simplifies for any azimuthal velocity profile $V_\theta(r)$ to the gradient-wind equation:

$$\frac{V_\theta^2}{fr} + V_\theta = V_g = \frac{g}{f}\frac{\partial \eta}{\partial r} \tag{7}$$

where $V_g(r)$ is the geostrophic velocity profile associated to the free surface deviation η. Cyclonic eddies correspond to $V_\theta > 0$ while for anticyclonic eddies $V_\theta < 0$. To study various velocity profiles, we use the generic function Eqn.(4) for the azimuthal velocity. The relation between the geostrophic velocity and the cyclogeostrophic velocity will then depend both on the dimensionless Rossby number Ro and the steepness parameter α. For very small Rossby number, the eddy satisfies the geostrophic balance and therefore $V_\theta \simeq V_g$. However, when the Rossby number starts to increase, the centrifugal acceleration should be taken into account and due to the non-linear term of Eqn.(7) it induces an asymmetry between cyclonic and anticyclonic eddies. Hence, if we compare geostrophic velocities of opposite sign but of the same intensity (i.e. same amplitude of the free surface deviation) the cyclogeostrophic velocity could differ significantly even if the Rossby number is moderate. We should make here the distinction between the geostrophic vortex Rossby number $Ro_g = max(|V_g|)/fR_{maxg}$ computed from the maximum value of geostrophic velocity and the real Rossby number Ro associated to the complete velocity of the gradient-wind equation Eqn.(7). We illustrate in Figure 3.5 this asymmetry in the cyclogeostrophic correction for some examples of isolated mesoscale eddies the characteristics of which could be observed in the Mediterranean Sea. The comparison is made between eddies of distinct shape (i.e. steepness parameter $1 \leq \alpha \leq 3$ in agreement with Figure 3.2(c) but with the same size $R_{max} = 30\,km$ and the same geostrophic amplitude $max(|V_g|) = 42\,cm\,s^{-1}$. For these cases the geostrophic Rossby number is moderate $Ro_g = 0.14$ but nevertheless the cyclogeostrophic velocity profiles differ significantly from the geostrophic solution. The amplitudes of anticyclonic (cyclonic) eddies are amplified (attenuated). The maximum velocity of the anticyclones increases up to $V_{max} = -52\,cm\,s^{-1}$ while, for cyclones, it decreases slightly down to $V_{max} = 36\,cm\,s^{-1}$. Moreover, depending on their specific shape, the characteristic radii R_{max} of the anticyclones (cyclones) are reduced (increased) in comparison with their geostrophic signature.

To investigate a wider range of parameters and quantify more precisely the deviation between the cyclogeostrophic and the geostrophic velocity profiles we plot, for three distinct profiles, the percentage of the relative error on the vortex Rossby number:

$$\Sigma_{Ro} = \frac{Ro - Ro_g}{Ro_g} \tag{8}$$

and on the characteristic eddy radius:

$$\Sigma_R = \frac{R_{max} - R_{maxg}}{R_{maxg}} \tag{9}$$

as a function of the geostrophic Rossby number Ro_g which is the only dynamical parameter that can be initially deduced from the altimetry data-sets. The cyclostrophic corrections are more pronounced for anticyclonic eddies than for cyclonic ones (Figure 3.6). The standard geostrophic velocity provided by the AVISO/DUACS products underestimate the intensity of mesoscale circular anticyclones especially when their geostrophic Rossby number exceeds 0.1. Besides, this analysis shows that the cyclostrophic correction is indeed profile dependent. The percentage of the cyclostrophic correction depends both on the vortex intensity (i.e. Ro_g) and the steepness parameter α of the velocity profile. Hence, the vortex intensity, is not the single parameter that controls the deviation from the geostrophic approximation.

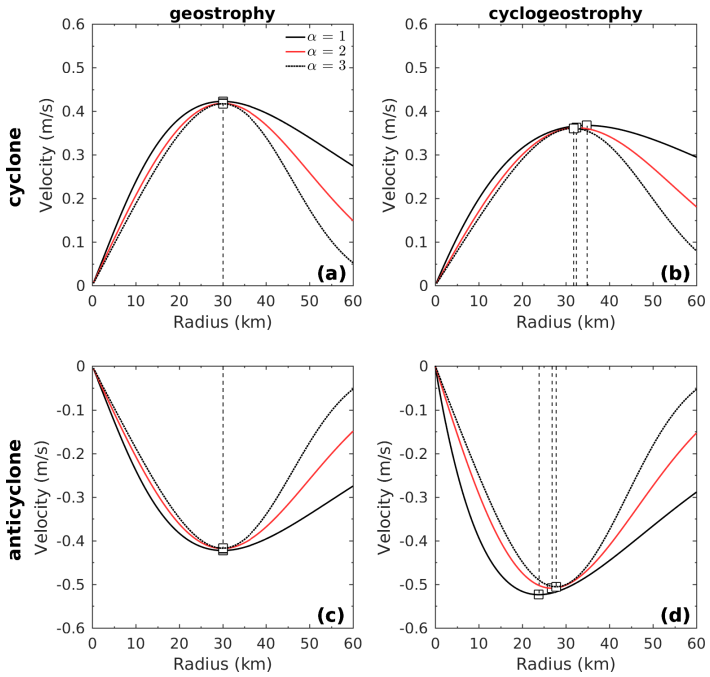

Figure 3.5: *Comparison of geostrophic vs. cyclogeostrophic velocity profiles of both cyclonic and anticyclonic eddies having the same geostrophic Rossby number ($Ro_g = 0.14$) but distinct steepness parameters: $\alpha = 1$ (black solid line), a Gaussian eddy $\alpha = 2$ (red line) and $\alpha = 3$ (black dashed line).*

Accuracy of the iterative method on circular eddies

The analytical solutions, obtained in the previous section for circular eddies, can then be used to test the accuracy of the iterative method Eqn.(6). We first project the geostrophic velocity components of the circular vortex on a regular $1/8°$ grid which is identical to the standard AVISO/DUACS gridded products. In a second step, this geostrophic velocity field is interpolated on a higher resolution grid at $1/24°$ to improve the computation of the velocity gradients in the non linear terms of the Eqn.(6). The iterative scheme is then applied to this new velocity field and the corrected circular velocity profile is then estimated at each step of the iteration. In order to prevent local divergence, the iteration process is stopped when the local residual $\left\|\mathbf{U}^{n+1} - \mathbf{U}^{n}\right\|$ starts to increase. As shown in Figure 3.7 this iterative scheme may, or may not, converge to the exact cyclogeostrophic solution but due to the constrain on the decay of local residual it will not diverge. The iteration scheme applied on two Gaussian anticyclones ($\alpha = 2$) with the same radius ($R_{maxg} = 30\,km$) but different intensities is depicted in Figure 3.7. When the initial geostrophic Rossby number is moderate ($Ro_g = 0.16$) the scheme converges rapidly, after 4 iterations, to the cyclogeostrophic solution (Figure 3.7(a)). The latter has a smaller radius ($R_{max} = 26\,km$) and a significantly higher Rossby number ($Ro = 0.24$) than the initial geostrophic velocity profile. However, when the anticyclone intensity ($Ro_g = 0.2$) gets closer to the critical value $Ro_c = 0.25$, the iteration scheme does not succeed to reach the cyclogeostrophic solution and a residual error of 17% on the Rossby number does persist after 5 iterations (Figure 3.7(b, c)). Cyclonic gaussian eddies were also tested and we did not find any convergence issue even for large Rossby number up to $Ro_g = 0.2$, which is the largest value found for Mediterranean cyclones. For these intense cyclonic eddies the residual errors of the iteration scheme were below 15%. Other iteration scheme using a relaxation parameter were tested on these few test

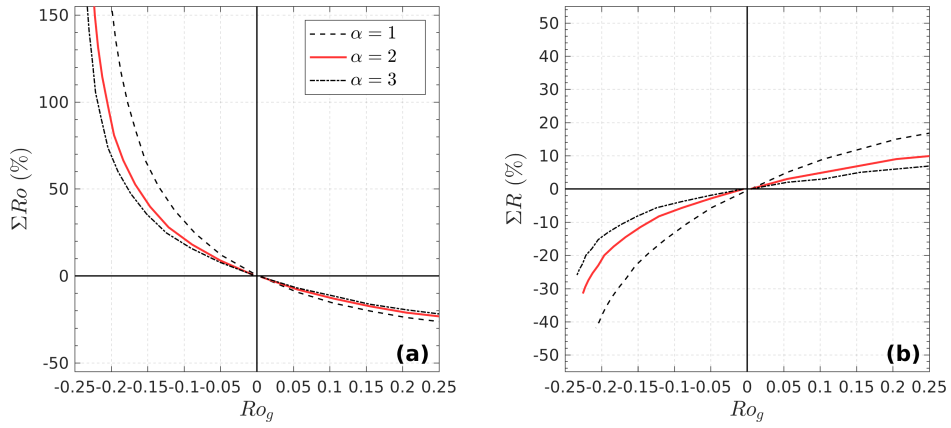

Figure 3.6: *Percentages of the relative errors, between the cyclogeostrophic and the geostrophic vortex solution, are plotted for the vortex Rossby number (a) and the characteristic eddy radius R_{max} (b) . Negative (positive) Rossby numbers correspond here to anticyclonic (cyclonic) eddies. Various circular eddies having distinct shape ($\alpha = 1$ dotted line, $\alpha = 2$ solid line and 3 dashed line) and intensity ($-0.25 < Ro_g \leq 0.25$) are considered.*

cases. The convergence is slower with this under-relaxation scheme but unfortunately it doesn't provide a better accuracy (section 3.7).

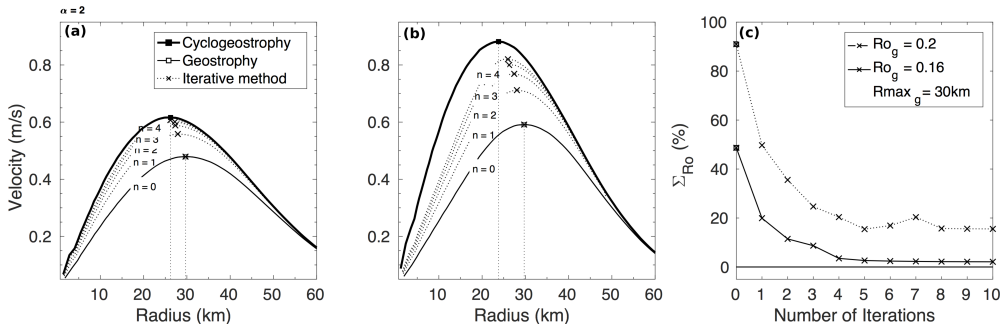

Figure 3.7: *Accuracy of the iteration scheme Eqn.(6) applied to two geostrophic gaussian anticyclones ($\alpha = 2$) having the same radius, $R_{max} = 30\,km$, but distinct Rossby number: $Ro_g = 0.16$ (a) and $Ro_g = 0.2$ (b). The initial geostrophic profiles $V_g(r)$ are plotted with thin dashed lines, while the targeted velocity profiles $V_\theta(r)$, solution of the cyclogeostrophic equation (Eqn.(7)), are plotted with a thick black line. (c) Relative error ($\Sigma_{Ro} = (Ro - Ro_i)/Ro_i$) between the Rossby number reached at every iterative step (Ro_i) and the corresponding exact cyclogeostrophic solution (Ro) for the two gaussian anticyclones.*

We also quantify how the initial interpolation on a finer grid, from $1/8°$ to $1/24°$, impacts the iteration scheme. The accuracy of the convergence is tested for three cases: no interpolation (open circle), in other words we stay on the initial AVISO/DUACS grid, a linear interpolation at $1/24°$ and a cubic interpolation at $1/24°$ (Figure 3.8). We have found that the cubic interpolation improves significantly the accuracy of the iterative scheme, both for the vortex intensity and its size. Higher order interpolation (quintic)

and also higher resolution $(1/48°)$ were tested with no significant improvements on the iteration scheme.

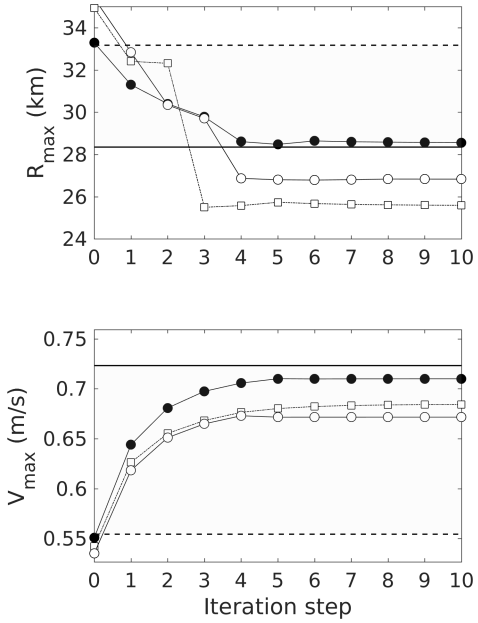

Figure 3.8: *Impact of the initial interpolation on the evolution of the characteristic radius R_{max} and the speed radius V_{max} at each step of the iteration scheme Eqn.(6) for an initial geostrophic gaussian eddy ($\alpha = 2$). The horizontal dashed lines correspond to the targeted values of the cyclogeostrophic solution. Three cases are plotted: no initial interpolation (open circle), a linear interpolation at $1/24°$ (open square) and a cubic interpolation (filled circle) at $1/24°$.*

The accuracy of this optimized iterative scheme was tested for the wide range of parameters (Ro_g, R_{maxg}, α) that were found for mesoscale anticyclonic eddies (Figure 3.2). The percentage of the relative error on the vortex Rossby number between the geostrophic and the cyclogeostrophic anticyclones were plotted at the initial stage (Figure 3.9(a, c)) and at the final stage of the iteration process (Figure 3.9(b, d)). We arbitrary fix the separation between weak (in green) and strong (in red) errors at 30%. The relative errors are almost negligible ($< 15\%$) when the vortex Rossby number is below 0.08. However, when Ro_g exceeds $0.12 - 0.15$ the deviations between the cyclogeostrophic and the geostrophic solution becomes strong (i.e. $> 30\%$) and the use of the standard AVISO/DUACS geostrophic velocity field will lead to a systematic underestimation of the intensity of circular anticyclones. This deviation tends to decrease when the steepness parameter α increases (Figure 3.9(b)). For almost all the anticyclones we studied, the iterative scheme reduces this initial deviation and the final result is much closer to the cyclogeostrophic solution than the initial one. Hence, we've shown here that the iterative scheme leads to a correct estimation of the ageostrophic terms, induced by the streamline curvature, for idealized circular eddies.

The (R_{max}, α) parameter space was not thoroughly investigated for cyclonic eddies because, their maximal amplitudes are generally weaker than the anticyclones in the AVISO/DUACS product (Figure 3.2). Besides, for the same geostrophic Rossby number the cyclostrophic correction is generally much weaker for cyclonic eddies than for anticyclonic ones (Figure 3.6(a)).

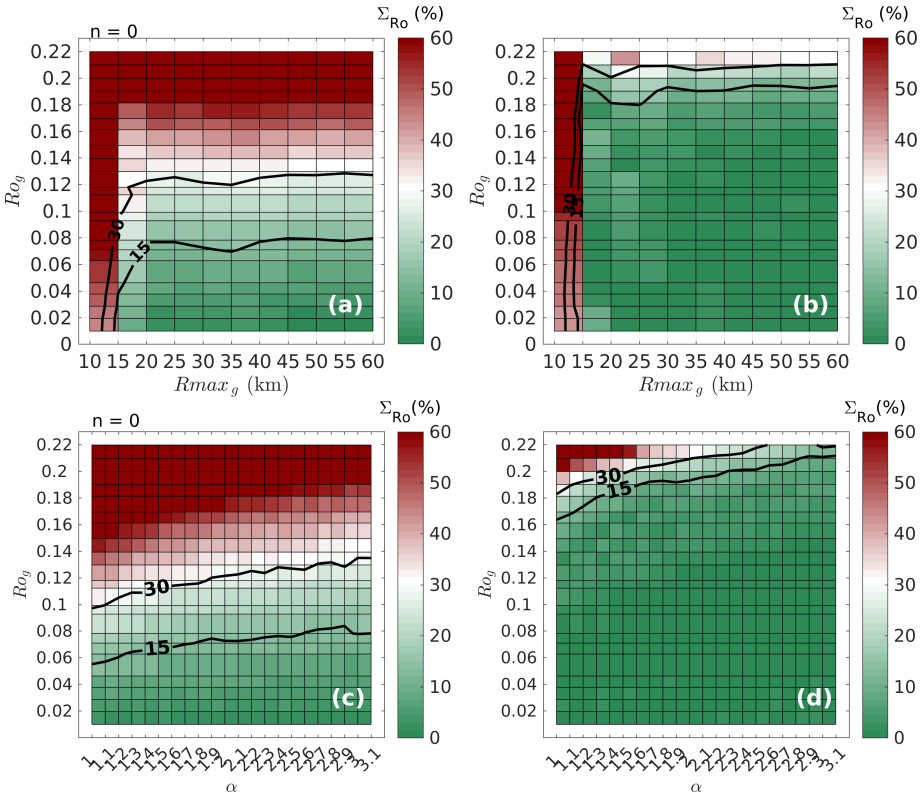

Figure 3.9: *Initial relative error on the vortex Rossby number between geostrophic and cyclogeostrophic circular anticyclones of various intensity (Ro_g), sizes (a), or profiles (b) when there is no corrections on the initial geostrophic velocity field. Relative error ($\Sigma_{Ro} = (Ro - Ro_i)/Ro_i$) between the Rossby number reached at the end of the iterative scheme (Ro_i) and the one corresponding to the exact cyclogeostrophic solution (Ro) for the same range of initial parameters (b,d).*

Accuracy of the iterative method on elliptical eddies

We have seen, in the previous section, that the iterative scheme provides a correct estimation of the full cyclogeostrophic profile for idealized circular anticyclones which are not too close to the divergent limit $Ro_g = 0.25$. However, according to the AVISO DUACS products, most of the detected eddies are elliptical (Figure 3.2(b)). Hence, the accuracy of the iterative scheme should also be tested on an elliptical eddy configuration. We first generate elliptical velocity fields which are non-divergent (i.e. $\nabla.\mathbf{V} = \mathbf{0}$). To do so, we started from a circular Gaussian velocity profile ($\alpha = 2$) and we apply a deformation, that conserves the area inside each streamline:

$$x^{'} = x\sqrt{1-\varepsilon} \tag{10}$$

$$y^{'} = y/\sqrt{1-\varepsilon} \tag{11}$$

This deformation will transform a circle of radius R_{max} into an ellipse of ellipticity (i.e. flattening) ε having for the semi-major $R/\sqrt{1-\varepsilon}$ and the semi-minor axis $R\sqrt{1-\varepsilon}$. We should then also transform the velocity field according to

$$V_x^{'}(x',\, y') = \sqrt{1-\varepsilon} V_x(x,\, y) \tag{12}$$

$$V_y^{'}(x',\, y') = V_y(x,\, y)/\sqrt{1-\varepsilon} \tag{13}$$

in order to get a non-divergent velocity field and the conservation of angular momentum for each fluid parcel. Such type of deformation could be induced in the real ocean by the external strain exerted on a circular eddy by its close neighbors.

We compute from the elliptical velocity field the geostrophic velocity components according to cyclogeostrophic balance Eqn.(5). Then we apply the iterative scheme Eqn.(6) (with constrain on the local residual) to these geostrophic velocity components and check how close they are to the initial cyclogeostrophic solution. We compare in Figure 3.10 the vortex Rossby numbers associated to the initial elliptical vortex (black square), to the corresponding geostrophic vortex (open square) and the results of the iterative scheme after five steps (crosses). We study here the impact of the ellipticity ε while the vortex Rossby number is kept fixed to $Ro_g = 0.18$. This initial value is quite large and the cyclostrophic corrections are therefore significant. Indeed, the vortex Rossby numbers of the cyclogeostrophic eddies are almost the double ($0.28 < Ro < 0.3$) of the initial geostrophic ones. The differences between the cyclogeostrophic solutions and the results of the iterative scheme remain small (less than 15%) and weakly impacted by a moderate ellipticity. We can see that the intensity (i.e. the Rossby number) of the elliptical structure obtained with the iterative scheme, after five iterations, is relatively close to the cyclogeostrophic one unless the ellipticity exceeds large values (above $\varepsilon > 0.6$). The agreement is even better when the intensity of the elliptical structure is weaker (not shown here). Hence, the methodology used in this paper to approximate the cyclostrophic velocity components provides accurate results for both circular and elliptical eddies.

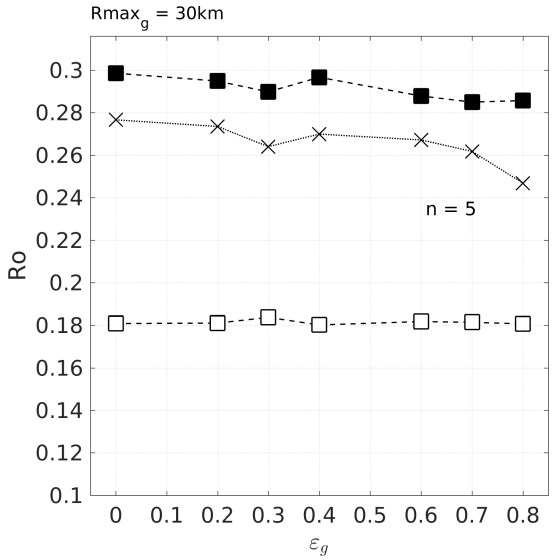

Figure 3.10: *Evolution of the vortex Rossby numbers for geostrophic (open square) and cyclogeostrophic (filled square) elliptical anticyclones as a function of their ellipticity $\varepsilon = 1 - b/a$, where a and b are respectively the semi-major and semi-minor axis. The elliptical velocity fields were obtained from the deformation (Eqn.(10) - Eqn.(13)) of a circular Gaussian velocity profile having a characteristic radius $R_{max} = 30\,km$ and a maximum azimuthal speed $V_{max} = 0.9\,m.s^{-1}$. The vortex Rossby numbers of the elliptical eddies obtained by the iterative scheme Eqn.(6) applied to the geostrophic solutions are plotted with crosses.*

3.5 Cyclostrophic corrections of mesoscale eddies in the Mediterranean Sea

Statistical analysis

We now apply the iterative scheme to fifteen years (2000-2015) of surface geostrophic velocity fields provided by AVISO/DUACS for the Mediterranean Sea. Then we use the AMEDA algorithm to detect and track eddies on the corrected velocity field in order to quantify the impact of cyclogeostrophy on the Mediterranean eddies. The statistical properties of the mesoscale eddies (i.e. $R_{maxg} > 18\,km$) of the initial geostrophic eddy field are compared to the mesoscale eddies detected on the new cyclogeostrophic velocity field. As expected the cyclostrophic correction mainly impacts the mesoscale anticyclones (Figure 3.11). We should note that ageostrophic submesoscale eddies cannot be detected on the AVISO/DUACS altimetry products and therefore only large mesoscale eddies ($R_{max} > R_d$) are considered in this analysis.

The probability distribution functions of the vortex Rossby numbers, for both cyclones and anticyclones, are impacted by the cyclostrophic correction when $Ro_g > 0.1$. However, the impact is much stronger for anticyclonic eddies for which the maximum intensities of the probability distribution function almost double (Figure 3.11(a)) and reach values up to $Ro = 0.4$. While for cyclonic structures, the maximum intensities of cyclogeostrophic eddies are slightly attenuated in comparison with the geostrophic ones (Figure 3.11(c)).

Besides, as we have seen on idealized circular eddies (Figure 3.7) the cyclostrophic corrections also modify the velocity profile, especially in the core of anticyclones, where it may significantly amplify the core vorticity (Ioannou et al., 2017). This change on the velocity profiles is also visible on the distribution of the steepness parameter α. The probability distribution of mesoscale anticyclones is shifted toward lower value of

α (Figure 3.11(b)) while it remains unchanged for cyclones (Figure 3.11(d)). Lower values of the steepness parameter correspond to a steeper velocity gradient in the eddy core (i.e. stronger core vorticity) and a lower velocity decay at the eddy periphery.

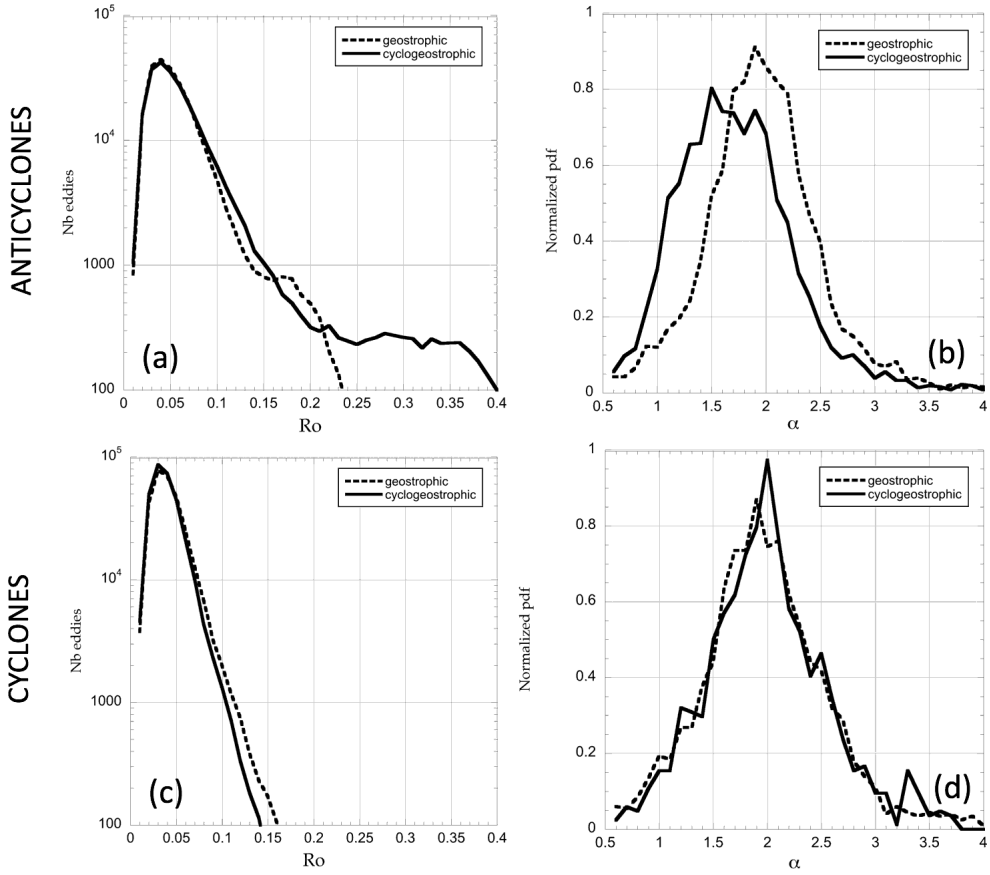

Figure 3.11: *Probability distribution function of the vortex Rossby numbers Ro_g and Ro (a,c) and the steepness parameters α (b,d) of the mesoscale eddies detected by the AMEDA algorithm on the AVISO/DUACS geostrophic velocity field (dashed line) and on the corrected velocity field where cyclogeostrophic components are estimated (black solid line).*

Areas where cyclostrophic corrections are significant

The statistical analysis provides an overall view of the impact of the cyclostrophic corrections but does not allow to identify the areas in the Mediterranean sea where this correction is the most needed. Therefore, we plot in the Figure 3.12(a), at each grid point, the maximal amplitude of the cyclostrophic correction $\|\mathbf{V} - \mathbf{V}_g\|$ during the 2000 - 2015 period. We plot here the amplitude of this correction (i.e. the difference between cyclogeostrophic and geostrophic velocities) only if it exceeds $10\,cm\,s^{-1}$. This graph allows us to immediately identify two "hot spots" where the cyclostrophic correction may exceed $50\,cm\,s^{-1}$. These two places correspond to the usual locations of the Alboran and the Ierapetra anticyclones.

The Alboran eddy is generated by the recirculation of the incoming jet of Atlantic Water (AW) flowing continuously through the Strait of Gibraltar due to the differential pressure gradient that exists between the Mediterranean Sea and the Atlantic Ocean

across the Gibraltar Strait. This intense anticyclone constitutes the strongest dynamical feature of the Western Mediterranean mean circulation, with surface currents of up to $1.5\,m\,s^{-1}$(Viudez et al., 996a,b; Gomis et al., 2001; Flexas et al., 2006). It is therefore normal to observe a strong ageostrophic component in the velocity or the vorticity field (Viudez, 1997). The analysis of Gomis et al. (2001) has already showed the existence of large ageostrophic velocities up to $40\,cm\,s^{-1}$, induced by the cyclostrophic acceleration of this intense mesoscale anticyclone. Our analysis shows that these ageostrophic components of the velocity field can be even stronger (Figure 3.12(a)).

The Ierapetra Eddy (IE), which is generally formed during the summer months at the south-east corner of Crete, is one of the strongest anticyclones of the Eastern Mediterranean Sea. This first estimation of the core vorticity of the Ierapetra anticyclones, performed by Matteoda and Glenn (1996), was relatively large in comparison with the local Coriolis parameter *f*. More recently, Mkhinini et al. (2014) and especially Ioannou et al. (2017) performed a thorough study of the IEs intensities based on the AVISO/DUACS surface velocity fields. Assuming a circular eddy shape, Ioannou et al. (2017) computed the cyclogeostrophic velocity profiles of the IEs during their formations or intensification stages and found that the core vorticity ζ_0 could sometimes exceed the standard threshold of inertial instability $\zeta_0 < -f$. Hence, it is not surprising that the cyclogeostrophic corrections, computed by the iterative scheme, are very strong in the formation or intensification area of the IEs.

We quantify in Figure 3.12(a) the amplitude of the cyclostrophic corrections on the velocity magnitude but we could also consider how these corrections impact the intensity of the detected eddies. We plot in Figure 3.12(b) the location of all the anticyclones having a Rossby number higher than 0.2 after the cyclostrophic correction. This simple criterion selects intense anticyclones which satisfy the cyclogeostrophic balance with finite core vorticity (i.e. $\zeta/f < -0.6$ for circular Gaussian eddies). About 5000 eddy detections satisfy this criterion during the 15 year period. Since we consider here daily detections, several points could correspond to the same eddy. The large majority of these cyclogeostrophic eddies correspond to the Alboran gyres (60%) or the Ierapetra anticyclones (30%). However, apart from these two « hot spots » it appears that few other anticyclones may also show strong deviations from the standard geostrophic balance in the Mediterranean Sea. Two other areas are concerned: the Algerian basin and a fraction of the Levantine basin, off the Libyo-Egyptian coast.

The first area in the Algerian basin corresponds to the detachment and the recirculation area of long-lived anticyclones named Algerian Eddies (AE) (Escudier et al., 2016; Pessini et al., 2018; Garreau et al., 2018). These large mesoscale anticyclones, that are formed by the meanders of the Algerian Current, are generally considered to have small Rossby numbers and satisfy the geostrophic balance. We show in Figure 3.13(a) the temporal evolution of the Rossby number Ro and the relative core vorticity for an AE detected in 2005. This anticyclone was studied by (Pessini, 2019) and exhibits a significant intensification when it interacts with the Balearic front six months after its formation. During this event, the geostrophic Rossby number reaches a large value up to 0.2 which indicates that the cyclogeostrophic balance should be taken into account. Then, when the cyclostrophic correction is applied the vortex Rossby number exceeds 0.3 and the core vorticity could reach intense negative values below $-f$ for several days or weeks.

The second area is located in the Levantine basin ($31^\circ - 34^\circ N, 27^\circ - 30^\circ E$) and overlays the Herodotus Trough. It has been poorly studied and has very few in-situ observations. Nevertheless, Mkhinini et al. (2014) have shown that the Herodotus Trough is a formation area of long-lived anticyclones. These mesoscale anticyclones, often called Mersa-Matruh Eddies, have been mentioned in several studies (Horton et al., 1994; Hamad et al., 2006; Amitai et al., 2010; Menna et al., 2012) but never identified as intense eddies. The Figure 3.13(b) shows that such type of eddy could also satisfy the

cyclogeostrophic balance and reach intense negative vorticity. The instabilities of the Libyo-Egyptian Current or the local changes of the mean shelf slope could explain the formation of intense meanders or coastal anticyclones in this area.

This analysis confirms that the Alboran and the IE anticyclones are the most intense mesoscale eddies in the Mediterranean Sea. However, the cyclostrophic correction applied to the whole Mediterranean Sea revealed that few other mesoscale eddies that were not identified before as ageostrophic could also exhibit a strong negative core vorticity during their lifetime.

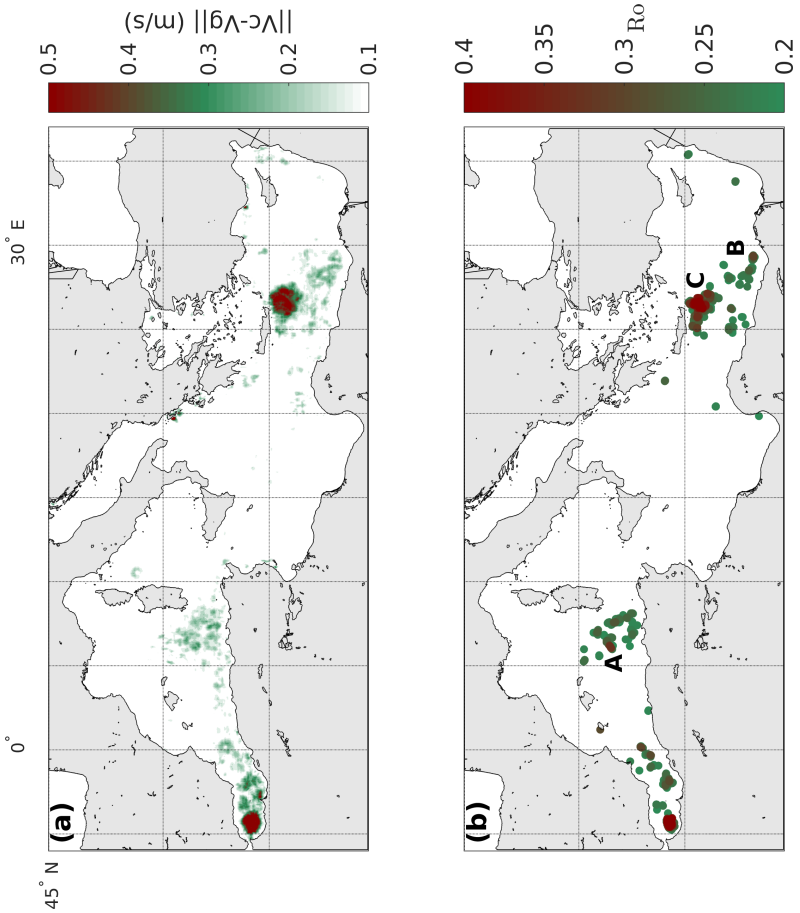

Figure 3.12: *The localization of the maximal velocity correction, averaged for 5 days at each grid point, during the 15 year period (2000-2015) is plotted in the upper panel (a). Velocity corrections having an amplitude* $\|\mathbf{V} - \mathbf{V}_g\|$ *below* $10\,cm\,s^{-1}$ *are not plotted. The location of eddies detected by the AMEDA algorithm (once the cyclostrophic correction is applied) having a vortex Rossby number higher than* 0.2 *are plotted in the lower panel (b).*

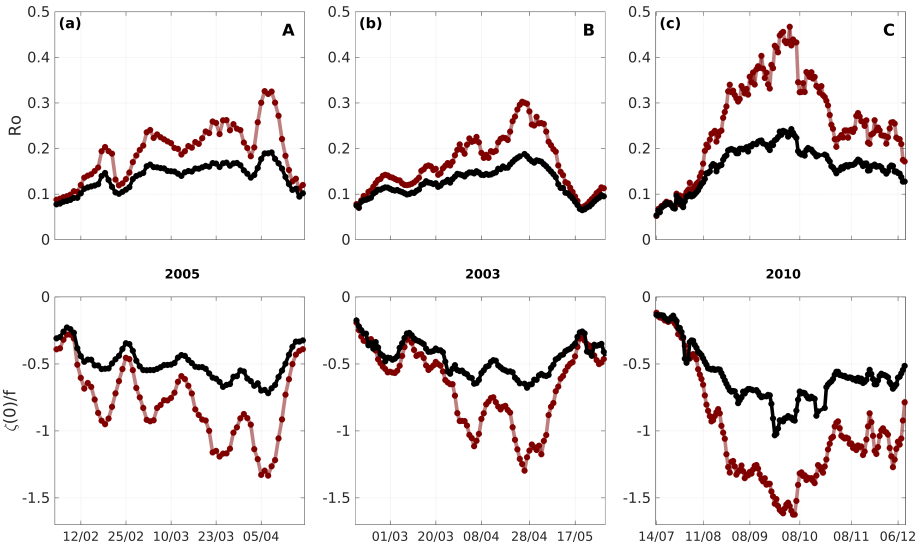

Figure 3.13: *Temporal evolution of the vortex Rossby number Ro and the relative core vorticity $\zeta(0)/f$ for a) an Algerian Eddy detected in 2005 b) a Libyo-Egyptian eddy detected in 2003 and c) for an Ierapetra Eddy detected in 2010. The characteristics of the mesoscale eddies are illustrated with the black filled circles as detected by the AMEDA algorithm applied on the AVISO/DUACS geostrophic velocity fields and with the filled red circles when applied on the corrected cyclogeostrophic velocity fields.*

Comparison with in-situ measurements

This study would not be complete without a comparison with in-situ data, to verify that the proposed method effectively corrects the AVISO/DUACS fields so that they are closer to the observations. This requires two conditions that are not easy to obtain during oceanographic surveys. The first one is to find an intense eddy for which the cyclogeostrophic correction will be significant and the second one is to locate accurately the eddy center in order to perform enough velocity measurements within the eddy core. One of the goals of the Atalante cruise during the last PROTEVS/PERLE campaign, held in October-November 2018, was to survey thoroughly the Ierapetra anticyclone in autumn, when its intensity is usually strong. Among the large amount of measurements performed during this campaign, we focus our analysis on two VMADCP transects, which were performed close to the eddy center on 29 October (Figure 3.14) and on November 1 (Figure 3.15). First, the geostrophic surface velocities, provided by AVISO/DUACS, were interpolated along the boat trajectory and compared to the VMADCP averaged between $30\,m$ and $70\,m$. For these two transects (Figure 3.14(a) and Figure 3.15(a)), the magnitude of the geostrophic velocity vectors (black arrows) are significantly weaker than the measured ones (blue arrows) while their directions are almost similar. Indeed, the magnitude of the strongest geostrophic velocity component does not exceed $42\,cm\,s^{-1}$ while the maximum surface velocity measured by the VMADCP reaches $62\,cm\,s^{-1}$. Thanks to the AMEDA algorithm, the characteristic contours of the geostrophic anticyclone were computed (black contour) and the characteristic speed radius was estimated around $R_{max} \simeq 34\,km$. Hence, we can estimate the geostrophic vortex Rossby number $Ro_g \simeq 0.13$ for this Ierapetra anticyclone. According to our analysis (Figure 3.9) for such values of the geostrophic Rossby number, the cyclostrophic corrections will be significant. Therefore, in a second step we apply the iterative corrections Eqn.(6) to the surface velocity field and we compare these

new velocity fields (in red) to the in-situ measurements (in blue). We observe in the Figure 3.14(b) and Figure 3.15(b) better agreements with the observations despite a clear difference in the position of the eddy center. We should mention here that the accuracy of the AVISO/DUACS products is affected by the spatio-temporal distribution of the altimetry tracks and the correlation lengths used in the interpolation scheme (LeTraon et al., 1998) to build the gridded maps from multiple satellites. It is thus, not surprising to find a shift of the order of $10\,km$ ($\sim 1/8°$) in the positioning of the eddy center. Nevertheless, the maximal amplitude of the cyclogeostrophic velocity field reaches $59\,cm\,s^{-1}$ which is in better agreement with the observation. The speed radius of the corrected anticyclone is reduced ($R_{max} \simeq 30\,km$) which leads to a strong increase of the vortex Rossby number up to $Ro \simeq 0.2$. Besides, according to the fine comparison of the meridional and latitudinal velocity profiles, plotted in the panels (c, d) of the Figure 3.14 and Figure 3.15, we do see that the iterative method improves significantly the velocity gradients in the eddy core. In order to perform relevant comparisons between the VMADCP measurements and the velocities profiles from the geostrophic and cyclogeostrophic fields, any misalignments of the velocity profiles were first minimized. The RMSE between the VMADCP measurements and the velocity profiles (geostrophic and cyclogeostrophic) were then estimated. The RMSE error of the velocity norm based on the cyclogeostrophic profiles was found of the order $9\,cm/s$ and $8\,cm/s$ for each transect respectively. The cyclogeostrophic RMSE remained $30-40\%$ lower than the geostrophic one ($13\,cm/s$ and $14\,cm/s$). This example shows that the cyclostrophic corrections of the AVISO/DUACS surface velocities, that we used, are relevant for intense mesoscale anticyclones. Thanks to the optimized iterative method we obtained corrected velocity fields that were much closer to the in-situ observations.

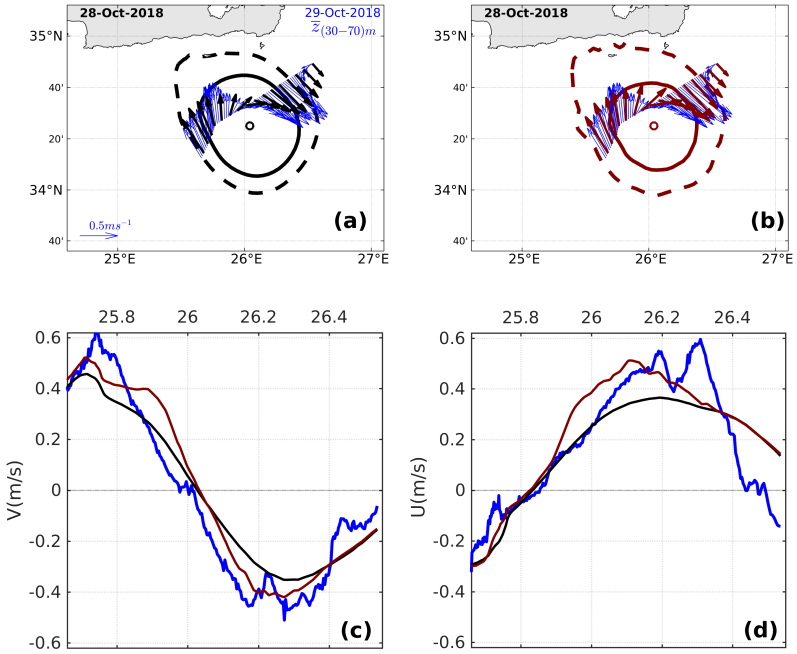

Figure 3.14: *Comparison between the geostrophic surface velocities provided by the AVISO/DUACS product (black lines or arrows) and the VMADCP in-situ measurements (blue lines or arrows) performed the 29 October 2018. The cyclogeostrophic velocity field obtained by the iterative method (Eqn.(6)) is plotted in red. The upper panels show the surface geostrophic (a) or the cyclogeostrophic (b) velocity vectors along the boat trajectory in comparison with the VMADCP measurements. The characteristic contours (solid lines) and the last closed streamlines (dashed lines) computed by the AMEDA algorithm are both plotted for the geostrophic (in black, panel (a)) and the cyclogeostrophic (in red, panel (b)) surface velocity fields. The meridional and the latitudinal velocity profiles, of the geostrophic (black), the cyclogeostrophic (red) and the in-situ measurements (blue), are plotted respectively in the lower panels (c) and (d).*

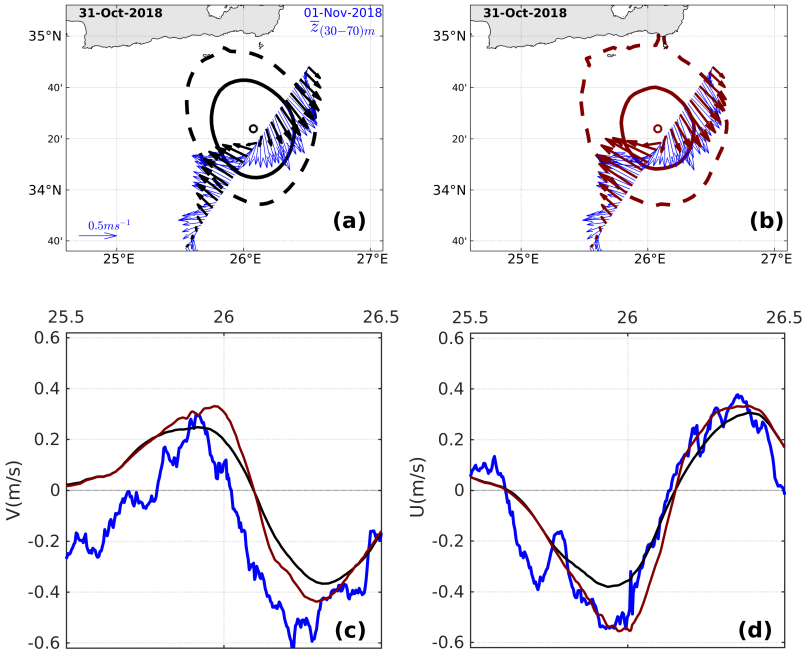

Figure 3.15: *Comparison between the geostrophic surface velocities provided by the AVISO/DUACS product (black lines or arrows) and the VMADCP in-situ measurements (blue lines or arrows) performed the 1st of November 2018. The panels are in the form identical to*

This example shows that the cyclostrophic corrections of the AVISO/DUACS surface velocities, that we used, are relevant for intense mesoscale anticyclones. Thanks to the optimized iterative method we obtained corrected velocity fields that were much closer to the in-situ observations.

3.6 Conclusions

This study investigates the cyclogeostrophic balance of intense mesoscale eddies in the Mediterranean Sea. To do so, we optimized an iterative scheme, that was initially developed for atmospheric flows (Endlich, 1961; Arnason et al., 1962) and recently used for oceanic eddies in the Mozambique Channel (Penven et al., 2014). This iterative method computes with the best accuracy the cyclostrophic terms from the geostrophic surface velocity of the AVISO/DUACS products. We have tested the performance of this method on a wide range of idealized mesoscale eddies of different sizes, intensities and shapes that can be detected in the Mediterranean Sea. Since, we can obtain exact cyclogeostrophic solutions for these analytical eddies, we were able to compare the results obtained at the end of the iterations with the exact solutions and therefore validate the accuracy of the whole methodology. The thorough analysis of the various eddy parameters show that the amplitude of the cyclostrophic corrections depend not only on the vortex intensity but also on the vortex shape: the steepness parameter α or the vortex

ellipticity ε for instance. The main advantage of this type of iterative method is that cyclostrophic corrections can be calculated for a very wide range of vortices of different shapes, be they circular or moderately elliptical.

We found that the cyclostrophic correction is needed for most of the mesoscale anticyclones that have a geostrophic vortex Rossby number larger than $Ro_g = max(|V_g|)/fR_{maxg} > 0.1$. This threshold is below the one chosen by Douglass and Richman (2015). Indeed, these authors used the value of the mean relative vorticity $\bar{\zeta}/f$ inside the eddy contour to quantify the vortex intensity instead of the vortex Rossby number. For Gaussian eddies, we get the simple relation $Ro_g = \bar{\zeta}/2f$ and therefore the threshold $\bar{\zeta}/f = 0.3$ proposed by Douglass and Richman (2015) to classify strong cyclogeostrophic eddies correspond to $Ro_g = 0.15$. The lower value, that we propose, for this correction threshold, is also justified by the intensive survey of the Ierapetra eddy performed during the 2018 PROTEVS-PERLE campaign. Even if the initial vortex Rossby number of this mesoscale anticyclone seems week $Ro_g \simeq 0.13$, below the threshold proposed by Douglass and Richman (2015), the corrections that we applied to the AVISO/DUACS geostrophic velocities were significant (54%) and the corrected velocities were much closer to the VMADCP measurements.

We apply this cyclostrophic correction to fifteen years (2000-2015) of AVISO/DUACS geostrophic velocity fields, gridded at $1/8°$ for the Mediterranean Sea. We found that velocity errors up to $50\,cm\,s^{-1}$ could occur for large and intense anticyclones, due to the initial geostrophic approximation. The two most intense anticyclones of the Mediterranean Sea, the Alboran and the Ierapetra eddies, should be corrected but not only. Our analysis suggest that other anticyclones in the Algerian basin or the Levantine basin may also benefit from this ageostrophic correction. The statistical analysis shows that this cyclostrophic correction have a strong impact on the most intense mesoscale anticyclones while it is quite weak for cyclonic eddies. This may seem surprising because in high resolution numerical simulations the most intense and ageostrophic eddies are generally cyclonic (Klein et al., 2008; Roullet and Klein, 2010; Qiu et al., 2014). But, we must not forget, that these very intense cyclones correspond to submesoscale eddies, whose radii are less than the local deformation radius, which is around $R_d = 8 - 12\,km$ in the Mediterranean Sea. Since, the effective resolution of altimetric products is coarse, such intense submesoscale cyclones cannot be resolved by the standard AVISO/DUACS regional products gridded at $1/8°$ (Amores et al., 2018). Therefore, only large mesoscale cyclones can be detected on altimetry products and they are generally less stable and coherent than their anticyclonic counterpart Stegner and Dritschel (2000). Several stability analysis have shown that ageostrophic effects, finite Rossby numbers or finite isopycnal deviations, tend to increase the baroclinic instability for cyclones and weaken it for anticyclones (Dewar and Killworth, 1995; Baey and Carton, 2002; Benilov and Flanagan, 2008; Lahaye and Zeitlin, 2015; Mahdinia et al., 2017). On the other hand, surface intensified anticyclones could remain stable to baroclinic or centrifugal instabilities, even if they reach finite Rossby numbers up to $Ro = 0.4$ (Lazar et al., 2013b; Yim et al., 2018).

Such methodology could be easily applied to other sub-basins or marginal seas at mid-latitude in order to improve substantially the estimation of surface velocities. The accuracy of these cyclostrophic corrections depend on the initial resolution of the AVISO/DUACS products and is therefore more relevant on altimetry products gridded at $1/8°$. These regional products will be more numerous in the years to come, thanks to the growing number of conventional nadir altimeter satellites that will be deployed in the next two years (Jason-C, HY-2C, HY-2D, HY-2E). We could then expect "all sat merged" series at higher resolution that will combines up to 5 or 7 altimeters, for several years, with a significant reduction of the inter-track distance. Besides, the operational development of SWOT mission (launched in 2021) will provide wide-swath altimetric measurements of the ocean surface topography leading to an unprecedented increase of

the sea surface signature of oceanic mesoscale and submesoscale eddies.

3.7 Appendix

We quantify in this section how another iterative scheme that uses an under-relaxation factor λ (Iversen and Nordeng, 1982, 1984) may improves on the accuracy of convergence to the cyclogeostrophic solution. In accordance with Figure 3.7, the accuracy of convergence was tested for two Gaussian anticyclones ($\alpha = 2$) of the same radius ($R_{maxg} = 30\,km$) but different initial geostrophic intensities ($Ro_g = 0.16$ and $Ro_g = 0.2$). Based on the iterative method with under-relaxation, only a fraction λ of the previous correction is applied at each iteration step (Eqn.(14)-Eqn.(15)). The iterative scheme with under-relaxation writes as follows:

$$\mathbf{U^{n+1}} = \mathbf{U_g} + \frac{1}{f}\mathbf{k} \times (\mathbf{U^n}.\nabla \mathbf{U^n}) \tag{14}$$

$$\begin{aligned} \mathbf{U}^{\mathbf{n+1}}_{\mathbf{under-relaxation}} &= \mathbf{U^n} + \lambda\,(\mathbf{U^{n+1}} - \mathbf{U^n}) \\ &= (1-\lambda)\,\mathbf{U^n} + \lambda\,\mathbf{U^{n+1}} \end{aligned} \tag{15}$$

When $\lambda = 1$, there is no under-relaxation and we recover the classical iterative method that was used in this study (full correction at each iteration step). High λ parameters provide lower weight to the solution of step $\mathbf{U^n}$. Two under-relaxation factors were tested ($\lambda = 0.4$ and $\lambda = 0.6$). We compare in Figure 3.16 the accuracy of the under-relaxation scheme to converge at the corresponding analytical cyclogeostrophic solution for the two anticyclones. The relative error Σ_{Ro} is computed at each iteration step for the free (Figure 3.16(a,d)) and the constrained iterative method (Figure 3.16(c,f)). The normalized residual drop $\left\|\mathbf{U}^{n+1} - \mathbf{U}^{n}\right\|$ of the velocity norm illustrates the convergence of the geostrophic field to the cyclogeostrophic solution at each iteration step (Figure 3.16(b,e)). As mentioned in Figure 3.4, in order to prevent local divergence, the iteration process is constrained when the local residual $\left\|\mathbf{U}^{n+1} - \mathbf{U}^{n}\right\|$ starts to increase. For the eddy example with moderate initial geostrophic Rossby intensity ($Ro_g = 0.16$), all iterative methods converge with high accuracy to the same cyclogeostrophic solution. The relative error Σ_{Ro} remains below 5%. The under-relaxation delays the the iterative method convergence requiring more iterations to reach the same final solution. Yet it does not prevent the local divergence (Figure 3.16(b)). The performance of the iterative method is also shown for the eddy example with the strong intensity ($Ro_g = 0.2$) in Figure 3.16(d-f). Similarly, in this case the convergence is slower but the iterative scheme does not succeed to reach the cyclogeostrophic solution. The residual errors for the constrained iterative method with under-relaxation are estimated 23% and 29% for $\lambda = 0.6$ and $\lambda = 0.4$ respectively. The under-relaxed iterative scheme does not provide for a better accuracy while the residual errors are estimated slightly higher than the standard iteration scheme (17% when $\lambda = 1$).

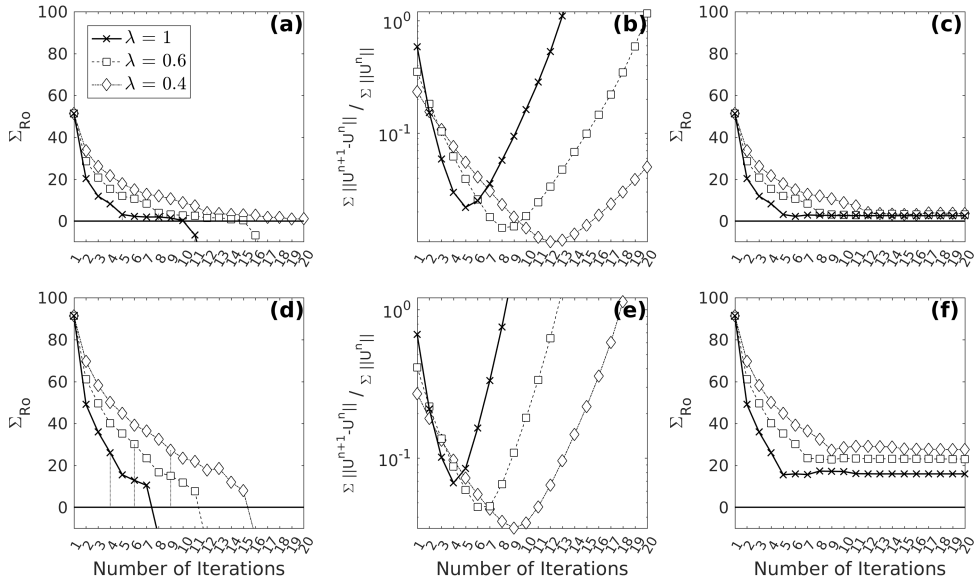

Figure 3.16: *Accuracy of the different iterative schemes (Eqn.(14)-Eqn.(15)) applied on two geostrophic anticyclones with $Ro_g = 0.16$ in the upper panels and $Ro_g = 0.2$ in the lower panels as described in Figure 7. The classical iterative method (crosses) and the iterative method with the under-relaxation parameter $\lambda = 0.4$ (diamonds) and $\lambda = 0.6$ (squares) are shown with the different markers. The Relative error ($\Sigma_{Ro} = (Ro - Ro_i)/Ro_i$) between the Rossby number reached at every iteration step (Ro_i) and the corresponding exact cyclogeostrophic solution (Ro) is illustrated in panels a) and b). The normalized residual drop of the velocity norm is shown in panels b) and e) at every iteration step. The relative error Σ_{Ro} of the constrained iterative schemes is shown in panels c) and f).*

CHAPTER 4

Estimation of an Ierapetra eddy vertical structure from Argo floats

In this chapter we examine the spatial and temporal evolution of an Ierapetra eddy by analyzing 4 Argo floats that were trapped in its core. This is one of the rare occasions that Argo floats were trapped in a IE for a significant time period (almost four months) providing a great opportunity to investigate the eddy subsurface characteristics apart from the surface altimetric maps. We introduce a methodology to reconstruct the IE vertical structure and compare the eddy estimated dynamical characteristics with the ones observed by satellite observations. The problematic that we need to address is having sparse data at different locations and times along the IE dynamical evolution.

4.1 Introduction

Satellite observations of sea surface height in combination with automatic detection algorithms has enabled the 2D characterization of mesoscale eddies. Substantial information on the horizontal dynamics of eddies can be provided while the eddy surface signature could be followed daily for long time periods. Contrary, the characterization of the vertical structure of the eddies remains a difficult task as the only source of data could come from in-situ measurements. Still little do we know on how eddies are varying in the vertical and how different process may impact their vertical structure. This requires a lot of sampling for a given eddy and dedicated and frequent campaigns which are most of the time difficult to achieve.

Towards providing information on the eddy vertical structures recent studies have combined Argo floats measurements and satellite altimetry by collocating the surface eddy detection and the floats positions. Argo floats may sample eddies at different periods and positions along their trajectory. Due to sparsity of measurements that cross a given eddy, most of the studies have focused on composite eddy reconstructions. Such techniques have been previously presented by Chaigneau et al. (2011); Pegliasco et al. (2015) and are very useful methods for identifying general eddy characteristics and comparing the vertical structure of eddies in different areas.

With the constantly increasing number of Argo floats more and more information is acquired and the monitoring of a single eddy vertical structure starts to become possible. In March 2014 in the Northern Atlantic 17 Argo floats were deployed within a single anticyclone collecting 3000 profiles (Xu et al., 2016). In the Southern Atlantic ocean, a specific Agulhas Ring was followed and analyzed based on Argo float measurements in combination with the eddy surface signature evolution from altimetry (Laxenaire et al., 2018).

In the same context, we attempt in this section the reconstruction of a single Ierapetra eddy during winter 2017 where 4 Argo floats remained trapped in its core for approximately 4 months. The provided vertical profiles will be used to reconstruct the eddy. Moreover, different assumptions during the reconstruction methodology will be assessed in order to provide for a more accurate description of the IE vertical structure.

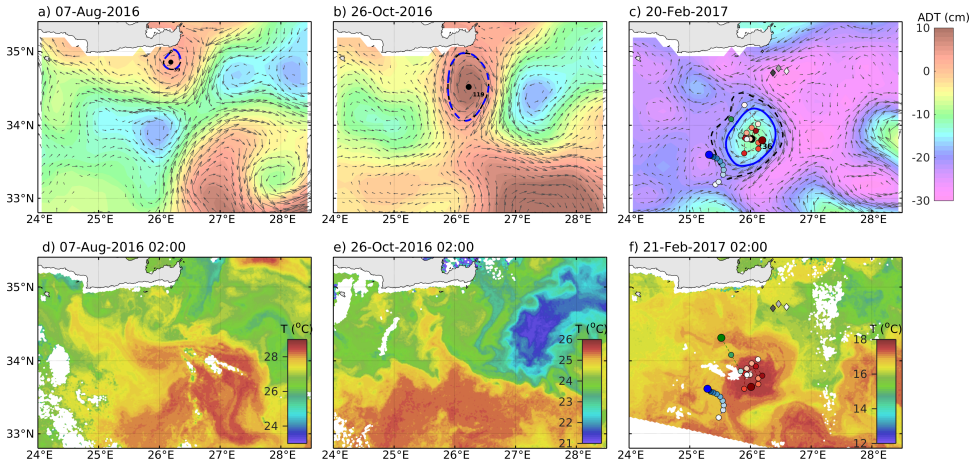

Figure 4.1: *Snapshots of the temporal evolution of the Ierapetra eddy (IE16) during the a) formation stage b) the maturity stage in October 2016 and c) the quasi steady stage in 20 February 2017. The background colors correspond to the Absolute Dynamic Topography (ADT) and the vectors superimposed are the geostrophic velocities. The characteristic contours as computed by AMEDA algorithm are plotted with the blue colors for the anticyclone. The corresponding Sea Surface Temperature fields for the same dates are shown in the lower panels (d-f). In panels c) and f) the position of the Argo floats is illustrated with the circled filled points. Each Argo float is distinguished with a different color as well as their proceeding positions during a 10 day period.*

4.2 Argo Floats trapped in the Ierapetra eddy (IE16)

During winter-spring 2017, the Ierapetra eddy (IE16) remained relatively stationary at position $(25.8^oE, 34^oN)$ in the lee of Crete island. During that period, 4 Argo floats were trapped in the eddy core and sampled vertically the eddy at various locations in time. Based on the AVISO/AMEDA detection method, the Ierapetra eddy was initially formed the proceeding summer, firstly detected in 30 June 2016. Three different snapshots along the IE seasonal evolution of the eddy sea surface signal are shown in Figure 4.1. Based on the altimetric sea surface height and the applied AMEDA algorithm, the eddy was firstly detected near the Kasos-Crete Strait at a position $(26.18^oE, 34.85^oN)$. The characteristic contours of the anticyclone as tracked with AMEDA detection algorithm are depicted in Figure 4.2 with the blue colors. After generation, the IE16 drifted southward, entered the mean climatological position during autumn while remained quasi-stationary during winter 2017 at position $(25.8^oE, 34^oN)$, Figure 4.2(e). The eddy trajectory was in accordance with previous detection of IEs.

In Figure 4.2 (a-d) we show the monthly averaged geostrophic dynamical characteristics of the eddy radius, velocity, vorticity and ellipticity. As expected, during summer and autumn the eddy increases in size and intensity. The maturity stage (maximum intensity Ro) for the IE16 was detected in November. The eddy reached a vortex Rossby number of $Ro = 0.1$ with characteristic radius of $R_{max} = 40\,km$. The estimated core vorticity was found around $\zeta(0)/f = -0.4$.

In order to estimate the typical velocity profile for the eddy we plot in Figure 4.3 the mean profile $(\langle R \rangle, \langle V \rangle)$ computed by the AMEDA algorithm and averaged during the three months period (black solid line) from the AVISO geostrophic surface velocity. The geostrophic characteristics of the eddy exceed velocities of $V_g > 0.4\,m\,s^{-1}$ for given days. Thus as shown in chapter 3 from the cyclogeostrophic corrections, the expected underestimation on the eddy velocities will account for at least 30%. Thus, for the period of investigation we applied the iterative method to recover the IE16 cyclogeostrophic

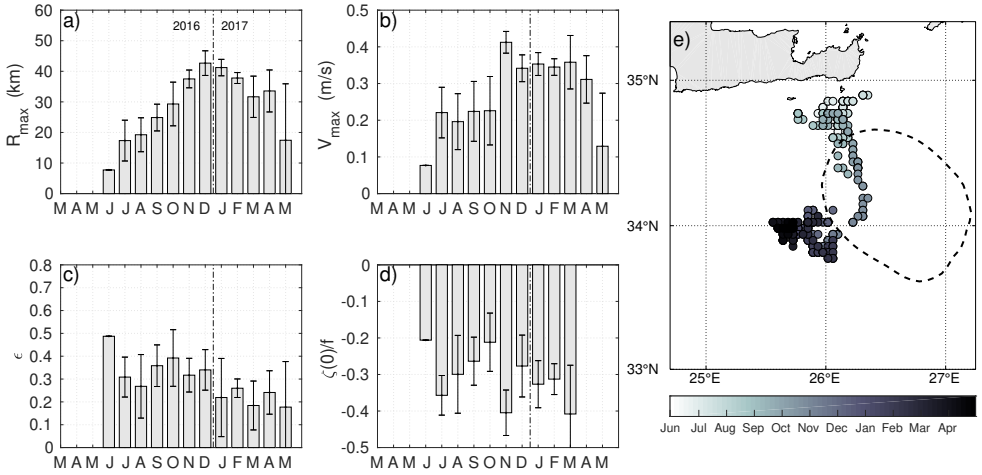

Figure 4.2: *Temporal evolution of (a) the characteristic Radius R_{max} (km), (b) tangential velocity V_{max} (m/s), (c) the ellipticity ($\epsilon = 1 - a/b$) and (d) the estimated core vorticity $\zeta(0)/f$ of the Ierapetra anticyclone formed in 2016 (IE16) as detected from AVISO data set and AMEDA detection algorithm. The error bars correspond to the monthly RMS of the parameters. The trajectory of the IE16 is shown in panel (e). The dashed line indicates the mean climatological position of the IE.*

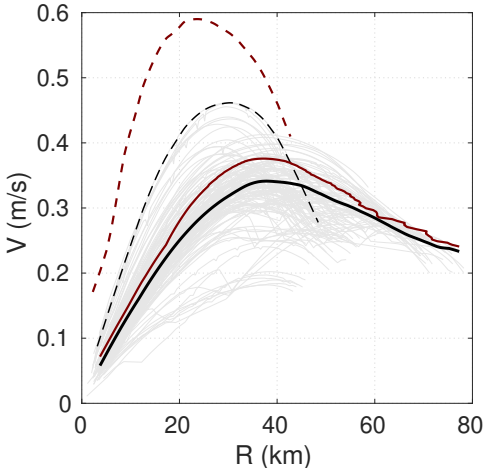

Figure 4.3: *The velocity profiles of IE16 as computed from AMEDA algorithm applied on the AVISO dataset geostrophic fields are illustrated with the gray color. The dashed line depicts the most intense velocity profile reached during this period on the 8 March 2016. The applied cyclogeostrophic corrections are shown in red for the two profiles.*

Table 4.1: *Information of the Argo floats trapped in the IE16 from 01 January to 11 June in 2017.*

Argo Float WMO	Parking Depth (m)	Sampling Rate (days)	Number of profiles
6902770	100	1	108
3901853	200	5	30
6903204	350	5	33
6900422	350	1	89

corrections. In Figure 4.3, the cyclogeostrophic eddy characteristics are compared for the retrieved maximum velocity profile during the total period as well from the mean eddy profile during the 4 months. The maximum estimated cyclogeostrophic eddy velocity reached $V_{max} = 0.6\,m/s$ with a corresponding radius $R_{max} = 39\,km$.

During winter-spring 2017, the four Argo floats were trapped within the IE16 core for at least 3 months. Their positions were superimposed in the satellite fields of SSH and SST in Figure 4.1(c)&(d)) for the 21 February 2017. The floats provided for the eddy vertical hydro graphic characteristics measuring temperature T and salinity S at different locations depending on their pre-assigned cycle. The characteristics of the Argo floats are summarized in Table 4.1. The Argo float 6902770 was released in the eddy core in 27 January 2017 completing daily sampling cycles. It remained trapped until 11 June collecting in total 108 profiles. It later it escaped and drifted southeastward. The parking depth was set at $100\,m$. Later around 20 of February, the 6900422 float entered the IE from a southern location and looped closer to the eddy core until the 04 May 2017. Through this period the floats 6903204 and 3901853 were also completing profiles in a 5 day cycle inside and outside the eddy. In total, 260 profiles were collected over the 162 days that we analyzed.

Figure 4.4(a) shows the warm core of the eddy as acquired from the collected floats and averaged between $200 - 400\,m$ depth. The vertical temperature T and salinity S profiles are plotted in Figure 4.4 (b-c). For each profile the vertical distribution of the density $\rho = \rho\,(T, S, p)$ was estimated based on the equation of state Figure 4.4 (d). The different hydro-graphic characteristics that are inside and outside of the eddy are easily recognized. In order to define the eddy anomaly from the surrounding environment, a $60\,km$ radius is selected, outside of which we compute the mean oceanic seawater properties. This allowed us to define the regional background reference stratification during that time. The reference profile $q_{ref} = (T, S, \rho)$ is illustrated with the black line in Figure 4.4 (d) for the temperature, salinity and density profiles. The reference profiles was subtracted from the Argo profiles in order to derive the eddy anomaly $\delta q_A = (q_s(z) - q_{ref}(z))$.

The density evolution of all Argo measurements of float 6902770 is shown in Figure 4.5 (a) with the estimation of the MLD. Among the acquired profiles, a strong homogenization was detected in the first $50 - 200\,m$. To determine the mixed layer depth MLD, the threshold method was used (Thomson and Fine (2002)). According to this method, a criterion of density difference $\delta\rho$ is selected along the vertical from a near surface value, usually at $10\,m$ depth. To detect the based of the mixed -layer depth we used here a density difference of $\delta\rho \sim 0.03\,kgm^{-3}$. An example of the estimated MLD is shown in Figure 4.5 (b) for a specific vertical profile in 29 March 2017. What was surprising to observe is that the IE experienced a re-stratification below the first MLD detection (in the first 50 meters) Thus, the threshold method was applied for each profile twice in order to recover the maximum depth at which the characteristics of the water column were homogeneous (Figure 4.5). The estimation of the first MLD is probably associated with air-sea interactions during spring that re stratified the ocean surface while the deeper homogeneous water columns is a result of the winter mixing and cooling.

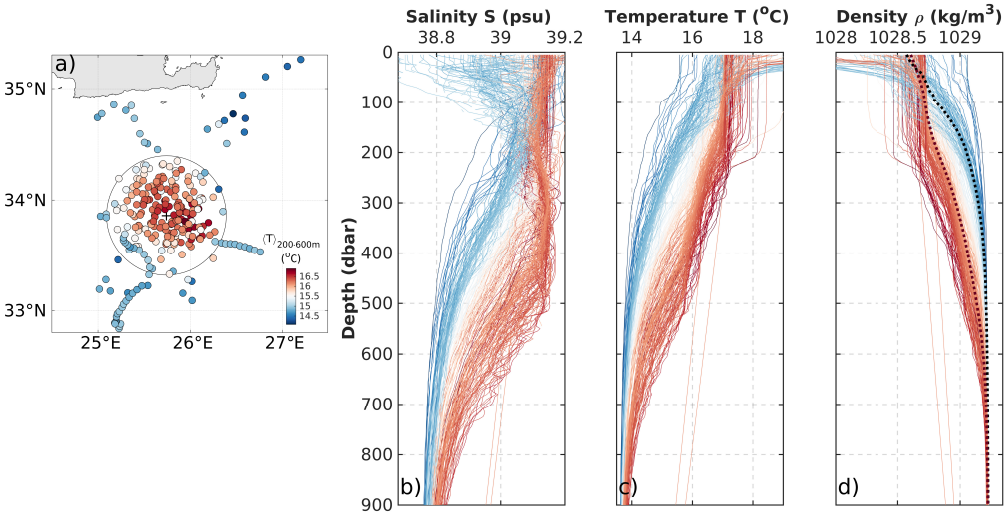

Figure 4.4: *a) Sampling positions for the 4 Argo floats during the period 27 January to 05 May 2017. Colors indicate the averaged Temperature* $\overline{T}\,(^oC)$ *between* $200 - 600\,m$ *depth. All acquired profiles of Salinity* $S\,(psu)$ *(b) , Temperature* $T\,(^oC)$ *(c) and Density* $\rho\,(kgm^{-3})$ *(d) are shown with red color when inside the circle of* $60\,km$ *radius and with blue colors when outside. The mean background reference profile* ρ_{ref} *is illustrated with the black dashed line and the mean eddy core density profile with the red dashed line.*

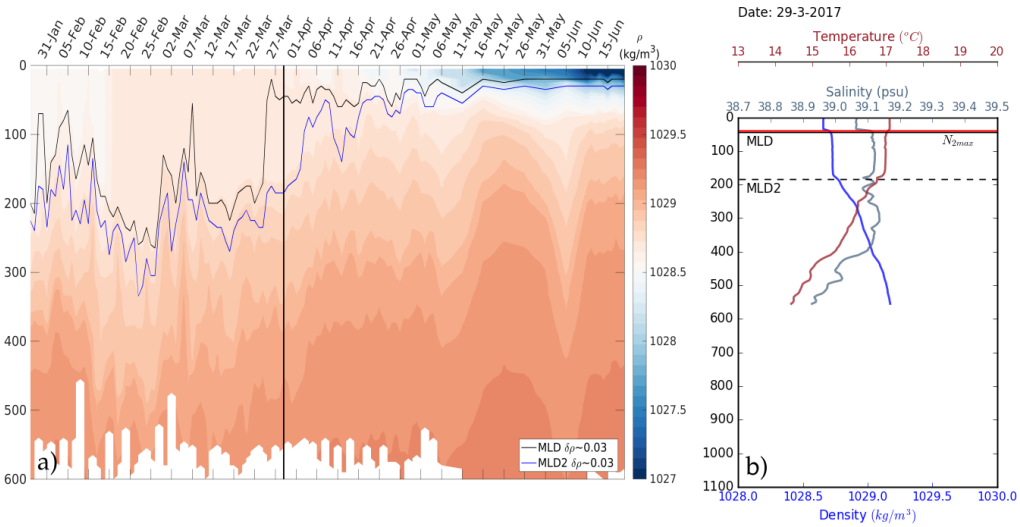

Figure 4.5: *(a) Temporal evolution of density* $\rho\,(kgm^{-3})$ *for the Argo float 6902770 along its trajectory. Estimations of the Mixed Layer Depths are shown with the blue and black lines for each float measurement. (b) Argo vertical profile measurements of Temperature (red), Salinity (gray) and the computed Density (blue) for the 31 March 2017. The different estimations of the MLD depths are shown with the horizontal lines as estimated based on the threshold method (black solid and dashed line) and the minimum Brunt-Väisäla frequency (red line).*

4.3 Methods

3-D Eddy Reconstruction

The numerous profiles collected for the IE in 2017 allow for a single eddy vertical reconstruction. Such techniques have been previously presented by Chaigneau et al. (2011); Pegliasco et al. (2015) for deriving global eddy composites and more recently for individual eddies such as the Agulhas Rings (Laxenaire et al., 2018). We present in what follows a similar approach for the Ierapetra anticyclone.

At first order approximation, we assume that the IE remains circular and axis-symmetric during the period of investigation. The maximum eddy anomaly (T_A, S_A, ρ_A) is located in its center and thus each float profile can be re-referenced respectively from the eddy core. We further suppose that the eddy remains quasi-stationary at a mean position of $(26^oE, 34^oN)$. The low drifting speeds detected from the eddy trajectory justify this assumption. Moreover, any diffusion processes are neglected considering that the eddy retains its anomaly without substantial heat lose during the 4 months. Four different estimations of the eddy center are tested for re-referencing the profiles. The resulting reconstructions are compared.

At second order approximation, we perform a 3-D reconstruction by taking into account the variations of the eddy shape during the 4 months period by lateral strain and shear. The realistic sea surface temperature and velocity fields indicate differences in the eddy shape during this period. By assuming a circular eddy unavoidably profiles that are considered further away from the eddy center are in reality much closer to the eddy core. Reversely, profiles that are outside of the elliptical eddy shape could be estimated in a much closer distance to the center. We introduce a method to distribute the Argo profiles by taking into account these eddy elliptical shapes. Differences between the resulting reconstructions are discussed.

Eddy Center Estimations

One of the first steps to reconstruct the eddy core is to identify accurately the eddy center. Even though this is a relatively easy task, given the automatic detection of the eddy from the satellites observations and the AMEDA tracking algorithm, there are periods where the satellite altimetry provides indeed a good estimation of the eddy position but also specific periods where there is a misalignment of the eddy position and floats positions. The superposition of the SST and the Argo floats (see Figure 4.6) was proven very helpful to examine the spatio-temporal coherence of the eddy position and the detected shape from altimetry (AVISO/AMEDA).

We examined 4 different centers, two constant in time and two moving in time, in order to optimize the radial re-distribution of the Argo floats from the eddy core. The constant centers were computed as the averaged eddy center position estimated from the AMEDA detection and the averaged profile positions as given by the floats. Then, the eddy center temporal evolution was taken into account and it was estimated from AMEDA daily tracking as well as from the orbital movement of the Argo floats (called moving center Argos hereby). The latter was computed by applying a temporal filtering in the orbital float motion. Assuming that the floats will certainly loop around the eddy core, the eddy center would be located in a mean position along the maximum/minimum orbital float movements.

A comparison between the moving centers is shown in Figure 4.6. The distance between the daily centers detected by AVISO/AMEDA and the moving Argos is estimated. Both the eddy center computed by the eddy barycenter (blue thick line) and minimum angular momentum center (LNAM) were compared with the moving center from the floats (black dashed line). On average the eddy center differences remained below $30\,km$. Two representative dates are marked Figure 4.6 a). One is representing, a case

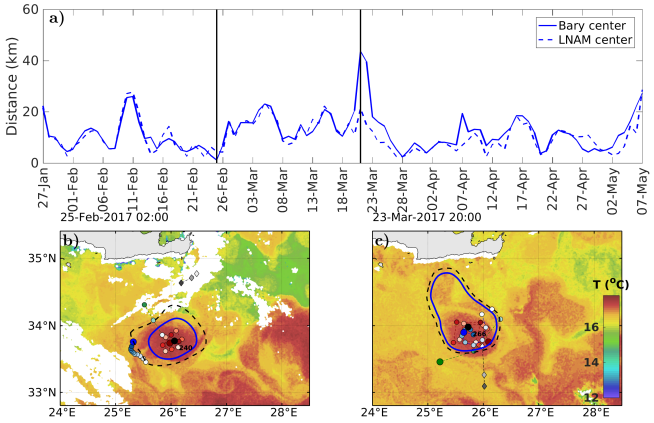

Figure 4.6: *a) Distance (km) between eddy centers as detected by satellite altimetry and AMEDA detection algorithm with the estimation from Argo looping. b) The SST fields are shown for the 25 February and the 23 March. The eddy center and the characteristic eddy contours as detected from altimetry are shown with the black point, blue and black lines. Each Argo float is shown with the colored points. Their positions are displayed during a 10 day period before the corresponding date.*

in 25 February 2017 where both methods detect accurately the eddy core. The relative difference remained below $d < 5\,km$. The second case represents the maximum center difference that was estimated above $d > 40\,km$ for the 23 March 2017 and corresponds to the relative distance of the eddy barycenter and the moving center position. The extended shape of the eddy resulted in a shift in the center estimation in comparison with the center as estimated by the minimum angular momentum (LNAM). As illustrated in Figure 4.6 b), the erroneous detection is mainly a result of the stretched and elongated eddy contour shape that results in an offset of the eddy barycenter for the given day. The Argo floats are clearly looping further south.

In order to evaluate the radial distribution of each float based on the selected four eddy center estimations, we defined the integrated density anomaly as follows:

$$\Sigma\delta\rho_A = \int_{z_{min}}^{z_{MLD}} (\rho(z) - \rho_{ref}(z))dz \tag{1}$$

The integrated density anomaly $\Sigma\delta\rho_A$ represents the mean eddy core anomaly imposed by the eddy presence in the unperturbed density field. It could be then used as a measure to quantify the Argo float distance from the eddy core given the maximum anomaly is located in the eddy core. The $\Sigma\delta\rho_A$ is computed for each profile from a prescribed deeper lower depth level z_{min} until the estimated mixed-layer depth z_{MLD} (around $200 - 600\,m$). Strong vertical density variations inside the eddy mixed-layer depth are thus avoided. It is then desirable to minimize the dispersion of the integrated density anomaly $\Sigma\delta\rho_A$ as a function of the distance r from the eddy center. The integrated density anomaly $\Sigma\delta\rho_A$ was used as an index for the optimal re-distribution of the floats along the radial direction. Figure 4.7 shows the integrated density anomaly for each chosen center: the fixed AVISO center, the fixed Argo position, the moving AVISO center and the moving Argo center as a function of radial distance from the eddy core. In order to evaluate the variance of the data we estimated the coefficient of determination R^2. The smallest dispersion was computed for the moving Argo center ($R^2 \simeq 0.87$) and

thus was chosen as the most adequate center for re-referencing all the Argo floats and proceeding further with the 3-D reconstruction.

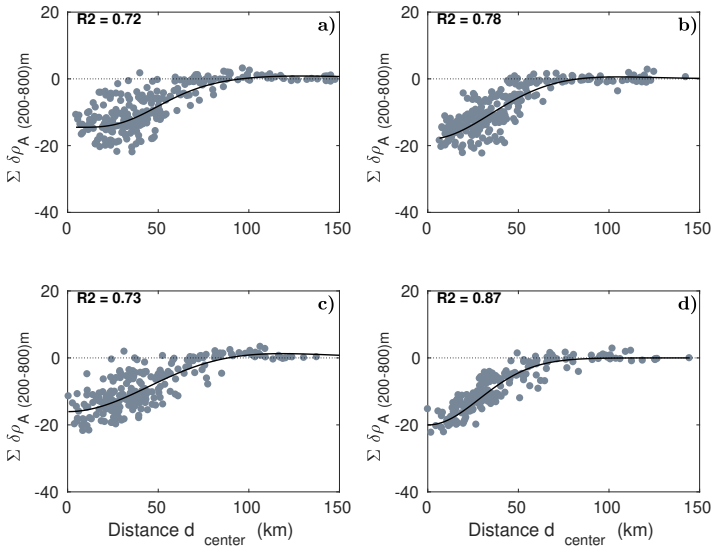

Figure 4.7: *Integrated density anomaly $\Sigma\delta\rho_A$ for all Argo profiles when re-referenced based on different eddy center estimation a) mean center from AVISO/AMEDA eddy detection b) mean center from all Argo floats positions c) moving eddy barycenter from AVISO/AMEDA eddy detection d) moving center estimated from Argo orbital movement.*

Fitting function

Once the eddy center is estimated, each Argo float is radially distributed in respect with the chosen eddy center. The eddy anomaly fields could be then parametrized with the following function:

$$\delta q_A(r) = \delta q_A \, r e^{-\frac{1}{a}\left(\frac{r}{R_{max}}\right)^a} \tag{2}$$

where δq_A the eddy anomaly of temperature δT_A, salinity δS_A and density $\delta\rho_A$ and R_{max} is the characteristic radius of the eddy. The steepness parameter α can range between $\alpha = 1.3 - 3.1$. The 3D reconstruction was obtained for each field $q_A = (T_A, S_A, \rho_A)$ performing an optimized fitting at each depth. Once the reconstruction of the density anomaly $\delta\rho_A$ is completed an estimation on the 3-D eddy velocity could be derived with the non-linear thermal wind equation. The non-linear thermal wind writes as follows:

$$\frac{\partial}{\partial z}\left(\frac{V^2}{r} + fV\right) = -\frac{g}{\rho_o}\frac{\partial}{\partial z}\delta\rho_A \tag{3}$$

Assuming a reference level of zero velocity at $z = -1000\,m$ we can estimate, according to the thermal wind relation, a vertical section of the cyclogeostrophic velocity across the eddy core. Information on the eddy vertical velocity structure can be thus retrieved.

Argo Floats looping

Apart from the 3D reconstruction of the vertical velocity, the daily sampling of the floats (6902770 & 6900422) could provide additional information on the eddy orbital motion. These floats looped inside the eddy with a typical period of 10 days completing

consecutive loops at different radial distances. For several distinct time periods both floats exhibited a quite distinct swirling motion (Figure 4.8). During the 10 day period, both floats complete similar looping patterns regardless their different drifting parking depths ((100 m and 350 m respectively). The looping patterns of the floats suggest a vertical extend of velocities that occupies at least the first 350 m depth. To recover a quantitative estimation on the eddy orbital motion, each float trajectory was split in segments of at least 5 days time spread. Each loop was fitted with an ellipse. The trajectory segments were shifted in time (daily) updating the Argo loops. Only the ones that remained almost circular, with ellipticity lower than $\epsilon < 0.4$, were kept. The selected loops correspond to quasi-circular trajectories in the relative frame of the eddy center, and we calculate, for all of them the time averaged radius R_i and the mean tangential velocity V_i. The relative size of the eddy is first computed from the equivalent area surrounded from the fitted ellipse as in Eqn.(4). The tangential eddy velocity is then estimated from the time the Argo required for completing the estimated ellipse perimeter (Eqn.(5)).

$$\langle R \rangle = \sqrt{A/\pi} \tag{4}$$

$$\langle V \rangle = P_e/\tau_e \tag{5}$$

where P_e is the ellipse perimeter and τ_e is the revolution period of the eddy. Even though the Argo floats can not provide high accuracy in the temporal position as in the case of drifters, their daily sampling cycle was enough the provide for an estimation of the eddy tangential velocities.

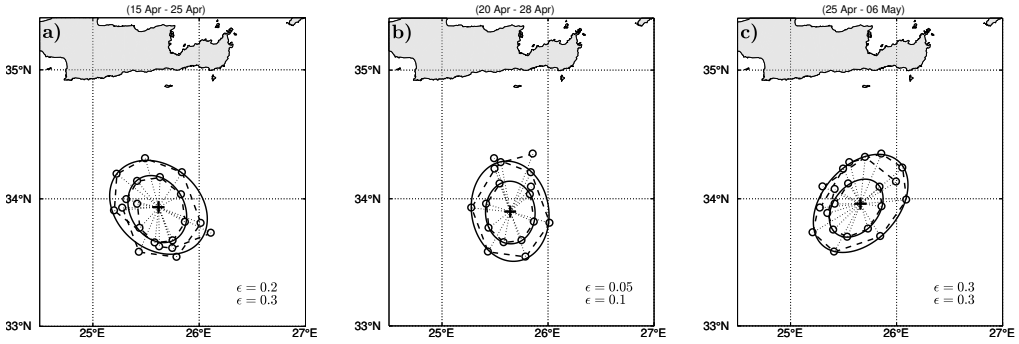

Figure 4.8: *Distinct loops completed by the Argo floats 6902770 and 6900422 looping within the IE16 during the period of 15 April to 06 May 2017. The segments of their trajectories as well as the fitted ellipse are illustrated with the points and line respectively.*

4.4 Reconstruction of Ierapetra eddy vertical structure

Circular axis-symmetric eddy

We proceed with the reconstruction of the eddy core based on the moving Argo center that was proven the most adequate for the Argo float co-localization (section 4.3). The resulting estimations of the core anomalies $(\delta T_A, \delta S_A, \delta \rho_A)$ are shown in Figure 4.9 (a-c). Each field was derived by optimized fitting of the Eqn.(2) at each vertical level. The vertical velocities associated with the density anomaly vertical structure were computed from the non-linear thermal wind equation (Eqn.(3)). They are recovered in Figure 4.9(d). The 3-D reconstruction shows a maximum temperature anomaly of about $+1.8\,^{\circ}C$ centered at 400 m depth. The estimated meridional geostrophic velocity was of the order of 30 $cm\,s^{-1}$ at 100 m depth, with maximum velocities near eddy-core edges

in a distance $R = 30\,km$. The MLD redistribution was found to scale linearly with the distance from the eddy core. The maximum layer depth was thus located close to the center of the eddy and could reach at least $200\,m$ depth. Such horizontal variations of the surface mixed layer emphasize the strong air-sea interactions within the eddy and strong ageostrophic velocities within the mixed layer.

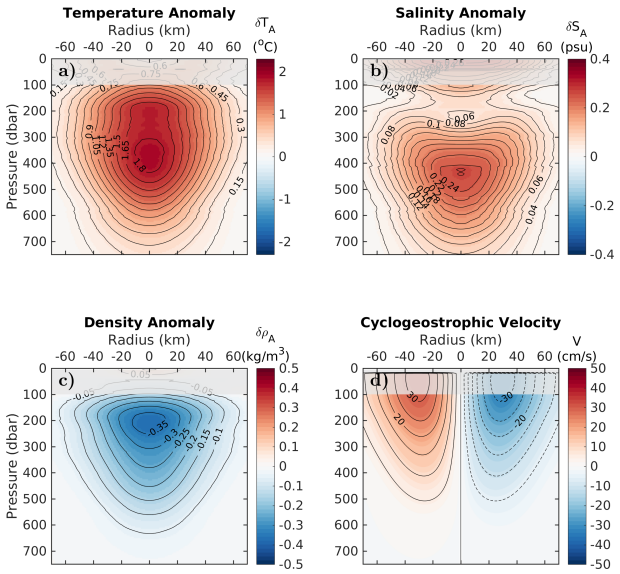

Figure 4.9: *Vertical section of reconstructed circular eddy based on floats re-referencing with the moving Argo center. a) temperature anomaly $\delta T_A\,(^oC)$ b) salinity anomaly $\delta S_A\,(psu)$, c) density anomaly $\delta \rho_A\,(kgm^{-3})$ and d) Vertical velocity estimation $V\,(cm/s)$ from thermal wind equation Eqn.(3) is shown along the radial distance r from the eddy center.*

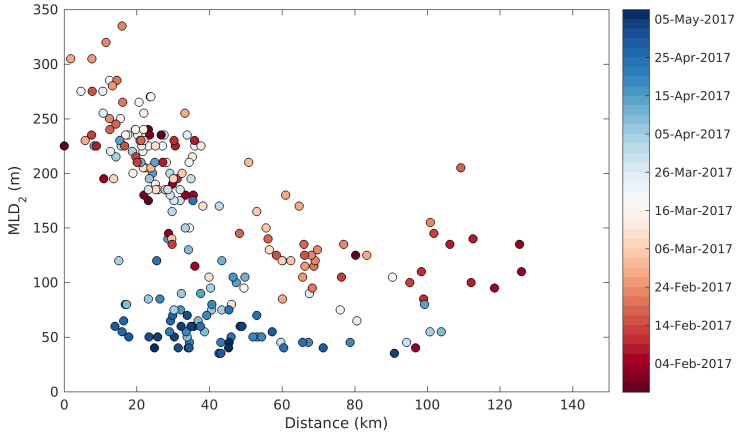

Figure 4.10: *Mixed Layer Depth (m) as function of the estimated distance of the eddy core.*

Accounting for eddy shape variations

In the analysis so far we assumed an axis-symmetric eddy and we neglected any variations of the eddy shape during the 4 months period. However, the time series of the SST and SSH fields, showed that the IE exhibited changes in its shape and ellipticity during the period of investigation. Thus, at a specific time a profile with lower $\Sigma\delta\rho_A$

could be re-referenced closer to the eddy core as a result of the eddy elliptical shape. Moreover, at given times a float may be erroneously interpreted as outside the eddy or vice-versa, thus leading to erroneous distribution of the eddy anomaly in the radial direction.

In order to account for the eddy ellipticity, radially co-centric ellipses were fitted along the eddy radial distance r. This was achieved in combination with the floats looping around the eddy. Accounting for the elliptical shape of the eddy, a more accurate identification of the radial distance of each float was obtained. An example of the fitting is shown in Figure 4.11 (a). By taking into account the eddy elliptical shape, all profiles that are along the same co-centric ellipse are re-referenced in the same radial distance from the eddy center d_{center}. This is valid when comparing the vertical structure of the different profiles characteristics in Figure 4.11 (b-c). All fields positioned along the same ellipse periphery have the same hydrographic characteristics (colors that align with each other).

Based on the circular eddy assumption all these profiles would be distributed in different radii causing dispersion in the eddy anomaly radial distribution. The radial distribution of the profiles when eddy ellipticity was taken into account is shown in Figure 4.11. For the eddy reconstruction, again a circular eddy was considered although the gradients of the density and temperature anomalies were distributed taking into account the eddy shape variations Figure 4.11(d).

The 3-D reconstruction of the IE16 when ellipticity was taken into consideration is shown in Figure 4.12. The maximum temperature anomaly was estimated of the order of $+2.25\,^{\circ}C$ centered at $350\,m$. The derived density anomaly leads to a meridional geostrophic velocity of the order of $45\,cm/s$ in $100\,m$ depth, with maximum velocities near distance $R = 30\,km$. The gradients are evidently stronger than the circular case and the resulting velocities are higher by at least 50%.

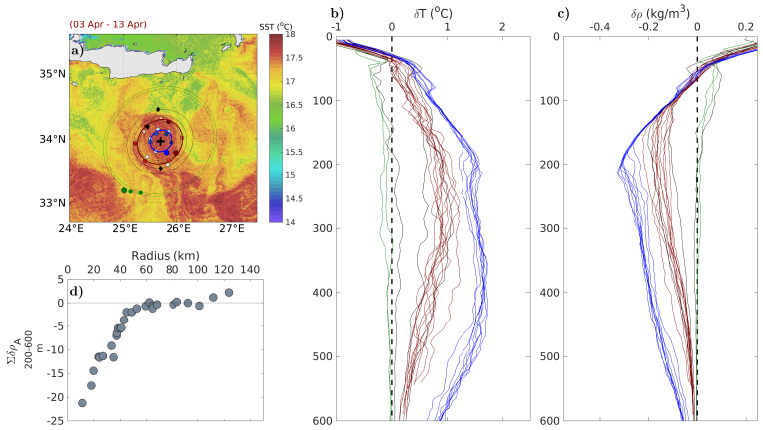

Figure 4.11: *a) Argo floats locations during 03-13 April and the corresponding co-centric ellipses. b) Density and c) Temperature anomaly profiles along the fitted ellipses. Each float is illustrated with the different colors. d) Integrated density anomaly $\Sigma\delta\rho_A$ for all Argo profiles when re-referenced based on the elliptical shape of the eddy.*

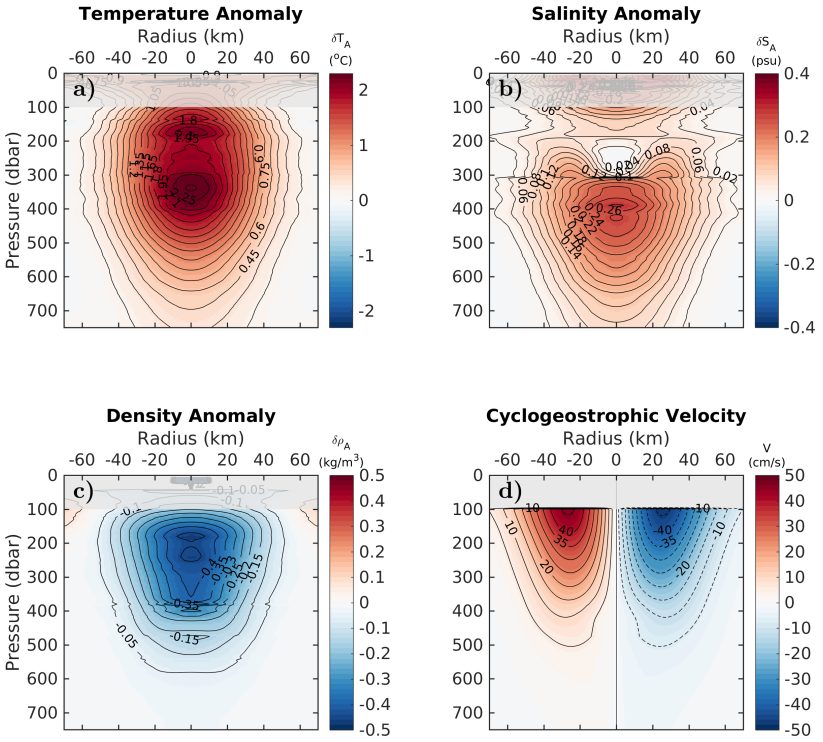

Figure 4.12: *Vertical section of reconstructed eddy when ellipticity is taken into account for the re-distribution of the Argo profiles. a) temperature anomaly $\delta T_A\,(^oC)$ b) salinity anomaly $\delta S_A\,(psu)$, c) density anomaly $\delta \rho_A\,(kgm^{-3})$ and d) Vertical velocity estimation $V\,(cm/s)$ from thermal wind equation Eqn.(3) is shown along the radial distance r from the eddy center.*

Eddy Velocity Comparisons

In order to test the accuracy of the performed eddy reconstructions, all estimated velocities for the IE16 are compared in Figure 4.13. Firstly, the velocities from the "circular" and "elliptical" eddy reconstruction were extracted at the corresponding parking depths of the Argo floats $(100\,m\,, 350\,m)$. Moreover, Figure 4.13 shows with points the data pairs of $(R_i,\, V_i)$ that correspond to the different loops completed by the two different Argos that daily sampled the eddy. Only loops with ellipticity lower than $\varepsilon < 0.4$ were kept. The floats are estimated to loop in radial distances of $R \sim 20 - 40\,km$ from the eddy core. For several circular loops (green colors) the eddy velocities estimations reached $V_{max} = 45\,cm/s$. These velocities corresponded to the float with drifting parking depth of $100\,m$. The lower drifting speeds observed by the second float (squared points) could be explained if considering its deeper pre-assigned drifting parking depth $(350\,m)$ or that it loops around closed contour that is located closer to the eddy center. In order to compare these velocity measurements with the typical velocity profile estimated from the AVISO geostrophic and cyclostrophic surface velocity we plot on Figure 4.13 the mean profile $(\langle R\rangle\,,\,\langle V\rangle)$ computed by the AMEDA algorithm and averaged during the three months period. The dashed black lines correspond to the geostrophic fields and red dashed to the cyclostrophic ones. When cyclostrophic corrections are taken into account the maximum eddy velocity profile is estimated to reach $60\,cm/s$. The velocity estimation from the elliptical eddy reconstruction compares well with the cyclogeostrophic velocities (only 20% underestimation).

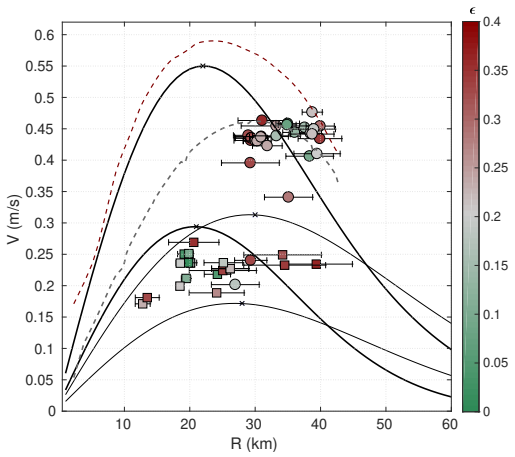

Figure 4.13: *Points of mean tangential velocity V_i and mean eddy radius R_i with their rms error (errorbars) corresponding to the quasi-circular loops performed by the two ARGO floats 6902770 (triangles) and 6900422 (circles) inside the IE16 from January to May 2016. The black solid curves indicate the estimated velocities extracted from the 3-D reconstruction at $100\,m$ and $350\,m$ depths. The thicker black line corresponds to the elliptical eddy reconstruction and the thinner line to the circular reconstruction. The gray dashed line represents the maximum velocity profile detected from AMEDA algorithm from the geostrophic AVISO data set during the 3 month period. The red dashed line depicts the most intense velocity profile reached during this period on the 8 March 2016 as detected from AMEDA algorithm from the geostrophic AVISO data set. The red dashed line indicates the strongest cyclogeostrophic velocity profile during the same period.*

4.5 Summary & Conclusions

In this chapter, we have observed the vertical structure of a single Ierapetra anticyclone with Argo floats measurements during winter 2017. This eddy was sampled by a 4 different Argo floats providing us with a lot of information on the eddy hydrographic characteristics. By collocating the Argo floats measurements and the eddy surface signature from AVISO/AMEDA detection method, we attempted the IE vertical structure reconstruction in comparison with the hydrographic properties of the surrounding environment.

First, a methodology to recover the eddy three-dimensional structure from the Argo floats vertical profiles was demonstrated. The optimal distribution of the Argo profiles in respect with the eddy center was found of major importance in order to accurately describe the eddy density gradients. The heterogeneity between the eddy center detection from AVISO/AMEDA method and the Argo floats position at given times could erroneously detect the float radial position. For that reason, four different eddy centers estimations were examined in order to obtain the lowest possible dispersion of the floats and thus their best possible radial distribution. For that purpose a new index quantity that estimates the integrated eddy density anomaly ($\Sigma\rho_A$) was found very useful for minimizing the profiles dispersion.

Starting with the assumption of a circular and axis-symmetric eddy that is sampled at different times and locations during the 4 month period we progress with the 3D reconstruction. Based on the optimum float distribution the eddy reconstruction showed a 2^oC anomaly in temperature with the sou rounding environment that could extend to depths of $400 - 500\,m$.

Investigating further the eddy evolution from its surface signature based on sea surface temperature but also satellite observations slight shape deformations were observed

during the sampling period. During distinct periods the Argos floats exhibited and completed elliptical loops along which the obtained vertical hydro graphic properties were the same. Based on the axis-symmetric reconstruction these profiles would be radially distributed in different radius even though having roughly the same properties. Thus in order to reduce further the data dispersion, such elliptical loops were identified and the floats with similar properties were distributed in a radial distance that was computed from the area delimited by the ellipse. This ensured that profiles of same characteristics to be distributed in the same eddy radius capturing better the eddy density gradients. This "elliptical" eddy reconstruction showed that IE16 could exhibit a stronger density anomaly in its core that may reach $\delta\rho_A = -0.5\,kg\,m^{-3}$. Moreover, from this orbital movements of the floats refereed as "Argo looping" an estimation of the eddy velocities was obtained for every detected loop.

Lastly, the predictions of the eddy velocities by the various 3D reconstructions and the Argo looping were compared with the observations from satellite altimetry (geostrophic and cyclogeostrophic). We concluded that the shape variations of the eddy were pivotal in order to capture better the eddy density gradients. Even if the "circular" reconstruction differed slightly from "elliptical" reconstruction in terms of the core anomaly estimations, the smoother eddy gradients resulted in lower estimated eddy velocities (50% underestimation compared with the cyclogeostrophic estimations). On the other hand, velocities estimated from the "elliptical" reconstruction were found much closer to the the cyclogeostrophic estimations with an error of 20% more accurately representing the eddy density gradients.

Our analysis shows that the Ierapetra eddies apart from eddies with strong sea surface signal could have also strong vertical anomalies. Based on the IE16 vertical sampling during 2017, the maximum eddy anomalies were found in $400\,m$ depth and extended until at least depths of $700\,m$. The colocalisation of the Argo floats and satellite altimetry was found very useful in order to characterize the eddy vertical evolution below their surface signature as well as estimate the eddy vertical velocities.

CHAPTER 5

Generation and intensification of mesoscale anticyclones by orographic wind jets: the case of Ierapetra eddies forced by the Etesians

It has been illustrated so far, that the generation as well as the intensification of the Ierapetra eddies was mainly observed during summer months, a fact that coincided with the seasonal Etesians winds period. In this chapter, a forcing function that could represent the orographic wind forcing South-East of Crete is estimated. The oceanic response is then simulated with the reduced gravity model. The main parameters of the applied wind forcing that control the oceanic response are discussed. The following analysis has been submitted recently to JGR.

Generation and intensification of mesoscale anticyclones by orographic wind jets: the case of Ierapetra Eddies forced by the Etesians

Artemis Ioannou, Alexandre Stegner, Thomas Dubos, Briac LeVu and Sabrina Speich

(Submitted to JGR)

Abstract Motivated by the recurrent formation and intensification of the Ierapetra anticyclones in the southeast of Crete, we investigated with a reduced gravity model the response of the oceanic surface layer to a seasonal wind jet that varies slowly (over several weeks or months) and mimics the Etesian winds. Our study answers why the oceanic response to such forcing is mainly a large and intense anticyclone. We build a dimensionless parameter that integrates in time the Ekman pumping and quantifies the relative amplitude of the isopycnal displacement induced by the local wind stress curl. According to the range of the wind forcing parameter, the oceanic response to a symmetric wind jet could be a symmetric dipole or a strongly asymmetric structure dominated by an intense and robust anticyclone. This intrinsic asymmetry is driven by the finite isopycnal displacements that occur when the wind forcing parameter reaches unity. Since, the anticyclonic wind shear, for the Etesian wind jet, is two times larger than the cyclonic one, the asymmetry of the oceanic response is enhanced. Several

weeks after the wind forcing has stopped, an intense mesoscale anticyclone which satisfies the cyclogeostrophic balance remains. Moreover, if a similar wind jet blows on a pre-existing anticyclone, the latter remains robust and coherent and gets re-intensified in agreement with the previous analysis of remote sensing observations. Hence, this paper is the first numerical study which provides a dynamical understanding for the formation of the single Ierapetra anticyclones and explains their intensification one year after formation.

5.1 Introduction

The prevailing wind regime over the Eastern Mediterranean Sea (EMS) is dominated by persistent northern winds called Etesians. Every summer, numerous islands in the Aegean are subject to the Etesian wind forcing which results in strong upwelling regions along the east part of the Aegean (Bakun and Agostini, 2001). The complex topography of the islands acts as an obstacle for wind propagation inducing channeling and deflection effects towards the south Aegean and the Levantine basin. Kotroni et al. (2001) were the first to demonstrate the blocking and the deflection of the Etesians by Crete island. Performing simulations with and without Crete, they concluded that the Crete orography (3 mountains in the row with height around $2000\,m$) creates a blocking effect resulting in a deceleration region upstream of the mountains which modifies the Etesian intensity and pathways. Miglietta et al. (2013) simulated the influence of the orography in the south east of Crete, capturing the lee waves patterns in the wakes of the Crete, Karpathos, Kasos and Rhodes islands. Based on observational data from meteorological stations, Koletsis et al. (2009, 2010) confirmed that the Etesians decelerate upstream of Crete and deflect leftward while intensifying between the mountain gaps. Velocities of the maximum wind gusts were recorded to reach $25\,m\,s^{-1}$ in 2007 persisting for 3 days. The Etesians are observed every summer while their duration is intermittent. They are characterized by recurrent periods of gale-force northerlies interrupted by quieter spells (Tyrlis and Lelieveld, 2013). Based on Etesian trends and climatology from 1979 to 2009 (Poupkou et al., 2011), the total number of Etesian days from June to September is on average 45 days with wind forcing values that range between $5 - 15\,m\,s^{-1}$.

Meanwhile, several long lived oceanic eddies are formed downstream of Crete, in the North Levantine basin. For instance, in the south east corner of Crete, the mesoscale Ierapetra anticyclone is recurrently formed during summer. The role of these Ierapetra eddies (IEs) on the circulation of the Levantine basin has been subject of numerous studies (Larnicol et al., 1995; Matteoda and Glenn, 1996; Hamad et al., 2005, 2006; Taupier-Letage et al., 2007). More recently, thanks to the efficiency of automatic eddy detection algorithms applied to high-resolution AVISO/DUACS maps (gridded at $1/8^{\circ}$ in the Mediterranean Sea), the seasonal evolution and the inter annual variability of the IE's were investigated for more than twenty years (Ioannou et al., 2017). The Ierapetra anticyclones were found to be the most intense eddies of the Levantine basin. The Rossby numbers experience a strong seasonal and interannual variability and could vary by a factor 4 from one year to another. Besides, it was found that the geostrophic assumption underestimates the intensity of these anticyclones and therefore the cyclostrophic corrections should be added to the geostrophic surface velocity field derived for altimetry maps (Ioannou et al., 2019). According to these corrections, the core vorticity could reach intense negative values up to $-f$. Moreover, we also found that after their formation, IEs could reintensify (Ioannou et al., 2017). This intensification process may lead to a doubling of the eddy intensity in less than 4 months. Both the formation or the intensification stages coincide with the period of strong Etesian winds when the IEs are located in the southeast of Crete in the lee of the Kasos strait.

The pioneering studies of (Horton et al., 1994; Fusco et al., 2003) have suggested that the IEs were wind forced. Moreover, the statistical analysis of the monthly surface

wind (averaged over 20 years) performed by (Mkhinini et al., 2014) confirmed the presence of strong negative wind stress curl in the south east corner of Crete. Such seasonal correlations between the formation area of the Ierapetra anticyclones and the location of this region of negative wind stress curl seems to confirm the hypothesis that IEs are wind induced. But, correlation does not imply causation and the main goal of this paper is to investigate if the specific orographic wind jet induced by the Crete orography could indeed explain the generations and the intensifications of strong Ierapetra anticyclones.

Several cases of coastal eddies induced by orographic winds have been previously observed in several regions. For instance, the formation of both cyclonic and anticyclonic eddies are frequently observed in the lee of mountainous islands (Yoshida et al., 2010; Jia et al., 2011; Caldeira et al., 2014; Couvelard et al., 2012; Piedeleu et al., 2009; Kersalé et al., 2011; Barton et al., 2000; Jiménez et al., 2008; Caldeira and Marchesiello, 2002; Caldeira and Sangrá, 2012). The role of the local wind stress as a driver of oceanic vortices was first noted by Patzert (1969), in a discussion of the role of Ekman pumping in generating Hawaiian lee eddies. Yoshida et al. (2010) compared the timescale variability of the kinetic energy and sea surface height of the eddies with the wind stress curl variability downstream of the Hawaii archipelago. A lag of 2 weeks between the oceanic and atmospheric response was found, emphasizing that the ocean acts like an integrator of the wind forcing for low frequencies. For the Hawaiian case, the interaction between the North Equatorial Current and the archipelago is enough to generate eddies, but high resolution wind stress curl were needed in the numerical models to get the correct eddy intensities in agreement with observations (Calil et al., 2008; Kersalé et al., 2011; Jia et al., 2011). For Madeira Island, both numerical simulations (Couvelard et al., 2012) and oceanic observations (Caldeira et al., 2014) indicate that the orographic wind wakes could be the main mechanism of oceanic eddy generation. For larger coastal mountain chains orographic gaps or valleys could locally amplify the upstream synoptic winds and lead to strong wind jets on the sea. The numerical study of Pullen et al. (2008) has shown that intensified wind jets in the lee of Mindoro and Luzon Islands induce the generation and the migration of a pair of counter-rotating oceanic eddies. More recently, Zhai and Bower (2013) investigated the response of the Red Sea to the Tokar wind jet. Remote sensing and in situ observations both showed that an intense dipolar eddy is formed during the summer monsoon season and that its strength is closely correlated with the wind variability. Besides, the dipolar response of a 1.5-layer shallow water model, forced by an idealized wind jet, showed a correct agreement with the oceanic observations. All these studies exhibit a dipolar response to the wind jet, in other words both cyclonic and anticyclonic eddies are expected to be formed in the coastal ocean. These results seem to contradict the hypothesis that the Ierapetra anticyclones are mainly driven by the Etesian winds. Why would the main response of the wind jet in the Kasos strait be only a large and intense anticyclone ? The underlying mechanism responsible for such asymmetry is not clear. The paper of McCreary et al. (1989), which studied the response of the ocean to the gap winds in the Gulf of Tehuantepec, is the only one which exhibit an asymmetric response which favors the formation of a large scale anticyclone. However, they used a specific shallow-water model which includes a parametrization of the entrainment of cool water into the surface layer. Therefore, it is difficult to determine whether the source of this asymmetry is due to the dynamical response of the oceanic layer or to thermodynamic processes.

In order to study the role of Etesian winds on the formation of intense Ierapetra anticyclones, we will use an idealized reduced gravity shallow water model to mimic the various responses of the upper oceanic layer, above the thermocline, to orographic wind jets. This oceanic layer will be forced only by the surface wind stress and the internal mixing or the atmospheric heat fluxes will be not be taken into account. The main objective of this study is to determine whether Etesian winds alone can explain the formation

and the intensification of IE's in agreement with our previous analysis of remote sensing data sets (Ioannou et al., 2017). The paper is organized as follows. In section 5.2, we describe the 1.5-layer rotating shallow water model as well as the eddy detection and tracking algorithm AMEDA that we use to quantify the dynamical properties of the generated eddies. Section 3 presents the spatio-temporal characteristics of the wind jet according to the regional wind climatology. In Section 4 we present the characteristics of the oceanic eddies generated by symmetric and asymmetric Etesian wind jets. The impact of the Etesian wind on pre-existing anticyclone is then presented in section 5. Finally, we discuss, in section 6, the asymmetry of the oceanic response to the Etesian wind jets and compare it to the dynamical characteristics of observed IE's.

5.2 Data & Methods

Wind data

We use the ALADIN atmospheric data-set (Tramblay et al., 2013; Hamon et al., 2016) to analyze the spatial structure of the Etesian wind forcing and their temporal variations. Based on dynamical downscaling of the ERA-Interim reanalysis, the ALADIN datasets provide the wind stress components for the Mediterranean Sea at a grid resolution of $1/12^o$ with a time interval of $3\,h$. Wind forcing data were extracted for the Eastern Part of the Mediterranean from 1993 to 2012. As we are interested in the slow response of the ocean to the wind forcing a 7 day sliding window is applied in order to filter out short-term variations of the forcing. For the region of interest we additionally collected wind and temperature data from the Greek National Meteorological Service from available meteorological stations in the islands of Crete and Karpathos.

Rotating shallow-water model

In order to study the dynamical response of the oceanic surface layer to a transient wind jet, we use an idealized 1.5-layer model. This idealized rotating shallow-water model also called the reduced gravity model, represents the upper oceanic thermocline with a single active layer of density ρ_1 which overlays a motion less layer of infinite depth with higher density ρ_2. The unperturbed layer thickness H of the upper layer and the reduced gravity $g^{'} = \dfrac{\delta\varrho\,(=\varrho_2-\rho_1)}{\rho_2}g$ are the two key parameters that we prescribe according to the non uniform stratification of the area (section 5.7). We estimate first the baroclinic deformation radius to be $R_d = 10-13\,km$ (Chelton et al., 1998) while we choose the unperturbed layer thickness $H = 100\,m$. The momentum and continuity equations for the 1.5-layer model are:

$$\frac{\partial \underline{\mathbf{u}}}{\partial t} + \underline{\mathbf{u}}\cdot\nabla\underline{\mathbf{u}} + f\mathbf{k}\times\underline{\mathbf{u}} = -\nabla\phi + \frac{g'\underline{\boldsymbol{\tau}}}{\varrho\phi} + A_h\,\triangle^2\,\underline{\mathbf{u}} \quad (1)$$

$$\frac{\partial \phi}{\partial t} + \nabla\cdot(\phi\underline{\mathbf{u}}) = 0 \quad (2)$$

where $\underline{\mathbf{u}}$=(u,v) is the horizontal velocities in both directions, f is the Coriolis parameter ($f = 10^{-4}$), $g' = 0.02\,ms^{-2}$ is the reduced gravity, $\phi = g'h$ is the geopotential height with h the deviation of the layer thickness and $\underline{\boldsymbol{\tau}} = (\tau_x, \tau_y)$ the wind stress vector. A bi-Laplacian dissipation is used in order to filter out small scale numerical noise that may occur at grid scale. We define four dimensionless numbers associated to such transient wind forcing, the Rossby number Ro_W, the Burger number Bu_W, the dimensionless wind evolution t_W and the equivalent Reynolds Re_W number as follows

$$Ro_W = \frac{U_E}{fW} \qquad Bu_W = \left(\frac{R_d}{W}\right)^2 \quad t_W = Tf \quad Re_W = \frac{U_E W^3}{A_h}$$

where $R_d = \frac{\sqrt{g'H}}{f}$ is the first baroclinic deformation radius, $U_E = \frac{\tau_o}{\rho f H}$ is the Ekman velocity, W the width of the wind jet and A_h the hyperviscocity coefficient.

When the wind Rossby number is small ($Ro_W \ll 1$) and the wind evolution is slow enough ($t_W \gg 1$), the first two terms of the momentum equation Eqn.(1) are negligible in relation to the Coriolis acceleration and the initial response of the oceanic layer will satisfy the geostrophic balance. Since we consider relatively slow variations of the wind forcing ($t_W \gg 1$), most of the work induced by the wind stress at the ocean surface will be transfered to the balanced flow while the generation of inertia gravity waves will be strongly reduced. The Burger number compares the wind jet width to the baroclinic deformation radius while the equivalent Reynolds number compares the relative amplitude of the advective terms to the dissipative terms. The hyper viscosity coefficient was fixed to the constant value $A_h = 10^6\, m^4 s^{-1}$ in order to get at the grid scale $U_E(\Delta x)^3/A_h \sim 1$ while $Re_W \gg 1$.

The rotating shallow water equations are solved with a doubly periodic boundary condition in a square domain of size $L_x \times L_y = 600 \times 600\, km$. This domain was chosen to be much larger than the wind jet width W. The horizontal resolution is $\Delta x = \Delta y = 1\, km$ for all simulations in order to be significantly smaller than the radius of deformation $R_d = 13\, km$. Moreover, the convergence of the numerical solution was tested by comparing the results obtained with decreasing grid sizes.

The AMEDA eddy detection and tracking algorithm

To track eddies in the computational domain we use the Angular Momentum Eddy Detection and tracking Algorithm (AMEDA) (Le Vu et al., 2018). Applied to the velocity fields AMEDA identifies the eddy characteristics based on the physical parameters and the velocity field geometrical properties. The eddy centers are first identified and correspond to an extrema of the local normalized angular momentum. The streamlines surrounding this center are then computed (Figure 5.1). The mean radius $\langle R \rangle$ and the mean velocity $\langle V \rangle$ are evaluated for each closed streamline. This mean radius $\langle R \rangle$ is defined as the equivalent radius of a circular disc with the same area A as the one delimited by the closed streamline (Eqn.(3)), while the mean velocity amplitude $\langle V \rangle$ is derived from the circulation along the closed streamline C, where L_p is the streamline perimeter (Eqn.(4)).

$$\langle R \rangle = \sqrt{A/\pi} \tag{3}$$

$$\langle V \rangle = \frac{1}{L_p} \oint_C V dl \tag{4}$$

We plot in Figure 5.1(c) the pair of the mean eddy velocity $\langle V \rangle$ and the mean radius $\langle R \rangle$ for each closed streamline. We can see on this example that the mean velocity increases when the radius increases until a maximum velocity V_{max} is reached. The corresponding radius is named R_{max}, also called the speed radius (Chelton et al. (2011); Le Vu et al. (2018); Laxenaire et al. (2018)). The *characteristic contour* of the detected eddy (blue contours in Figure 5.1) is associated with the closed streamline of maximal speed. After this maxima, the azimuthal speed of the eddy decreases until the last closed streamline is reached. The latter is plotted with a black dashed line in Figure 5.1. From the characteristic eddy velocity V_{max} and the corresponding radius R_{max}, we compute the vortex Rossby number to quantify the eddy intensity and the Burger number to quantify the relative size of the eddy in respect with the deformation radius R_d:

$$Ro = \left| \frac{V_{max}}{f\, R_{max}} \right| \tag{5}$$

$$Bu = \left(\frac{R_d}{R_{max}} \right)^2 \tag{6}$$

where f is the Coriolis parameter. We also introduce the dimensionless amplitude of the isopycnal deviation induced by the eddy

$$\lambda = \frac{\eta}{H} \tag{7}$$

where $\eta = h(r=0) - H$ is the deviation of the surface layer in the eddy core and H the thickness of the unperturbed layer.

Moreover to characterize the eddy shape two geometrical parameters were used. The first one is the ellipticity ε of the characteristic contour. The second one is the steepness parameter α which is used to fit the mean velocity profile $\langle V \rangle = F(\langle R \rangle)$ of quasi-circular eddies ($\varepsilon < 0.2$) with the generic functions:

$$V_\theta(r) = \frac{V_{max}}{R_{max}} r e^{(1-(r/R_{max})^\alpha)/\alpha} \tag{8}$$

Such generic profiles were used by Carton et al. (1989); Stegner and Dritschel (2000); Lazar et al. (2013b); Yim et al. (2018) to study the stability of various isolated eddies. According to (Ioannou et al. 2017,2019) quasi-circular eddies detected by the AMEDA algorithm on the AVISO/DUACS products, and especially the Ierapetra eddies, are correctly approximated by this generic velocity profile (Eqn.(8)). The steepness parameter α varies between $\alpha = 1.2$ and $\alpha = 2.7$ while the highest probability is close to the Gaussian shape ($\alpha = 2$).

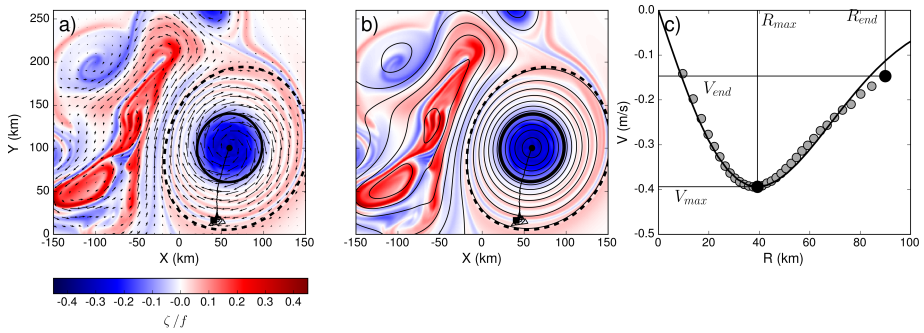

Figure 5.1: *The first panel (a) shows the characteristic contour (solid blue line) and the last contour (black dashed line) calculated by the AMEDA algorithm for an anticyclone. The background colors correspond to the relative vorticity fields ζ/f and the black vectors to the surface velocity components. The central panel (b) shows the streamlines associated with the velocity field as well as the characteristic (solid dark line) and the last closed contour (black dashed line). The velocity profile $\langle V \rangle = F(\langle R \rangle)$ deduced from the streamlines analysis is plotted in the right panel (c). We use here negative values for the mean velocities $\langle V \rangle$ of anticyclones. The shape parameter is $\alpha = 1.9$.*

5.3 Characteristics of the Etesian wind jets between Crete and Kasos

Etesian wind forcing climatology

Figure 5.2 shows the 20 year averaged (1993-2012) wind stress components $\langle \tau \rangle$ and the wind stress curl $\langle \nabla \times \tau \rangle$ obtained from ALADIN data for the winter (a) and the

summer months (b). Areas of positive and negative vorticity fields are distinguished downstream of the islands. The strongest negative wind stress curl, which is expected to induce a strong downwelling of the isopycnals, is found in summer at the south-east of Crete downstream of Kasos strait. This is a result of the Etesian wind blocking caused by the Crete's, Kasos and Karpathos orography, that creates funneling effects between the mountain gaps and the straits separating the islands (Kotroni et al., 2001; Zecchetto and Biasio, 2007). During the winter months, the negative wind stress curl is less intense and confined to a much smaller area Figure 5.2(a). The mean climatological position of the Ierapetra anticyclone, derived from 20 years averaged sea surface height, is marked in Figure 5.2(b) with a black contour. The first detection of all Ierapetra eddies from 1993-2014 are illustrated with the black dots as found in Ioannou et al. (2017). This correlation between the formation of IE's, its mean location and the area of strong negative wind stress curl was already highlighted by (Mkhinini et al., 2014). Although, this represents a mean state of the Etesian forcing and does not account for the spatiotemporal variations of this orographic wind jet. Hence, to illustrate the variations of the Etesian forcing near the mean IE position, we select a circled area of radius $R = 60\,km$ centered at $(27.10^oE, 34.7^oN)$ near the maximum wind stress Figure 5.2(a). Figure 5.2(c) and (d) shows the monthly means of the wind stress components $\langle\tau\rangle$ and the wind stress curl $\langle\nabla \times \tau\rangle$ averaged for the 20 years. Even though the wind stress can be relatively high among all seasons (Figure 5.2(c)) the strongest negative wind stress curl is observed during the summer months Figure 5.2(b, d).

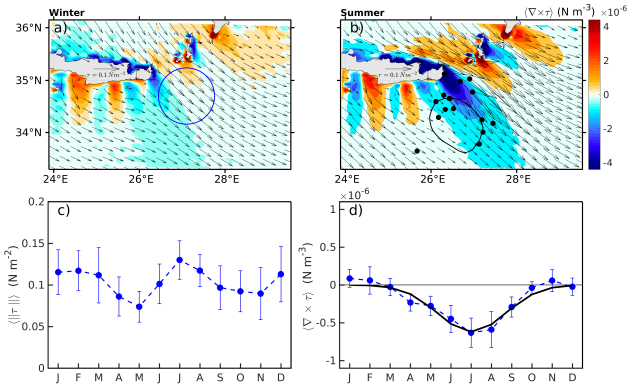

Figure 5.2: *(a) Climatological wind stress $\langle\tau\rangle$ (vectors) and wind stress curl $\langle\nabla \times \tau\rangle$ (colors) for the winter (a) and summer months (b) based on ALADIN datasets (1993-2012). The climatological position of the Ierapetra eddy (1993-2014) is shown with the black contour and the position where all Ierapetra eddies were detected with the black points. The selected area for analyzing the wind forcing climatology is illustrated with the blue circle. (b) The mean monthly climatological wind stress $\langle\tau\rangle$ and wind stress curl $\langle\nabla \times \tau\rangle$ variations in 20 years are shown in panels (c) and (d) respectively.*

In order to simplify the problem we will use, as McCreary et al. (1989) or Zhai and Bower (2013), an idealized wind jet having roughly the same characteristics as the Etesian wind forcing. We therefore extract the monthly wind stress and wind stress curl components along 4 sections (Figure 5.3(a)), one parallel to the mean direction of the wind and 3 other ones, that spans from 26^oE to 28^oE in 3 different latitudes $(34.8^oN, 35^oN, 35.2^oN)$, cross to the mean climatological wind forcing during the same period. The shape of the mean normalized wind forcing is shown for the climatological August in Figure 5.3 (c) and (d). At the first order approximation, we will use the following gaussian functions Eqn.(9) to describe the surface wind stress.

$$\tau_y(x,y,t) = \tau_o\, e^{-\frac{1}{2}\left(\frac{t-t_o}{T_o}\right)^2} e^{-\frac{1}{2}\left[\left(\frac{x}{W}\right)^2+\left(\frac{y-y_o}{L}\right)^2\right]} \qquad x \geq 0 \tag{9}$$

$$\tau_x(x,y,t) = 0 \tag{10}$$

$$\tau_y(x,y,t) = \tau_o\, e^{-\frac{1}{2}\left(\frac{t-t_o}{T_o}\right)^2} e^{-\frac{1}{2}\left[\left(\frac{x}{cW}\right)^2+\left(\frac{y-y_o}{L}\right)^2\right]} \qquad x < 0 \tag{11}$$

$$\tau_x(x,y,t) = 0 \tag{12}$$

The characteristic width and the length of these Gaussian functions are fixed $(W, L) = (40, 100)\, km$ in order to fit the spatial pattern of the Etesian forcing. The width W of such wind jet is almost at least three times larger than the deformation radius $R_d = 14.1\, km$ and the corresponding Burger number is therefore small $Bu_W = 0.13$. Such small value indicates that the oceanic response to this specific wind forcing will contain a higher amount of potential energy than kinetic energy.

Although the regional wind forcing is better represented by an asymmetric shape, due to the weaker wind shear in the cyclonic side (Figure 5.3(c)), we will first evaluate the ocean's response to a symmetric wind forcing (c = 1) and later on, we will use an asymmetric forcing (c = 2) that is more representative of the Etesian winds Figure 5.3(c). For simplicity the meridional component of the wind stress τ_x is set to zero. To investigate the transient effect of the wind forcing in the ocean surface, we progressively increase the wind stress intensity as shown in Figure 5.2(b) over the 3 month summer period. The characteristic time parameter was varied from $T_o = 4\, days$ to $T_o = 17\, days$. The default value was set to $T_o = 10\, days$ which corresponds to a total wind duration of about $60\, days$. The dimensionless wind forcing parameter associated to such duration is larger than unity $t_W = 1.5 - 20$ and we therefore expect that the oceanic response will not contain a large amount of inertia-gravity waves. The spatial distribution of the wind stress and the wind stress curl is illustrated in Figure 5.2(d) for the symmetric case when the forcing reaches its maximal values τ_o at t = 0. This maximal value is located at the core of the wind jet $\tau_o = max(\tau_y(x = 0, y = 0, t))$ and is generally reached during summer months. In agreement with the interannual variability of τ_o, the core wind stress was varied from $\tau_o = 0.05\, N\, m^{-2}$ to $\tau_o = 0.7\, N\, m^{-2}$ in the idealized simulations. Such surface wind stress will induce relatively low Ekman velocities $U_E = 1 - 10\, cm\, s^{-1}$ and relatively small Rossby numbers $Ro_W \backsimeq 0.01$. Hence, the initial flow induced in the oceanic surface layer by the Ekman pumping is expected, after one or two days of geostrophic adjustment, to satisfy the geostrophic balance.

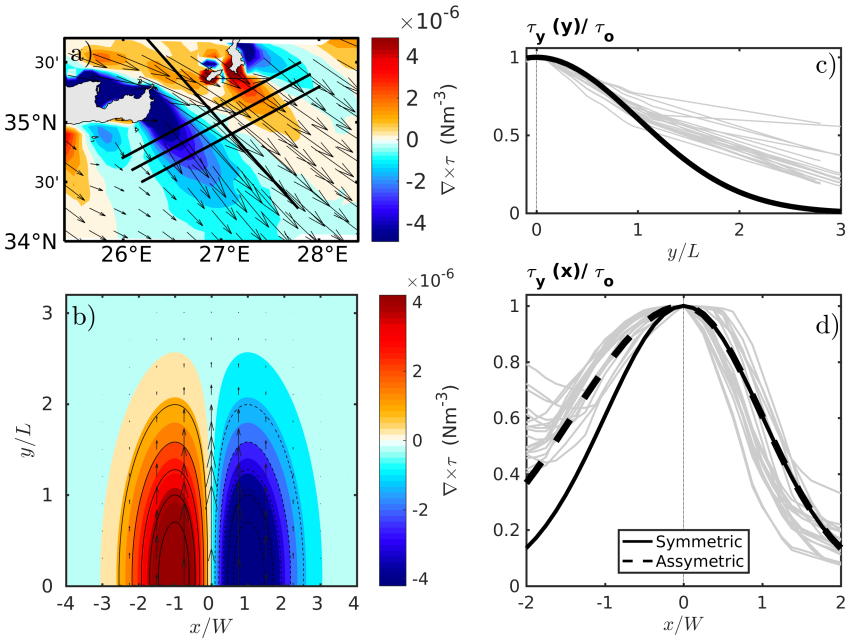

Figure 5.3: *(a) Mean monthly climatological (1993-2012) wind stress $\langle\tau\rangle$ (vectors) and wind stress curl $\langle\nabla\times\tau\rangle$ (colors) for the summer months based on ALADIN datasets. The black lines correspond to the four sections chosen to extract the mean Etesian shape, 3 normal to the wind and one along the mean wind direction that span from 26^oE to 28^oE in 3 different latitudes ($34.8^oN, 35^oN, 35.2^oN$). (b) Spatial distribution of the idealized symmetric wind stress curl when the wind forcing reaches its maximum value $\tau_y(t_o=0)=\tau_o=0.4\,Nm^{-2}$. (c) Normalized wind stress shape extracted parallel to the mean wind forcing direction (along y) as shown in (a). (d)Normalized wind stress shape extracted along the cross wind sections (along x) shown in (a). The fitted Gaussian shape is illustrated with the black color while the asymmetric Gaussian shape with the dashed black line.*

5.4 Dynamical characteristics of Etesian wind induced eddies

Oceanic response to a symmetric wind jet

The temporal evolution of the response of the surface layer to a symmetric wind forcing corresponding to $\tau_o = 0.4\,N\,m^{-2}$, $T_o = 10$ days and $(W, L) = (40, 100)\,km$ is shown in Figure 5.4. These snapshots depict the non-linear evolution of the relative vorticity ζ/f (colors) and the isocontours of positive (thin solid contours) and negative (thin dashed contours) wind stress curl. Initially, the layer thickness is at rest (a) then the wind forcing increases gradually until the wind stress reaches its maximum intensity (c). During this first period, the oceanic response follows roughly the symmetry of the wind forcing Figure 5.4 (b). Anticyclonic and cyclonic oceanic vorticity are generated respectively on the anticyclonic and the cyclonic side of the wind jet. Once the wind forcing has reached its maximum intensity τ_o, an asymmetry in the oceanic response appears. The area of negative vorticity starts to spiral and form a large scale elliptical anticyclone (ellipticity $\varepsilon \sim 0.5$) while on the cyclonic side of the wind jet, the oceanic vorticity patch is stretched and strongly elongated (Figure 5.4 (d)). Thirty days after the wind forcing has reached its maximum intensity (Figure 5.4 (e)) there is no longer any atmospheric forcing and the oceanic layer evolves freely. One month later, we could consider that the oceanic layer reached a final stage with a fully developed mesoscale anticyclone having a quasi-circular shape (ellipticity $\varepsilon \sim 0.19$) and several smaller el-

liptical cyclones. The movie of this dynamical evolution (see supplementary materials) clearly shows that this final anticyclone remains robust and coherent with time while the smaller surrounding structures, especially the elongated cyclones, evolve quickly in time and are deformed in the strain field of the large anticyclone.

In order to quantify more precisely the dynamical characteristics of this large scale mesoscale anticyclone, we use the AMEDA automatic eddy detection algorithm to track and follow the evolution of its size, its intensity and its thickness. The Figure 5.5 shows the various stages of the evolution of the vortex radius R_{max}, its maximal velocity V_{max}, the relative isopycnal displacement λ and the relative vorticity ζ/f of the eddy core in addition with the ellipticity ϵ of the characteristic contour. Almost all of these parameters follow the integral response of the wind stress curl, in other words the anticyclone accumulates the momentum and the energy transfered by the wind. We confirm here that the intensity and the depth of this robust and coherent anticyclone are reached shortly after the wind stops. On the other hand, the ellipticity reaches a quasi-steady state at least one month later (Figure 5.5(f)) which indicates that the axisymmetrization of the wind induced anticyclone is an intrinsic mechanism which is not driven by the wind forcing. The typical size of the eddy seems to be also decorrelated to the wind forcing, since from the very beginning the characteristic radius is around $R_{max} = 45 - 50\,km$ and at the final stage it is estimated to be at $R_{max} = 46\,km$ which is close to the width $W = 40\,km$ of the wind jet. All the dynamical parameters of this specific wind induced anticyclone, namely its vortex Rossby number $Ro = 0.07$ and its Burger number $Bu = 0.08$, are in correct agreement with the robust mesoscale Ierapetra eddies that have radii two or three times greater than the deformation radius R_d (Ioannou et al., 2017).

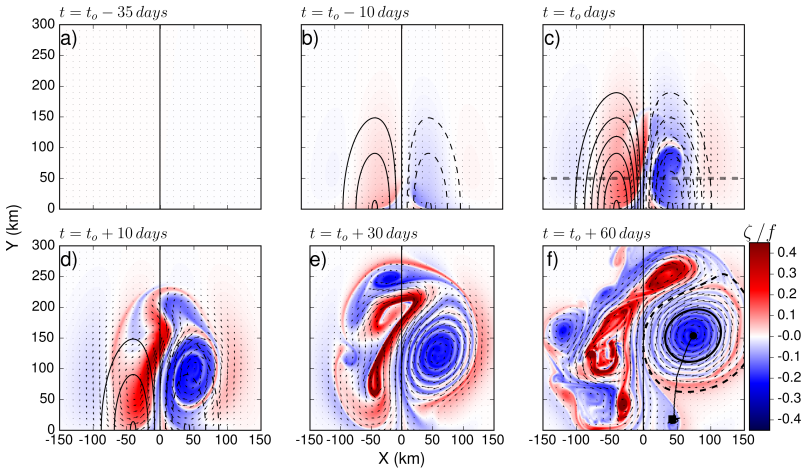

Figure 5.4: *Evolution of the relative vorticity fields ζ/f (colors) of the ocean surface forced by a symmetric wind having the following characteristics $(W, L) = (40, 100)\,km$, intensity $\tau_o = 0.4\,Nm^{-2}$ and duration $T_o = 10$ days. The black contours indicate the location of the negative (dashed contours) and the positive (solid contours) wind stress curl applied in the top of the ocean layer. The characteristic contour (solid) and the last closed streamline (dashed), computed with AMEDA algorithm are shown for the final anticyclone in panel (f). Section positioned at a distance $y = 50\,km$ away from the maximum forcing is represented with the dashed line in panel (c).*

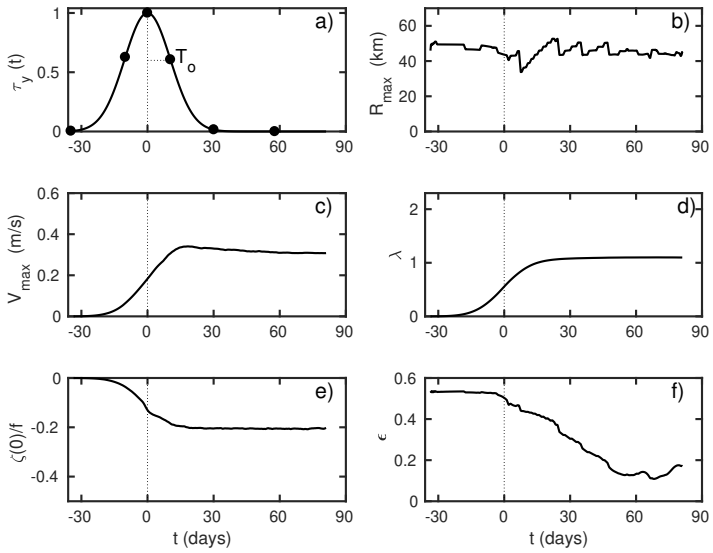

Figure 5.5: *(a) Temporal variation of the wind forcing Eqn.(9) for a characteristic time $T_o = 10\,days$. The evolution of the dynamical characteristics of the large anticyclone, computed by the AMEDA algorithm, are shown in the panels (b) radius R_{max} (km), (c) velocity V_{max} (m/s) d) Maximum isopycnal displacement λ e) relative vorticity and f) ellipticity ε.*

Cumulative impacts of the wind forcing and its duration: the wind forcing parameter

During the first days of the wind forcing (Figure 5.4) the oceanic response follows the spatial pattern of the surface wind stress curl. As far as we consider seasonal wind variations, which evolve slowly (i.e. $T_o^{-1} \ll f$), we assume a quasi-steady response of the surface oceanic layer and use the steady Ekman pumping theory (Ekman, 1905; Stern, 1965). The local wind stress curl will drive horizontal divergence and convergence of the Ekman transport and induce a vertical Ekman pumping velocity W_E. The cumulative effect of the Ekman pumping leads to an isopycnal displacement η_E that is directly proportional to the wind stress intensity τ_o and its characteristic duration T_o while it is inversely proportional to the width W of the wind jet (Eqn.(13)).

$$\eta_E = \int_0^t W_E \, dt = \int_0^t -\frac{1}{\rho} \nabla \times \left(\frac{\boldsymbol{\tau}}{f} \right) dt \tag{13}$$

In order to take into account the relative vorticity of the oceanic current, Stern (1965) derives a non-linear relation to estimate the Ekman pumping induced by strong wind shears. The isopycnal displacement induced by the cumulative wind forcing is then given by the following relation

$$\eta_S = \int_0^t W_E \, dt = \int_0^t -\frac{1}{\rho} \nabla \times \left(\frac{\boldsymbol{\tau}}{f + \zeta} \right) dt \tag{14}$$

where $t = t_0$ is the beginning of the wind forcing, $\tau = (\tau_x, \tau_y)$ is the wind stress vector, ρ the density of water, f the Coriolis parameter and ζ the flow vorticity. This means that the Ekman transport will be enhanced in regions of anticyclonic vorticity and reduced in regions of cyclonic vorticity, already introducing an asymmetry in the ocean's response.

At the initial stage of the wind forcing, before the formation of the non-linear dipole, we can assume that the wind jet will induce a unidirectional response in the oceanic layer. In other words, the wind jet will first induce an oceanic jet that ultimately destabilizes and generates a symmetric or asymmetric dipole. The Figure 5.6(a) compares for the case shown in Figure 5.4, the isopycnal displacements $\eta_{E,S}$ predicted by the linear and non-linear Ekman pumping (i.e. Eqn.(13) and Eqn.(14)) with the results of the RSW model. Since, in all of our simulations, the core of the initial dipole is formed $40-60\,km$ away from the coast, we estimate the isopycnal displacement at the distance $y = 50\,km$ (dashed line in Figure 5.4 (c)). Both the isopycnal displacement $\eta(x)$ and the cross shore geostrophic velocity $v_g(x) = \frac{g^*}{f}\partial_x\eta$ are plotted at $t = 0$ when the wind jet reached its maximum intensity. The relative isopycnal displacements $\lambda = max(\eta)/H$ are quite large with an amplitude of 50% both in the cyclonic and the anticyclonic side. These values are accurately predicted by the steady Ekman pumping theory even if the standard Ekman formula (Eqn.(13)) slightly overestimates the displacement for the cyclonic part while the Stern formula slightly overestimate the displacement for the anticyclonic part. The numerical model confirms that the isopycnal displacement induced by the Ekman pumping is geostrophically balanced and that the cross shore velocities match the geostrophic velocity v_g (Figure 5.6(b)). The Rossby number of the oceanic jet is quite small $Ro_{jet} = \dfrac{max(v)}{fW} \simeq 0.1$. Hence, the non-linear effects of the Ekman pumping are negligible and therefore both Ekman and Stern predictions remain close, with errors less than 10%.

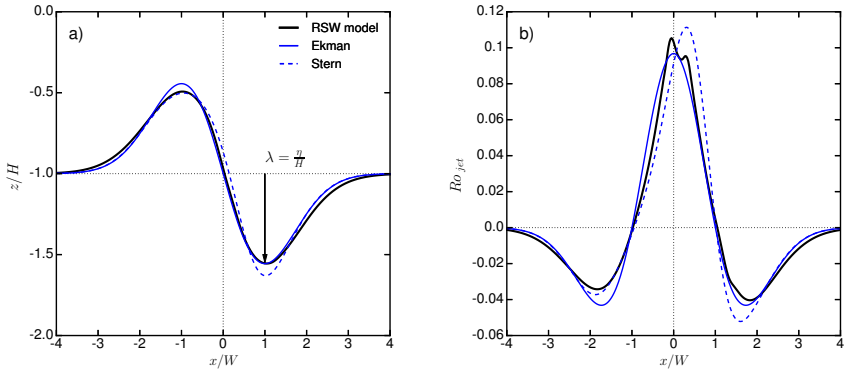

Figure 5.6: *Relative isopycnal displacements $\eta(x)/H$ (a) and dimensionless cross shore velocities $v(x)/fW$ (b) of the oceanic jet induced by the wind jet at $y = 50\,km$ when the wind forcing is maximum ($t = 0$). The maximum wind forcing intensity is $\tau_o = 0.4\,N\,m^{-2}$ and the characteristic duration $T_o = 10$ days as in Figure 5.4. The values of the RSW model (black line) are compared to the predictions of the steady Ekman pumping theory of Ekman (blue solid line) and Stern (blue dashed line).*

Since the initial response of the ocean to this seasonal wind variation is mainly driven by the Ekman pumping formula Eqn.(13) we can use the later to build a wind forcing parameter that quantifies the intensity of the oceanic response to the orographic wind jet. If we use the Eqn.(9) (with $c = 1$) for the wind stress in Eqn.(13) while considering that the wind forcing starts approximately at $t_0 = -3\,T_o$ we get:

$$\eta_E(x) = \int_{-3T_0}^{0} -\frac{1}{\rho f}\,\partial_x \tau_y\, dt = \frac{\tau_o}{\rho f W^2}\, x e^{-\frac{1}{2}(x/W)^2} \int_{-3T_o}^{0} e^{-\frac{1}{2}(t/T_o)^2}\, dt \simeq \frac{\tau_o T_o}{\rho f W^2}\, x e^{-\frac{1}{2}(x/W)^2} \int_{-\infty}^{0} e^{-\frac{1}{2}\xi^2}\, d\xi \tag{15}$$

where $\xi = t/T_o$ is a dimensionless variable. Since the maximal isopycnal displacement is found at $x \simeq \pm W$, we obtain:

$$\lambda = \frac{max(\eta)}{H} \simeq \frac{\tau_o T_o}{\rho f H W} \sqrt{\frac{\pi}{2e}} \tag{16}$$

We therefore introduce the dimensionless wind forcing parameter

$$\gamma = \frac{\tau_o T_o}{\rho f H W} \tag{17}$$

which quantifies the relative amplitude of the isopycnal displacement induced by the wind jet. We then investigate a wide range of parameters varying either the wind intensity τ_o or its characteristic duration T_o. We plot, in Figure 5.7 for various wind forcing τ_o and various duration T_o, the maximum (positive) and minimum (negative) isopycnal displacement reached when the wind stress is maximum at $t = 0$. Positive (negative) isopycnal displacement refers to the anticyclonic (cyclonic) side of the oceanic jet flow. The black circles correspond to simulations performed with constant duration $T_o = 10\,days$ but variable wind stress intensities τ_o, conversely open white squares illustrate simulations performed with constant intensity $\tau_o = 0.3\,N\,m^{-2}$ but various duration T_o. This graph confirms the linear relation between the dimensionless wind forcing parameter γ and the maximum isopycnal displacement λ of the surface oceanic layer. In agreement with the Ekman (Eqn.(13)) or the Stern (Eqn.(14)) formula, finite values of λ are obtained when γ is around unity. Large values of γ correspond to strong wind intensity or long wind forcing duration. We also estimate the Rossby number of the oceanic jet $Ro_{jet} = \dfrac{V_{jet}}{fW}$ induced by the Etesian wind forcing.

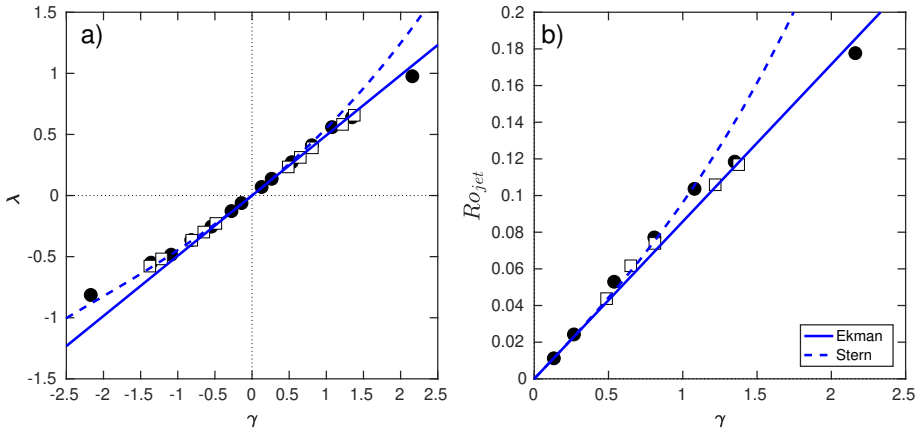

Figure 5.7: *a) Maximum isopycnal displacement λ and b) Rossby number of the oceanic jet Ro_{jet} reached at $t = 0$ (when the wind forcing is maximum) as a function of wind forcing parameter γ for various simulations. The black circles correspond to simulations performed with constant duration $T_o = 10\,days$ while open square correspond to a constant wind stress $\tau_o = 0.3\,N\,m^{-2}$.*

Once the maximum wind forcing is reached, the wind amplitude decreases slowly and after $t = 3\,T_o$ the oceanic flow evolves freely. The destabilization of the oceanic jet

leads to the formation of a free dipole which is more or less symmetric and propagates offshore. We illustrate in Figure 5.8 the end state ($t = 6\,T_o$ days after the maximum forcing) of the full non-linear flow evolution for different wind forcing parameters. To track and quantify the dynamical contours of the cyclonic and anticyclonic eddy of each dipole, we use the AMEDA eddy detection and tracking algorithm (Le Vu et al., 2018). The sea surface height and the characteristic contours (i.e. the streamline corresponding to the maximum eddy velocity) of these dipolar structures are plotted Figure 5.8.

For relatively low value of the forcing parameter $\gamma < 0.2$, corresponding here to a maximum wind forcing lower than $7\,m\,s^{-1}$, a quasi-symmetric dipole is formed. When the wind forcing parameter becomes finite ($\gamma > 0.6$) the asymmetry of the dipole becomes significant with a robust quasi-circular anticyclone and a strongly elliptical cyclone. If the shape of the anticyclone remains unchanged the cyclonic partner is often stretched and deformed by the strain field of the anticyclone and, for the most intense cases, it could even split in two or three smaller cyclones (Figure 5.8(f)). Hence, when the wind jet is strong enough, in other words when γ is around unity, a large and robust anticyclone is formed instead of a symmetric dipole.

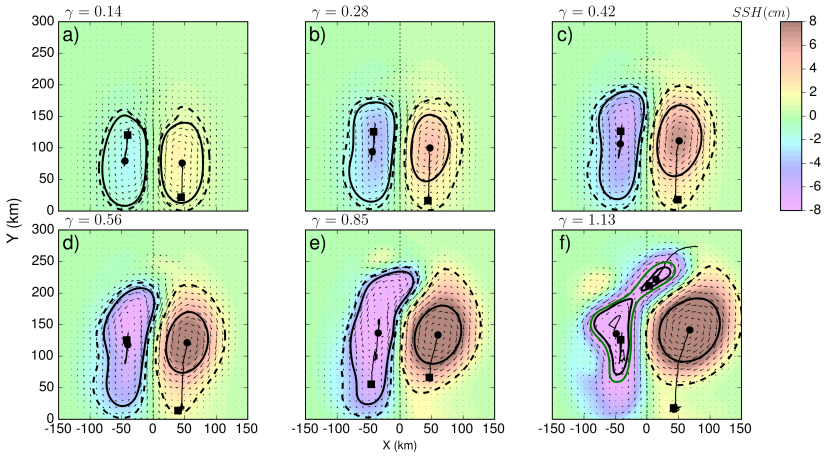

Figure 5.8: *Snapshots of oceanic response to symmetric transient wind forcing for different wind stress intensities a)* $\tau_o = 0.05\,Nm^{-2}$ *b)* $\tau_o = 0.1\,Nm^{-2}$ *c)* $\tau_o = 0.15\,Nm^{-2}$ *d)* $\tau_o = 0.2\,Nm^{-2}$ *e)* $\tau_o = 0.3\,Nm^{-2}$ *f)* $\tau_o = 0.4\,Nm^{-2}$*. These sea surface heights (SSH) are shown 60 days after the maximum forcing occurs. The trajectories of the eddy centers are plotted with a black line. Black square indicates the beginning of each trajectory.*

In order to investigate how the wind forcing impacts the dynamical characteristics of the final eddies which are formed, we plot their dimensionless numbers as a function of the wind forcing parameter γ in Figure 5.9 and Figure 5.10, for the anticyclones and cyclones respectively. All the parameters associated to the eddy intensity, such as the vortex Rossby number Ro, the isopycnal displacement λ and the relative vorticity $\zeta(0)/f$ increase with γ. The strength of the initial Ekman pumping controls the intensity of the final eddies that remain once the wind forcing is over. However, unlike the initial oceanic jet, the intensity of the final anticyclones (the Rossby number and the relative core vorticity) saturate for finite values of γ. On the other hand, the Burger number $Bu = \left(\dfrac{R_d}{R_{max}}\right)^2$ follows a very different behavior. When the wind forcing is low, the characteristic eddy radius R_{max} is fixed by the width of the wind jet $W = 40\,km$. Since, the later is large in comparison with the deformation radius $R_d = 13\,km$, the Burger

number is small and about $\left(\frac{R_d}{W}\right)^2 \simeq 0.1$. Hence, the amount of potential energy contained in the anticyclonic (or cyclonic) eddies is much greater than the kinetic energy. As the wind forcing parameter γ increases, the radius of the vortex increases slightly and the corresponding Burger number decays. Therefore, the isopycnal displacements λ could reach finite values even if the Rossby numbers remain moderate. This is a source of asymmetry between the cyclonic and the anticyclonic part of the wind induced dipole. There is indeed a physical limitation to the isopycnal displacement of cyclonic eddies. When λ reaches unity, the thickness of the surface layer will vanish in the core of a cyclonic eddy while there is no limitation for the anticyclonic structure. The anticyclonic core could strongly thicken if the lower layer is deep enough. This asymmetry is confirmed by the Figure 5.10(c) where the isopycnal displacements in the core of the anticyclones always exceed those of the cyclones. The isopycnal displacement λ is larger than unity only in the core of anticyclones for finite values of the wind forcing parameter. If we increase the wind forcing parameter above $\gamma = 0.6$ the upper layer thickness will almost vanish in the cyclonic eddies and numerical instabilities (i.e. shocks) will occur due to large values of the local Froude number. This is one of the main limitations of the rotating shallow-water model.

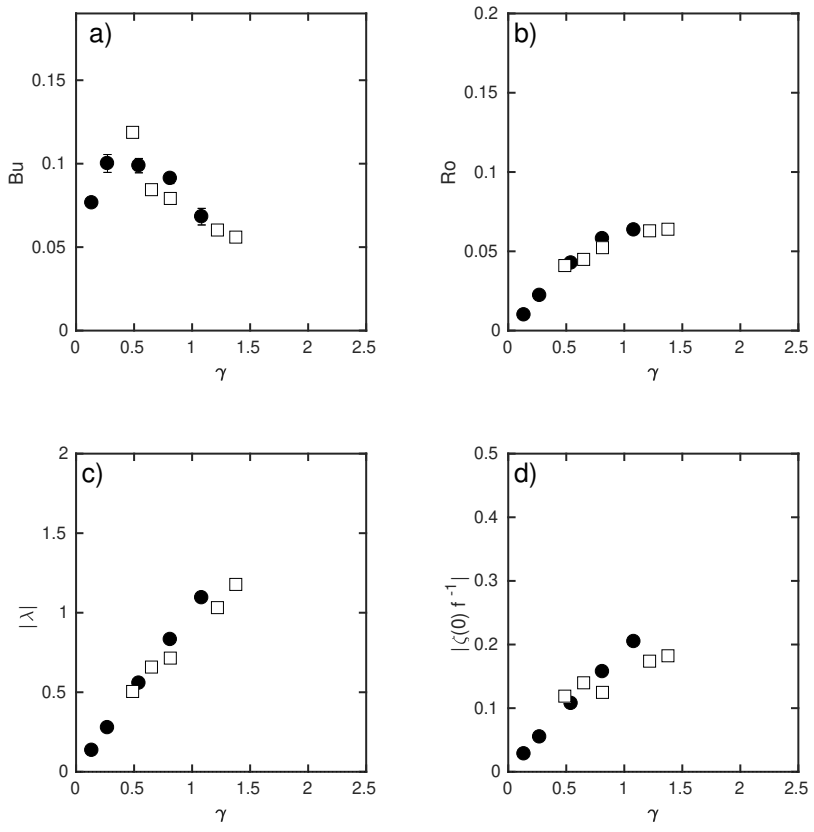

Figure 5.9: *Dynamical characteristics of the final anticyclonic eddies estimated according to the AMEDA algorithm. The Burger number $Bu = (R_d/R_{max})^2$ (a), the vortex Rossby number $Ro = V_{max}/(fR_{max})$, the isopycnal displacement λ (c) and relative core vorticity $\zeta(0)/f$ (d) are plotted for various values of the wind forcing parameter γ. As for Figure 5.7 the black circles correspond to simulations performed with constant duration $T_o = 10\,days$ while open square correspond to a constant wind stress $\tau_o = 0.3\,N\,m^{-2}$.*

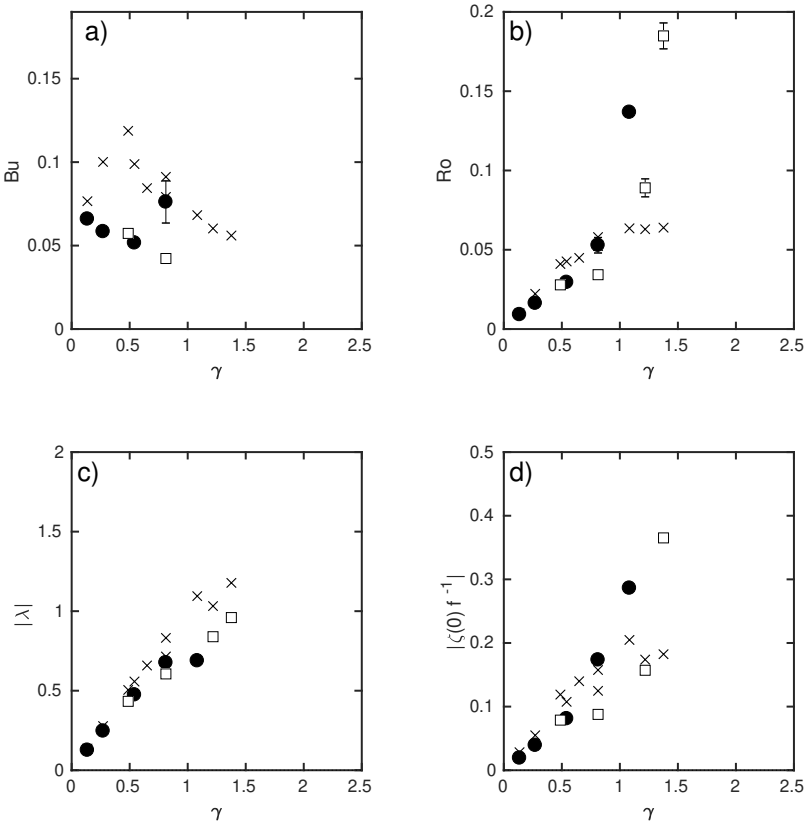

Figure 5.10: *Same as Figure 5.9 but for the cyclonic eddies. For comparison, the dynamical parameters of the anticyclonic eddies are plotted with gray crosses.*

Asymmetric forcing

We have seen, in the previous section, that a symmetric wind jet could induce an asymmetric dipole and, for finite value of γ, the final stage could lead to a large and robust anticyclone having a quasi-circular shape. Although the climatological analysis of the Etesians (see Figure 5.3) shows that this specific orographic wind jet is not symmetric but asymmetric. The anticyclonic wind shear is on average twice as strong as the cyclonic shear and we naturally expect an asymmetric response of the oceanic surface layer. We therefore compare in Figure 5.11 the oceanic response to a symmetric and an asymmetric wind jet having the same anticyclonic wind stress curl. The wind stress intensity is set to $\tau_o = 0.4\,N\,m^{-2}$ with a typical duration fixed by $T_o = 10$ days and we set the parameter $c = 2$ (Eqn.(11)) for the asymmetric wind jet to mimic the Etesian winds. Because, the cyclonic shear is weaker, the cyclonic structure generated in the oceanic layer is significantly weaker for the asymmetric wind jet in comparison with the symmetric one. As for the symmetric case, coherent cyclonic eddies did not form and the weak cyclonic filaments are stretched and elongated. The reduction of the cyclonic wind shear also impacts the formation of the anticyclonic eddy. The final anticyclone is more circular (ellipticity $\epsilon = 0.08$) and slightly smaller ($R_{max} \backsimeq 39\,km$) than in the symmetric wind forcing case where $\epsilon = 0.16$ and $R_{max} \backsimeq 46\,km$. Moreover, the vortex Rossby number of the anticyclone is 13% stronger. The cyclonic part of the dipolar structure being less intense, this reduces the strain applied by the cyclone on the anticyclone and therefore the ellipticity of the latter. Besides, the self-advection of the asymmetric dipolar structure is also reduced and the anticyclonic eddy stays closer to the coast and the stronger winds, which amplifies its intensity and limits its radial extension.

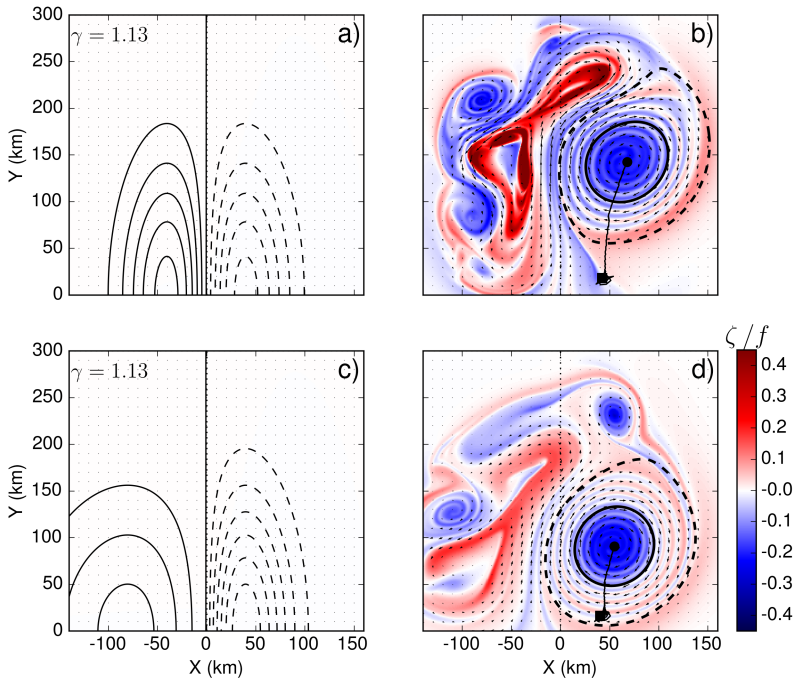

Figure 5.11: *The symmetric and asymmetric wind stress curl applied to the shallow-water flow are plotted in the upper and lower left panels, (a) and (c) respectively. The cyclonic wind stress curl is two times smaller for the asymmetric (c) than for the symmetric case (a). The wind stress intensity is* $\tau_o = 0.4\,Nm^{-2}$ *and the forcing duration* $T_o = 10$ *days. The ocean responses to symmetric and asymmetric wind forcing are plotted in panels (b) and (d) respectively. These relative vorticity fields* ζ/f *correspond to the end state* $t = 60$ *days after maximum forcing occurs.*

We also investigate the ocean response to increasing values of the wind forcing parameter γ. For such asymmetric wind forcing, the main oceanic response is a quasi-circular anticyclone which stays close to the coast and a linear trend is found between the eddy intensity (i.e. Ro, λ and $\zeta(0)/f$) and the wind forcing Figure 5.12. Since, the cyclonic wind shear is weaker, the thickness of the upper layer will vanish in the cyclonic vorticity core for a stronger wind jet and we could reach higher intensity of the wind stress, up to $\tau_o = 0.7\,Nm^{-2}$, without numerical instabilities. The core vorticity of the anticyclonic eddy could then reach much higher values and will therefore satisfy the cyclogeostrophic balance. On the other hand, the eddy radius is weakly affected by the wind forcing and seems to be mainly controlled by the width W of the anticyclonic wind shear.

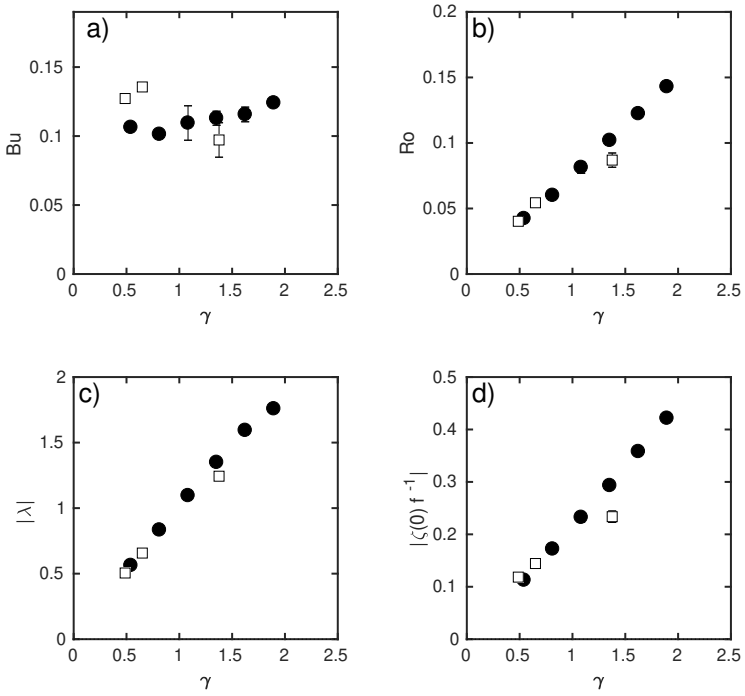

Figure 5.12: *Evolution of the Burger number Bu (a), the Rossby number Ro (b), the isopycnal displacement parameterλ (c) and the relative core vorticity ζ/f (d) as a function of the wind forcing parameter γ. These dynamical characteristics are estimated with the AMEDA algorithm for the final eddy state more than 30 days after the end of the wind forcing. As for Figure 5.9 and Figure 5.10 the black circles correspond to simulations performed with constant duration $T_o = 10\,days$ while open squares correspond to a constant wind stress $\tau_o = 0.3\,N\,m^{-2}$.*

5.5 Intensification of a pre-existing anticyclone by the Etesian wind

Our previous work on the dynamical characteristics of IEs over a 22 years period (Ioannou et al., 2017) revealed that these large mesoscale anticyclones could be re-amplified, or in other words that they could gain a large amount of energy, one year after their formation. This intensification process coincides with the period of strong Etesian forcing. During such re-amplification stage, the intensity of the anticyclone could double in less than 4 months while keeping its mean radius almost unchanged. For instance, the Rossby number of the IE98 varies from $Ro = 0.08$ in May 1999 to $Ro = 0.16$ in September 1999 (Ioannou et al., 2017). Similar re-amplification events were detected four times from 1993 to 2014.

In order to verify that such re amplification phenomenon can indeed be induced by the Etesian wind forcing, we investigate the effect of the asymmetric wind jet ($c = 2$) on a pre-existing anticyclone. The latter is an isolated axis-symmetric Gaussian vortex, identical to the IE98, with an initial radius $R_{max} = 40\,km$ and $Ro = 0.08$. The anticyclone is located $100\,km$ away from the coast at the position of the maximum anticyclonic wind stress (i.e. $x = W$). The Figure 5.13 shows the dynamical evolution of this initial anticyclone forced by a wind jet intensity of $\tau_o = 0.7\,Nm^{-2}$. The total duration of this varying asymmetric wind jet is about 60 days when $T_o = 10\,days$ (see Figure 5.5 (a)). During the initial stage of the forcing, the pre-existing anticyclone tends to roll up, around its center, the oceanic jet induced by the wind. According to Figure 5.13(c) two bands of cyclonic and anticyclonic vorticity, spiral around the initial eddy core. The position of the latter is not modified even if its shape tends to be slightly elongated along

the wind jet. Later on, after $30 - 40\,days$ the negative vorticity filament tends to merge into the anticyclonic eddy core while the positive vorticity filament, which stays at the eddy periphery, splits into several smaller cyclonic structures Figure 5.13(e). A month after the wind stopped (Figure 5.13(f)), we get an intense and large, quasi-steady anticyclone on the right side and a mix of smaller unsteady structures of both signs on the left side of the initial wind jet. This specific wind forcing, which mimics the mean seasonal wind forcing, clearly re-amplifies the pre-existing anticyclone. The vorticity in the eddy core doubles from $\zeta(0)/f = -0.27$ to $\zeta(0)/f = -0.6$ while the vortex Rossby number increases by factor of 2.25 and reaches the final value of $Ro = 0.18$ (Figure 5.14). The ellipticity of the anticyclone strongly varies during the wind forcing, but at the final state it recovers its initial value corresponding to a quasi-circular ($\epsilon = 0.015$). The steepness parameter α changes from a Gaussian velocity profile ($\alpha = 2 - 2.2$) to a more wide profile after the wind forcing reaches its maximum intensity (Figure 5.14(f)) and reaches a steepness parameter of $\alpha = 1.1$ at the final state. More surprisingly, the radius of the vortex remains almost constant during the total simulation time slightly decreasing by 4% at the final state, reaching a radius of $R_{max} = 36\,km$. The characteristic eddy radius has the same scale with the applied wind forcing width and is the reason why no significant change in the eddy size is observed. This idealized example shows that the shape of a mesoscale anticyclone will be weakly affected by a local wind jet forcing while its intensity could strongly increase. Such dynamical process is in correct agreement with the previous analysis of remote sensing AVISO/DUACS data set of Ioannou et al. (2017). Hence, the re-amplification of an IE can be explained by the seasonal orographic wind jet when the latter occurs over the pre-existing anticyclone. Conversely, if a pre-existing cyclone is located below the positive wind shear, the initial eddy will be rapidly stretched and deformed, while an anticyclonic eddy will form on the right side of the wind jet (i.e. the negative wind-stress curl area). This example shown in section 5.8 confirms the asymmetric response of mesoscale oceanic eddies to such orographic wind jet. Only large mesoscale anticyclones remain robust, quasi-circular and could gain energy from the Etesian winds in the southeast of Crete.

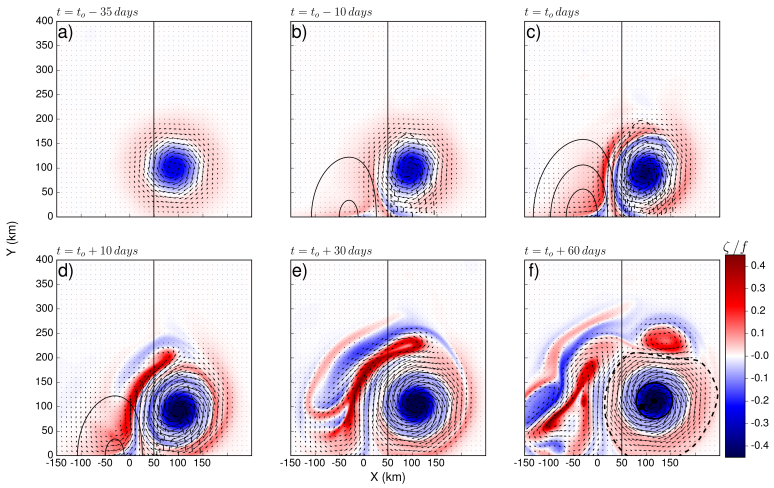

Figure 5.13: *Evolution of the relative vorticity fields ζ/f (colors) of an initial Gaussian anticyclone ($Ro = 0.08$ and $R_{max} = 40\,km$) forced by a asymmetric wind jet ($c = 2$) having the following characteristics $(W, L) = (40, 100)\,km$, intensity $\tau_o = 0.7\,Nm^{-2}$ and forcing time $T_o = 10$ days. The black contours indicate the location and the intensity of the negative (dashed contours) and the positive (solid contours) wind stress curl applied in the top of the ocean layer. The characteristic contour (solid) and the last closed streamline (dashed), computed with AMEDA algorithm are shown for the final anticyclone in panel (f).*

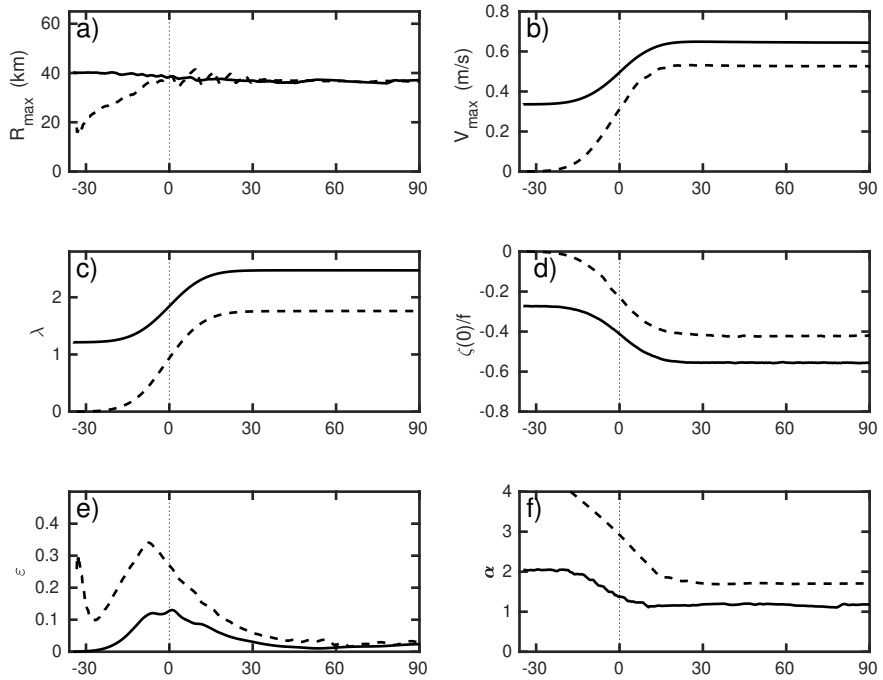

Figure 5.14: *Evolution of the dynamical parameters corresponding to the anticyclonic eddy of (Figure 5.13). The characteristics eddy radius R_{max} (km) (a), the maximal velocity V_{max} (b), the relative isopycnal displacement λ (c), the dimensionless core vorticity $\zeta(0)/f$ (d), the eddy ellipticity ϵ (e) and the steepness parameter α (f) of the mean velocity profile (Eqn.(8)) are computed by the AMEDA algorithm.*

5.6 Summary and conclusions

In this study we investigated with a reduced gravity model, the mean oceanic response to a seasonal wind jet that varies slowly over several weeks or months. Motivated by the repeating formation and the intensification of the Ierapetra eddies in the southeast of Crete (Mkhinini et al., 2014; Ioannou et al., 2017), we study the relation between the intensity and the duration of the wind forcing and the dynamical characteristics of the wind induced eddies. The spatial structure of the mean wind jet was first established according to climatological wind data in order to mimic the Etesian winds blowing during summer between Crete and Kasos strait.

Even if the climatological wind jet is asymmetric, we started our analysis with a symmetric wind profile to understand the mechanisms responsible for the formation of a single large and intense anticyclone. Indeed, we found that, for a specific range of parameters, the oceanic response to a symmetric wind jet could be a strong asymmetric dipole which leads, when the wind forcing ends, to a single and intense anticyclone. The asymmetry of the oceanic response is mainly controlled by a dimensionless parameter that integrates in time the Ekman pumping. This wind forcing parameter γ quantifies the relative amplitude of the isopycnal displacement induced by the local wind stress curl. It is therefore proportional to the wind jet intensity and its duration but is inversely proportional to its width. Our analysis shows that for a small value of this wind forcing parameter, in other words when the isopycnal displacement remains weak, the oceanic response to a symmetric wind jet is a symmetric dipole. But, when the wind forcing parameter increases and gets close to unity, the isopycnal displacement becomes finite and the oceanic response is strongly asymmetric. This initial asymmetry can be explained by the drastic reduction of the upper oceanic layer for positive wind stress curl which prevents the formation of a large scale cyclone. On the other hand, there is no limit to the thickening of this layer when the wind stress curl is negative. Hence, the first response to an intense wind jet is an asymmetric dipole composed by a robust anticyclone and a strongly elongated cyclonic structure. When the wind forcing stops, this initial asymmetry increases due to the stretching of the cyclonic structure by the large and robust anticyclone. The latter becomes more circular as the initial cyclonic structure often divides into several smaller unsteady cyclones. Similar dynamical behavior was found by (Poulin and Flierl, 2003; Perret et al., 2006a, 2011) who study the stability of oceanic jets or wakes flows. The asymmetry of these unsteady symmetric flows occur in the cyclogeostrophic or the frontal regimes and tend to form large scale and robust anticyclones while the cyclones are stretched and elongated. In our case, the initial dipole induced by the orographic wind forcing can be seen as a localized oceanic jet. Since the width of this initial oceanic dipole is larger than the deformation radius, the Burger number Bu is small and even for moderate Rossby numbers Ro the localized oceanic jet will (i.e. the initial dipolar response) correspond to a frontal regime. Therefore, these two intrinsic mechanisms favor the formation of a mesoscale anticyclone when a large and strong wind jet blows perpendicular to the coast.

In a second step, we use an asymmetric wind jet having an anticyclonic wind shear two times larger than the cyclonic one to mimic the Etesian winds in this area. For this realistic configuration, intense mesoscale anticyclones that satisfy the cyclogeostrophic balance, as the real IE's, could be formed. According to our analysis, the vortex Rossby number of these anticyclones evolve linearly with the wind forcing parameter γ, while the eddy radius remains almost constant and scales as the width of the orographic wind jet. For the strongest wind forcing, the final response of the surface layer correspond to a single large scale and intense anticyclone surrounded by positive vorticity filaments and few sub mesoscale anticyclones. The typical Burger and Rossby numbers of these wind induced anticyclones obtained in our idealized simulations are compared with the most intense annual values of IE anticyclones estimated for several years of re-

mote sensing analysis (Ioannou et al., 2017, 2019) and from the DYNED-Atlas data base which provides 17 years of eddy detection and tracking in the Mediterranean Sea (https://doi.org/10.14768/2019130201.2). The Figure 5.15 shows that the size (i.e. R_{max}/R_d eddy characteristic radius compared with the deformation radius) of the final anticyclones is in good agreement with the observations even if the intensity of the real IE's seems to be somewhat higher that in our numerical simulations. Indeed, we didn't succeed, with the simplified shallow-water model, to reach Rossby numbers higher than $Ro = 0.18$ or negative potential vorticity core (i.e. $\zeta(0) < -f$ in the eddy core) diagnosed by (Ioannou et al., 2017, 2019). More realistic oceanic models which account for the vertical stratification and the mixed layer should be used to study the complex wind eddy interaction and especially the turbulent ageostrophic structures that may emerge in the core of such intense anticyclones (Brannigan, 2016; Brannigan et al., 2017).

Finally, we study how the seasonal variations of the Etesian wind jet impacts the dynamical characteristics of a pre-existing mesoscale anticyclone. In agreement with the remote sensing observations (Ioannou et al., 2017), the anticyclone remains robust and coherent, its intensity increases significantly while its radius hardly varies. The Etesian wind forcing is therefore the main source of the IE's intensification when the pre-existing IE is close enough to the orographic wind jet. Even if several studies (Horton et al., 1994; Fusco et al., 2003; Mkhinini et al., 2014) have suggested that the IEs are forced by the Etesian winds, this paper is the first numerical study which provides a dynamical understanding for the formation of a single Ierapetra anticyclone in the southeast of Crete and explains its possible intensification one year after its formation. The numerical simulations also reveal that a strong submesoscale activity, with unstable filaments and intense cyclones, occurs on the cyclonic side of the wind jet when the Etesian reaches their maximum intensity. The formation of these submesoscale structures is enhanced by the asymmetry of the oceanic response, in other words when the mesoscale anticyclone is strong enough to stir and stretch the cyclonic side of the initial dipole. Unlike the IE's, these submesoscale features cannot be accurately captured by satellite altimetry due to its coarse resolution. Moreover, regional models should also reach a minimum resolution to reproduce accurately these submesoscale patterns that may impact locally the Rhodes gyre during Etesian episodes.

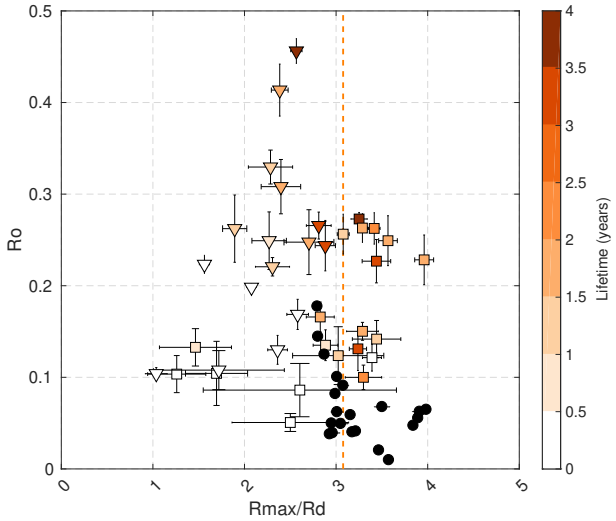

Figure 5.15: *Dynamical characteristics of the Ierapetra anticyclones illustrated with the squares based on (Ioannou et al., 2017) and with triangles from the DYNED-Atlas data base (https://doi.org/10.14768/2019130201.2). The vortex relative size R_{max}/R_d and the vortex Rossby number Ro are plotted during the months were the eddies are more intense. The lifetime of each detected anticyclone is depicted with the different colors. The black circles correspond to the retrieved anticyclones with the RSW model for various simulations. The dimensionless wind forcing scale W/R_d used in the RSW model is illustrated with the orange dashed line.*

5.7 Estimation of the oceanic layer thickness

In order to select a layer thickness that represents the seasonal stratification of the area, we estimate the regional climatological density profile. Argo profiles that cross the Ierapetra area from 2000 to 2015 are selected only if their position was detected outside of the last contour of an eddy based on AMEDA eddy and tracking detection algorithm (Le Vu et al., 2018). Based on these profiles we obtain a mean seasonal density profile that could describe the unperturbed seasonal stratification in the region South-East of Crete (Figure 5.16 (a)). In order to build a two-layer stratification, having the same dynamical properties of a continuous stratification, we solve for the linear eigenmodes of the ocean's vertical structure. The node of the first baroclinic eigenmode fixes the thickness of the upper and the lower layer for the equivalent two-layer system. According to Figure 5.16, the characteristic thickness of the upper layer is estimated $H = 100\,m$.

$$\frac{\partial}{\partial z}\frac{f^2}{N^2}\frac{\partial}{\partial z}\phi_n + \frac{1}{R_d^2}\phi_n = 0$$

with $\dfrac{\partial \phi_n}{\partial z} = 0$ at $z = 0, H$

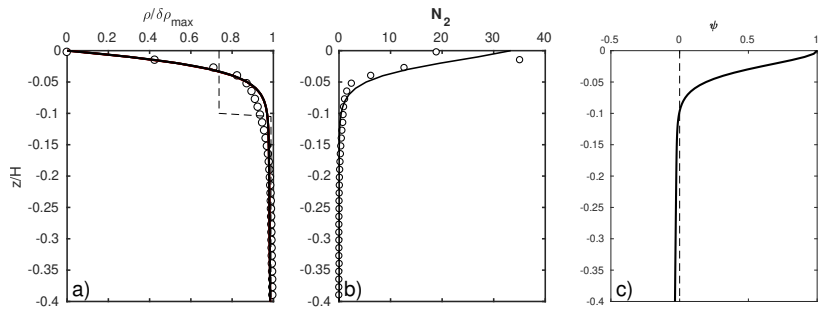

Figure 5.16: *(a) Mean climatological density ϱ profile as computed from ARGO floats that we detected outside from an eddy from 2001-2015 and the associated Brunt-Väisälä frequency in (b). (c) The first mode of the baroclinic structure of the ocean for the region of Ierapetra.*

5.8 Asymmetric wind forcing above pre-existing cyclone

We illustrate in this section the effect of a transient asymmetric wind forcing applied on a pre-existing cyclonic eddy. For that purpose a cyclonic eddy of $R_{max} = 30\,km$ and vortex Rossby number $Ro = 0.05$ is initialized respectively in the positive side of the wind stress curl as shown in Figure 5.17 (left panel). The eddy is subject to an asymmetric wind forcing of intensity $\tau_o = 0.3\,Nm^{-2}$ and duration of $T_o = 10$ days. The non-linear evolution of the flow is depicted in Figure 5.17 (right panel) at time $t = 60$ days, after the maximum forcing has occurred. In the presence of the positive wind stress curl the cyclonic eddy does not retain its shape. At the final state the cyclonic eddy is stretched and elongated in cyclonic filaments. Contrary on the negative side of the wind stress curl as expected a new anticyclonic eddy is formed. Only mesoscale anticyclones could be re-amplified while remaining robust under the influence of a negative wind stress curl.

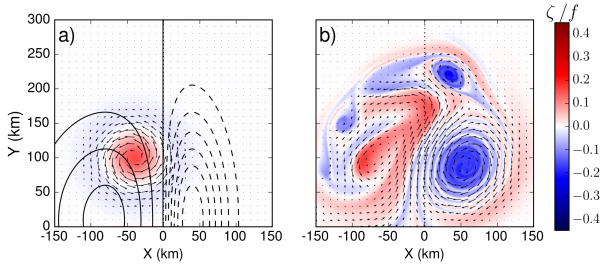

Figure 5.17: *Asymmetric wind forcing with characteristics $(W, L) = (40, 100)\,km$, intensity $\tau_o = 0.3\,Nm^{-2}$ and duration $T_o = 10$ days applied above a cyclonic eddy of initial characteristics $R_{max} = 30\,km$ and Rossby number $Ro = 0.05$ as shown in panel (a) at the time of maximum forcing ($t = 0$). The vorticity fields ζ/f of the oceanic response are illustrated at $t = 60$ days after the maximum forcing in panel (b).*

CHAPTER 6

Conclusions

6.1 Concluding Remarks

In this thesis, we have investigated the dynamical evolution of the mesoscale Ierapetra eddies (IEs) that occur during summer in the Eastern Mediterranean Sea. Satellite observations and AMEDA eddy tracking algorithm were used in order to identify the key dynamical characteristics that describe the anticyclone along the years of evolution. Comparisons were made with in-situ measurements that provided dynamical information on the eddy vertical structure. Moreover, the forcing of the IE's by regional wind forcing was investigated with the help of idealized simulations. Thus, we were able to address several remaining questions for the IEs and their connection with the Etesian wind forcing.

In chapter 2, main questions regarding the eddy recurrent formation, main pathways in the Levantine basin but also their intensity variability were addressed. Over the 22 years, the size, the intensity and the trajectory of each individual l Ierapetra was identified. We found that the IEs eddies recurrently formed over the 22 year period South-East of Crete but they are not steady eddies. They can interact with neighboring structures or interact and merge with IEs of previous years or even prevent the formation of a new one. In total 16 Ierapetra's were identified in the 22 years, while 2002 was the only year where no Ierapetra eddy was detected.

The IEs lifetime or its trajectory could strongly vary from one year to another. They could remain relatively stationary (more than 56% of the time the IEs remained in the Mean climatological position (MDT)) but also drift long distances. Their trajectories were most commonly detected to drift to the South, South-West and West. Most of the Ierapetra eddies survived almost a year but some specific IEs persisted for more than 3 years. AMEDA eddy detection algorithm was able to recover several major merging events between IEs, some of which identified well with previous detections from thermal images (Hamad et al., 2006; Taupier-Letage, 2008).

In regards to the IE dynamical characteristics, we were able to quantify their surface dynamical characteristics during their lifetimes (Ro, Bu, $\zeta(0)/f$). The Ierapetra anticyclones exhibited a "typical evolution" composed by distinct dynamical stages: an initial generation, a maturity stage which corresponds to a maximum intensity during autumn and a decaying phase during winter. The IE size after generation stayed relatively constant and ranged between $R_{max} = 30 - 40km = 3 - 4R_d$. On the other hand, the IEs intensity exhibited strong seasonal and interannual variations. Their estimated velocities ranged from $30\,cm\,s^{-1}$ to almost $1\,m\,s^{-1}$. Furthermore, we found that some specific IEs re-intensify one year after their formation. The intensification of a pre-existing Ierapetra was observed, for the first time, in this study. Such process may double the eddy velocity in less than 3 months. The mean eddy position during intensification stage was less disperse in comparison with the eddy generation suggesting a more localized mechanism that took place. The intensification acts mainly on the eddy tangential velocities ($Ro_g = 0.1 - 0.18$) while the eddy radius remained relatively constant ($Bu = 0.1$). The geostrophic vortex Rossby number of the IEs during maturity and intensification stages frequently exceeding $Ro_g > 0.1$, which indicates that the

cyclogeostrophic balance should be taken into account.

In chapter 3, we evaluated the importance of cyclogeostrophic corrections in the whole Mediterranean Sea. An optimized iterative method was applied directly in the geostrophic velocity provided by the standard AVISO/DUACS products. The performance of the iterative method was first tested on circular but also elliptical idealized eddies to retrieve with best accuracy the cyclogeostrophic components of the velocity field. A range of idealized anticyclones with different parameters (R_{max}, Ro, α, ϵ) were investigated. We found that for mesoscale anticyclones with $Ro_g > 0.1$, omitting cyclogeostrophic corrections will underestimate their intensity by 30%. The application of cyclogeostrophy in the total MED revealed that areas prone to frequent corrections were areas of high mesoscale activity and especially the Alboran and the Ierapetra region. The IE were among the anticyclones that required strong ($\|V_c - V_g\| > 0.5\, ms^{-1}$) and frequent (>3 years) corrections. When accounting for cyclogeostrophy, the IEs core vorticity could reach finite values $\zeta(0)/f = -1$.

Among the years of our study, there were few campaigns (EGYPT-EGITTO, BOUM and PERLE) that crossed an Ierapetra allowing a comparison between in-situ measurements and satellite observations. Quite surprisingly, both EGYPT-EGITTO and BOUM campaign crossed the same Ierapetra eddy IE05 in different years and different dynamical stages of intermediate intensity. Both in-situ measurements showed a systematic underestimation of the eddy surface velocities. In 2005, the estimation of the eddy velocities from few drifters trapped in their core showed good agreement with the cyclogeostrophic estimations. However, during BOUM campaign in 2008, VMADCP measurements that crossed IE05 core showed $\sim 60\%$ underestimation of the eddy surface geostrophic velocities. At that time the cyclogeostrophic corrections could not provide sufficient enhancement on the eddy intensity given the initial low geostrophic fields ($V_g < 0.5\, m/s$). More recently, in 2018 during PERLE/PROTEVS campaign, VMADCP measurements that crossed the Ierapetra eddy IE18 core compared well with the cyclogeostrophic velocity fields (error less than 13%) while the geostrophic approximation induced an underestimation of the Rossby number (error 40%).

Moreover, in-situ measurements showed that the Ierapetra eddy velocities could have a deeper vertical extend. During BOUM campaign, the IE05 significant velocity that exceeded $20\, cm/s$ extended down to $300\, m$ depth. VMADCP measurements showed that the IE05 subsurface signal was stronger than the surface one by $16 - 25\%$. Also, in winter 2017, the investigation of the IE16 vertical structure from few Argo floats confirmed the strong isopycnal deviations of the eddy core. In chapter 4, we were able to quantify the temperature, salinity and density anomalies associated to the Ierapetra anticyclone. The eddy density anomaly was estimated to reach $\Delta\rho = -0.5\, kg\, m^{-3}$ difference with the surrounding environment. Moreover, we take into account the eddy ellipticity for the 3D reconstruction of the eddy velocities. Argo floats revealed that the MLD varies along the eddy diameter and could reach at least $200\, m$ in the eddy core. Such horizontal variation of the surface mixed layer suggested that the eddy modify locally the air-sea interactions.

One of the main goals of this study was to identify if the regional wind forcing could be the main mechanism of the IEs formation. The IEs have been already proposed to be wind-forced. Although, so far only a correlation between the formation area of the IEs and the area of negative wind stress curl caused by the Etesian forcing confirms this hypothesis (Mkhinini et al., 2014). Our analysis showed that not only the period of generation but also the intensification of the IEs coincided with the period of the Etesian wind forcing.

Motivated by these correlations, in chapter 5 a shallow water model was used in order to evaluate the capacity of the negative wind stress curl, occurring in the South-East corner of Crete, to generate oceanic eddies. Idealized numerical simulations were used to response of the ocean to the Etesian wind forcing. We used climatological wind

data to build an idealized mean wind jet that could mimic the orographic wind forcing between Crete and Kasos strait. The oceanic response to this transient orographic wind jet was studied for two cases. A symmetric wind forcing jet and an asymmetric one. We began the analysis with a symmetric gaussian wind forcing and then we switched to a more realistic asymmetric wind and we compare the response of the ocean to these two different wind forcing. The effect of the orographic wind forcing was characterized by few dimensionless numbers; the wind forcing intensity Ro_W, the Burger number of the forcing Bu_W and the wind evolution t_W. Moreover, we defined the wind forcing parameter $\gamma = \frac{Ro_W}{t_W} = \frac{\tau_o T_o}{\rho f H W}$ which quantifies the integrated Ekman pumping on the upper oceanic layer induced by the orographic wind forcing.

We have seen, for the specific range of parameter corresponding to the Etesians, that this wind jet favored the formation of coherent mesoscale anticyclones. Instead of a symmetric dipole, we get a strong and coherent anticyclonic eddy surrounded by smaller elliptical cyclones. The intensity of the generated anticyclone depended linearly on the wind forcing parameter. Its characteristic size R_{max} remained almost independent of the wind forcing intensity but is mainly driven by the width W of the wind forcing.

Furthermore, apart from generation, the orographic wind jet was able to re-intensify pre-existing eddies. The negative wind stress curl could intensify a pre-existing anticyclone without affecting the eddy coherence. Conversely, cyclonic eddies were totally deformed in the presence of a positive wind stress curl. The core vorticity of the anticyclonic eddies in these numerical simulations reached finite values $\zeta(0)/f < -0.6$ but did not reach the most intense negative vorticity $\zeta(0)/f < -1$ estimated by the satellite observations. We suspect that the RSW model plays here a limiting factor.

Based on these idealized simulations, the orographic wind jet was found to be a major mechanism of formation of meso-scale anticyclones in the southeast of Crete. The emergence of a single anticyclone depends on few dynamical parameters. First the asymmetric shape of the orographic wind jet, that enhanced the negative wind stress curl region, a priori favored the formation of anticyclones. On the other hand, we have seen that a symmetric orographic wind jet could also trigger an asymmetric oceanic response. In that case the oceanic response was controlled by both the γ parameter and the Burger number of the wind forcing jet $Bu_W = 0.1$. In that case, the width of the forcing W remained larger than the radius of deformation ($W > R_d$). When the eddy radius is larger than the deformation radius R_d the isopycnal displacement become large in comparison with the layer thickness. For cyclones, the ocean surface is a strong constrain for upwelling of the isopycnals. Conversely, for anticyclones, the isopycnal downwelling is unbounded for the reduced gravity shallow-water as well as for the realistic ocean with a bathymetry that extends down to $4000\,m$ depth. Therefore, for high γ values, when the isopycnal displacements are strong enough, a single anticyclone could emerge while the corresponding cyclone is elongated and deformed. At low γ values, the oceanic response to the symmetric orographic jet was found symmetric, resulting in the formation of an oceanic dipole. The cyclonic vorticity in the symmetric wind forcing case caused higher drifting speeds of the anticyclone as a result of the cyclone/anticyclone advection. Contrary, on the asymmetric wind forcing case, the anticyclones were found more circular and quasi-stationary as a result of the suppressed cyclonic circulation. For both cases, the γ parameter appeared to be the major parameter that control the intensity of the formed anticyclones.

To summarize, the analysis brought knew elements in the dynamical knowledge of the Ierapetra anticyclones. For the first time the Ierapetra eddies were quantified for more than 20 years. Moreover, the Etesian orographic wind forcing was identified as the main formation mechanism of the IE's. We filled the gap in the bibliography regarding the lack of information for the Ierapetra eddies intensities. The IEs are found among the strongest anticyclones ($Ro = 0.2 - 0.3$, $Bu = 0.1$) in the MED that satisfy the cyclogeostrophic balance and undergo strong seasonal and interannual variations.

These eddies experience strong isopycnal displacements in their core and therefore are able to trap water for long-time periods. One of the most important outcomes of this study was that the IEs could re-intensify. Our analysis confirms that both the generation and also the intensification of the IEs result from the Etesian orographic wind jet. The width, the intensity and the duration of the orographic wind forcing control the generation of long-lived mesoscale anticyclones having the same characteristics of IE's, namely $Bu = 0.1$ and $Ro = 0.05 - 0.18$. The asymmetric shape of the Etesian orographic wind jet can explain the formation of a single anticyclone south-east of Crete. Strong γ values that characterize the Etesians and the Burger number of the forcing $Bu_W = 0.1$ are found also necessary preconditions that enhance the prevalence of anticyclones. For the case of the Etesian regime ($Ro_W = 0.1 - 1$, $Bu_W = 0.1$, $t_W \gg 1$) both conditions were met. Thus, the isolated localized-negative wind stress curl is enough to explain the emergence of an anticyclonic eddy like Ierapetra but also explain their dynamical behavior, both generation and intensification.

6.2 Perspectives

There are more aspects that arise from this dissertation and require further investigation. Our analysis focused on the particular dynamics of the Ierapetra eddy and on the response of the orographic wind jet for the specific range of parameters that described the Etesian regime ($Ro_W = 0.1 - 1$, $Bu_W = 0.1$, $t_W \gg 1$). Although the analysis could have universal aspects that remain to be unraveled. The orographic wind jet was found a contributing mechanism in the prevalence of anticyclones in the ocean while its effect in the ocean surface has been only discussed in few studies (McCreary et al., 1989; Chang et al., 2012; Zhai and Bower, 2013; Nicholls et al., 2015). Not only in the Eastern Mediterranean but also in the Western Mediterranean and further away in the global ocean there are similar cases of orographic wind jets and the corresponding oceanic eddies. A full parametric study of the ocean response to different orographic wind jet characteristics (Ro_W, Bu_W, t_W) could be a interesting future direction that is missing so far from the literature. Moreover, our scaling analysis indicated the major controlling parameter γ that is responsible for this asymmetry, apart from the asymmetric wind forcing shape. The γ parameter could be thus used as an index to evaluate the wind forcing in other regions but also predict the oceanic response. However, high resolution data should be acquired to describe accurately the orographic wind jets.

In addition, even if this study focused only in the isolated effect of the wind forcing on the ocean, south-East of Crete is an area of high dynamic complexity that needs to be addressed in future studies. The dynamic complexity includes a steep bathymetric slope (Hellenic Trench), possible interactions of the Aegean and the Levantine Seas through the narrow straits of Kasos-Crete and Kasos-Karpathos as well as the possible connections with neighboring structures such as the Rhodes Gyre and the Asia Minor current. Therefore, the Etesian wind forcing could be a contributing mechanism to a more complex situation. Thus, the Etesian wind forcing could be further investigated under the influence of steep topography but also under the influence of upstream or neighboring currents. The above could be effective improvements towards understanding the complexity of the region and the effect of each forcing mechanism separately.

Lastly, the oceanic response to the orographic wind jet apart from the coherent anticyclones revealed the occurrence of many submesoscale cyclonic eddies as a result of the elongation of the cyclonic circulation in the positive wind stress curl region. The emergence of many submesoscale eddies was more evident during intensification by the asymmetric wind forcing. There is an interesting possible connection with the Rhodes Gyre dynamics that should be further investigated. Few studies discuss on the importance of the Ierapetra eddy presence bounding the Rhodes Gyre (Lascaratos et al., 1999; Theocharis et al., 1993). Although the asymmetric wind shape seems sufficient

to generate both an a mesoscale anticyclone but also submesoscale cyclonic eddies. The biological impact caused by the orographic wind forcing jet should be addressed. Likewise, in the core of the Ierapetra eddy during PERLE campaign many submesoscale processes where recorded in the mixed layer of the Ierapetra. Therefore, the impact of submesoscale air-sea interactions through the eddy-wind heat fluxes and their role to the regional biological productivity could be an interesting advancement. Besides the Ierapetra eddy remains an example of wind-eddy interaction (Gaube et al., 2015) that persists for long-time period, promote spreading of water masses and thus may contribute to the enhancement of the biological productivity in the Levantine Basin.

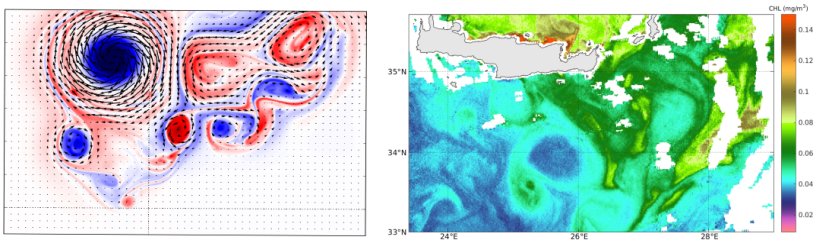

Figure 6.1: *Submesoscale cyclonic eddies generated in the cyclonic side of the applied wind forcing jet. b) Sea surface chlorophyll concentration for the region of Ierapetra the 16 April 2017.*

APPENDIX **A**

Wind forced rotating shallow-water model

To study the influence of wind forcing in the ocean surface we will use the shallow water equations (SWE). The SWE can be obtained from the Navier-Stokes equations by vertical averaging across each layer depth assuming incompressibility, the Boussinesq approximation and hydrostatic balance. Idealized simulations are powerful in order to investigate the dynamical response of the system to a single mechanism, here the wind forcing, by decomposing the complexity the ocean dynamics in the necessary components. We use the simplest representation of the ocean as one layer of fluid, that lies above a second inactive layer and that it will be subject to a transient wind forcing. The numerical method used for the shallow-water discretization is presented. The spatial and temporal discretization as well as the stability of the model are discussed. In order to prove convergence of the model, the effect of artificial smoothing and grid resolution is investigated for the same simulation set-up. After implementation and validation the model has been used for simulating the Etesian wind forcing in the South-East corner of Crete in chapter 5.

A.1 Governing Equations

Depth averaged shallow water equations (1.5 layer)

We demonstrate briefly the derivation of the shallow water equations starting from the Navier-Stokes equations for an incompressible fluid ($\frac{\partial \varrho}{\partial t} = 0$). The momentum and continuity equations write as follows:

$$\frac{\partial \underline{u}}{\partial t} + \underline{u} \cdot \nabla \underline{u} + f \times \underline{u} = -\frac{1}{\varrho}\nabla p + \nu \nabla^2 \underline{u} + \underline{g}k + \frac{1}{\varrho}\underline{F}_s \qquad (1)$$

$$\nabla \cdot \underline{u} = 0$$

where $\underline{u} = (u, v, w)$ is the velocity components in zonal, meridional and vertical direction, p pressure, ρ density, ν viscosity of seawater, g gravity, f the Coriolis term, and $\underline{F}_s = (F_x, F_y)$ external forces in the horizontal direction. Incompressibility does not allow density to change in time or position stating that the mass conservation $\frac{\partial \varrho}{\partial t} + \nabla \cdot (\varrho u) = 0$ could be reduced to a conservation of volume. Moreover, based on the *Boussinesq approximation*, the density can be decomposed in a reference density ρ_o and a variable one ρ' related to the fluid stratification $\varrho = \varrho_o + \varrho'(x, y, z, t)$. The density variations are relatively small and do not depart from the reference value ρ_o. This allows the replacement of the density term with the reference density everywhere apart from gravity term. Based on the *hydrostatic approximation*, the vertical accelerations $\frac{Dw}{Dt} = 0$ could be also neglected when comparing with horizontal accelerations. This assumption is valid if we consider the small aspect ratio of the ocean, vertical scale versus the horizontal one $\frac{H}{L} << 1$. This allows the equations to be reduced further in

the z direction retrieving the hydrostatic approximation $-\frac{1}{\varrho_0}\frac{\partial p}{\partial z} - g = 0$. Conceptually, the shallow water equations decompose the ocean to layers of fluid one above the other. Each layer is characterized by its own density ρ which is considered constant across the layer thickness h. The simplest way to represent the ocean is the case of one moving layer of fluid. The more the layers the more realistic the idealized representation of the ocean stratification. Material surfaces separate the layers and do not allow mass exchanges between them. In this configuration, we will decompose the ocean as two layers of fluid one above the other. As discussed in chapter 1, the interactions of the wind forcing occupy the first few meters of the ocean. In a first order approximation, the first layer of fluid could represent the movements of the thermocline, and the second one a stagnant deeper layer. The upper layer has the degree of freedom to move in the horizontal and vertical and lies above the lower layer of infinite depth that is at "rest" and adapts to the upper layer motion. The ocean stratification is approximated with a step function in this case and will approximate the displacement of the thermocline subject to wind forcing. The reduced gravity model allows to approximate the first mode of the ocean stratification, although it does not allow for any baroclinic phenomena to occur.

To describe the movement of the upper layer, Eqn.(1) are vertically averaged from the surface ε downwards till the interface displacement η, over the total layer thickness h. Starting from the pressure term and integrating from surface downwards, at a given depth z, in the upper layer, the pressure writes as $\pi_1 = \pi_o - \rho_1 g(z - \varepsilon)$. In the lower layer the pressure is given by the weight of the fluid above it and defined as $\pi_2 = \pi_0 + \rho_1 g h - \rho_2 g(z + h - \varepsilon)$. The main assumption of the 1.5-layer is that the lower layer has infinite depth and so the pressure gradient variations are comparably small and so they could be considered zero $\left(-\frac{\nabla \pi_2}{\rho_2} = 0\right)$. This leads to the following relation of the free surface ε with the interface between the 2 layers:

$$\frac{\rho_2 - \rho_1}{\rho_1} g \nabla \eta = g \nabla \varepsilon \tag{2}$$

where $g' = \frac{\rho_2 - \rho_1}{\rho_1} g$ is defined as the reduced gravity. The upper layer dynamics are basically dominated the density difference $\Delta\rho$ between the two layers. Because $g' < g$, any deviation of the surface displacements will have strong impact on the isopycnal deviation and vice versa. Considering that no fluid particle can cross the surface layer the boundary condition (B.C.) $\frac{D\varepsilon}{Dt} = w(\varepsilon)$ should be satisfied. The B.C. states that the Lagrangian derivative of the isopycnals should be compensated by their vertical displacement. Same condition is required for the interface displacement $\frac{D(-h)}{Dt} = w(-h)$. The vertical averaging of the continuity equation (Eqn.(1)) then leads to:

$$\int_{-h}^{\varepsilon} (\nabla \cdot \underline{u}) = 0$$

$$\int_{-h}^{\varepsilon} \frac{\partial u}{\partial x} dz + \int_{-h}^{\varepsilon} \frac{\partial v}{\partial y} dz + w(\varepsilon) - w(-h) = 0$$

$$\frac{\partial}{\partial x} \int_{-h}^{\varepsilon} u + \frac{\partial}{\partial y} \int_{-h}^{\varepsilon} v + \frac{\partial h}{\partial t} = 0$$

The Leibniz integration rule is applied here for each term $\int_{-h}^{\varepsilon} \frac{\partial u}{\partial x} dz = \frac{\partial}{\partial x} \int_{-h}^{\varepsilon} u dz - u_{z=\varepsilon} \frac{\partial \varepsilon}{\partial x} + u_{z=-h} \frac{\partial(-h)}{\partial x}$ and $\int_{-h}^{\varepsilon} \frac{\partial v}{\partial y} dz = \frac{\partial}{\partial y} \int_{-h}^{\varepsilon} v dz - v_{z=\varepsilon} \frac{\partial \varepsilon}{\partial y} + u_{z=-h} \frac{\partial(-h)}{\partial y}$ and with the

mean velocity fluxes defined as u $=\int_{-h}^{\varepsilon} u dz = \bar{u}h$ and v$=\int_{-h}^{\varepsilon} v dz = \bar{v}h$, we retrieve the depth averaged continuity equation for the 1.5-layer system.

$$\frac{\partial h}{\partial t} + \nabla \cdot (h\bar{u}) = 0$$

Similarly, the momentum equations are vertically averaged and the flow is split to mean and fluctuations part $u = \bar{u} + u'$ (similar to Reynolds decomposition). The flow fluctuations are considered small compared with the mean flow variations. Thus, we recover the shallow water equations as shown in Eqn.(3) where all variables are now depth averaged quantities.

$$\begin{aligned} \frac{\partial (h\bar{u})}{\partial t} + \bar{u}\frac{\partial}{\partial x}(h\bar{u}) + \bar{v}\frac{\partial}{\partial y}(h\bar{u}) - f(h\bar{v}) &= -gh\frac{\partial h}{\partial x} + \frac{\bar{\tau}_x}{\varrho_o} \\ \frac{\partial (h\bar{v})}{\partial t} + \bar{u}\frac{\partial}{\partial x}(h\bar{v}) + \bar{v}\frac{\partial}{\partial y}(h\bar{v}) + f(h\bar{u}) &= -gh\frac{\partial h}{\partial y} + \frac{\bar{\tau}_y}{\varrho_o} \\ \frac{\partial h}{\partial t} + \frac{\partial (h\bar{u})}{\partial x} + \frac{\partial (h\bar{v})}{\partial y} &= 0 \end{aligned} \tag{3}$$

Depending on the spatial and temporal structure of the wind stress acting on the layer thickness, the expected response differs. At first leading order, spatially uniform wind will be compensated by the Coriolis force driving the Ekman drift U_E. Contrary in the presence of a non-uniform wind forcing, will drive a divergence that will lead to the downwelling and upwelling of the isopycnals towards the interior/exterior of the ocean. The Ekman transport can vary also in a temporal basis having an unsteady impact on the ocean. The interface displacement depends then on the frequency spectrum of the wind stress forcing. Two different dynamical responses of the ocean can be distinguished related to the frequency of the forcing. If the frequency of the forcing is larger that the local Coriolis parameter $\omega < f$, the fast modulation of the thermocline would mainly lead to the generation of inertia-gravity waves (IGW). When the frequency of the forcing is lower that the local Coriolis parameter $\omega < f$ the response is expected to be a balanced localized flow. In this study we will consider an unsteady shear wind forcing. The wind shear will represent the climatological characteristics of the Etesian forcing blocked by Crete's orography (Figure A.2). Two spatial scales are considered for the wind forcing, its width W and lateral extend L, that will cause positive and negative wind stress curl regions.

Non-dimensionalisation

The vertically averaged equations that describe the motion of the upper layer motion in the one-and-a-half shallow-water model (1.5-RSW) can be summarized as follows:

$$\begin{aligned} \frac{\partial \underline{\mathbf{u}}}{\partial t} + \underline{\mathbf{u}} \cdot \nabla \underline{\mathbf{u}} + f\mathbf{k} \times \underline{\mathbf{u}} &= -\nabla\phi + \frac{g'\underline{\boldsymbol{\tau}}}{\varrho\phi} + \nu\nabla^2\underline{\mathbf{u}} \\ \frac{\partial \phi}{\partial t} + \nabla \cdot (\phi\underline{\mathbf{u}}) &= 0 \end{aligned} \tag{4}$$

where $\underline{\mathbf{u}} = (u, v)$ is the horizontal velocities in both directions, f is the Coriolis parameter, $h(x, y, t)$ the total deviation of the layer thickness, $\underline{\boldsymbol{\tau}} = (\tau_x, \tau_y)$ the wind stress component and ν the kinematic viscosity. The wind forcing term $\underline{\boldsymbol{\tau}}(x, y, t)$ will vary both spatially and temporally. It will be the only source of energy in the simulations. The variations of Coriolis with latitude are neglected assuming here the f plane approximation. We define here the geopotential height $\phi = g'h$ that expresses both the reduced

gravity g' and the layer thickness h as one variable, as there is no coupling between the pressures of the two layers. The density difference that is chosen should represent the regional stratification and is constrained by the deformation radius $Rd = \sqrt{g'H}/f$ and the initial layer thickness H. The system Eqn.(4) can be then characterized by few independent dimensionless parameters. For the wind forcing we consider 4 main variables: its intensity $\tau_o/\rho\,[L^2T^{-2}]$, its duration $T_o\,[T]$ and its spatial scales; the zonal width $W\,[L]$ and the meridional extend of the forcing $L[L]$. We choose the zonal width $W\,[L]$, the smaller spatial scale, as the dominant horizontal scale that characterizes the wind forcing shear that will act on the ocean surface. Based on Eqn.(4) the remaining controlling parameters are the Coriolis term $f\,[T^{-1}]$ and the geopotential height $\phi\,[L^2T^{-2}]$. The following reference quantities are defined and denoted with the tilde for the 1.5-RSW:

$$\begin{aligned} \widetilde{t} &= \frac{1}{T} \quad \widetilde{x} = \frac{x}{W} \quad \widetilde{y} = \frac{y}{W} \\ \widetilde{h} &= \frac{h}{H} \quad \widetilde{u} = \frac{u}{U} \quad \widetilde{v} = \frac{v}{U} \\ \widetilde{\tau_x} &= \frac{\tau_x}{\tau_o} \quad \widetilde{\tau_y} = \frac{\tau_y}{\tau_o} \end{aligned}$$

As a result of the above selected non-dimensionalization, we choose the following dimensionless numbers to describe the dynamics of the wind-forced shallow-water model:

$$Ro_W = \frac{U_E}{fW} \qquad Bu_W = \left(\frac{R_d}{W}\right)^2 \qquad t_W = T_o f$$

where Rossby number Ro_W characterizes the intensity of the wind stress τ_o related to the Ekman velocity $U_E = \dfrac{\tau_o}{\rho f H}$ and the Burger number of the forcing Bu_W which compares the first baroclinic deformation radius $R_d = \dfrac{\sqrt{g'H}}{f}$ to the wind forcing geometric scale W. For the case of the Etesian regime we are interested in a slow varying forcing term

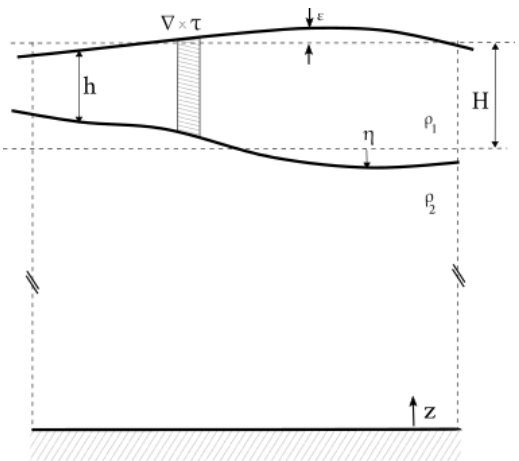

Figure A.1: *Schematic representation of 1.5-layer shallow-water model configuration.*

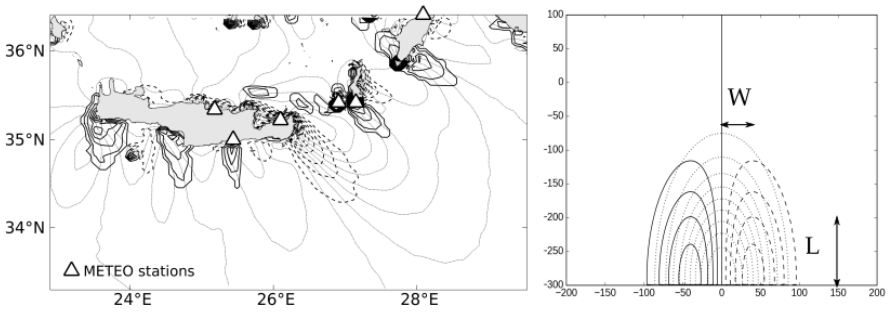

Figure A.2: *a) Climatological wind stress norm $\langle||\tau||\rangle$ and wind stress curl $\langle\nabla\times\tau\rangle$ caused by the Etesian wind forcing as obtained from ALADIN datasets for the summer months. b) Idealized representation of wind forcing in the shallow water model.*

that could represent the summer period ($t_W \ggg 1$).

$$\{1/t_W\}\frac{\partial\widetilde{h}}{\partial\widetilde{t}} + \{Ro_W\}\nabla\widetilde{h}\widetilde{u} = 0$$
$$\{1/t_W\}\frac{\partial\widetilde{u}}{\partial\widetilde{t}} + \{Ro_W\}\widetilde{u}\cdot\nabla\widetilde{u} + \{1\}\,k\times\widetilde{u} = -\left\{\frac{Bu_W}{Ro_W}\right\}\nabla\tilde{h} + \{1\}\,\frac{\tilde{\tau}}{\varrho\tilde{h}} + \left\{\frac{Ro_W}{Re_W}\right\}\nabla^2\underline{\mathbf{u}} \tag{5}$$

A.2 Numerical method

The numerical method used for the discretization of the governing equations is described here. In order to obtain the discretized form of Eqn.(4), we start by re-writing the momentum balance Eqn.(4) in the vector-invariant form. This leads to the following set of equations:

$$\frac{\partial\underline{\mathbf{u}}}{\partial t} + \nabla(\phi + \frac{1}{2}\underline{\mathbf{u}}^2) + (curl(\underline{\mathbf{u}}) + \mathbf{f})\times\underline{\mathbf{u}} = \frac{g'\boldsymbol{\tau}}{\varrho\phi} + A_h\triangle^2\underline{\mathbf{u}} \tag{6}$$

$$\frac{\partial\phi}{\partial t} + \nabla\cdot(\phi\underline{\mathbf{u}}) = 0 \tag{7}$$

In order to achieve a stable scheme and prevent accumulation of energy or enstrophy as small scales, artificial dissipation term is added to the right hand side of Eqn.(6). We used a bi-laplacian operator instead of standard diffusion, in order to suppress more efficiently the small scale noise. The bi-laplacian operator is the square of the diffusion Eqn.(8) and is defined as follows:

$$D = A_h\triangle^2\underline{\mathbf{u}} = A_h\nabla^4\underline{\mathbf{u}} \sim A_h\frac{U}{L^4} \tag{8}$$

where A_h is an operator that parametrizes the fluid kinematic viscosity, referenced as hyper-viscosity. The hyper-viscosity term A_h should be tuned accordingly such as to act on the grid scale of the domain. Details on the numerical dissipation are presented in the next section (see Eqn.(A.2)). With the definition of potential vorticity $q = \dfrac{\frac{\partial v}{\partial x} - \frac{\partial u}{\partial y} + f}{h}$ and the Kinetic energy $K = \frac{1}{2}\left(\underline{u}^2 + \underline{v}^2\right)$, and omitting for simplicity the artificial dissipation terms the system reduces to:

$$\begin{aligned}
\frac{\partial u}{\partial t} + \frac{\partial}{\partial x}(\mathrm{K}+\phi) - hqv &= g' \frac{\tau_x}{\varrho\phi} \\
\frac{\partial v}{\partial t} + \frac{\partial}{\partial y}(\mathrm{K}+\phi) + hqv &= g' \frac{\tau_y}{\varrho\phi} \\
\frac{\partial \phi}{\partial t} + \frac{\partial\,(\phi u)}{\partial x} + \frac{\partial\,(\phi v)}{\partial y} &= 0
\end{aligned} \tag{9}$$

Spatial discretization

The space discretization used was based on central finite differences (FD). The numerical domain with dimensions $L_x \times L_y$ and divided in N_x and N_y points in the x and y direction. The computational mesh is considered to contain square cells of equal size. The boundary conditions used were periodic in both directions ($h(x + L_x) = h$). The domain was chosen $10 - 15$ times larger than the scales of interest in order to reduce any effect of the side boundaries and retain accuracy. The computational mesh is staggered containing the flow variables in the different positions within the control cell (Figure A.3). The position of each variable is shown in Figure A.3a) where the height h or geopotential height $\phi = g'h$ centered at the control cell in position ik while the velocities $\underline{\mathbf{u}}(u, v)$ and the wind forcing $\underline{\tau}(\tau_x, \tau_y)$ are positioned in the cell edges at positions $i + 1/2$ and $k + 1/2$. Specific indexing is chosen to simplify the positions in the staggered mesh. Full levels are indexed with i in x direction or k in y direction and the half levels with j and l respectively ($j = i + 1/2,\ l = k + 1/2$). Staggering of variables has been proven beneficial for several reasons one of which is the avoidance of the odd-even decoupling between the grid cells. When the gradient of a variable is required at a different point than where it is stored, an averaging is required in order to bring the quantity in the right position. Depending on the way the dynamical quantities are averaged within the control cell an energy or enstrophy conservation scheme can be ensured (Sadourny, 1974). For numerical simplicity, within the model, we choose to simulate the fluxes quantities in and out of the control cell. Specific metric factors $x = Xdx$, $y = Ydy$ are introduced in order to translate the equations from the physical space to computational one (Figure A.3b). The physical grid cell of size Δx is converted to the computational coordinate system where each cell has unit size. Consequently, covariant components of the physical velocities can be also introduced such that $h_{phys} = {}^{h_{ik}}/_{dxdy}$, $u_{phys} = {}^{u_{jk}}/_{dx}$ and $v_{phys} = {}^{v_{il}}/_{dy}$. The control mass flux and the velocities across the control cell edges are defined as:

$$\begin{aligned}
\mathbf{m_{ik}} &= \phi_{ik} dx dy \\
\mathbf{U_{ik}} &= \frac{dy}{dx} u_{jk} h_{ik} \\
\mathbf{V_{il}} &= \frac{dx}{dy} v_{il} h_{ik}
\end{aligned}$$

Similarly the potential vorticity will transform to

$q_{phys} = f + \left(\frac{\partial v}{\partial x} - \frac{\partial u}{\partial y}\right)/h = f + \left(\frac{\partial\left(\frac{v_{il}}{dy}\right)}{\partial x} - \frac{\partial\left(\frac{u_{jk}}{dx}\right)}{\partial y}\right)/h = \frac{1}{dxdy}(f dx dy + \partial v_{il} - \partial u_{jk})/\frac{m_{ik}}{g * dx * dy} \ldots = g * q_{jl}$

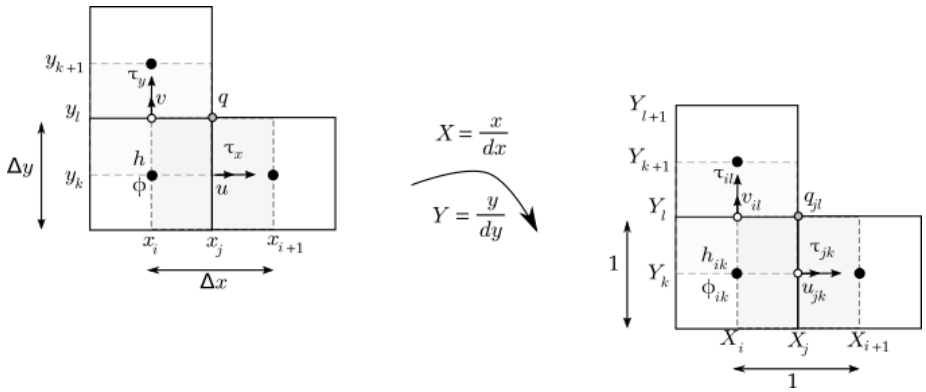

Figure A.3: *Schematic illustration of the control cell and the variable position of the dynamical quantities in the staggered mesh grid. Transformation from the physical to the computational space is depicted.*

The final discretized mass and momentum equations are written in the flux form as follows:

$$\delta_t u_{jk} + \delta_i \left(K_{ik} + g' h_{ik}\right) = +q_{jl} V_{il} + g' \frac{\tau_{jk}}{\varrho \phi_{ik}}$$
$$\delta_t v_{il} + \delta_k \left(K_{ik} + g' h_{ik}\right) = -q_{jl} U_{jk} + g' \frac{\tau_{jk}}{\varrho \phi_{ik}}$$
$$\delta_t m_{ik} + \delta_i U_{jk} + \delta_k V_{il} = 0$$

Based on Sadourny (1974), depending on the way we average the dynamical quantities within the control cell we ensure an energy or enstrophy conservation scheme. Based on his analysis, the energy conservation scheme results in a transfer of energy in small scales, a fact that is opposite to the 2D turbulence theory. On the other hand, by ensuring enstrophy conservation unphysical transfer of energy to small scales can be avoided while still conserving energy quite well. We will use in what follows the enstrophy conservation scheme as it is proved more relevant. To ensure an enstrophy conservation scheme the averaging that should be applied is shown in (Eqn.(10)-Eqn.(12)). The system of equations has then to be solved at every grid point.

$$\delta_t u_{jk} + \delta_i \overline{\phi_{ik}}^{j} = -\delta_i \overline{K_{ik}}^{j} + \overline{q_{jl}}^{k} \overline{V_{il}}^{jk} + g' \frac{\tau_{jk}}{\varrho \bar{\phi}^{j}_{ik}} \tag{10}$$

$$\delta_t v_{il} + \delta_k \overline{\phi_{ik}}^{l} = -\delta_k \overline{K_{ik}}^{l} - \overline{q_{jl}}^{i} \overline{U_{jk}}^{il} + g' \frac{\tau_{il}}{\varrho \bar{\phi}^{l}_{ik}} \tag{11}$$

$$\delta_t m_{ik} + \delta_i \overline{U_{jk}}^{i} + \delta_k \overline{V_{il}}^{k} = 0 \tag{12}$$

Time Stepping & Stability

The discretized equations Eqn.(10)-Eqn.(12) are advanced in time with a 4th order Runge-Kutta scheme. The stability of the scheme is controlled with the CFL condition which bounds the time step Δt or the distance that the information will travel within the computational domain. Is defined as follows:

$$\Delta t \leq CFL \frac{\triangle x}{\lambda} \tag{13}$$

where CFL is the Courant number. In physical terms, λ is the maximum speed by which the information propagates in the domain and represents the maximum eigenvalue of

the Jacobian matrix. For the shallow-water model the time stepping Δt is bounded based on the fastest waves which for the 1.5-layer model are the Inertia Gravity waves $c = \sqrt{g'H}$. The CFL number is chosen accordingly in order to fulfill the stability criterion.

Convergence - sensitivity tests

As in all numerical simulations optimizing the computational time is a priority. One of the simplest ways to accelerate the model is to reduce the grid resolution. However, the grid resolution and thus the computational cost is limited by the accuracy and desired precision we want to achieve in order to fully resolve the scales of the dynamics we are interest in. Coarser grids result in under-resolved gradients that lead to large discontinuities in the numerical solutions and create numerical noise. These non-physical oscillations will accumulate and eventually contaminate the model results. Numerical noise is most of the times unavoidable and it is need to be treated with the application of artificial smoothing. The tuning of the hyper-viscosity term $A_h(m^4 s^{-1})$ should be such so that it is sufficient for the numerical noise without affecting the dynamics of interest. In order to scale accordingly the model artificial dissipation Eqn.(8) we define the equivalent Reynolds number Re_h associated to the bi-laplacian operator as follows:

$$Re_h = \frac{\underline{\mathbf{u}} \cdot \nabla \underline{\mathbf{u}}}{A_h \triangle^2 \underline{\mathbf{u}}} = \frac{UL^3}{A_h} \tag{14}$$

By design, imposing low Reynolds number at the grid scale $L = \Delta x = \Delta y$ the hyper-viscosity will dump sufficiently the numerical noise at grid scales while leave unharmed the large scale motions.

In order to verify the relevance of the artificial smoothing tuning we examined the model performance at the same numerical simulation but for different configuration set-ups. Both the grid resolution $\Delta x = \Delta y$ and the hyperviscosity A_h were changed in the configurations. The same initial conditions were imposed. A symmetric Gaussian wind forcing of intensity $\tau_o = 0.4 N m^{-2}$ and duration $T_o = 10$ days was considered to act on an initially unperturbed fluid layer of thickness $H = 100\, m$. Simulations were performed in a square domain of size $L_x \times L_y = 600 \times 600\, km$. We compare the different simulations at the "end stage" (time step=80 days) for all simulations, where the flow was fully developed.

In order to quantify how the scaling of the bi-laplacian separately affects small and large scales we define the equivalent Reynolds number at the grid scale and the Reynolds number of the anticyclone as follows:

$$Re_h = \frac{U_E \left(\Delta x\right)^3}{A_h} \tag{15}$$

$$Re = \frac{V_{max} \left(R_{max}\right)^3}{A_h} \tag{16}$$

Figure A.4 compares the response of the model in the same initial conditions but in 6 different configurations. Overall, the same response is recovered for the large scales proving our model convergence. In regards to the different set-ups, the grid Reynolds number Re_h is progressively decreased by increasing the hyper-viscocity A_h term. The upper panels (a-c) corresponds to simulations of the same grid resolution $\Delta x = \Delta y = 1\, km$. When grid resolution is decreased panels (d-f) from $1\, km$ to $4\, km$ the hyper-viscocity is tuned accordingly in order to retain small grid Reynolds Re_h. For relatively large Re_h ($Re_h = 400$), numerical noise is visible, small scales are not sufficiently smoothed

and the numerical gradients are not accurately resolved. For smaller Reynolds numbers $Re_h < 40$ numerical noise is avoided. When comparing the flows at small grid $Re_h = 1$, the numerical noise is drastically reduced and we recover the same response in the large scales. The vortex Reynolds number for the anticyclones is $Re = 710^5$ and $Re = 10^4$ between finer ($1\,km$) and coarser resolution ($4\,km$) (panels (c) and (f)) having 1-2 orders of magnitudes difference, and so the large scales are not substantially affected. Although, moving towards smaller scales, the oceanic response differs. The effect of the grid resolution is more evident in the cyclonic part where filaments of cyclonic vorticity in the higher resolution run ($\Delta x = 1\,km$) (panel (c)) are not captured in the coarser grid ($\Delta x = 4\,km$) run (panel (f)) but rather a cyclonic circulation is simulated.

In order to account for a more detailed analysis we evaluated how the eddy characteristics may change between the runs by running AMEDA detection algorithm for all cases. The detected characteristics for the anticyclonic eddy are shown in Figure A.5. Little dispersion in regards to the hyperviscosity tuning is observed. All flow quantities agree well with one another for the formed mesoscale anticyclone. Reducing the wind model resolution down to $dx = 4\,km$ seems to not affect drastically the dynamical characteristics of the anticyclone. An anticyclone of same size and intensity is recovered.

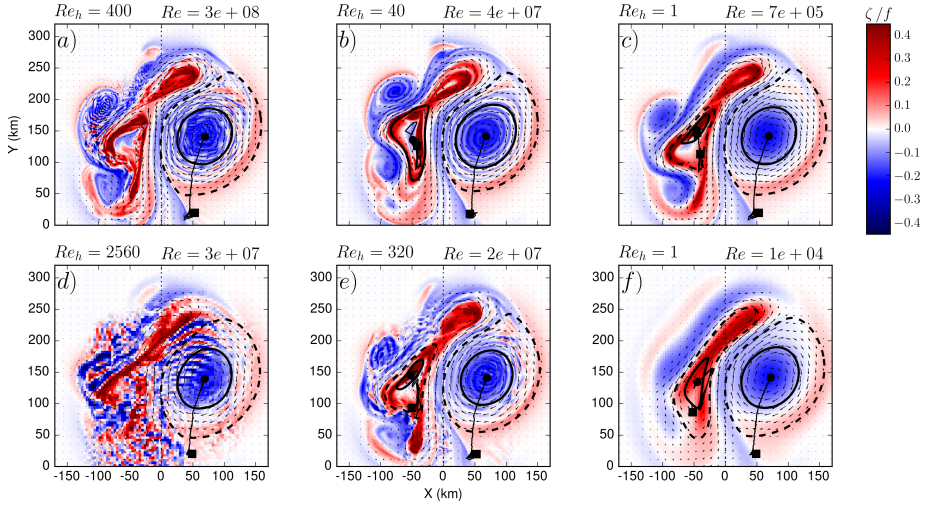

Figure A.4: *Sensitivity test for same initial wind forcing conditions of intensity $\tau_o = 0.4 Nm^{-2}$ and duration $T_o = 10$ days. Relative vorticity fields ζ/f of the oceanic response are shown at the end state of the simulations. The black contours illustrate the AMEDA eddy detection for the anticyclone. In the upper panels the Re_h is progressively decreased by increasing hyperviscosity constants a) $A_h = 10^5\,m^4s^{-1}$ b) $A_h = 10^6\,m^4s^{-1}$ c) $A_h = 4\,10^7\,m^4s^{-1}$. The grid resolution is kept $\Delta x = \Delta y = 1\,km$. In the lower panels the Re_h is progressively decreased by changing both resolution and hyperviscosity constants in d) $dx = 4\,km$ & $A_h = 10^6\,m^4s^{-1}$ noise is not efficiently smoothed b) $dx = 2\,km$ & $A_h = 3\,10^8\,m^4s^{-1}$ c) $dx = 4\,km$ & $A_h = 3\,10^9\,m^4s^{-1}$.*

Having in mind regional models (such as NEMO, MED-CORDEX, ALADIN etc.) with standard resolutions $1/24^o \approx 4\,km$, $1/12^o \approx 8\,km$, $1/8^o \approx 12\,km$ we wonder what would be the impact of drastic reduction of the grid resolution and the necessary application of strong artificial smoothing below $\Delta x = 4\,km$. The same configuration is tested by decreasing further the spatial resolution. The comparison between the oceanic response is shown in Figure A.6. The impact of artificial smoothing combined with the under resolved dynamics is unavoidable in such coarser grids even in the large scales. The tracked anticyclonic eddy characteristics are shown in Figure A.6 (d-f). The response seems similar between the different runs in terms of the size of the anticyclone, although

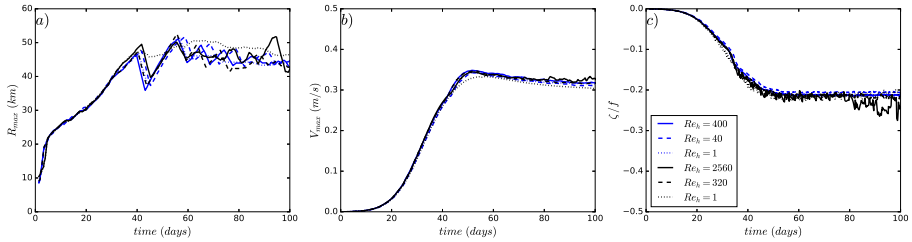

Figure A.5: *Detected characteristics of a) R_{max} (km) b) V_{max} (m/s) c) relative vorticity ζ/f for the anticyclonic eddy are shown from first to last detection as computed from AMEDA algorithm during the total simulation time.*

its intensity starts to be affected by the coarser grid. At least 20% underestimation in the anticyclonic eddy intensity is detected by AMEDA for the $dx = 12\,km$ run. We conclude that mesoscale scale anticyclones can be systematically underestimated as a result of the grid resolution. Both mesoscale and submesoscale dynamics cannot be reproduced accurately and captured in the coarser grid simulations.

Based on the above design criteria, numerical *stability* and *convergence* is ensured for the RSW model. All the results presented in the next chapters are obtained with the 4th-order Runge-Kutta scheme in a computation domain of $L_x \times L_y = 600 \times 600\,km$, *resolution* $\Delta x = \Delta y = 1\,km$, and bi-laplacian operator was kept constant at $A_h = 10^6 m^4 s^{-1}$. The CFL number used was 0.7-1 for most numerical experiments.

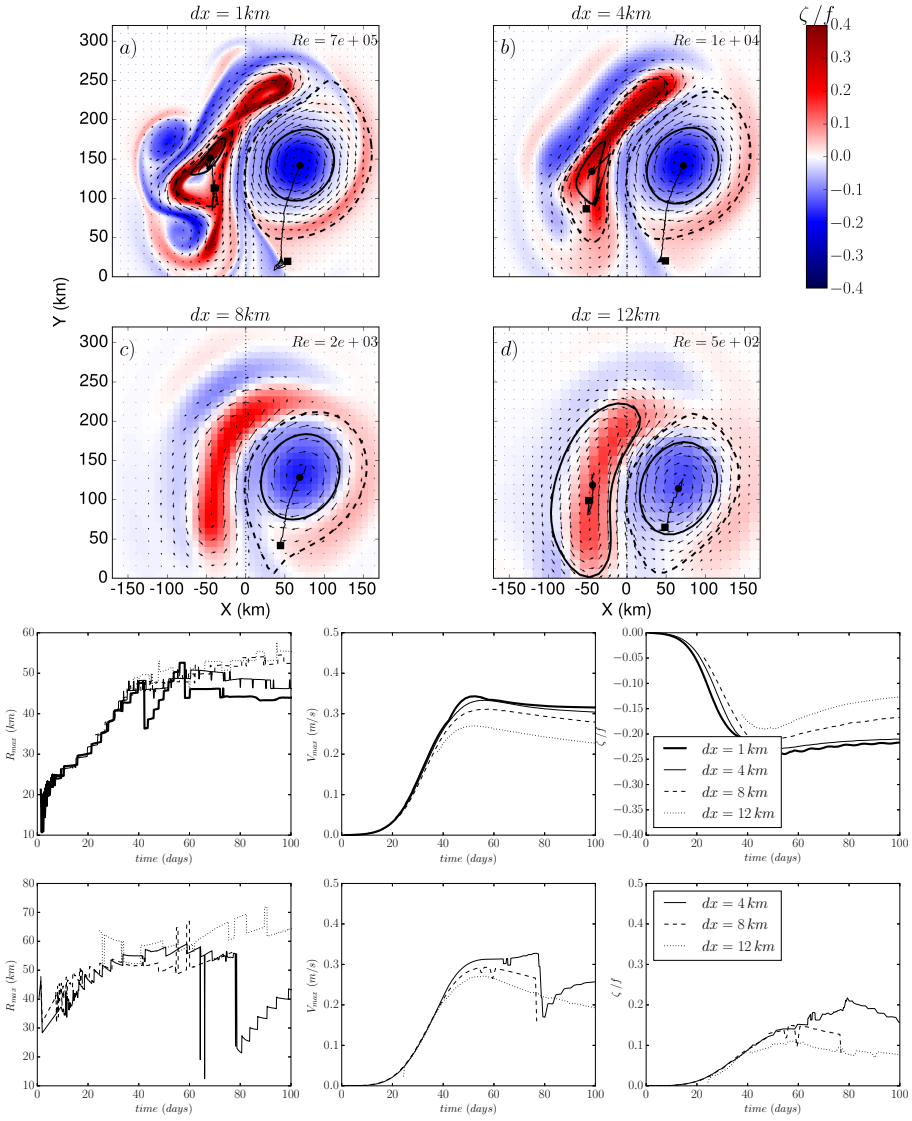

Figure A.6: *Sensitivity test for same initial wind forcing conditions of intensity* $\tau_o = 0.4Nm^{-2}$ *and duration* $T_o = 10$ *days. The oceanic response is shown for three coarser grid resolutions a)* $dx = 4\,km$ *b)* $dx = 8\,km$ *and c)* $dx = 12\,km$*. The Reynolds number of the grid is set to* $Re_h = 1$*. Detected characteristics of a)* R_{max} *(km) b)* V_{max} *(m/s) c) relative vorticity* ζ/f *for the anticyclonic eddy are shown from first to last detection as computed from AMEDA algorithm.*

APPENDIX **B**

ADT vs SLA for the Ierapetra eddies

In the present study we used oceanic sea surface height data for the period of 1993-2018 produced by SSALTO/ Data Unification and Altimeter Combination System (DUACS) and distributed by AVISO. The "all sat merged" series distributed regional product for the Mediterranean Sea combines, up-to-date datasets with up to four satellites at a given time, using all the missions available at a given time [TOPEX/Poseidon, ERS-1 and ERS-2, Jason-1 and Jason-2, the Ka-band Altimeter (AltiKa) on the Satellite with the Argos Data Collection System (Argos) and AltiKa (SARAL), Cryosat-2 and Envisat missions]. This merged satellite product, for the Mediterranean Sea, is projected on a $1/8^o$ Mercator grid, with a time interval of 24 h. The spatial resolution of this regional dataset is 2 times higher than the global altimetric products which are at $1/4^o$.

Regarding the distributed products, two different variables of sea level are provided; The Sea Level Anomaly (SLA) and the Absolute Dynamic topography (ADT). In order to measure the Sea Surface Height (SSH) obtained from satellites a reference of the bottom ocean surface should be defined. The ocean Sea Surface Height (SSH) is measured in respect of two types of references; one is a temporal reference level that is obtained by a 20 year average of sea surface height (MSS) and the second is to use the Earth's reference Geoid (see Figure B.1). The Geoid corresponds to the shape that the surface of the oceans would take under the influence of Earth's gravitation and rotation alone. Being interested only in perturbing forces of the ocean (winds,waves,tides etc.) the ocean Geoid is subtracted from the SSH signal. The Mean Dynamic Topography (MDT) corresponds only to perturbing forces of the ocean (winds,waves,tides etc.) over a 20 year period. Then the Sea Level Anomaly (SLA) corresponds to the difference between the sea surface height and the Mean Dynamic Topography (MDT). On the other hand, the Absolute Dynamics Topography (ADT) corresponds to the relevant distance of the sea surface height from the Geoid of the Earth ($ADT = SLA + MDT$).

There are several aspects that should be taken into consideration when using SLA or ADT fields for identifying eddy structures. Unlike the seal level anomaly (SLA), which represents the variable part of sea surface height, the ADT is the sum of this variable part and the constant part averaged over a 20-year reference period. When using SLA fields, we should take into consideration that a temporal averaging of 20 years period, that contains a physical signal, is priori extracted from the oceanic topography (SSH). This physical signal may lead to a loss of information and may result to less number of identified eddies or reduction in their estimated intensity. Such difference may result in different eddy detection prognostics.

In order to investigate which fields SLA or ADT are more relevant for our study we analyzed their difference for a specific case. We chose the Ierapetra eddy IE05 in summer 2006 where there were available measurements from drifters trapped in the eddy. During that time the pre-existing IE05 merged with a newly formed Ierapetra eddy IE06. We run AMEDA eddy detection and tracking algorithm with both SLA and ADT datasets in order to compare the derived eddy dynamical characteristics. The temporal evolution of the radius R_{max} and the tangential velocity V_{max} for the Ierapetra eddy IE05 as tracked by AMEDA is shown in Figure B.2. The merging event is visible in 18 July 2006

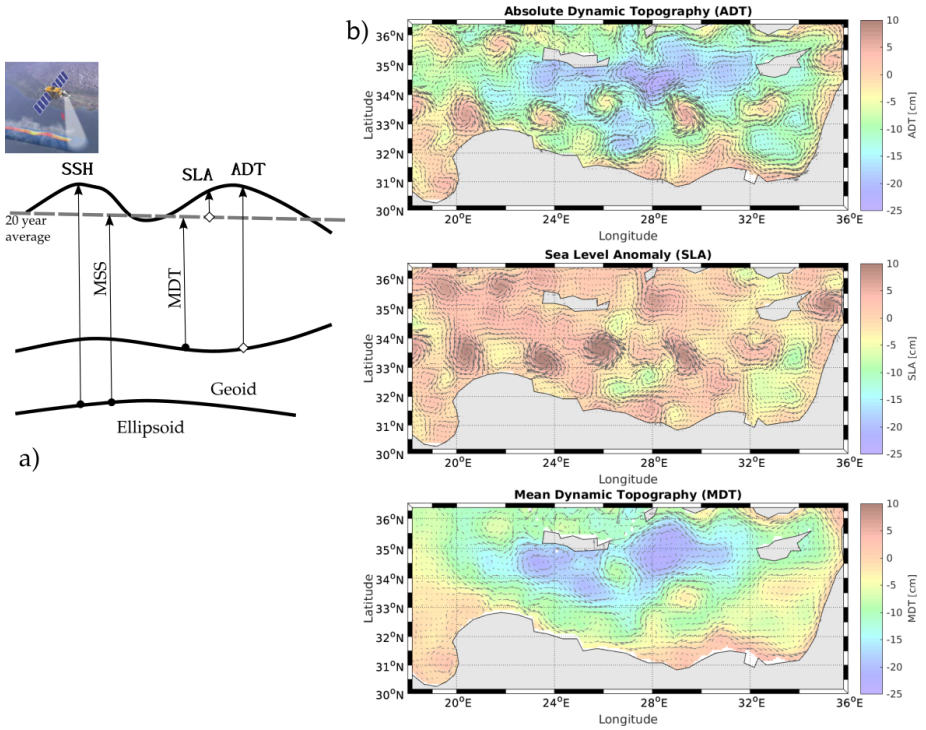

Figure B.1: *a) Schematic representation of the distributed DUACS/AVISO products for the oceanic sea surface heights. b) Sea Surface Topography from satellite altimetry using Sea Level Anomaly (SLA) and Absolute Dynamic Topography (ADT) fields. The Mean Dynamic Topography (MDT) derived from 20 years averaged sea surface height is also illustrated in the bottom diagram for the Eastern Mediterranean Sea.*

corresponding to the sudden reduction in the velocity V_{max} and radius R_{max} . Before the merging event, both detections from SLA and ADT seem to relate and roughly the same eddy characteristics are tracked. A slight tendency to underestimated the eddy velocities from the SLA fields is observed in comparison with the ADT few weeks before the merging event. However, after the merging event, a systematic underestimation of the eddy velocity is shown from the SLA fields. A constant shift between the velocity estimation is visible in Figure B.2(a) while there is no significant difference in the estimated radius. In order to understand the nature of this shift we analyzed the positions of the eddy as tracked by SLA, ADT and the MDT. Figure B.2 shows the eddy contours corresponding to the detection from SLA (red), ADT (blue) and MDT (black) fields for two characteristic dates one before and one after the merging. The shift observed in the time series can be explained by the superposition of the SLA - MDT contours. When both contours overlay (SLA and MDT), by definition the 20 year averaged MDT physical signal is extracted from the SSH field and results to underestimated SLA field. This is illustrated better in Figure B.2(b) where we estimated the distance of the MDT from the SLA and ADT contours. When the distance of the ADT and SLA is at least 1 mean MDT radius away, there is no significant bias between the SLA and ADT fields. At small distances less than $< 0.4\, R_{MDT}$ of the mean MDT radius, the MDT is removed from the SSH to compute the SLA. Their superposition thus leads to systematic underestimation of the eddy velocities. Besides estimation of the eddy velocities from drifters during that period showed that even the eddy velocities from the ADT fields detection may underestimate the eddy intensity. When cyclogeostrophic corrections were included, the velocity estimations where closer the measured velocities from in-situ.

Thus, we chose the velocity fields derived from the Absolute Dynamic Topography (ADT) to identify eddies instead of the Sea Level Anomaly (SLA) which is widely used in several eddy tracking algorithms (Chaigneau et al., 2009a; Chelton et al., 2011). We found that at least for the case of Ierapetra eddies, the eddy detection from the ADT fields seems more relevant for the correct eddy identification.

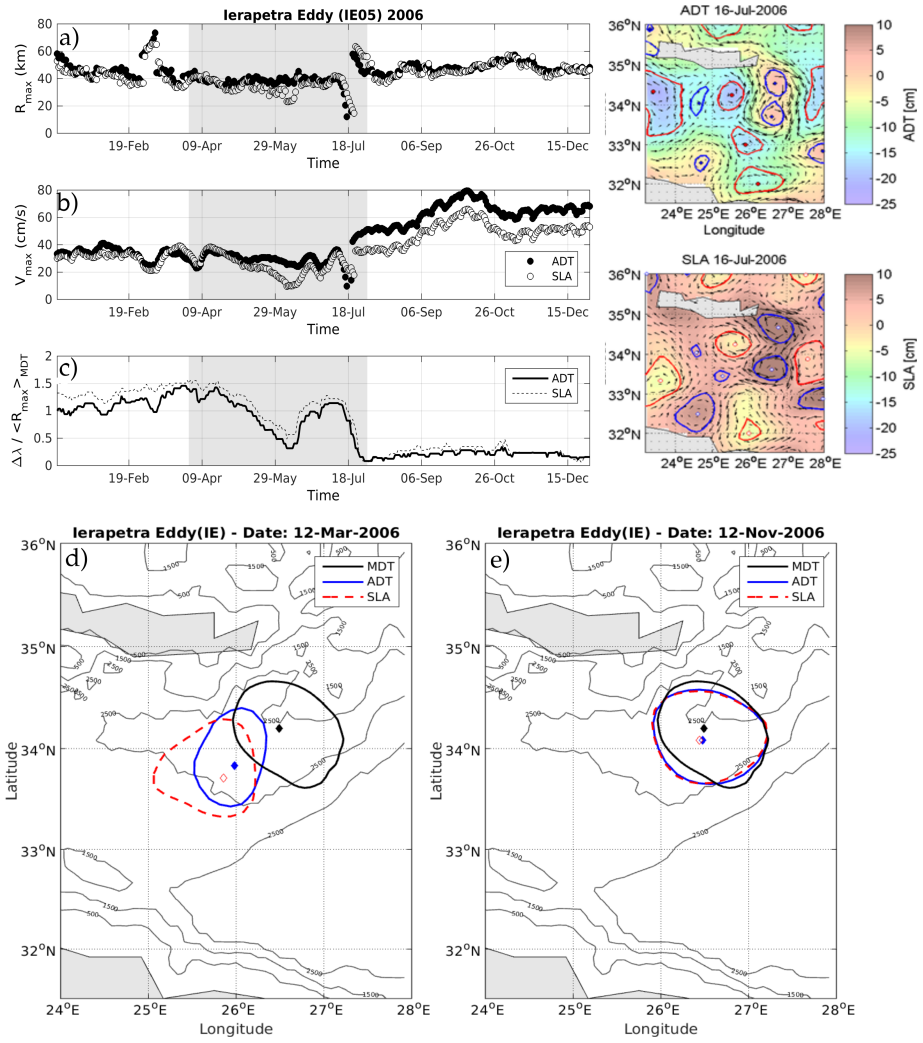

Figure B.2: *Ierapetra Eddy characteristic radius R_{max} (km) in panel a) and maximum velocities V_{max} (cm/s) in panel b) as detected from SLA and ADT fields with AMEDA algorithm. The normalized distance from mean position of Ierapetra eddy 05 in year 2006 is shown in panel c). Eddy contours as derived from SLA, ADT and MDT fields are shown with the red, blue and black color respectively for two representative dates; the 12-March-2006 (left panel) where no significant bias between SLA and ADT velocities is detected and for the 12-November-2006 (right panel) during the period where a systematic bias between SLA-ADT is observed.*

Bibliography

Alhammoudand, B., Béranger, K., Mortier, L., Crépon, M., and Dekeyser, I. (2005). "Surface circulation of the Levantine Basin: Comparison of model results with observations". *Progress in Oceanography*, 66:299–320. doi:10.1016/j.pocean.2004.07.015.

Amitai, Y., Lehahn, Y., Lazar, A., and Heifetz, E. (2010). "Surface circulation of the eastern Mediterranean Levantine basin: Insights from analyzing 14 years of satellite altimetry data". *Journal of Geophysical Research*, 115(C10):C10058. doi:10.1029/2010JC006147.

Amores, A., , Jordà, G., and Le Sommer, T. A. . J. (2018). "Up to what extent can we characterize ocean eddies using present-day grid-ded altimetric products?". *Journal of Geophysical Research: Oceans*, 123. https://doi.org/10.1029/2018JC014140.

Arnason, G., Haltiner, G. J., and Frawley, M. J. (1962). "HIGHER-ORDER GEOSTROPHIC WIND APPROXIMATIONS". *Monthly Weather Review*, 90(5):175–185. doi:10.1175/1520-0493(1962)090<0175:HGWA>2.0.CO;2.

Ayoub, N., Traon, P.-Y. L., and Mey, P. D. (1998). "A description of the Mediterranean surface variable circulation from combined ERS-1 and TOPEXPOSEIDON altimetric data". *Journal of Marine Systems*, 18:3–40.

Baey, J. and Carton, X. (2002). "Vortex multipoles in two-layer rotating shallow-water flows". *J. Fluid Mech*, 460:151–175. https://doi.org/10.1017/S0022112002008170.

Bakun, A. and Agostini, V. N. (2001). "Seasonal patterns of wind-induced upwelling/downwelling in the Mediterranean sea". *SCIENTIA MARINA*, 65(3):243–257. doi:10.3989/scimar.2001.65n3243.

Barton, E., Basterretxea, G., Flament, P., Mitchelson-Jacob, E., B.Jones, Aristegui, J., and Herrera, F. (2000). "Lee region of Gran Ca-naria". *Journal of Geophysical Research*, 105:17173–17193.

Bashmachnikov, I., Neves, F., Calheiros, T., and Carton, X. (2015). "Properties and pathways of Mediterranean water eddies in the Atlantic". *Progress in Oceanography*, 137:149–172. doi:http://dx.doi.org/10.1016/j.pocean.2015.06.001.

Benilov, E. and Flanagan, J. (2008). "The effect of ageostrophy on the stability of vortices in a two-layer ocean". *Ocean Modelling*, 23:49–58. doi:10.1016/j.ocemod.2008.03.004.

Béranger, K., Drillet, Y., Houssais, M. N., Testor, P., Badie, R. B., Alhammoud, B., Bozec, A., Mortier, L., Aubertot, P. B., and Crépon, M. (2010). "Impact of the spatial distribution of the atmospheric forcing on water mass formation in the Mediterranean Sea". *Journal of Geophysical Research*, 115(C12041):1–22. doi:10.1029/2009JC005648.

Brannigan, L. (2016). "Intense submesoscale upwelling in anticyclonic eddies". *Journal of Geophysical Research Letters*, 43:3360–3369. doi:10.1002/2016GL067926.

Brannigan, L., Marshall, D. P., Naveira Garabato, A. C., Nurser, A. J. G., and Kaiser, J. (2017). "Submesoscale Instabilities in Mesoscale Eddies". *Journal of Physical Oceanography*, 47(12):3061–3085. doi:10.1175/JPO-D-16-0178.1.

Caldeira, R. and Sangrá, P. (2012). "Complex geophysical wake flows Madeira Archipelago case study". *Journal of Ocean Dynamics*, 62:683–700. doi:10.1007/s10236-012-0528-6.

Caldeira, R. M. A. and Marchesiello, P. (2002). "Ocean response to wind sheltering in the Southern California Bight". *Journal of Geophysical Research Letters*, 29(13):1–4. doi:10.1029/2001GL014563.

Caldeira, R. M. A., Stegner, A., Couvelard, X., Araujo, I. B., Testor, P., and Lorenzo, A. (2014). "Evolution of an oceanic anticyclone in the lee of Madeira Island: In situ and remote sensing survey". *Journal of Geophysical Research: Oceans*, 119(2):1195–1216. doi:10.1002/2013JC009493.

Calil, P. H., Richards, K. J., Jia, Y., and Bidigare, R. R. (2008). "Eddy activity in the lee of the Hawaiian Islands". *Deep-Sea Research II*, 55:1179–1194. doi:10.1016/j.dsr2.2008.01.008.

Carton, X. J., Flierl, G. R., and Polvani, L. M. (1989). "The Generation of Tripoles from Unstable Axisymmetric Isolated Vortex structures". *Europhysics Letters*, 4:339–344. doi:10.1209/0295-5075/9/4/007.

Chaigneau, A., Eldin, G., and Dewitte, B. (2009a). "Eddy activity in the four major upwelling systems from satellite altimetry (1992-2007)". *Progress in Oceanography*, 83(1):117–123. doi:10.1016/j.pocean.2009.07.012.

Chaigneau, A., Gizolme, A., and Grados, C. (2009b). "Mesoscale eddies off peru in altimeter records: Identification algorithms and eddy spatio-temporal patterns". *Progress in Oceanography*, 79:106–119. https://doi.org/10.1016/j.pocean.2008.10.013.

Chaigneau, A., Le Texier, M., Eldin, G., Grados, C., and Pizarro, O. (2011). "Vertical structure of mesoscale eddies in the eastern South Pacific Ocean: A composite analysis from altimetry and Argo profiling floats". *Journal of Geophysical Research: Oceans*, 116(C11):1–16. doi:10.1029/2011JC007134.

Chang, C.-H., Xie, S.-P., Schneider, N., Qiu, B., Small, J., Zhuang, W., Taguchi, B., Sasaki, H., and Lin, X. (2012). "East Pacific ocean eddies and their relationship to subseasonal variability in Central American wind jets". *Journal of Geophysical Research*, 117(C10001):1–20. doi:10.1029/2011JC007315.

Chang, M.-H., Tang, T. Y., Ho, C.-R., and Chao, S.-Y. (2013). "Kuroshio-induced wake in the lee of Green Island off Taiwan". *J. Geophys. Res. Oceans*, 118:1508–1519. doi:10.1002/jgrc.20151.

Charney, J. (1955). "The Use of the Primitive Equations of Motion in Numerical Prediction". *Tellus*, 7(1):22–26. https://doi.org/10.1111/j.2153-3490.1955.tb01138.x.

Chavanne, C., Flament, P., Lumpkin, R., Dousset, b., and A., B. (2002). "Scatterometer observations of wind variations induced by oceanic islands: Implications for wind-driven ocean circulation". *Canadian Journal of Remote Sensing*, 28(3):466–474.

Chavanne, C. P., Heywood, K. J., Nicholls, K. W., and Fer, I. (2010). "Observations of the Antarctic Slope undercurrent in the southeastern Weddell Sea". *Geophys. Res. Lett.*, 37(L13601). doi:10.1029/2010GL043603.

Chelton, D. B., DeSzoeke, R. A., Schlax, M. G., Naggar, K. E., and Siwertz, N. (1998). "Geographical Variability of the First Baroclinic Rossby Radius of Deformation". *Journal of Physical Oceanography*, 28:433–460.

Chelton, D. B., Schlax, M. G., and Samelson, R. M. (2011). "Global observations of nonlinear mesoscale eddies". *Progress in Oceanography*, 91(2):167–216. doi:10.1016/j.pocean.2011.01.002.

Chelton, D. B., Schlax, M. G., Samelson, R. M., and de Szoeke, R. (2007). "Global observations of nonlinear mesoscale eddies". *Geophysical Research Letters*, 34(15):L15606. doi:10.1029/2007GL030812.

Couvelard, X., Caldeira, R., Araújo, I., and Tomé, R. (2012). "Wind mediated vorticity-generation and eddy-confinement, leeward of the Madeira Island: 2008 numerical case study.". *Journal of Atmospheres and Oceans*, 58:128–149. http://dx.doi.org/10.1016/j.dynatmoce.2012.09.005.

Demirov, E. and Pinardi, N. (2002). "Simulation of the Mediterranean Sea circulation from 1979 to 1993: Part I. The interannual variability". *Journal of Marine Systems*, 33–34:23–50.

Dewar, W. K. and Flierl, G. R. (1987). "Some Effects of the Wind on Rings". *Journal of Physical Oceanography*, 17(10):1653–1667. doi:10.1175/1520-0485(1987)017<1653:SEOTWO>2.0.CO;2.

Dewar, W. K. and Killworth, P. D. (1995). "On the stability of oceanic rings". *Journal of Phys. Oceanogr*, 25:1467–1487.

Doglioli, A. M., Blanke, B., S.Speich, and Lapeyre, G. (2007). "Tracking coherent structures in a regional ocean model with wavelet analysis: Application to Cape Basin eddies". *Journal of Geophysical Research: Oceans*, 112(C5043). doi:10.1029/2006JC003952.

Douglass, E. M. and Richman, J. G. (2015). "Analysis of ageostrophy in strong surface eddies in the Atlantic Ocean". *Journal of Geophysical Research: Oceans*, 120:1490–1507. doi:10.1002/ 2014JC010350.

Du, Y., Yi, J., Wu, D., He, Z., Wang, D., and Fuyuan, L. (2014). "Mesoscale oceanic eddies in the South China Sea from 1992 to 2012: evolution processes and statistical analysis". *Acta Oceanologica Sinica*, 33(11):36–47. doi:10.1007/s13131-014-0530-6.

Ducet, N. (2000). "Global high-resolution mapping of ocean circulation from TOPEX/Poseidon and ERS-1 and -2". *Journal of Geophysical Research*, 105(C8):119,447–19,498.

Ekman, W. (1905). "On the influence of the earth's rotation on ocean-currents". *Arkiv Fur Matematik Astronomi Och Fysik.*, 11:355–367.

Endlich, R. (1961). "Computation and uses of gradient winds". *Mon. Weather Rev.*, 89:187–191. https://doi.org/10.1006/rwos.2001.0376.

Escudier, R., Mourre, B., Juza, M., and Tinto, J. (2016). "Subsurface circulation and mesoscale variability in the Algerian subbasin from altimeter-derived eddy trajectories". *Journal of Geophysical Research: Oceans*, 121(8):6310–6322. doi:10.1002/2016JC011760.

Flexas, M., Gomis, D., Ruiz, S., Pascual, A., and Leon, P. (2006). "In situ and satellite observations of the eastward migration of the Western Alboran Sea Gyre". *Progress in Oceanography*, 70:486–509. doi:10.1016/j.pocean.2006.03.017.

Fusco, G., Manzella, G. M. R., Cruzado, A., Gacic, M., Gasparini, G. P., Kovacevic, V., Millot, C., Tziavos, C., Velasquez, Z. R., Walne, A., Zervakis, V., and Zodiatis, G. (2003). "Variability of mesoscale features in the Mediterranean Sea from XBT data analysis". *Annales Geophysicae*, 21(1):21–32. doi:https://doi.org/10.5194/angeo-21-21-2003.

Garreau, P., Dumas, F., Louazel, S., Stegner, A., and B.Le Vu (2018). "High resolution in situ observations and tracking of a dual core anticyclonic eddy in the Algerian Basin". *J. Geophys. Res. Oceans*. https://doi.org/10.1029/2017JC013667.

Gaube, P., Chelton, D. B., Samelson, R. M., Schlax, M. G., and O'Neill, L. W. (2015). "Satellite Observations of Mesoscale Eddy-Induced Ekman Pumping ". *Journal of Physical Oceanography*, 42:39–61. doi:10.1175/JPO-D-14-0032.1.

Gerin, R., Poulain, P. M., Taupier-Letage, I., Millot, C., Ismail, S. B., and Sammari, C. (2009). "Surface circulation in the Eastern Mediterranean using drifters (2005-2007)". *Ocean Science*, 5(4):559–574. doi:10.5194/os-5-559-2009.

Gomis, D., Ruiz, S., and Pedder, M. (2001). "Diagnostic analysis of the 3D ageostrophic circulation from a multivariate spatial interpolation of CTD and ADCP data.". *Deep-Sea Research I*, 48:269–295. https://doi.org/10.1016/S0967-0637(00)00060-1.

Hamad, N., Millot, C., and Taupier-Letage, I. (2005). "A new hypothesis about the surface circulation in the eastern basin of the Mediterranean Sea". *Progress in Oceanography*, 66(2-4):287–298. doi:10.1016/j.pocean.2005.04.002.

Hamad, N., Millot, C., and Taupier-Letage, I. (2006). "The surface circulation in the Eastern basin of the Mediterranean Sea". *SCIENTIA MARINA*, 70(3):457–503.

Hamon, M., Beuvier, J., Somot, S., Lellouche, J.-M., Greiner, E., Jordà, G., Bouin, M.-N., Arsouze, T., Béranger, K., Sevault, F., Dubois, C., Drevillon, M., and Drillet, Y. (2016). "Design and validation of MEDRYS, a Mediterranean Sea reanalysis over the period (1992-2013)". *Ocean Science*, 12(2):577–599. doi:10.5194/os-12-577-2016.

Hasegawa, D., Yamazaki, H., Lueck, R. G., and Seuront, L. (2004). "How islands stir and fertilize the upper ocean". *Geophys. Res. Lett.*, 31(L16303). doi:10.1029/2004GL020143.

Hecht, A. and Gertman, I. (2001). "Physical features of the eastern Mediterranean resulting from the integration of POEM data with Russian Mediterranean Cruises". *Deep-Sea Research I*, 48:1847–1876.

Holton, J. (1992). *"An Introduction to Dynamic Meteorology, Volume 48 - 3rd Edition*".

Horton, C., Kerling, J., Athey, G., Schmitz, J., and M.Clifford (1994). "Airborne expendable bathythermograph surveys of the eastern Mediterranean". *Journal of Geophysical Research: Oceans*, 99(C5):9891–9905. doi:10.1029/94JC00058.

Ioannou, A., Stegner, A., LeVu, B., Taupier-Letage, I., and Speich, S. (2017). "Dynamical Evolution of Intense Ierapetra Eddies on a 22 Year Long Period". *Journal of Geophysical Research:Oceans*, 122. https://doi.org/10.1002/2017JC013158.

Ioannou, A., Stegner, A., Tuel, A., LeVu, B., Dumas, F., and Speich, S. (2019). "Dynamical Evolution of Intense Ierapetra Eddies on a 22 Year Long Period". *Journal of Geophysical Research: Oceans*.

Isern-Fontanet, J., GarcÃa-Ladona, E., and Font, J. (2006). "Vortices of the Mediterranean Sea: An Altimetric Perspective". *Journal of Physical Oceonography*, 36(1):87–103. doi:10.1175/JPO2826.1.

Iudicone, D., Santoleri, R., Marullo, S., and Gerosa, P. (1998). "Sea level variability and surface eddy statistics in the Mediterranean Sea from TOPEX/POSEIDON data". *Journal of Geophysical Research*, 103(C2):2995–3011.

Iversen, T. and Nordeng, T. E. (1982). "A Convergent Method for Solving the Balance Equation". *Monthly Weather Review*, 110:1347–1353. https://doi.org/10.1175/1520-0493(1982)110<1347:ACMFST>2.0.CO;2.

Iversen, T. and Nordeng, T. E. (1984). "Static initialization of primitive equation models on a bounded, extratropical region ". *Tellus*, 36(A):21–29. https://doi.org/10.1111/j.1600-0870.1984.tb00219.x.

Jia, Y., Calil, P. H. R., Chassignet, E. P., Metzger, E. J., Potemra, J. T., Richards, K. J., and Wallcraft, A. J. (2011). "Generation of mesoscale eddies in the lee of the Hawaiian Islands". *Journal of Geophysical Research*, 116. doi:10.1029/2011JC007305.

Jiménez, B., Sangá, P., and Mason, E. (2008). "A numerical study of the relative importance of wind and topographic forcing on oceanic eddy shedding by tall, deep water islands". *Journal of Ocean Modelling*, 22:146–157. doi:10.1016/j.ocemod.2008.02.004.

Kersalé, M., Doglioli, A. M., and Petrenko, A. A. (2011). "Sensitivity study of the generation of mesoscale eddies in a numerical model of Hawaii islands". *Ocean Science*, 7:227–291. doi:10.5194/os-7-277-2011.

Klein, P., Hua, B. L., Lapeyre, G., Capet, X., Gentil, S. L., , and Sasaki, H. (2008). "Upper ocean turbulence from high-resolution 3D simulations.". *Journal of Phys. Oceanogr.*, 38:1748–1763. doi:10.1175/ 2007JPO3773.1.

Kloosterzielt, R., Carnevale, G. F., and Orlandi, P. (2007). "Inertial instability in rotating and stratified fluids: barotropic vortices". *Journal of Fluid Mechanics*, 583:379–412. doi:10.1017/S002211200700632.

Kloosterzielt, R. and Heijst, G. V. (1991). "An experimental study of unstable barotropic vortices in a rotating fluid". *Journal of Fluid Mechanics*, 223:1–24. doi:10.1017/S0022112091001301.

Knox, J. A. and Ohmann, P. R. (2006). "Iterative solutions of the gradient wind equation". *Comput. Geosci.*, 32:656–662. doi:10.1016/j.cageo.2005.09.009.

Koletsis, I., Lagouvardos, K., Kotroni, V., and Bartzokas, A. (2009). "The interaction of northern wind flow with the complex topography of Crete Island-Part 1: Observational study". *Natural Hazards and Earth System Sciences*, 9:1845–1855.

Koletsis, I., Lagouvardos, K., Kotroni, V., and Bartzokas, A. (2010). "The interaction of northern wind flow with the complex topography of Crete Island-Part 2: Numerical study". *Natural Hazards and Earth System Sciences*, 10:1115–1127. doi:10.5194/nhess-10-1115-2010.

Kontoyiannis, H., Balopoulos, E., Gotsis-Skretas, O., Pavlidou, A., Assimakopoulou, G., and Papageorgiou, E. (2005). "The hydrology and biochemistry of the Cretan Straits (Antikithira and Kassos Straits) revisited in the period June 1997-May 1998". *Journal of Marine Systems*, 53:37–57. doi:10.1016/j.jmarsys.2004.06.007.

Kontoyiannis, H., Theocharis, A., Balopoulos, E., Kioroglou, S., Papadopoulos, V., Collins, M., Velegrakis, A. F., and Iona, A. (1999). "Water fluxes through the Cretan Arc Straits, Eastern Mediterranean Sea: March 1994 to June 1995". *Progress in Oceanography*, 44:511–529.

Kotroni, V., Lagouvardos, K., and Lalas, D. (2001). The effect of the island of Crete on the Etesian winds over the Aegean Sea. *Journal of the Royal Meteorological Society*, 127(576):1917–1937. doi:10.1002/qj.49712757604.

Lacombe, H. and Tchernia, P. (1972). "Caractères hydrologiques et circulation des eaux en Méditeranée ". *The Mediterranean Sea: a natural sedimentation laboratory*, pages 25–36.

Lahaye, N. and Zeitlin, V. (2015). "Centrifugal, barotropic and baroclinic instabilities of isolated ageostrophic anticyclones in the two-layer rotating shallow water model and their nonlinear saturation". *J. Fluid Mech*, 762:5–34.

Larnicol, G., Ayoub, N., and Traon, P. L. (2002). "Major changes in Mediterranean Sea level variability from 7 years of TOPEX/Poseidon and ERS-1/2 data". *Journal of Marine Systems*, 33-34:63–89. doi:10.1016/S0924-7963(02)00053-2.

Larnicol, G., Traon, P.-Y. L., Ayoub, N., and Mey, P. D. (1995). "Mean sea level and surface circulation variability of the Mediterranean Sea from 2 years of TOPEX/POSEIDON altimetry". *Journal of Geophysical Research: Oceans*, 100:25163–25177. doi:10.1029/95JC01961.

Lascaratos, A. and Nittis, K. (1998). "A high-resolution three-dimensional numerical study of intermediate water formation in the Levantine Sea". *Journal of Geophysical Research*, 103(C9):18497–18511.

Lascaratos, A., Roether, W., Nittis, K., and Klein, B. (1999). "Recent changes in deep water formation and spreading in the eastern Mediterranean Sea: a review". *Progress in Oceanography*, 44:5–36.

Lascaratos, A. and Tsantilas, S. (1997). "Study of the seasonal circle of the Ierapetra gyre, using satelite images". *Proc. Hell. Symp. Oceanogr.*, pages 165–168.

Laxenaire, R., S., S., Blanke, B., A., C., C., P., and A., S. (2018). "Anticyclonic eddies connecting the western boundaries of indian and atlantic oceans". *J. Geophys. Res. Oceans*. https://doi.org/10.1029/2018JC014270.

Lazar, A., Stegner, A., Caldeira, R., Dong, C., Didelle, H., and Viboud, S. (2013a). "Inertial instability of intense stratified anticyclones.part 2.Laboratory experiments". *Journal of Fluid Mechanics*, 732:485–509. doi:10.1017/jfm.2013.413.

Lazar, A., Stegner, A., and E.Heifetz (2013b). "Inertial instability of intense stratified anticyclones.part 1.Generalized stability criterion". *Journal of Fluid Mechanics*, 732:457–484. doi:10.1017/jfm.2013.412.

LeTraon, P. Y., Nadal, F., and Ducet, N. (1998). "An Improved Mapping Method of Multisatellite Altimeter Data". *JOURNAL OF ATMOSPHERIC AND OCEANIC TECHNOLOGY*, 15:522–533.

Le Vu, B., Stegner, A., and Arsouze, T. (2017). "Angular momentum eddy detection and tracking algorithm (ameda) and its application to coastal eddy formation". *J. Atmos. Oceanic Technol*, 35:739–762. doi:10.1175/JTECH-D-17-0010.1.

Le Vu, B., Stegner, A., and Arsouze, T. (2018). "Angular momentum eddy detection and tracking algorithm (ameda) and its application to coastal eddy formation". *J. Atmos. Oceanic Technol*, 35:739–762. doi:10.1175/JTECH-D-17-0010.1.

Li, Q.-Y., Sun, L., Liu, S.-S., Xian, T., and Yan, Y.-F. (2014). "A new mononuclear eddy identification method with simple splitting strategies". *Remote Sensing Letters*, 5(1):65–72. doi:10.1080/2150704X.2013.872814.

Mahdinia, M., Hassanzadeh, P., Marcus, P. S., and Jiang, C.-H. (2017). "Stability of 3d gaussian vortices in an unbounded, rotating, vertically-stratified,boussinesq flow: Linear analysis". *Journal of Fluid Mech*, 824:97–134. doi:10.1017/jfm.2017.303.

Malanotte-Rizzoli, P., Manca, B., d'Alcala, M. R., Theocharis, A., Bergamasco, A., Bregant, D., Budillon, G., Civitarese, G., Georgopoulos, D., Michelato, A., Sansone, E., Scarazzato, P., and Souvermezoglou, E. (1997). "A synthesis of the Ionian sea hydrography and circulation and water mass pathways during POEM-Phase I". *Progress in Oceanography*, 39(3):153–204. doi:10.1016/S0079-6611(97)00013-X.

Margirier, F., Bosse, A., Testor, P., l'Hévéder, B., Mortier, L., and Smeed, D. (2016). "Characterization of Convective Plumes Associated With Oceanic Deep Convection in the Northwestern Mediterranean From High-Resolution In Situ Data Collected by Gliders". *Journal of Geophysical Research: Oceans*, 122:9814–9826. doi:10.1002/2016JC012633.

Marullo, F., E.Napolitano, Santoleri, R., Manca, B., and Evans, R. (2003). "Variability of Rhodes and Ierapetra Gyres during Levantine Intermediate Water Experiment: Observations and model results". *Journal of Geophysical Research*, 108(C9, 8119):21–38. doi:10.1029/2002JC001393.

Mason, E., Pascual, A., and McWilliams, J. C. (2014). "A New Sea Surface Height Based Code for Oceanic Mesoscale Eddy Tracking". *Journal of Atmospheric and Oceanic Technology*, 31:1181–1188. doi:10.1175/JTECH-D-14-00019.1.

Matteoda, A. and Glenn, S. (1996). "Observations of recurrent mesoscale eddies in the eastern Mediterranean". *Journal of Geophysical Research*, 101(C9):20687–20709. doi:10.1029/96JC01111.

McCreary, P., H.Lee, and Enfield, D. (1989). "The response of the coastal ocean to strong offshore winds: With application to circulations in the Gulf of Tehuantepec and Gulf of Papagayo". *Journal of Marine Research*, 47:81–109.

McGillicuddy, D. J., Anderson, L. A., Bates, N. R., Bibby, T., Carlson, K. O. B. C. A., Davis, C. S., Ewart, C., Falkowski, P. G., Goldthwait, S. A., Hansell, D. A., Jenkins, W. J., Johnson, R., Kosnyrev, V. K., Ledwell, J. R., Li, Q. P., Siegel, D. A., and Steinberg, D. K. (2007). "Eddy/Wind Interactions Stimulate Extraordinary Mid-Ocean Plankton Blooms". *Science*, 316:1021–1026. doi:10.1126/science.1136256.

McIntyre, M. (2015). "Balanced Flow". *Encyclopedia of Atmospheric Sciences, 2nd edition*, 2:298–303.

Menna, M., Poulain, P., Zodiatis, G., and Gertman, I. (2012). "On the surface circulation of the Levantine sub-basin derived from Lagrangian drifters and satellite altimetry data". *Deep-Sea Research*, 65:46–58. doi:10.1016/j.dsr.2012.02.008.

Miglietta, M. M., Zecchetto, S., and Biasio, F. D. (2013). "A comparison of WRF model simulations with SAR wind data in two case studies of orographic lee waves over the Eastern Mediterranean Sea". *Journal of Atmospheric Research*, 120-121:127–146. http://dx.doi.org/10.1016/j.atmosres.2012.08.009.

Millot, C. (1985). "Some features of the Algerian Current". *Journal of Geophysical Research: Oceans*, 90:7169–7176. doi:10.1029/JC090iC04p07169.

Millot, C. and Gerin, R. (2010). "The Mid – Mediterranean Jet Artefact". *Journal of Geophysical Research Letters*, 37(L12602):1–6. doi:10.1029/2010GL043359.

Millot, C. and Taupier-Letage, I. (2005). “Circulation in the Mediterranean Sea". volume 5 Part K of *The Handbook of Environmental Chemistry*, pages 29–66. Springer Verlag Berlin Heidelberg. doi:10.1007/b107143.

Mkhinini, N., Coimbra, A. L. S., Stegner, A., Arsouze, T., Taupier-Letage, I., and Béranger, K. (2014). “Long-lived mesoscale eddies in the eastern Mediterranean Sea: Analysis of 20 years of AVISO geostrophic velocities". *Journal of Geophysical Research: Oceans*, 119(12):8603–8626. doi:10.1002/2014JC010176.

Moutin, T. and Prieur, L. (2012). “Influence of anticyclonic eddies on the Biogeochemistry from the Oligotrophic to the Ultraoligotrophic Mediterranean (BOUM cruise)". *Biogeosciences*, 9:3827–3855. doi:10.5194/bg-9-3827-2012.

Mutabazi, I. and Normand, C. (1992). “Gap size effects on centrifugally and rotationally driven instabillites". *Journal of Phys.Fluids*, 4(6):1199–1205. doi:10.1063/1.858238.

Napolitano, E., Oguz, T., Malanotte-Rizzoli, P., Yilmaz, A., and Sansone, E. (2000). “Simulations of biological production in the Rhodes and Ionian basins of the eastern Mediterranean". *Journal of Marine Systems*, 24:277–298.

Nencioli, F., Dong, C., Dickey, T., Washburn, L., and McWilliams, J. (2010). “A vector geometry-based eddy detection algorithm and its application to a high-resolution numerical model product and high-frequency radar surface velocities in the Southern California Bight". *Journal of Atmos. Oceanic Technol.*, 27(3):564–579. doi:10.1175/2009JTECHO725.1.

Nicholls, J. F., Toumi, R., and Stenchiko, G. (2015). “Effects of unsteady mountain-gap winds on eddies in the Red Sea". *J. Atmospheric Science Letters*, 16:279–284. doi:10.1002/asl2.554.

Nielsen, J. (1912). *“Hydrography of the Mediterranean and Adjacent Waters*".

Nittis, K., Lascaratos, A., and Theocharis, A. (2003). “Dense water formation in the Aegean Sea: Numerical simulations during the Eastern Mediterranean Transient". *Journal of Geophysical Research*, 108(C9, 8120):21–1–21–15. doi:10.1029/2002JC001352.

Ovchinnikov, I. (1966). “Circulation in the surface and intermediate layer of the Mediterranean". *Oceanology*, 6:48–59.

Paduan, J. and Washburn, L. (2013). "High-frequency radar observations of ocean surface currents". *J. Mar.Sci.* doi:10.1146/annurev-marine-121211-172315.

Pascual, A., Pujol, M., G.Larnicol, Traon, P. L., and Rio, M. (2007). “A mesoscale mapping capabilities of multi satellite altimetry missions:first results with real data in the Mediterranean Sea". *Journal of Marine Systems*, 65(1-4):190–211. doi:10.1016/j.jmarsys.2004.12.004.

Patzert, W. C. (1969). “Eddies in the Hawaiian Waters". *Tech.rep. Hawaii Institute of Geophysics, University of Hawaii*.

Pegliasco, C., Chaigneau, A., and Morrow, R. (2015). “Main eddy vertical structures observed in the four major Eastern Boundary Upwelling Systems". *Journal of Geophysical Research: Oceans*, 120:6008–6033. doi:10.1002/2015JC010950.

Pennel, R., Stegner, A., and Béranger, K. (2012). “Shelf Impact on Buoyant Coastal Current Instabilities". *Journal of Physical Oceanography*, 45(1):104–132. doi:10.1175/JPO-D-11-016.1.

Penven, P., Halo, I., Pous, S., and Marié, L. (2014). "Cyclogeostrophic balance in the Mozambique Channel". *Journal of Geophysical Research: Oceans*, 119(2):1–14. doi:10.1002/2013jc009528.

Perret, G., Dubos, T., and Stegner, A. (2011). "How Large-Scale and Cyclogeostrophic Barotropic Instabilities Favor the Formation of Anticyclonic Vortices in the Ocean". *Journal of Physical Oceanography*, 41(2):303–328. doi:10.1175/2010JPO4362.1.

Perret, G., Stegner, A., Dubos, T., Chomaz, J., and Farge, M. (2006a). "Stability of parallel wake flows in quasigeostrophic and frontal regimes". *Physics of Fluids*, 18(12):126602. doi:10.1063/1.2397563.

Perret, G., Stegner, A., Farge, M., and T.Pichon (2006b). "Cyclone-anticyclone assymetry of large scale wakes in laboratory". *Physics of Fluids*, 18(3):036603. doi:10.1063/1.2179387.

Pessini, F., Olita, A., Cotroneo, Y., and Perilli, A. (2018). "Mesoscale Eddies in the Algerian Basin: do they differ as a function of their formation site?". *Ocean Sci. Discuss.*, 14:669–688. doi:10.5194/os-14-669-2018.

Pessini, F. a. (2019). "Life history of an anticyclonic eddy in the Algerian basin from altimetry data, tracking algorithm and in situ observations". *Journal of Marine Systems*.

Piedeleu, M., Sangrá, P., Sánchez-Vidal, A., Fabrés, J., Gordo, C., and Calafat, A. (2009). "An observational study of oceanic eddy generation mechanisms by tall deep-water islands (Gran Canaria)". *Geophysical Research Letters*, 36(L14605):1–5. doi:10.1029/2008GL037010.

Pinardi, N. and Masetti, E. (2000). "Variability of the large scale general circulation of the Mediterranean Sea from observations and modelling: a review". *Journal of Palaeogeography, Palaeoclimatology, Palaeoecology*, 158:153–173.

Poulin, F. and Flierl, G. (2003). "The Nonlinear Evolution of Barotropically Unstable Jets". *Journal of Physical Oceanography*, 33(10):2173–2192.

Poupkou, A., Zanis, P., Nastos, P., Papanastasiou, D., Melas, D., Tourpali, K., and Zerefos, C. (2011). "Present climate trend analysis of the Etesian winds in the Aegean Sea". *Journal of Theoretical and Applied Climatology*, 106:459–472. doi:10.1007/s00704-011-0443-7.

Project, M. J. M. M. (2010). "ghrsst level 4 mur global foundation sea surface temperature analysis. ver. 2. po.daac, ca, usa.". http://dx.doi.org/10.5067/GHGMR-4FJ01. Dataset Accessed: 2015-11-05.

Puillat, I., Taupier-Letage, I., and Millot, C. (2002). "algerian Eddies lifetime can near 3 years". *Journal of Marine Systems*, 31(4):245–259. doi:10.1016/S0924-7963(01)00056-2.

Pujol, M.-I. and Larnicol, G. (2005). "Mediterranean sea eddy kinetic energy variability from 11 years of altimetric data". *Journal of Marine Systems*, 58:121–142. doi:10.1016/j.jmarsys.2005.07.005.

Pullen, J., Doyle, J. D., May, P., Chavanne, C., Flament, P., and Arnone, R. A. (2008). "Monsoon surges trigger oceanic eddy formation and propagation in the lee of the Philippine Islands". *Journal of Geophysical Research Letters*, 35(7):L07604. doi:10.1029/2007GL033109.

Qiu, B., Chen, S., Klein, P., Sasaki, H., and Sasai, Y. (2014). "Seasonal mesoscale and submesoscale eddy variability along the North Pacific Subtropical Countercurrent". *Journal of Phys. Oceanogr*, 12:3070–3098. doi:10.1175/JPO-D-14-0071.1.

Rio, M.-H., Poulain, P.-M., Pascual, A., Mauri, E., Larnicol, G., and Santoleri, R. (2007). "A Mean Dynamic Topography of the Mediterranean Sea computed from altimetric data, in-situ measurements and a general circulation model". *Journal of Marine Systems*, 65:484–508. doi:10.1016/j.jmarsys.2005.02.006.

Robinson, A. and Golnaraghi, M. (1993). "Circulation and dynamics of eastern Mediterranean Sea; quasi-Synoptic data-driven simulation". *Deep-Sea Research*, 40(6):1207–1246. doi:10.1016/0967-0645(93)90068-X.

Robinson, A., Hetch, A., N.Pinardi, Bishop, J., Leslie, W., Rosentroub, Z., Mariano, A., and Brenner, S. (1987). "Small synoptic/mesoscale eddies and energetic variability of the eastern Levantine basin.". *Nature*, 327(6118):131–134. doi:10.1038/327131a0.

Robinson, A., M.Golnaraghi, W.G.Leslie, A.Artegiani, Hecht, A., Lazzoni, E., Michelato, A., Sansone, E., Theocharis, A., and Unluata, U. (1991). "The eastern Mediterranean general circulation: features, structure and variability". *Dynamics of the Atmosphere and the Oceans*, 15(3-5):215–240. doi:10.1016/0377-0265(91)90021-7.

Robinson, A. R., Leslie, W. G., Theocharis, A., and Lascaratos, A. (2001). "Mediterranean Sea circulation". *Encyclopedia of Ocean Sciences,J. H. Steele, Ed., Academic Press*, pages 1689–1705. https://doi.org/10.1006/rwos.2001.0376.

Roullet, G. and Klein, P. (2010). "Cyclone-anticyclone asymmetry in geophysical turbulence". *Phys. Rev. Lett.*, 104(218501). doi:10.1103/PhysRevLett.104.218501.

Sadourny, R. (1974). "The Dynamics of Finite-Difference Models of the Shallow Water Equations". *Journal of Atmospheric Sciences*, 32:680–689.

Schaeffer, A., Gramoulle, A., Roughan, M., and Mantovanelli, A. (2017). "Characterizing frontal eddies along the East Australian Current from HF radar observations". *J. Geophys. Res. Oceans*. https://doi.org/10.1002/2016JC012171.

Schott, F., Visbeck, M., Send, U., Fischer, J., and Stramma, L. (1996). "Observations of Deep Convection in the Gulf of Lions, Northern Mediterranean, during the Winter of". *Journal of Physical Oceanography*, 26:505–524.

Sofianos, S. S. and Johns, W. E. (2007). "Observations of the summer Red Sea circulation". *Journal of Geophysical Research*, 112(C06025):1–20. doi:10.1029/2006JC003886.

Souza, J. M. A., de Boyer Montégut, C., and Traon, P.-Y. L. (2011). "Comparison between three impleamentations of automatic identification algorithms for the quantification and characterization of mesoscale eddies in the South Atlantic Ocean". *Ocean Sci.*, 7:317–334. https://doi.org/10.5194/os-7-317-2011.

Stegner, A. (2014). "Oceanic Island Wake Flows in the Laboratory, in Modeling Atmospheric and Oceanic Flows: Insights from Laboratory Experiments and Numerical Simulations". *Remote Sensing Letters*, pages 265–276. doi:10.1080/2150704X.2013.872814.

Stegner, A. and Dritschel, D. (2000). "A numerical investigation of the stability of isolated shallow water vortices". *Journal of Physical Oceanography*, 30(10):2562–2573. doi:10.1175/1520-0485(2000)030<2562:ANIOTS>2.0.CO;2.

Stern, M. E. (1965). “Interaction of a uniform wind stress with a geostrophic vortex". *Deep Sea Research and Oceanographic Abstracts*, 12:355–367.

Stumpf, H. G. and Legeckis, R. V. (1977). “Satellite Observations of Mesoscale Eddy Dynamics in the Eastern Tropical Pacific Ocean". *Journal of Physical Oceanograophy*, 7:648–658.

Sutyrin, G., Stegner, A., Taupier-Letage, I., and Teinturier, S. (2009). “Amplification of a Surface-Intensified Eddy Drift along a Steep Shelf in the Eastern Mediterranean Sea". *Journal of Physical Oceonography*, 39:1729–1741. doi:10.1175/2009JPO4106.1.

Taupier-Letage, I. (2008). “On the Use of Thermal Images for Circulation studies: Applications to the Eastern Mediterranean Basin". In Barale, V. and Gade, M., editors, *Remote Sensing of the European Seas*, pages 153–164. Springer Netherlands. doi:10.1007/978-1-4020-6772-3_12.

Taupier-Letage, I., Barbanti, R., El Gindy, A., Emelianov, M., and Fuda, J. (2007). “New Elements on the Surface Circulation in the Eastern Basin of the Mediterranean". *CIESM 38th Congress, Istanbul*, pages 38–204.

Taupier-Letage, I., Millot, C., Fuda, J., Rougier, G., Gerin, R., Poulain, P., Pennel, R., Béranger, K., Emelianov, M., Font, J., Ismail, S. B., and Sammari, C. (2010). “The surface circulation in the Eastern Basin of the Mediterranean and the impact of the mesoscale eddies". *CIESM 39th Congress, Venice, Italy,Rapp. Comm. Int. Mer Medit.*, page 38:189.

Taupier-Letage, I., Puillat, I., Millot, C., and Raimbault, P. (2003). “Biological response to mesoscale eddies in the Algerian Basin". *Journal of of Geophysical Research*, 108:3245. doi:10.1029/1999JC000117.

Teinturier, S., Stegner, A., Viboud, S., and Didelle, H. (2010). “Small-scale instabilities of an island wake flow in a rotating shallow-water layer". *Dynamics of Atmosphere and Ocean*, 49(1):1–24. doi:10.1016/J.Dynatmoce.2008.10.006.

Testor, P., Bosse, A., Houpert, L., Margirier, F., Mortier, L., Legoff, H., Dausse, D., Labaste, M., Karstensen, J., Hayes, D., Olita, A., Schroeder, A. R. K., Chiggiato, J., Onken, R., Heslop, E., Mourre, B., D’ortenzio, F., Mayot, N., Lavigne, H., de Fommervault, O., Coppola, L., Prieur, L., Taillandier, V., de Madron, X. D., Bourrin, F., Many, G., Damien, P., Estournel, C., Marsaleix, P., Taupier-Letage, I., Raimbault, P., Waldman, R., Bouin, M., Giordani, H., Caniaux, G., Somot, S., Ducrocq, V., and Conan, P. (2017). “Multiscale Observations of Deep Convection in the Northwestern Mediterranean Sea During Winter 2012–2013 Using Multiple Platforms". *Journal of Geophysical Research: Oceans*, pages –. https://doi.org/10.1002/2016JC012671.

Testor, P. and Gaspard, J.-C. (2003). “Large-Scale Spreading of Deep Waters in the Western Mediterranean Sea by Submesoscale Coherent Eddies". *Journal of Physical Oceanography*, 33:75–87. doi:.

Theocharis, A., Georgopoulos, D., Lascaratos, A., and Nittis, K. (1993). “Water masses and circulation in the central region of the Eastern Mediterranean: Eastern ionian, South Aegean and Northwest Levantine,1986-1987". *Deep-Sea Research Part II: Topical Studies in Oceanography*, 40(6):1121–1142. doi:10.1016/0967-0645(93)90064-T.

Thomson, R. and Fine, I. (2002). “Estimating Mixed Layer Depth from Oceanic Profile Data". *Journal of Atmospheric and Oceanic Technology*, 20:319–329.

Tramblay, Y., Ruelland, D., Somot, S., Bouaicha, R., and Servat, E. (2013). "High-resolution Med-CORDEX regional climate model simulations for hydrological impact studies: a first evaluation of the ALADIN-Climate model in Morocco". *Journal of Hydrol.Earth Syst.Sci*, 17:3721–3739. doi:10.5194/hess-17-3721-2013.

Tuel, A., Stegner, A., and Le Vu, B. (2016). "Cyclogeostrophic correction of the AVISO surface velocities for intense surface eddies and its application to the Mediterranean Sea. *CIESM The Mediterranean Science Commission*. personal communication.

Tyrlis, E. and Lelieveld, J. (2013). "Climatology and Dynamics of the Summer Etesian Winds over the Eastern Mediterranean". *Journal of Atmospheric Sciences*, 70:3374–3396. doi:10.1175/JAS-D-13-035.1.

Uchida, H., Imawaki, S., and Hu, J. (1998). "Comparison of Kuroshio surface velocities derived from satellite altimeter and drifting buoy data". *J. Oceanogr.*, 54:115–122.

Velaoras, D., Kassis, D., Perivoliotis, L., P.Pagonis, Hondronasios, A., and Nittis, K. (2013). "Temperature and salinity variability in the Greek Seas based on POSEIDON stations time series: preliminary results". *Journal of Mediterranean Marine Science*, pages 5–18. http://dx.doi.org/10.1016/j.jcp.2013.06.025.

Velaoras, D., Krokos, G., Nittis, K., and Theocharis, A. (2014). "Dense intermediate water outflow from the Cretan Sea: A salinity driven, recurrent phenomenon, connected to thermohaline circulation changes". *Journal of Geophysical Research:Oceans*, 119:4797–4820. doi:10.1002/2014JC009937.

Violette, P. E. L., Price, J. A., Mosher, R., and Kotsovinos, N. (1998). "The Surface Ciruclation around Crete Iferred from Satellite, Drifter buoys, AXBTS data and a physical model". *Rapp. Comm. int. Mer Médit.ESM*, 35:1–2.

Viudez, A. (1997). "An Explanation for the Curvature of the Atlantic Jet past the Strait of Gibraltar". *Journal of Physical Oceanography*, 27:1804–1810.

Viudez, A., Haney, R., and Tintoré, J. (1996b). "Circulation in the Alboran Sea as determined by quasi-synoptic hydrographic observations.II: Mesoscale ageostrophic motion diagnosed through density dynamical assimilation". *Journal of Physical Oceanography*, 26:706–724. https://doi.org/10.1175/1520-0485(1996)026<0706:CITASA>2.0.CO;2.

Viudez, A., Tintoré, J., and Haney, R. (1996a). "Circulation in the Alboran Sea as determined by quasi-synoptic hydrographic observations. I: Three dimensional structure of the two anticyclonic gyres". *Journal of Physical Oceanography*, 26:684–705. https://doi.org/10.1175/1520-0485(1996)026<0684:CITASA>2.0.CO;2.

Wang, G., Chen, D., and Su, J. (2007). "Winter Eddy Genesis in the Eastern South China Sea due to Orographic Wind Jets". *Journal of Physical Oceanography*, 38:726–732. doi:10.1175/2007JPO3868.1.

Xu, L., Li, P., Xie, S., Liu, Q., Liu, C., and Gao, W. (2016). "Observing mesoscale eddy effects on mode-water subduction and transport in the North Pacific". *Nature*, 7(10505). doi:10.1038/ncomms10505.

Yim, E., Stegner, A., and Billant, P. (2018). "Stability criterion for the centrifugal instability of surface intensified anticyclones". *J. Phys. Oceanography in press*. https://doi.org/10.1175/JPO-D-18-0088.1.

Yoshida, S., Qiu, B., and Hacker, P. (2010). "Wind generated eddy characteristics in the lee of the island of Hawaii". *Journal of Geophysical Research: Oceans*, 115(C3):C03019. doi:10.1029/2009JC005417.

Zecchetto, S. and Biasio, F. D. (2007). “Sea Surface Winds over the Mediterranean Basin from Satellite Data (2000–04): Meso- and Local-Scale Features on Annual and Seasonal Time Scales". *Journal of Applied Meteorology and Climatology*, 46:814–827. doi:10.1175/JAM2498.1.

Zervakis, V., Papadoniou, G., Tziavos, G., and Lascaratos, A. (2003). Seasonal variability and geostrophic circulation in the eastern mediterranean as revealed through a repeated XBT transect. *Annales Geophysicae.Atmospheres, Hydrospheres and Space Sciences*, 21(1):33–47. doi:10.1002/joc.1108.

Zhai, P. and Bower, A. (2013). “The response of the Red Sea to a strong wind jet near the Tokar Gap in summer". *Journal of Geophysical Research: Oceans*, 18:422–434. doi:10.1029/2012JC008444.